The analysis of dynamically loaded flexible journal bearings using higher-order finite elements.

McIvor, James David Colin

THE ANALYSIS OF DYNAMICALLY LOADED FLEXIBLE JOURNAL BEARINGS USING HIGHER-ORDER FINITE ELEMENTS

by

JAMES DAVID COLIN Mc IVOR B.Sc.(Eng)

A Thesis submitted for the degree of

Doctor of Philosophy

in the University of London.

Kings College London

(Department of Mechanical Engineering)

1988

To Mum and Dad

Abstract

An efficient and robust predictive technique has been developed for the analysis of dynamically loaded, flexible journal bearings using the finite element method. The work is in two parts. In the first part a fast predictive technique is developed for the analysis of dynamically loaded, rigid journal bearings. The finite element formulation of Reynolds equation is presented using both 3-node triangular and 8-node isoparamteric elements to model the lubricant film. The latter are shown to approximate the problem more closely using fewer nodal points and hence requiring fewer equations. The Gauss-Seidel over-relaxation method is used to solve the resulting system equations and the sparseness of these equations is exploited. Comprehensive results are presented for the Ruston and Hornsby 6VEB Mk III marine diesel engine connecting rod bearing. Two different time stepping methods are considered and the effects of incorporating various oil feed features in the analysis are also presented.

The second part of the work deals with the flexible bearing problem. The method of carrying out the structural modelling and the way in which the structural compliance relationships are obtained is described. A fast matrix inversion technique used to obtain these relationships is also described. Based on the rigid bearing work 8-node isoparametric elements are used to model the lubricant film. Two methods are presented for coupling the structural and lubrication analysis. The first method, the under-relaxation method, although proving straightforward to implement is shown to be unsatisfactory for this particular problem due to to convegnence problems. The second method is the Newton-Raphson method which is shown to be highly convergent. The Newton-Raphson method is subsequently highly modified to produce a fast solution method. This is shown to be several orders of magnitude faster than any previously developed method making this technique viable as a general design tool rather than just providing benchmarks against which to compare simpler analysis techniques. Again results are presented for the Ruston bearing showing the effect upon the predicted performance of incorporating elasticity into the analysis.

Acknowledgements

I am indebted to Dr D. N. Fenner for his continuous supervision and guidance during my work.

My thanks are given to :

Professor S. W. E. Earles for his help and suggestions.

Mr F. A. Martin for his encouragement and advice.

Mr P. di Cara and Mr D. Courtnell for their sometimes tireless efforts in providing the necessary computing facilities..

Linda for the meals and support.

The Department of Education for Northern Ireland for providing financial support for this work.

CONTENTS

			Page
Abstract			**3**
Acknowledgements			**4**
Contents			**5**
List of Figures			**8**
Nomenclature			**12**
Chapter	**1:**	**Introduction**	**14**
	1.1	Hydrodynamic lubrication	14
	1.2	Bearing analysis techniques	15
	1.3	Outline of the present *i* nvestigation	20
Chapter	**2:**	**Governing Equations**	**22**
	2.1	Introduction	22
	2.2	Reynolds equation	22
	2.3	Load generated and attitude angle	27
	2.4	Power loss in bearings	27
	2.5	Sommerfeld infinite bearing theory	30
	2.6	Narrow bearing theory.	32
Chapter	**3:**	**The Finite Element Method**	**39**
	3.1	Introduction	39
	3.2	Finte element discretisation and element types	39
	3.3	Finite element formulation for the rigid bearing problem	43
	3.4	Equation formulation	46
	3.4.1	Triangular element formulation	46
	3.4.2	Quadrilateral element formulation	48
	3.5	System matrices formulation	50
Chapter	**4:**	**Rigid Bearing Analysis**	**54**
	4.1	Introduction	54

	4.2	Solution method	56
	4.2.1	Successive over-relaxaton	56
	4.2.2	Cavitation	57
	4.2.3	Boundary conditions and oil feed	58
	4.2.4	Solution region and wrap around	59
	4.2.5	Calculation of the load vector	59
	4.2.6	Dynamic time stepping	60
	4.2.6.2	Implicit and explicit time stepping	64
	4.2.6.3	Squeeze term verification	65
	4.3	Relaxation optimisation	66
	4.4	Dynamically loaded engine cycle	69
	4.4.1	Load interpolation	69
	4.4.2	Startup	69
	4.4.3	Solution extrapolation	70
	4.5	Output parameters	70
	4.6	Choice of element type	72
	4.7	Results	73
	4.7.1	Sample bearing example	73
	4.7.2	Comparison of element types	74
	4.7.3	Time stepping and effect of time step size	77
	4.7.4	Effect of oil feed	79
	4.7.5	Other bearing examples	80
	4.8	Summary	81
Chapter	**5:**	**Structural Modelling and Compliance Matrix**	**124**
	5.1	Introduction	124
	5.2	Film thickness equations	124
	5.3	Finite element structural model.	125
	5.4	Stuctural compliance matrix.	127
Chapter	**6:**	**The Under-relaxation Solution Method.**	**139**
	6.1	Introduction	139
	6.2	Steady state analysis	145
	6.3	Dynamic loading	149

	6.4	Conclusions	151
Chapter	**7:**	**The Newton-Raphson Solution Method**	**157**
	7.1	Introduction	157
	7.2	Equation derivation	159
	7.2.1	The Newton-Raphson method	159
	7.2.2	Application to the lubrication problem	160
	7.2.3	Element matrix assembly	166
	7.3	Film cavitation	166
	7.4	Solution procedure	167
	7.4.1	The full Newton-Raphson method	167
	7.4.2	Modified Newton-Raphson method	168
	7.5	Results	172
	7.5.1	Example considered	172
	7.5.2	Graphics software	172
	7.5.3	Comparison of Newton-Raphson Methods	173
	7.5.4	Steadily loaded case	174
	7.5.5	Dynamic loading	175
	7.6	Summary	177
Chapter	**8:**	**Conclusions**	**209**
	8.1	Rigid bearing work	209
	8.2	Flexible bearing work	210
	8.3	Future work	212
References			**213**

List of Figures

Figure		Page
2.1	Stressed element in fluid	34
2.2	Flow into and out of fluid volume	35
2.3	Journal bearing configuration	36
2.4	Bearing load vector and components	37
2.5	Normal and shear tractions on fluid film	38
3.1	Examples of finite element meshes used to model the lubricant film	52
3.2	Element types used for the lubrication analysis	53
4.1	Finite element mesh showing redundant nodes	83
4.2	Flow diagram for journal position iterations	84
4.3	Journal centre orbit under static load	85
4.4	Journal and housing with rotating load	86
4.5	Journal centre orbit with steady rotating load	87
4.6	Number of iterations against tolerance for SOR	88
4.7	Effect of number of circumferential nodes on wf_{opt}	89
4.8	Effect of number of axial nodes on wf_{opt}	90
4.9	Effect of number of circumferential nodes using 3-node triangular elements	91
4.10	Number of nearest nodes for two different element types	92
4.11	Convergence of positive pressure region	93
4.12	Polar load diagrams	94
4.13	Steady state and transient response	95
4.14	Comparison of load and minimum film thickness position relative to the connecting rod axis	96
4.15	Interpolation scheme to find P_{max} for 8-node isoparametric elements	97
4.16	Polar load diagram for the Ruston and Hornsby 6VEB Mk III connecting rod, relative to connecting rod	98

4.17	Comparison of (a) calculated values of h_{min} and (b) Cyclic power loss	99
4.18	Comparison of journal centre orbits using the two element types	100
4.19	Variation of calculated load with number of circumferential nodes for (a) eccentricity=0.5 and (b) eccentricity=0.9	101
4.20	Illustration of way in which different mesh postions can result in different values of P_{max}	102
4.21	Variation of W as position of h_{min} moves relative to mesh	103
4.22	Cyclic variation of peak film pressure using 3-node triangular mesh	104
4.23	Cyclic variation of peak film pressures calculated using an 8-node isoparametric element mesh	105
4.24	Comparison of (a) peak film pressure and (b) computing time	106
4.25	Comparison of eccentricity for (a) medium and (b) heavy load	107
4.26	Comparison of peak film pressure for (a) medium and (b) heavy load	108
4.27	Comparison of predicted power loss for (a) medium and (b) heavy loads	109
4.28	Comparison of predicted side flow for (a) medium and (b) heavy loads	110
4.29	Comparison of journal centre orbits obtained using explicit and implicit time stepping methods	111
4.30	Comparison of peak film pressures using explicit and implicit time stepping methods	112
4.31	Predicted bearing power loss using explicit and implicit time stepping	113
4.32	Predicted side flow out of the bearing using explicit and implicit time stepping methods	114
4.33	Effects on journal centre orbit of full circumferential oil feed groove	115
4.34	Effect on journal centre orbit of partial groove in cap half of the bearing	116

4.35	Effect on journal centre orbit of partial groove in rod half of the bearing	117
4.36	Effect on journal centre orbit of an oil supply groove at 0 degrees	118
4.37	Distribution of the load on the bearing at discrete time steps relative to the connecting rod axis	119
4.38	Journal centre orbit for intermain bearing	120
4.39	Journal centre orbit for high speed connecting rod bearing	121
4.40	Predicted side flow for intermain bearing	122
5.1	Three-dimensional model of big-end bearing shown using mesh generation preprocessor	134
5.2	(a) Equivalent nodal point forces for the 8-node isoparametric element (b) 20-node brick element and 8-node isoparametric element showing coincident nodes	135
5.3	2D finite element ring element using 8-node brick elements	136
5.4	3D finite element model of connecting rod bearing using 20-node brick elements. Shaded portion is totally restrained	137
6.1	Schematic representation of (a) conventional and (b) simultaneous column multiplication	153
6.2	Applying under-relaxation to the film thickness	154
6.3	Applying under-relaxation to the pressure	155
6.4	Applying under-relaxation to the film thickness and pressure	156
7.1	The Newton-Raphson solution method applied to the EHD journal bearing problem	181
7.2	Typical frame produced by animated post processing software	182
7.3	Steady loaded flexible bearing (a) Min film thickness (b) Peak film pressure	183
7.4	Steady loaded flexible bearing (a) Power loss and (b) Side flow	184
7.5	Steady loaded bearing performance (a) Min film thickness (b) Peak film pressure	185
7.6	Steady loaded bearing performance (a) Power loss (b) Side flow	186

7.7	Midplane pressure profile for a rigid and elastic bearing under a steady load	187
7.8	Midplane film profile for a rigid and elastic bearing under a steady load	188
7.9	Comparison of journal centre orbits using 41x5 and 61x5 meshes	189
7.10	Comparison of journal centre orbits using 41x5 and 41x7 meshes	190
7.11	Peak film pressures obtained using 41x5 and 61x5 meshes	191
7.12	Peak film pressures obtained using 41x5 and 41x7 meshes	192
7.13	Effect of varying time step on predicted journal centre orbit	193
7.14	Peak film pressures obtained using 2 degrees and 1 degree time steps	194
7.15	Comparison of predicted journal centre orbits for the rigid and elastic bearing examples	195
7.16	Comparison of the predicted peak film pressures for the rigid and elastic bearing examples	196
7.17	Cyclic variation of the minimum film thickness for the rigid and elastic bearing examples	197
7.18	Cyclic power loss for the rigid and elastic bearing examples	198
7.19	Predicted side flow for the rigid and elastic bearing examples	199
7.20	Midplane pressure variation during an engine cycle for the rigid and elastic bearing	200
7.21	Vector plot of peak film pressure for the rigid bearing	201
7.22	Vector plot of peak film pressure for the elastic bearing	202
7.23	Vector plot of bearing loads	203
7.24	Pressure map for the rigid bearing example	204
7.25	Pressure map for the elastic bearing example	205
7.26	Variation of midplane film profile during engine cycle	206
7.27	Data plot at 360 degrees crank angle	207
7.28	Data plot at 0 degrees crank angle	208

Nomenclature

Symbols

a	weighting factor for Gauss-Legendre quadrature
A^e	area of element
B	length to diameter ratio
c	radial clearance
D	bearing diameter
E	Youngs modulus
e	eccentricity
F	load
H	power loss
h	oil film thickness
h_{def}	housing deformation
L	bearing length
$\dot{m}$	mass flow rate
M	number of circumferential nodes
N	shape function
P	oil film pressure
P_c	cavitation pressure
P_o	atmospheric pressure
P_s	oil supply pressure
q	oil flow
R	bearing radius
R_e	Reynolds number
T	friction torque
t	time
U	surface velocity
$\overline{U}$	average fluid velocity
u	velocity in x direction
u_r	radial displacement
v	velocity in y direction
W	bearing load

W_a	externally applied load
w	velocity in z direction
w_f	weighting factor for under-relaxation
wf	weighting factor for over-relaxation
z	coordinate in axial direction

Greek Symbols

α	crank angle
ε	eccentricity ratio e/c
η	local element coordinate
μ	dynamic viscosity
ν	Poissons ratio
ω	angular velocity
$\overline{\omega}$	average fluid angular velocity
ψ	attitude angle
ρ	density
τ	shear stress
θ	angle measured around the bearing
$\dot{\theta}_r$	relative angular velocity of two bearing surfaces
ξ	local element coordinate

Chapter 1

Introduction

1.1 Hydrodynamic Lubrication

Hydrodynamic lubrication deals with two surfaces in relative motion separated by a load carrying fluid film. Hydrodynamically lubricated bearings, which allow relative motion between machine elements and transmit loads, may be divided into two main types : those used to support or transmit radial loads, and those used to support thrust or axial loads. In the former category the most common type of bearing is the journal bearing, the analysis of which is one of the most important aspects of hydrodynamic theory.

A journal bearing consists of a central journal or shaft moving inside a housing. Journal and housing are normally cylindrical with a small clearance between the two surfaces for the lubricant. Either surface may contain holes or grooves to supply lubricant essential for the bearing operation and for certain applications the housing may be irregularly shaped.

One of the main applications of journal bearings in engineering is the connecting rod bearings and main bearings in an internal combustion engine. The connecting rod transmits the driving force from the piston through the big-end bearing to the crankshaft and the main bearings support the crankshaft. To achieve the high performance and reliability that these bearings are required to provide it is essential that the bearing performance can be predicted with a high degree of confidence at the design stage.

The main bearing parameters that the bearing designer is interested in are :

i) The minimum oil film thickness

ii) The power loss in the bearing

iii) The peak pressures generated in the oil film

iv) The flow of oil out of the bearing

The minimum oil film thickness is perhaps of most interest to the designer. It is a useful comparator for comparing the performance of similar engines and relating the predicted performance to experimental results. If it falls below a certain value during the engine cycle bearing damage may occur. This value depends on a

number of factors such as surface roughness, bearing alignment, temperature and oil feed. The minimum oil film thickness is generally of the order of a few microns.

The hydrodynamic power loss is important for heat balance calculations to determine the effective viscosity of the lubricant which is required for other bearing calculations. It provides an indication of how efficiently the bearing is operating and clearly it is desirable to minimise the power loss though reducing engine friction too much in highly loaded bearings can have an adverse effect on the bearing durability.

The peak pressures generated in the bearing can also serve as a useful comparator for bearing performance. The pressures are also required for calculating fatigue loading on the housing and for identifying the most highly loaded parts of the bearing.

The side flow or leakage from the bearing is required when calculating the engine heat balance. It is also required to determine if adequate oil feed features have been included in the bearing and for estimating the required oil pump capacity.

With the need to conserve energy, and with engines being designed to be lighter, engine bearings are being made smaller and are required to operate under higher loads with lower viscosity oils. In some cases bearings are therefore operating close to their limits of performance. This means it is increasingly important that the bearing performance can be predicted as accurately and realistically as possible at the design stage. Although many design techniques have been developed for the predictive analysis of engine bearings there is still a need to develop analysis techniques that allow the designer to consider more realistic operating conditions and to give greater understanding and insight into the processes occuring at the bearing and how these affect the bearing performance.

1.2 Bearing analysis techniques

The theoretical analysis of engine bearings is primarily based upon the solution of Reynolds equation, derived by Osborne Reynolds [1], which governs the generation of pressure in the lubricant film. Since the analytical solution of this partial differential equation is not generally possible early techniques for predicting bearing behaviour relied on no more than a rough assessment of the bearing operating

conditions and the experience of the designer with his knowledge of other bearings.

Initial attempts to solve Reynolds equation were achieved by making major assumptions about the bearing, such as the early work by Sommerfeld [2] who neglected pressure derivatives in the axial direction in order to achieve a closed-form analytical solution. An alternative method proposed by Mi chell [3], and later developed by Ocvirk and DuBois [4], neglected the circumferential pressure derivatives by assuming that the pressures were determined primarily by the conditions at the bearing edges. A comprehensive review paper by Campbell et al [5] presents a study of early bearing analysis methods. Most of these methods are only useful for assessing bearing behaviour on a qualitative and not quantitative basis. They can not accurately model oil feed features such as holes or grooves, and in some cases they over simplify the boundary conditions. One of the most notable of these early methods was a graphical method, the mobility method, developed by Booker [6]. This method, based on the short bearing theory, is still used extensively today for dynamically loaded bearing analysis and relies upon splitting the journal motion into two separate components, squeeze and whirl. This enables a dynamic analysis to be carried out without having to use iterative techniques. As pointed out by Jones [7] this technique is only really suitable for bearings with no oil feed features and medium eccentricities.

With the advent of the digital computer a third method for journal bearing analysis, along with theoretical and experimental methods, became available. Although experimental work is invaluable, and theoretical analysis provides useful results and can give quick solutions, numerical methods allow a more rigorous analysis to be carried out at the design stage. Numerical techniques such as the finite difference (FD) and finite element (FE) methods have been developed. These methods rely upon carrying out a large number of calculations, which is ideally suited to computerisation, to approximate Reynolds equation over the bearing. This allows complex boundary conditions such as oil feed features to be incorporated into the analysis and makes it possible to solve the finite bearing problem.

One of the earliest solutions for the finite journal bearing problem was achieved by Christopherson [8] using finite difference methods to model the oil film and a relaxation technique to solve the resulting set of equations to incorporate the Reynolds zero pressure gradient boundary condition. Similar methods were

employed by several other authors [9,10,11,12] enabling design charts to be developed to allow designers to more accurately predict finite journal bearing behaviour. The application of the finite difference method to the solution of Reynolds equation is covered in depth by Holmes and Ettles [13] who consider five different finite difference formulations and several different iterative schemes to solve the resulting set of equations.

The main difficulties with the finite difference method were incoporating irregularly shaped boundaries and graded meshes in the analysis. The finite element method can achieve this in a routine fashion and has been shown [14] to be superior to the finite difference method when applied to the lubrication problem. It was first applied to field problems by Zienkiewicz and Cheung [15] and Visser [16], the early development of functionals for the solution of the lubrication problem by Hayes [17] and Tao [18] provided the possibility of applying the finite element method to the lubrication problem. One of the earliest applications of the finite element method was by Reddi [19] who considered the incompressible lubrication problem, this work was later extended to cover the compressible lubrication problem by Reddi and Chu [20]. An extensive presentation of the finite element method as applied to the lubrication problem is given by Booker and Huebner [21]. The finite element method is now well-established as a useful and versatile method for journal bearing analysis. Goenka [22] at General Motors recently demonstrated the full versatility of the method by analysing 17 different bearing cases with a wide variety of shapes and oil feed features. Goenka [23] also produced a rapid curve fitting program using the results from a finite element analysis to predict the performance of an ideal bearing reducing the computer time by an order of magnitude.

The advances made in computer techniques has also meant that more realistic boundary conditions and oil flow effects can be incorporated into the bearing analysis. Early work simply considered that the pressure region extended over half of the bearing surface (π solution). More realistic conditions such as the Reynolds boundary condition are easily incoporated into numerical solution methods as shown by Christopherson [8] and Goenka [22] . Rohde and Mc Allister [24] showed that this boundary condition resulted from the variational formulation rather than being a condition imposed upon it.

The more comprehensive flow boundary conditions proposed by Jakobssen and Floberg [25] and Olsson [26] (the JFO theory) which takes into account oil transport within the cavitated region, proved considerably more complicated to implement. Elrod and Adams [27] developed an algorithm for incorporating this boundary condition by solving for a modified pressure variable. This analysis was developed further by Elrod [28] and was extended to the analysis of dynamically loaded bearings by Brewe [29]. Milne [30,31,32] working at the National Engineering Laboratory, adopted a more complex approach for keeping track of the oil flow by using a movable finite element mesh to locate the flow boundary examining both steady state and transient bearing behaviour. An easier method to keep track of the oil flow or ' oil film history ' using a fixed mesh, was developed by Jones [7,33] at the Glacier Metal Co. This method considered the internodal flows using control volumes around each node, a similar approach was adopted by Jakeman [34,35]. This work showed that in certain cases the oil film history could have a very marked effect on the predicted bearing perfromance.

The effect of incorporating the elastic distortion of the bearing housing, caused by the high pressures generated in the oil film, has also been shown to have a significant effect on the predicted bearing performance. The distortion of the housing can be several times greater than the predicted minimum film thickness which is typically of the order of a few microns. There has been a large amount of work carried out to investigate the elastohydrodynamic (EHD) behaviour of highly loaded contacts such as gear teeth. This work is extensively covered by Dowson and Higginson [36]. However, until recently there has been little work carried out on the EHD behaviour of journal bearings. This is due to the problems encountered with coupling the structural and lubrication analysis, which leads to a highly nonlinear problem, and the difficulties of modelling the housing accurately. With improved computing capabilities, especially memory and processing speed, and the development of more rigorous analysis techniques, especially the finite element method for structural modelling, it has become possible to attempt to examine this problem. Taylor and O'Callaghan [37] were amongst the first to apply the FE method to the lubrication problem They used a high degree of under-relaxation to couple the structural and lubrication problems which lead to a highly iterative solution procedure. This method has proved fairly straightforward to implement and has been used by a large number of authors [37-45]. All of this work has shown that the

bearing flexibility can significantly alter the predicted bearing performance.

The main problems with the under-relaxation method are the large number of iterations required and achieving a converged solution under heavy loading. This has meant that for a dynamically loaded bearing the required computing time for a complete analysis has proved prohibitively high, unless major simplifications are made.

Rohde and Oh [46] developed a robust, highly convergent method for predicting the EHD bearing performance by applying the Newton-Raphson method to the problem. Oh and Goenka [47] at General Motors recently presented the results of the analysis of a dynamically loaded engine bearing using this method. The computing time for the analysis was in the region of 35 hours which made it impractical as a design tool. In an attempt to improve upon this Goenka and Oh [48] proposed a short bearing theory which reduced the required computer time by an order of magnitude but showed some major discrepancies with the more rigorous analysis. Combining these two techniques [49] though provided the means for optimising a connecting rod design. The short bearing method was used on a qualitative basis to optimise the design and the more rigorous method was used at the final stages to obtain an accurate prediction of the bearing performance.

From the work carried out in journal bearing analysis it is clear that although simple, fast, analytical methods can provide useful information about bearing behaviour more rigorous methods are essential for obtaining a better understanding of the processes behind the bearing behaviour and for analysing the effect of incorporating new features into bearing design. The advances made in modern computer facilities and techniques have meant that previously lengthy and memory intensive forms of numerical analysis are more readily available to the designer. However with the need to integrate the bearing analysis into the design of the engine as a whole it is important that more efficient and realistic predictive techniques are developed, especially in the field of EHD lubrication.

1.3 Outline of the present investigation

The main object of the work described in this thesis was to develop an efficient finite element model for the predictive analysis of dynamically loaded flexible journal bearings.

Initially, as a first step towards this and to gain a better understanding of the problem, a fast predictive technique was developed for the analysis of dynamically loaded, rigid journal bearings. The finite element method was used to formulate Reynolds equation over the solution domain using 3-node triangular and 8-node isoparametric elements to model the lubricant film. The 8-node isoparametric elements were found to approximate the problem more closely than the 3-node elements requiring fewer nodal points and hence resulting in fewer equations [50]. The Gauss-Seidel over-relaxation solution method was used to solve the resulting equations for the nodal pressures using an algorithm similar to that used by Christopherson [8] to apply the non-negativity constraint upon the pressure distribution. The sparseness of the system equations was fully exploited and it was found that due to the high convergence rate of the Gauss-Seidel method the number of equations to be solved could be considerably reduced by exploiting the early definition of the cavitation region. Comprehensive results were obtained for the Ruston and Hornsby 6VEB Mk III marine diesel engine big-end bearing. Two different time stepping methods, the implicit and explicit methods, were investigated. It was found that the explicit method, although proving unstable when a large time step was employed, was considerably more efficient than the implicit method. The effects of incorporating various oil feed features in the analysis were also investigated and the results compared with similar work carried out by Goenka at General Motors [22].

The second part of the investigation was concerned with the flexible bearing problem. 8-node isoparametric elements were used to model the lubricant film and 20-node brick elements were used for the finite element structural analysis. From the structural analysis a structural compliance relationship was obtained in the form of a compliance matrix relating the nodal deformations to the nodal pressures which was then used in the lubrication part of the analysis. A fast matrix inversion technique was also developed which was used to obtain the compliance matrix.

Two methods were investigated for coupling the structural and lubrication analysis. The first of these, the under-relaxation method, proved straightforward to

implement but was unsatisfactory for this particular problem. This was due to the convergence problems encountered caused by the variation of the bearing load during the engine cycle. The second method that was used was the Newton-Raphson method which proved to be highly convergent for a wide range of load conditions but required a prohibitively large amount of computing time. This method was therefore subsequently highly modified to produce a fast solution method [51]. This proved to be several orders of magnitude faster than previous methods that had been developed by other workers making this method viable as a general design tool rather than a method for providing benchmarks against which to compare more simplified analysis techniques. Results were again presented for the Ruston bearing showing the effect upon the predicted performance of incorporating elasticity into the analysis.

Chapter 2

Governing Equations

2.1 Introduction

The analysis of hydrodynamically lubricated bearings is based upon the solution of Reynolds equation. This equation was derived by Osborne Reynolds [1] from the Navier-Stokes equations of fluid flow in an attempt to determine the generation of pressure in a lubricant film between two surfaces in relative motion.

Since the turn of the century this equation has been used in many forms to solve problems in fluid film lubrication. More recently, with the advances in computational solution techniques, more exact solutions have been achieved for a wide variety of problems, previously only possible analytically by making major simplifying assumptions.

In this chapter Reynolds equation is derived for the hydrodynamic journal bearing problem using appropriate assumptions. The equations for calculating the power loss in the bearing are also developed and the two most common analytical solutions of Reynolds equation are presented.

2.2 Reynolds equation

In order to derive Reynolds equation for the hydrodynamic journal bearing problem the following assumptions are made :

i) The flow is laminar.

In most engine bearings the dimensions and speeds are such that Reynolds number R_e is well below the critical value for the onset of turbulence so it is reasonable to assume laminar flow.

ii) The fluid is Newtonian.

That is the shear stress, τ, is related to the shear rate, $\partial u/\partial y$, through the viscosity , μ, as $\tau = \mu\frac{\partial u}{\partial y}$.

iii) The viscosity is constant through the film thickness.

iv) The fluid inertia forces may be neglected.

Provided that R_e is low the inertia forces are negligible compared to the viscous shear forces.

v) Body forces may be neglected..

This means that there are no external forces acting on the lubricant such as graviational or magnetic field forces.

vi) There is no slip at the solid liquid interface.

vii) The pressure is constant through the oil film.

As the oil film is very thin there can be no significant pressure variation across it.

viii) The curvature of the bearing surfaces is very large compared to the film thickness.

Consider two surfaces, one moving with velocities U_1 and V_1, the other with velocities U_2 and V_2 (Figure 2.1). For an infinitesimally small volume of liquid with the axes shown of side dx, dy and dz on which pressure and shear stresses act, the fluid velocities are u,v and w in the x,y and z directions. Equating forces in the x direction, assuming fluid acceleration effects are negligible, we have

$$p\ dy\ dz+(\tau_x+\frac{\partial \tau_x}{\partial y})\ dx\ dz-(p+\frac{\partial p}{\partial x}dx)\ dy\ dz-\tau_x\ dx\ dz = 0 \qquad (2.1)$$

where p and τ are the pressure and shear stress. Multiplying out (2.1) and cancelling, the expression reduces to

$$\frac{\partial p}{\partial x} = \frac{\partial \tau_x}{\partial y} \qquad (2.2)$$

where the shear stress is defined by (assumption (ii))

$$\tau_x = \mu\frac{\partial u}{\partial y} \qquad (2.3)$$

Combining (2.2) and (2.3) gives

$$\frac{\partial p}{\partial x} = \mu\frac{\partial^2 u}{\partial y^2} \qquad (2.4)$$

Similarily in the z direction

$$\frac{\partial p}{\partial z} = \mu \frac{\partial^2 w}{\partial y^2} \tag{2.5}$$

Note that there is no pressure variation in the y direction (assumption (vii))

Equations (2.4) and (2.5) may be integrated with respect to y, since the pressure is independent of y, to give

$$u = C_1 + C_2 + \frac{1}{2\mu} y^2 \frac{\partial p}{\partial x} \tag{2.6}$$

$$w = C_3 + C_4 + \frac{1}{2\mu} y^2 \frac{\partial p}{\partial z} \tag{2.7}$$

where C_1 ,C_2 ,C_3 and C_4 are the constants of integration.
Applying the boundary conditions of the system, given by

$$u = U_1 \; at \; y = 0 \; , \; u = U_2 \; at \; y = h$$

$$w = 0 \; at \; y = 0 \; , \; w = 0 \; at \; y = h$$

to (2.6) and (2.7) we obtain

$$u = U_1 + \frac{(U_2 - U_1)}{h} y - y \frac{(h-y)}{2\mu} \frac{\partial p}{\partial x} \tag{2.8}$$

and

$$w = -y \frac{(h-y)}{2\mu} \frac{\partial p}{\partial z} \tag{2.9}$$

The next step in the derivation is to consider flow continuity. Considering the volume flow rate per unit width, the flows in the x and z direction are calculated by integrating the velocities across the film thickness, h, to give

$$q_x = \int_0^h u \; dy = \overline{U}h - \frac{h^3}{12\mu} \frac{\partial p}{\partial x} \tag{2.10}$$

$$q_z = \int_0^h w \; dy = -\frac{h^3}{12\mu} \frac{\partial p}{\partial z} \tag{2.11}$$

where

$$\bar{U} = \frac{(U_1+U_2)}{2}$$

is the average fluid velocity in the oil film. Considering a volume of fluid of cross section $dx\ dz$ extending across the film thickness h (Figure 2.2), the net mass flow rate out of the volume is given by

$$\dot{m} = \frac{\partial}{\partial x}(\rho q_x)\ dx\ dz + \frac{\partial}{\partial z}(\rho q_z)\ dx\ dz \tag{2.12}$$

where ρ is the fluid density. To satisfy flow continuity this must equal the rate of change of mass in the volume and therfore

$$\frac{\partial}{\partial x}(\rho q_x)\ dx\ dz + \frac{\partial}{\partial z}(\rho q_z)\ dx\ dz = -\rho(V_2-V_1)\ dx\ dz \tag{2.13}$$

where V_2-V_1 can be expressed as the rate of change of film thickness $\partial h/\partial t$. Substituting equations (2.10) and (2.11) into (2.13) gives

$$\frac{\partial}{\partial x}\left[\frac{\rho h^3}{12\mu}\frac{\partial p}{\partial x}\right] + \frac{\partial}{\partial z}\left[\frac{\rho h^3}{12\mu}\frac{\partial p}{\partial z}\right] = \frac{\partial}{\partial x}(\rho \bar{U} h) + \frac{\partial(\rho h)}{\partial t} \tag{2.14}$$

Assuming the flow is incompressible, and that therefore ρ is constant we have

$$\frac{\partial}{\partial x}\left[\frac{h^3}{12\mu}\frac{\partial p}{\partial x}\right] + \frac{\partial}{\partial z}\left[\frac{h^3}{12\mu}\frac{\partial p}{\partial z}\right] = \frac{\partial}{\partial x}(\bar{U} h) + \frac{\partial h}{\partial t} \tag{2.15}$$

which is Reynolds equation in two dimensions for incompressible flow.

For the journal bearing problem Reynolds equation is expressed in a slightly different form. Figure 2.3 shows a journal bearing and housing with the appropriate sign convention. In this case the film thickness h is expressed as

$$h = c(1+\varepsilon\cos\theta) \tag{2.16}$$

where c is the radial clearance and ε is the eccentricity ratio given by

$$\varepsilon = \frac{e}{c} \tag{2.17}$$

The x coordinate, which is the distance around the bearing, is expressed as

$$x = R\theta$$

and therefore

$$\frac{\partial}{\partial x} = \frac{1}{R}\frac{\partial}{\partial \theta}$$

where R is the bearing radius and Reynolds equation for the bearing problem now becomes

$$\frac{\partial}{R^2 \partial \theta}\left[\frac{h^3}{12\mu}\frac{\partial p}{\partial \theta}\right] + \frac{\partial}{\partial z}\left[\frac{h^3}{12\mu}\frac{\partial p}{\partial z}\right] = \frac{1}{R}\frac{\partial}{\partial \theta}(\bar{U}h) + \frac{\partial h}{\partial t} \qquad (2.18)$$

It is useful to express this equation in dimensionless form using the following dimensionless quantities (where * indicates a dimensionless quantity) :-

$$z^* = z/L$$

$$h^* = h/c$$

$$B = R/L$$

$$p^* = pc^2/(6\omega_c R^2 \mu)$$

where R is the bearing radius, L is the bearing length and ω_c is the crank angular velocity.

Reynolds equation now becomes

$$\frac{\omega_c}{2}\frac{\partial}{\partial \theta}\left[h^{*3}\frac{\partial p^*}{\partial \theta}\right] + B^2\frac{\omega_c}{2}\frac{\partial}{\partial z^*}\left[h^{*3}\frac{\partial p^*}{\partial z^*}\right] = \frac{1}{R}\frac{\partial(h^*\bar{U})}{\partial \theta} + \frac{\partial h^*}{\partial t} \qquad (2.19)$$

Since the bearing load is defined as function of crank angle , α , it is convenient to take α as the dimensionless time variable where

$$\omega_c = \frac{d\alpha}{dt} \qquad (2.20)$$

Measuring relative to one of the two surfaces, the surface velocies are therefore given by

$$U_1 = 0 \, , \, U_2 = \frac{d\theta_r}{dt}R \qquad (2.21)$$

where $d\theta_r/dt$ is the relative angular velocity between the two surfaces. Further assuming that U is not a function of θ,

Reynolds equation may be written as (dropping * for clarity)

$$\frac{\partial}{\partial\theta}\left[h^3\frac{\partial p}{\partial\theta}\right]+B^2\frac{\partial}{\partial z}\left[h^3\frac{\partial p}{\partial z}\right]=\frac{d\theta_r}{d\alpha}\frac{dh}{d\theta}+2\frac{dh}{d\alpha} \tag{2.22}$$

This is the two-dimensional incompressible Reynolds equation in dimensionless form applied to the journal bearing problem.

2.3 Load generated and attitude angle

The resultant load vector caused by the pressures generated in the oil film is obtained by integrating the pressures over the bearing surface. For a small element on the bearing surface of side $r\partial\theta$ by dz at an angle θ and at a pressure p (Figure 2.4), the resultant load caused by the pressure, p , is $pRd\theta dz$. This load will have x and y components $pRd\theta dz\cos\theta$ and $pRd\theta dz\sin\theta$ and, ignoring the effect of shear stresses, the resultant load vectors in the x and y directions may then be obtained from

$$W_x=\int_0^L\int_0^{2\pi} p\cos\theta\, R\; d\theta\, dz \tag{2.23}$$

$$W_y=\int_0^L\int_0^{2\pi} p\sin\theta\, R\; d\theta\, dz \tag{2.24}$$

The attitude angle ψ, which is the angle between the line of centres and the resultant load vector, is given by

$$\psi=\tan^{-1}(W_y/W_x)-\tan^{-1}(e_y/e_x) \tag{2.25}$$

where e_x and e_y are the x and y components of the bearing eccentricity.

2.4 Power loss in bearings

The power loss in a journal bearing is made up of two components, one due to the shear tractions, the other due to the normal tractions on the fluid surfaces. The power loss is also known as the hydrodynamic friction power which is the rate of work done on the film or dissipated by it. Considering two surfaces moving relative to one another with velocities U_1 and U_2. The shear stress in any part of the film is given by

$$\tau = \mu \frac{\partial u}{\partial y} \tag{2.26}$$

and

$$\mu \frac{\partial^2 u}{\partial y^2} = \frac{\partial p}{\partial x} \tag{2.27}$$

Integrating (2.27) with respect to y gives us

$$\frac{\partial u}{\partial y} = \frac{1}{\mu} \frac{\partial p}{\partial x} y + C_1 \tag{2.28}$$

Applying the boundary conditions and substituting into equation (2.26) we obtain

$$\tau = \frac{\partial p}{\partial x} \frac{h}{2} \pm \frac{(U_1 - U_2)}{h} \mu \tag{2.29}$$

and putting

$$x = R\theta$$

(2.29) becomes

$$\tau = \pm \mu \Delta\omega \frac{R}{h} + \frac{h}{2R} \frac{\partial p}{\partial \theta} \tag{2.30}$$

Figure 2.5 shows the normal and shear tractions on the fluid surfaces where the indices 1 and 2 apply to the film surfaces. The normal and shear tractions are expressed as

$$p_i = p \tag{2.31}$$

and

$$\tau_i = \delta_i \mu \Delta\omega \frac{R}{h} + \frac{h}{2R} \frac{\partial p}{\partial \theta} \tag{2.32}$$

where

$$\Delta\omega = \omega_1 - \omega_2$$

$$\delta_1 = 1$$

$$\delta_2 = -1$$

The resultants of the normal tractions are obtained by integrating over the bearing surface as

$$F_{ix} = -\delta_i R \iint p \cos\theta \, d\theta \, dz \tag{2.33}$$

and

$$F_{iy} = -\delta_i R \iint p \sin\theta \, d\theta \, dz \tag{2.34}$$

The resultant moments of the shear tractions τ_i are given by

$$T_i = R \iint \tau_i dA = R^2 \iint \tau_i d\theta dz$$

$$= \delta_i R^2 \Delta\omega \iint \mu \frac{dA}{h} + \frac{1}{2} \iint h \frac{\partial p}{\partial \theta} dA \tag{2.35}$$

The rate of work done on the film is then given by

$$H = \sum_{i=1}^{2} [\mathbf{F}_i . \dot{\mathbf{e}} + \mathbf{T}_i . \omega_i] \tag{2.36}$$

T_i may be expressed as [52]

$$T_i = \delta_i R^2 \Delta\omega I_1 + I_2 \tag{2.37}$$

where

$$I_1 = \iint \mu \frac{dA}{h} \tag{2.38}$$

and

$$I_2 = \frac{R}{2} \iint h \frac{\partial p}{\partial \theta} dA \tag{2.39}$$

therefore

$$\sum_{i=1}^{2} \mathbf{T}_i.\omega_i = R^2\Delta\omega I_1\omega_1 - R^2\Delta\omega I_2\omega_2$$

$$= R^2 I_1\Delta\omega\Delta\omega + 2I_2\bar{\omega} \tag{2.40}$$

where $\bar{\omega}$ is defined as

$$\bar{\omega} = (\omega_1+\omega_2)/2$$

which is the average angular velocity of the fluid film. The power loss in the bearing may therefore be expressed as

$$H = \mathbf{F}.\dot{\mathbf{e}} + R^2\Delta\omega\Delta\omega I_1 + 2I_2\bar{\omega} \tag{2.41}$$

2.5 Sommerfeld infinite bearing theory

Reynolds equation as it stands cannot be solved directly using closed form analytical techniques. Sommerfeld [2] presented an analytical solution for Reynolds equation by assuming that the bearing was infinitely wide. In this case the pressure derivative in the axial direction, $\partial p/\partial z$, is zero, and Reynolds equation now becomes, for a steadily running bearing,

$$\frac{\partial}{\partial x}\left[\frac{h^3}{\mu}\frac{\partial p}{\partial x}\right] = 6U\frac{\partial h}{\partial x} \tag{2.42}$$

Integrating this equation gives

$$\frac{\partial P}{\partial x} = 6U\mu\frac{(h-\bar{h})}{h^3} \tag{2.43}$$

where $\bar{h}$ is the film thickness at the point of maximum pressure where $\partial p/\partial x = 0$. Using the substiutions

$$h = c(1+\varepsilon\cos\theta)$$

$$x = R\theta$$

(2.43) becomes

$$\frac{c^2\partial p}{6U\mu R} = \left\{\frac{d\theta}{(1+\varepsilon\cos\theta)^2} - \frac{(1+\varepsilon\cos\bar{\theta})d\theta}{(1+\varepsilon\cos\theta)^3}\right\} \tag{2.44}$$

where $\bar{\theta}$ is the angle at which $\bar{h}$ occurs.

To integrate this equation Sommerfeld used the substitution

$$\cos\gamma = \frac{\varepsilon+\cos\theta}{1+\varepsilon\cos\theta} \tag{2.45}$$

which has the property that at $\theta = 0, \pi$ and 2π , γ is also $0, \pi$ and 2π . This gives

$$\frac{c^2 p}{6U\mu R} = \frac{\gamma-\varepsilon\sin\gamma}{(1-\varepsilon^2)^{3/2}} - \left\{\frac{1-\varepsilon^2}{1-\varepsilon\cos\bar{\gamma}}\right\}\left\{\frac{\gamma-2\varepsilon\sin\gamma+\varepsilon^2\gamma/2+(\varepsilon^2\sin2\gamma)/4}{(1-\varepsilon^2)^{5/2}}\right\}+C \tag{2.46}$$

The value of C depends upon the boundary conditions used. The three main boundary conditions are :

i) $p = 0$ at $\theta = 2\pi$ *and* π .

This is the Sommerfeld condition and assumes a continuous fluid film around the bearing giving an antisymmetric pressure distribution about $\theta = \pi$. This gives rise to a large region of negative pressure which is only physically possible if these pressures are very small since it is physically impossible for the film to withstand a high negative pressure.

ii) $p = 0$ *for* $\theta \geq \pi$

This is the half Sommerfeld condition and assumes that the pressure distribution extends over half the bearing. This solution has the disadvantage that there is a discontinuity in the flow at $\theta = \pi$.

iii) $p = 0$ *at* $\partial p/\partial\theta = 0$ *at* $\theta > \pi$

This condition is known as the Reynolds condition and it states that the end of the pressure region is at the point where $\partial p/\partial\theta = 0$ which guarantees flow continuity.

2.6 Narrow bearing theory.

An alternative method for the solution of Reynolds equation was first proposed by Mi chell [3] who considered that the conditions at the edge of the bearing had more influence over the flow in a finite length bearing so the $\partial p/\partial x$ term could be ignored. Ocvirk and Du Bois [4] later refined the method considerably and provided a large amount of experimental data to demonstrate the validity of the narrow bearing theory.

Ignoring the $\partial p/\partial x$ term, Reynolds equation (2.15) becomes

$$\frac{\partial^2 p}{\partial z^2} = \frac{6U\mu}{h^3}\frac{\partial h}{\partial x} \tag{2.47}$$

and integrating this gives

$$p = \frac{6U\mu}{h^3}\frac{\partial h}{\partial x}\frac{z^2}{2} + C_1 z + C_2 \tag{2.48}$$

where the constants of integration, C_1 and C_2, are evaluated using the fact that $\partial p/\partial z = 0$ at the centre line and $p = 0$ at $z = \pm L/2$ giving

$$p = \frac{3U\mu}{h^3}\frac{\partial h}{\partial x}\left[z^2 - \frac{l^2}{4}\right] \tag{2.49}$$

Substituting

$$x = R\theta$$

$$h = c(1+\varepsilon\cos\theta)$$

into (2.49) results in

$$p = \frac{3U\mu}{Rc^2}\left[\frac{l^2}{4} - z^2\right]\frac{\varepsilon\sin\theta}{(1+\varepsilon\cos\theta)^3} \tag{2.50}$$

which gives a parabolic pressure distribution in the axial direction and sinusoidal distribution in the circumferential direction, positive pressures existing between $\theta = 0$ and π. Ocvirk and Du Bois obtained results simply by ignoring the negative pressures in the bearing, giving a half Sommerfeld boundary condition.

Both the short bearing theory and narrow bearing theory provide useful information about bearing behaviour. It has been shown, however, that these methods

can only produce results of any quantatative use for bearings with a length to diameter ratio, $L/D > 1$ for the short bearing theory and $L/D < 1/4$ for the narrow bearing theory. Most bearings however have an L/D ratio between 1/4 and 1/2 and for the accurate prediction of the performance of these bearings the simplified theories prove inadequate.

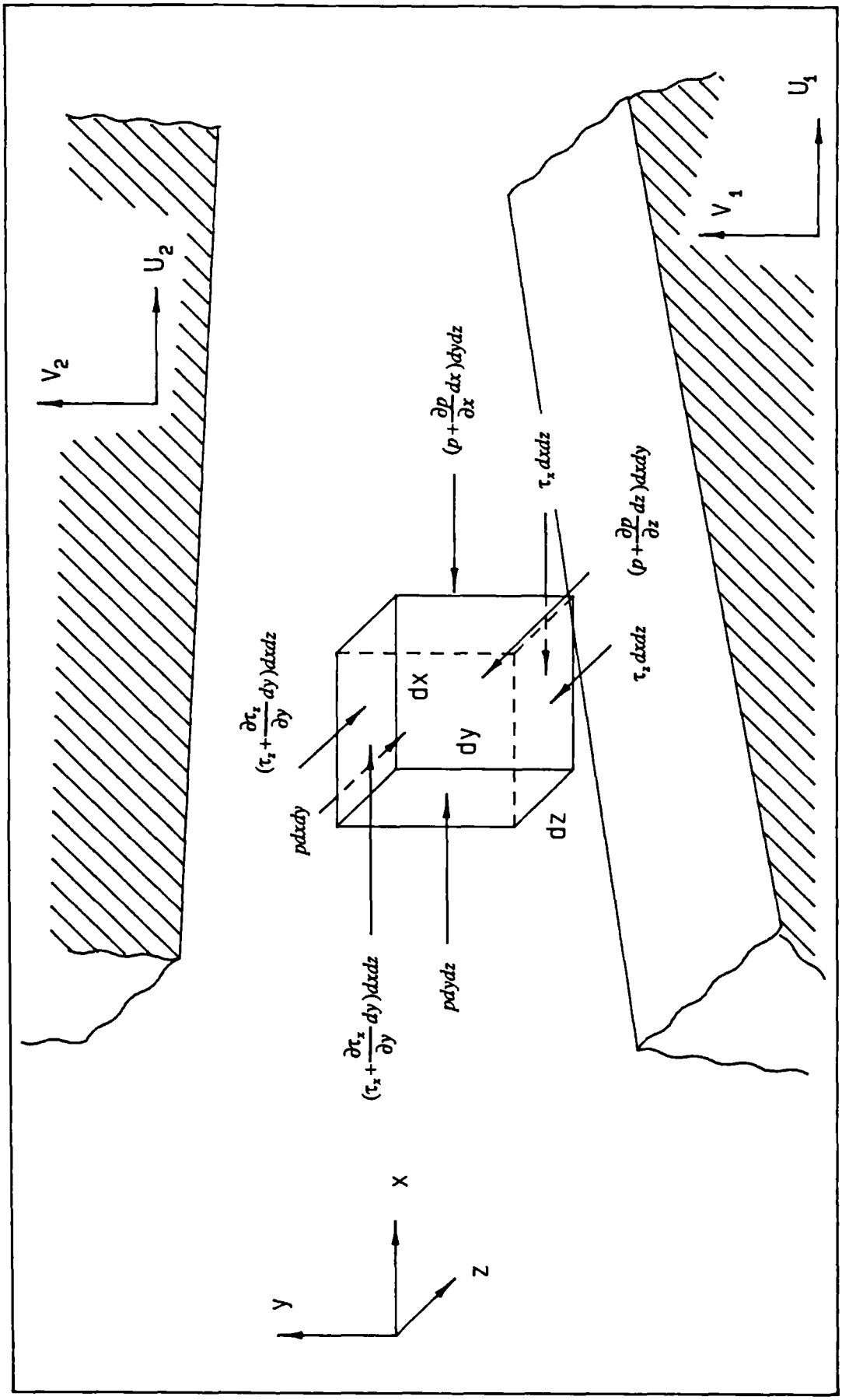

Figure 2.1 - Stressed element in fluid

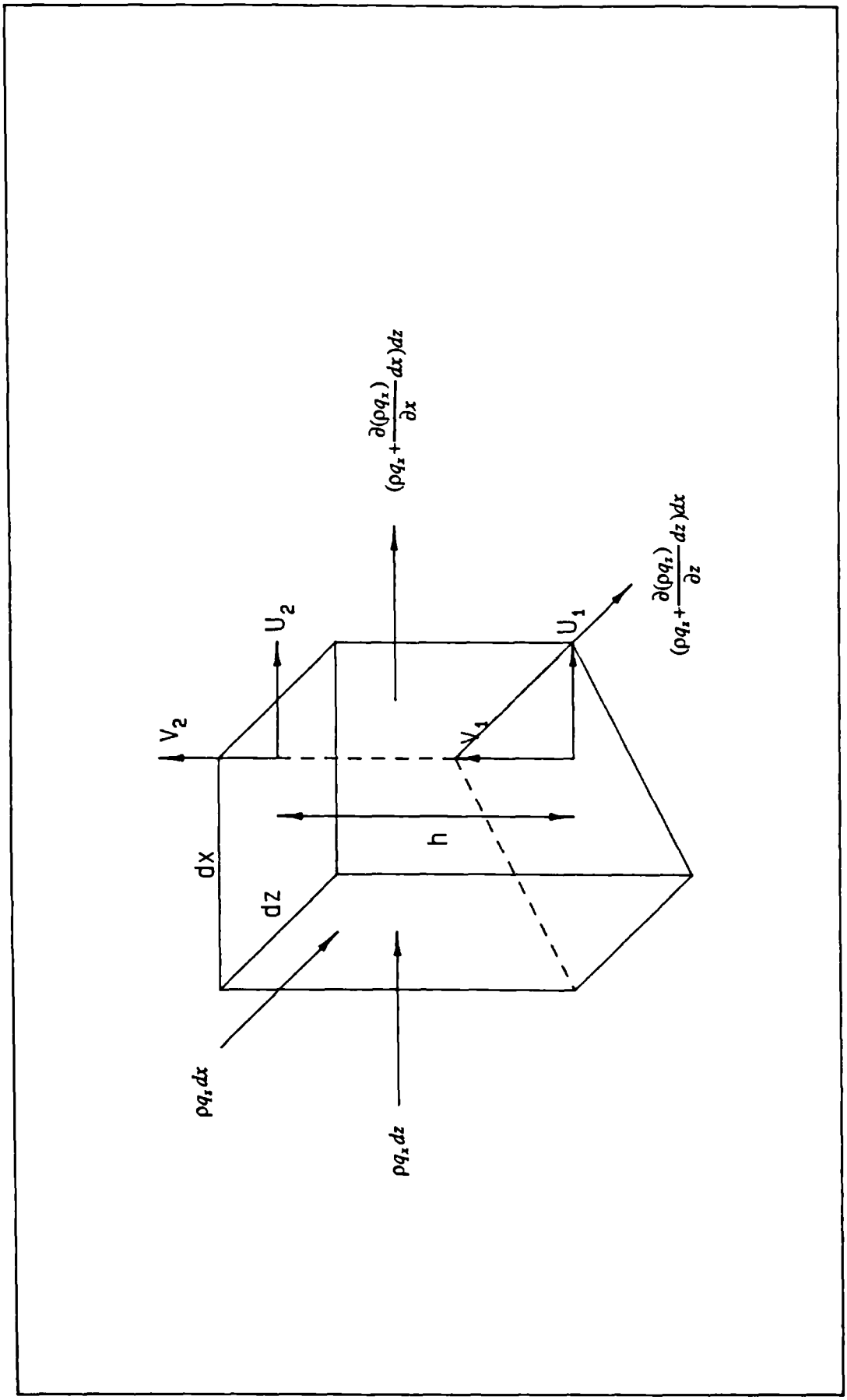

Figure 2.2 - Flow into and out of fluid volume

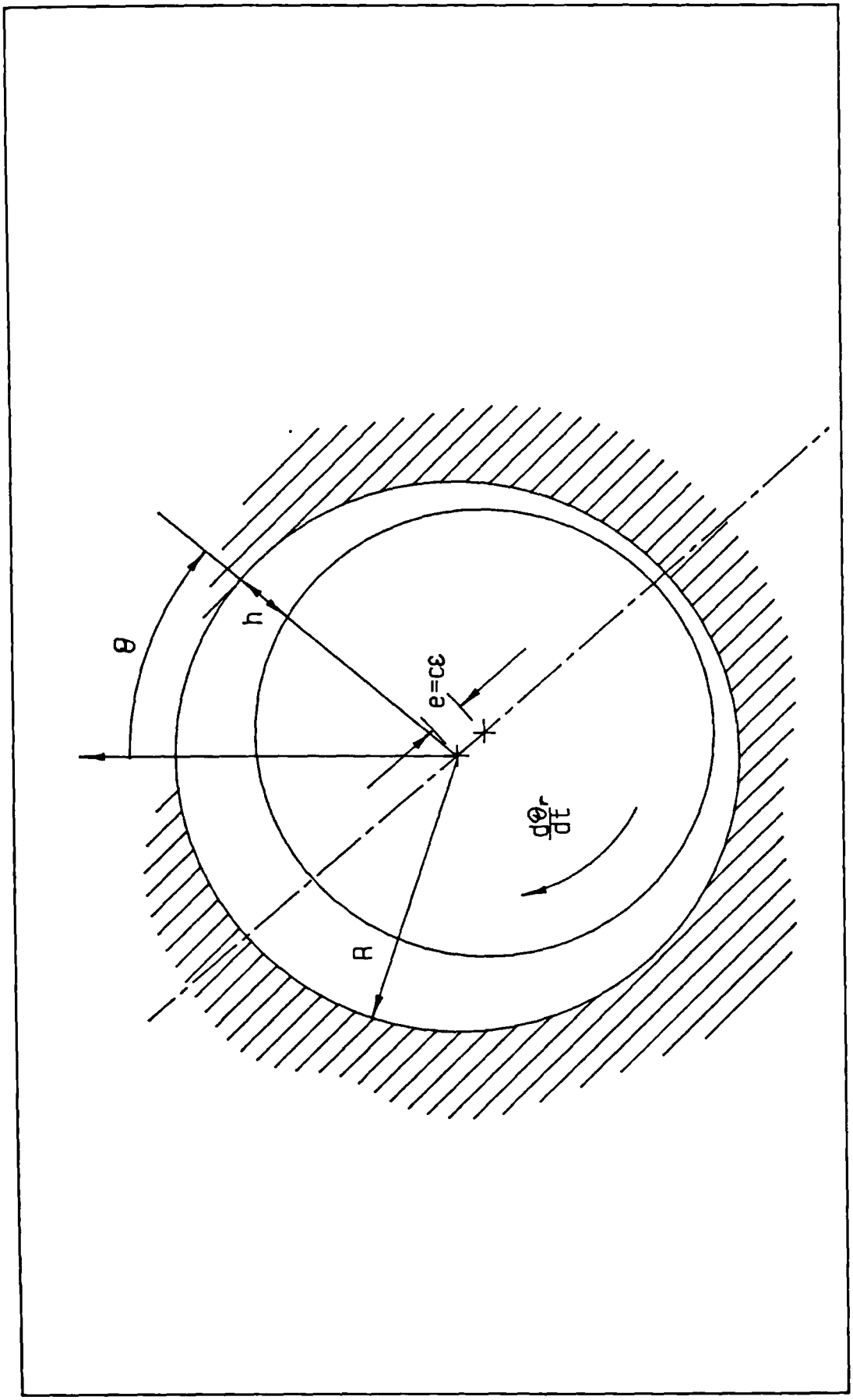

Figure 2.3 - Journal bearing configuration

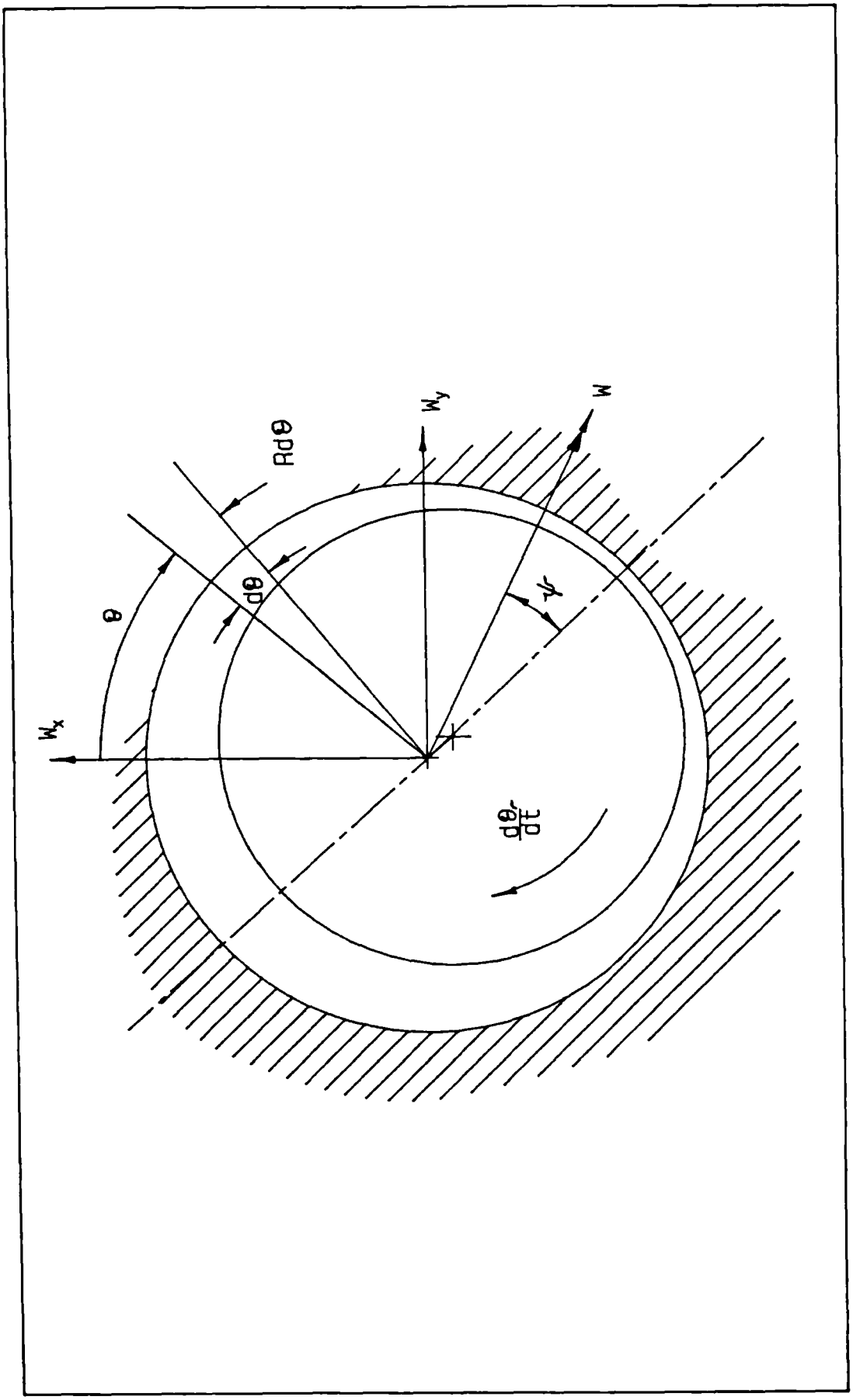

Figure 2.4 - Bearing load vector and components

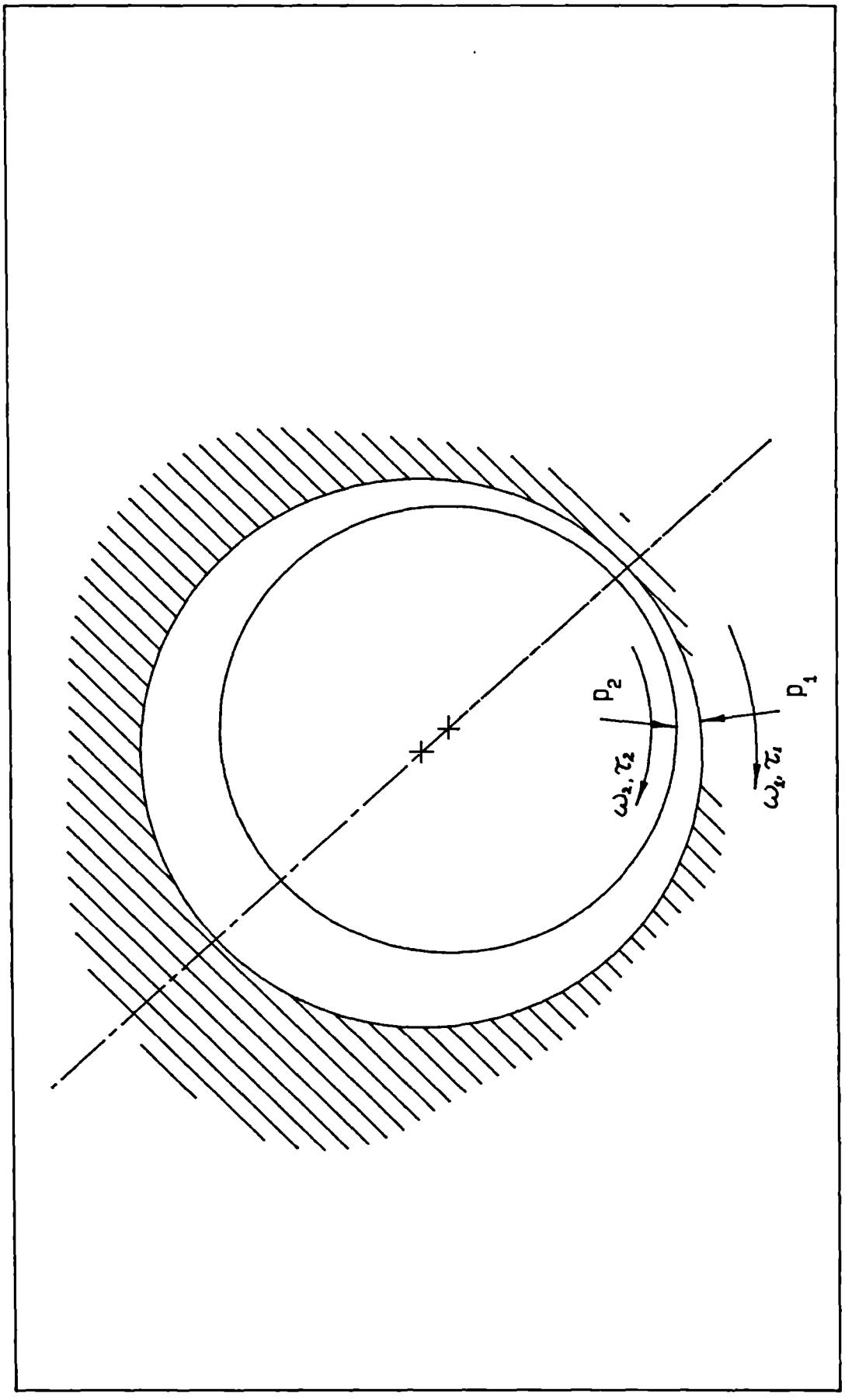

Figure 2.5 - Normal and shear tractions on fluid film

Chapter 3

The Finite Element Method

3.1 Introduction

The basic idea behind the finite element method (FEM) is to replace a complex problem by a simpler one. A closed-form analytical solution, where one exists, allows a solution to be found at all points within the solution domain. In the finite element method the problem is solved at a finite number of points.

The technique was pioneered in the late 1940's with the advent of jet powered aircraft when simplified structural analysis methods proved insufficiently accurate for analyzing the structures involved. The subsequent evolution of the method from a mathematicians toy to a powerful engineering design tool is evidenced by the amount of published matter on the subject and the number of computer packages currently in use. These are used to solve real engineering problems from electronic circuit design to large scale civil engineering projects.

This chapter gives a brief description of the method and describes the two element types used for the lubrication analysis. The formulation of the rigid bearing lubrication problem using the finite element method is given by way of an example to introduce the concepts involved in a finite element formulation and to introduce the rigid bearing problem.

3.2 Finite element discretisation and element types

In the finite element method an approximate solution is obtained for a problem by assuming that the behaviour of the continuum can be represented by a finite number of unknowns. To achieve this the continuum is divided into a series of discrete 'finite elements' connected at a finite number of nodal points. The accuracy of the approximation can be improved at the expense of computer time by increasing the number elements and hence the number of unknowns used to define the problem. Figure 3.1 shows two different finite element meshes used to model the lubricant film in a bearing.

The next step in the finite element analysis is to approximate the behaviour of the unknown ϕ within each element in terms of the nodal values [53]. This is

achieved by using localised functions, N_i , known as shape functions such that

$$\phi(x,y) = \sum_{i=1}^{n} N_i(x,y)\phi_i \tag{3.1}$$

where n is the number of nodal points in the element and ϕ_i are the nodal values of ϕ. The form that the shape function take depends on the type of finite element being used, and the accuracy of the element depends upon how well the shape functions model the exact behaviour of the unknown ϕ .

The shape function chosen to represent the behaviour of the unknown must satisfy two conditions:

i) Continuity of the unknown between elements.

ii) As the element size is reduced and the mesh refined, convergence of the solution must be ensured.

The two different element types used for the lubrication problem are shown in Figure 3.2. The first is a 3-node triangular element for which a linear variation of the unknown is assumed over the element. The second is an 8-node quadrilateral isoparametric element for which a quadratic variation is assumed. For the triangular element the unknown, ϕ, is assumed to vary as

$$\phi = \alpha_1+\alpha_2 x+\alpha_3 y \tag{3.2}$$

hence the nodal values at i, j and k are given by

$$\begin{aligned} \phi_i &= \alpha_1+\alpha_2 x_i+\alpha_3 y_i \\ \phi_j &= \alpha_1+\alpha_2 x_j+\alpha_3 y_j \\ \phi_k &= \alpha_1+\alpha_2 x_k+\alpha_3 y_k \end{aligned} \tag{3.3}$$

The value of ϕ is to be expressed as

$$\phi = \sum_{i=1}^{n} N_i(x,y)\phi_i = N_i(x,y)\phi_i+N_j(x,y)\phi_j+N_k(x,y)\phi_k \tag{3.4}$$

combining equations (3.3) and (3.4) therfore gives

$$N_i = \frac{(a_i+b_i x+c_i y)}{2A^e} \tag{3.5}$$

where A^e is the area of the element, and $a_i = x_j y_k - x_k y_j$, $b_i = y_j - y_k$, $c_i = x_k - x_j$ Similarily N_j and N_k may be obtained by a cyclic permutation of subscripts in (3.5).

Each of the shape functions, N, is equal to unity at the point to which it relates and is zero at the remaining nodal points. They also have the property that at any point (x,y)

$$N_i(x,y)+N_j(x,y)+N_k(x,y) = 1 \tag{3.6}$$

In matrix form equation (3.4) may be written as

$$\phi = \left[N^e\right]\left\{\phi^e\right\} \tag{3.7}$$

where

$$\left\{\phi^e\right\} = \begin{Bmatrix}\phi_i \\ \phi_j \\ \phi_k\end{Bmatrix}, \quad \left[N^e\right] = \left[N_i^e, N_j^e, N_k^e\right]$$

The second element considered is the higher order 8-node quadrilateral isoparametric element. The geometry of the element is defined in terms of the local coordinates, ξ and η, which have values from -1 to $+1$ over the element. This allows curvilinear shapes to be accomodated by using isoparametric mapping from local to global coordinates and allows all the elements matrices to be evaluated in a similar manner, the global mapping taking care of the differences between elements. Here the unknown, ϕ, is assumed to vary as [54]

$$\phi = \alpha_1+\alpha_2\eta+\alpha_3\xi+\alpha_4\eta\xi+\alpha_5\eta^2+\alpha_6\xi^2+\alpha_7\eta\xi^2+\alpha_8\eta^2\xi \tag{3.8}$$

and writing

$$\phi(\xi,\eta) = \sum_{i=1}^{n} N_i(\xi,\eta)\phi_i$$

the shape functions may be obtained as

$$N_1(\xi,\eta) = -(1-\xi)(1-\eta)(1+\xi+\eta)/4$$

$$N_2(\xi,\eta) = (1-\xi^2)(1-\eta)/2$$

$$N_3(\xi,\eta) = (1+\xi)(1-\eta)(-1+\xi-\eta)/4$$

$$N_4(\xi,\eta) = (1+\xi)(1-\eta^2)/2$$

$$N_5(\xi,\eta) = (1+\xi)(1+\eta)(-1+\xi+\eta)/4 \qquad (3.9)$$

$$N_6(\xi,\eta) = (1-\xi^2)(1+\eta)/2$$

$$N_7(\xi,\eta) = (1-\xi)(1+\eta)(-1-\xi+\eta)/4$$

$$N_8(\xi,\eta) = (1-\xi)(1-\eta^2)/2$$

It is important to note the orientation of the local coordinates since the shape functions are dependent upon these. The node numbering begins at a corner node in an anticlockwise direction. The positive ξ direction is defined by moving along an edge from the first nodal point, through the second to the third. Similarily the positive η axis is defined by moving along an edge from the third nodal point, through the fourth to the fifth.

The values of ϕ are now totally defined within each element. Using the shape function derivatives, the derivatives of ϕ can also be found as

$$\frac{\partial \phi}{\partial x} = \sum_{i=1}^{n} \frac{\partial N_i}{\partial x} \phi_i \qquad (3.10)$$

for the triangular element and as

$$\frac{\partial \phi}{\partial \xi} = \sum_{i=1}^{n} \frac{\partial N_i}{\partial \xi} \phi_i \qquad (3.11)$$

for the isoparametric element.

3.3 Finite element formulation for the rigid bearing problem

The finite element method was chosen for the present analysis due to the routine manner in which complex flow and geometric boundary conditions can be handled. It has been shown [14] to be more efficient than the finite difference method for modelling the lubrication problem and has been applied to the problem by many authors [19,20,21,22,55]. The method was also chosen since the structural modelling carried out for the elastic bearing problem also employed the finite element method and the coupling of the lubrication and structural problems could therfore prove easier if finite elements were used in both cases.

There are a number of different ways in which the lubrication problem may be formulated for solution by the finite element method. The problem may be formulated directly, although this is only possible for the one-dimensional problem. The problem may be formulated using a variational principle. This method is based upon the calculus of variations where the problem is reexpressed in terms of a functional which may characterise some aspect of the problem, and the solution is obtained by minimising the functional. For the rigid bearing problem the functional is based upon the flow within the system. In some cases though an equivalent variational problem may not exist. A much more powerful and straightforward method is to use the method of weighted residuals [56], which is the method adopted in the present analysis.

The first step in the method of weighted residuals is to assume the behaviour of the variables over the solution domain. In this case, using the finite element method, the shape functions are used to obtain the approximations. Consider a governing equation of the form

$$f[P(x,y)] = 0 \tag{3.12}$$

over a solution domain Ω where P represents the unknown function. P is approximated over the solution domain as an approximate function P' giving

$$P' = P'(x,y;\, a_1, a_2, \ldots, a_n) = \sum_{i=1}^{n} a_i N_i(x,y) \tag{3.13}$$

where $a_1, a_2, \cdots, a_n$ are constant but unknown parameters. If this approximate solution is substituted back into equation (3.12) some residual error R given by

$$f\,[P'(x,y;\,a_1,\,a_2,\,\cdots,\,a_n)] = R\,(x,y;\,a_1,\,a_2,\,\cdots,\,a_n) \tag{3.14}$$

will result due to the approximation.

The method of weighted residuals requires that the parameters $a_1, a_2, \cdots, a_n$ are solved by

$$\int_{\Omega} w_i(x,y)R\,(x,y;\,a_1,\,a_2,\,\cdots,\,a_n)\,d\Omega = 0 \quad i=1,2,...n \tag{3.15}$$

such as to minimise the error, where the functions $w_i(x,y)$ are n arbitrary weighting functions. The weighted residual method used for the present analysis is Galerkins method which is particularly suited to finite element analysis. Here the weighting functions are given by the shape functions $N_i(x,y)$. Applying this to Reynolds equation (2.22) on an element basis we obtain

$$\int_{A^e} N^T \left[\frac{\partial}{\partial\theta}\left[h^3\frac{\partial p}{\partial\theta}\right]+B^2\frac{\partial}{\partial z}\left[h^3\frac{\partial p}{\partial z}\right]-\frac{d\theta_r}{d\alpha}\frac{dh}{d\theta}-2\frac{dh}{d\alpha}\right] dA = 0 \tag{3.16}$$

In order to simplify this expression the Green-Gauss theorem must be used.
This theorem states that if β is a scalar and f a vector then

$$\int_A \beta\frac{\partial f}{\partial\theta}dA = \int_S \beta f n_\theta\,dS - \int_A \frac{\partial\beta}{\partial\theta}f\,dA \tag{3.17}$$

where S is the boundary of the area A and n_θ is the direction cosine of the outward normal unit vector. Similarily

$$\int_A \beta\frac{\partial f}{\partial z}dA = \int_S \beta f n_z\,dS - \int_A \frac{\partial\beta}{\partial z}f\,dA \tag{3.18}$$

Considering the first term in equation (3.16) putting

$$\beta = N^T$$

$$f = h^3\frac{\partial p}{\partial\theta}$$

we obtain

$$\int_{A^e} N^T\frac{\partial}{\partial\theta}\left[h^3\frac{\partial p}{\partial\theta}\right]dA = \int_S N^T h^3\frac{\partial p}{\partial\theta}n_\theta dS - \int_{A^e}\frac{\partial N^T}{\partial\theta}h^3\frac{\partial p}{\partial\theta}dA \tag{3.19}$$

Equation (3.16) may therefore be written as

$$-\int_{A^e}\left[\frac{\partial N^T}{\partial\theta}\left[h^3\frac{\partial p}{\partial\theta}\right]+B^2\frac{\partial N^T}{\partial z}\left[h^3\frac{\partial p}{\partial z}\right]\right]dA+\int_S N^T\left[h^3\frac{\partial p}{\partial\theta}n_\theta+B^2h^3\frac{\partial p}{\partial z}n_z\right]dS$$

$$+\int_{A^e}\frac{d\theta_r}{d\alpha}\frac{\partial N^T}{\partial\theta}h\ dA-\int_S N^T\frac{d\theta_r}{d\alpha}h\ n_\theta\ dS-\int_{A^e}2N^T\frac{dh}{d\alpha}\ dA=0 \qquad (3.20)$$

Combining all the boundary integrals gives

$$\int_S N^T\left\{h^3\frac{\partial p}{\partial\theta}n_\theta+B^2h^3\frac{\partial p}{\partial z}n_z-\frac{d\theta_r}{d\alpha}h\ n_\theta\right\}dS$$

In dimensionless terms, the flow rates q_θ and q_z may be written as

$$q_\theta=-h^3\frac{\partial p}{\partial\theta}+\frac{d\theta_r}{d\alpha}h \qquad (3.21)$$

$$q_z=-B^2h^3\frac{\partial p}{\partial z} \qquad (3.22)$$

The boundary integral may therefore be written as $\int_S N^T\left\{-q_\theta n_\theta-q_z n_z\right\}dS$ and since $q_n=q_\theta n_\theta+q_z n_z$ the boundary integral becomes $-\int_S N^T q_n\,dS$

Reynolds equation may now be written as

$$-\int_{A^e}\left\{\frac{\partial N^T}{\partial\theta}h^3\frac{\partial p}{\partial\theta}+B^2\frac{\partial N^T}{\partial z}h^3\frac{\partial p}{\partial z}\right\}dA+\int_{A^e}\frac{d\theta_r}{d\alpha}\frac{\partial N^T}{\partial\theta}h\ dA$$

$$-2\int_{A^e}N^T\frac{dh}{d\alpha}dA-\int_S N^T q_n\,dS=0 \qquad (3.23)$$

This equation may be expressed in matrix form as

$$[K_p{}^e]\{p^e\}=\{q^e\}+\{U^e\}+\{\dot{H}\} \qquad (3.24)$$

where the coefficients in the matrices are given by

$$K_{p_{ij}}{}^{e} = -\int_{A^e} h^3 \left[\frac{\partial N_i}{\partial \theta} \frac{\partial N_j}{\partial \theta} + B^2 \frac{\partial N_i}{\partial z} \frac{\partial N_j}{\partial z} \right] dA$$

$$U_i{}^{e} = -\int_{A^e} \frac{d\theta_r}{d\alpha} \frac{\partial N_i}{\partial \theta} h dA$$

$$\dot{H}_i{}^{e} = 2\int_{A^e} N_i \frac{dh}{d\alpha} dA \qquad (3.25)$$

$$q_i{}^{e} = \int_{S} N_i q_n dS$$

Equation (3.24) has a distinct physical meaning. The right hand side represents a linear combination of dimensionless flow terms caused by shear and squeeze. These flows are balanced by the nodal flows caused by the pressure generated in the oil film. Equations (3.25) totally describe the isothermal incompressible lubrication problem. It is important to note at this stage that the flow at the boundary $\{q^e\}$ need never be evaluated when solving for the pressures. Along the edge of the bearing the pressures, p_a, are known and it is therefore not necessary to solve Reynolds equation at any nodes that lie on this boundary. If symmetry is exploited this term vanishes at the line of symmetry since $q_n = 0$. This term may therefore be ignored for the moment.

3.4 Equation formulation

Now that a complete finite element description for the problem has been obtained the fluidity matrices and element equations can be evaluated. Two different methods were used for the two element types.

3.4.1 Triangular element formulation

Using the previous definition of the shape functions the element equations may be evaluated explicitly. For the triangular element the shape function is given by

$$N_i^e = \frac{a_i + b_i\theta + c_i z}{2A^e} \tag{3.26}$$

where the shape function derivatives may be obtained as

$$\frac{\partial N_i}{\partial \theta} = \frac{b_i}{2A^e} \quad , \quad \frac{\partial N_i}{\partial z} = \frac{c_i}{2A^e}$$

Using the first equation of (3.25) we obtain

$$K_{p_{ij}}^e = -\int_{A^e} \frac{h^3}{4(A^e)^2}(b_i b_j + B^2 c_i c_j)dA$$

$$= -\frac{(b_i b_j + B^2 c_i c_j)}{4(A^e)^2}\int_{A^e} h^3 dA$$

since b_i and c_i are constants.

To evaluate the integral

$$I = \int_{A^e} h^3 dA$$

h is assumed to vary as $h = h_i N_i + h_j N_j + h_k N_k$ giving

$$I = \int_{A^e} (h_i N_i + h_j N_j + h_k N_k)^3 dA$$

$$= \int_{A^e} (h_i^3 N_i^3 + h_j^3 N_j^3 + h_k^3 N_k^3 + 3h_i^2 h_j N_i^2 N_j + \ldots\ldots\ldots + 6h_i h_j h_k N_i N_j N_k)\, dA$$

All the values of h are constant nodal values therefore considering the first term

$$\int_{A^e} h_i^3 N_i^3 = h_i^3 \int_{A^e} N_i^3 dA$$

There is a convenient formula [57] for carrying out the integration of shape functions which is

$$\int_{A^e} N^\alpha N^\beta N^\gamma dA = \frac{\alpha!\beta!\gamma!}{(\alpha+\beta+\gamma+2)!} 2A^e \tag{3.27}$$

therefore

$$h_i^3 \int_{A^e} N_i^3 dA = \frac{h_i^3}{10}\, A^e$$

applying this formula to all the terms in the equation the integral I now becomes

$$I = (h_i^3+h_{j_3}+h_k^3+h_i^2h_j+h_i^2h_k+h_j^2h_i+h_j^2h_k+h_k^2h_i+h_k^2h_j+h_i h_j h_k)\frac{A^e}{10}$$

giving

$$K_{p_{ij}}{}^e = \frac{I}{4A^e}(b_i b_j+B^2 c_i c_j) \tag{3.28}$$

Similarily U_i^e may be obtained as

$$U_i^e = -\frac{d\theta_r}{d\alpha}\int_{A^e} h\frac{\partial N_i}{\partial\theta}dA = -\frac{d\theta_r}{d\alpha}\frac{b_i}{2A^e}\int_{A^e} hdA$$

Assuming a variation for h as before

$$\int_{A^e} hdA = \int_{A^e}(h_iN_i+h_jN_j+h_kN_k)dA = \frac{(h_i+h_j+h_k)}{3}A^e$$

therefore

$$U_i^e = \frac{d\theta_r}{d\alpha}\frac{(h_i+h_j+h_k)}{6}A^e \tag{3.29}$$

The squeeze term may be formulated in a similar manner, assumng $dh_i/d\alpha$ is not a function of θ or z

$$\dot{H}_i{}^e = 2\frac{dh}{d\alpha}\int_{A^e} N_i dAz = 2\frac{dh}{d\alpha}\frac{A^e}{3} \tag{3.30}$$

Therefore equations (3.28), (3.29) and (3.30) allow the element matrices for the triangular elements to be formulated

3.4.2 Quadrilateral element formulation

The element matrices for the higher order element can not be formulated so easily so a numerical integration must be employed to evaluate the matrix coefficients. The form of integration used is Gauss-Legendre Quadrature. This was chosen since it can be highly accurate and is relatively easy to implement. The general Gauss-Legendre formula in two dimensions is given by

$$I = \int_{-1}^{+1}\int_{-1}^{+1} \phi(\xi,\eta)\, d\xi d\eta = \sum_{i=1}^{n}\sum_{j=1}^{n} a_i a_j \phi(\xi_i,\eta_j) \qquad (3.34)$$

where n is the number of sampling points , a_i is the weighting factor , ξ_i,η_i are the coordinates of the ith sampling point.

Below is a table of sampling points and weights for values of n=2,3.

n	a	η
2	1.0	$\pm 1/\sqrt{3}$
3	5/9	$\pm\sqrt{0.6}$
	8/9	0

Table 3.1 Sampling points and weights for Gauss-Legendre Quadrature

In general taking two points in each direction should prove adequate for the quadrilateral element. It should also be noted at this stage that shape functions and derivatives are in terms of the local coordinates ξ and η and not the global coordinates θ and z. The global derivatives may be obtained in the following manner. Applying the chain rule

$$\frac{\partial N_i}{\partial \xi} = \frac{\partial N_i}{\partial \theta}\frac{\partial \theta}{\partial \xi} + \frac{\partial N_i}{\partial z}\frac{\partial z}{\partial \xi} \qquad (3.32)$$

$$\frac{\partial N_i}{\partial \eta} = \frac{\partial N_i}{\partial \theta}\frac{\partial \theta}{\partial \eta} + \frac{\partial N_i}{\partial z}\frac{\partial z}{\partial \eta} \qquad (3.33)$$

This may be written in matrix form as

$$\begin{Bmatrix} \frac{\partial N_i}{\partial \xi} \\ \frac{\partial N_i}{\partial \xi} \end{Bmatrix} = \begin{bmatrix} \frac{\partial \theta}{\partial \xi} & \frac{\partial z}{\partial \xi} \\ \frac{\partial \theta}{\partial \eta} & \frac{\partial z}{\partial \eta} \end{bmatrix} \begin{Bmatrix} \frac{\partial N_i}{\partial \theta} \\ \frac{\partial N_i}{\partial z} \end{Bmatrix}$$

where the 2 x 2 matrix on the right hand side of the equation is the Jacobian matrix J. Thus the cartesian derivatives can be obtained. It should be noted that

$$d\theta dz = |\det J|\, d\xi d\eta$$

which can be obtained from calculus.

It is now possible to obtain the element matrices as

$$K_{p_{ij}}{}^{e} = -\int_{A^e} h^3 \left[\frac{\partial N_i}{\partial \theta} \frac{\partial N_j}{\partial \theta} + B^2 \frac{\partial N_i}{\partial z} \frac{\partial N_j}{\partial z} \right] d\theta dz$$

$$= -\sum_{k=1}^{n} \sum_{l=1}^{n} a_k a_l h^3{}_{kl} \left[\frac{\partial N_i}{\partial \theta} \frac{\partial N_j}{\partial \theta} + B^2 \frac{\partial N_i}{\partial z} \frac{\partial N_j}{\partial z} \right] |\det J| \qquad (3.34)$$

Since the integration is carried out over the element in terms of local coordinates it is in the form $d\xi d\eta$ and is multiplied by $|\det J|$ to make it of the form $d\theta dz$. Similarily

$$U_i{}^{e} = -\int_{A^e} \frac{d\theta_r}{d\alpha} \frac{\partial N_i}{\partial \theta} h \, d\theta dz = \frac{d\theta_r}{d\alpha} \sum_{k=1}^{n} \sum_{l=1}^{n} h_{kl} \frac{dN_i}{d\theta} |\det J| \qquad (3.35)$$

and

$$\dot{H}_i{}^{e} = 2 \int_{A^e} N_i \frac{dh}{d\alpha} dA = \sum_{k=1}^{n} \sum_{l=1}^{n} 2N_i \frac{dh_{kl}}{d\alpha} |\det J| \qquad (3.36)$$

Hence the element matrices can be formulated for the isoparametric element.

3.5 System matrices assembly

The element matrices can now be evaluated over each element giving a set of matrices $[K_p{}^{e}]$, $\{ U^e \}$, $\{ \dot{H}^e \}$. If there are n nodes in the finite element mesh it is required that n equations are obtained to solve for the n unknown nodal pressures. A set of system matrices must therfore be assembled as $[K_p]$, $\{ U \}$, $\{ \dot{H} \}$ from the element matrices. To achieve this the individual contributions to each nodal point from each element must be summed. This is possible by transfering from local to global numbering. Each node as well as having an associated number for each element, known as the local number, also has a global number refering to the system as a whole. Assembly of the system matrices is then simply a matter of placing the particular element matrix coefficient in the correct place in the system matrix. This is achieved by summing the individual element coefficients as

$$K_{p_{is\,js}} = K_{p_{is\,js}} + K^{e}_{p_{ie\,je}}$$

where *is* and *js* are the global node numbers corresponding to the nodes *ie* and *je* in the element under consideration. Similarily

$$U_{is} = U_{is} + U_{ie}^{e}$$

and

$$\dot{H}_{is} = \dot{H}_{is} + \dot{H}_{ie}{}^{e}$$

Once this has been carried out for all the elements the system matrices are complete and the solution procedure can be started.

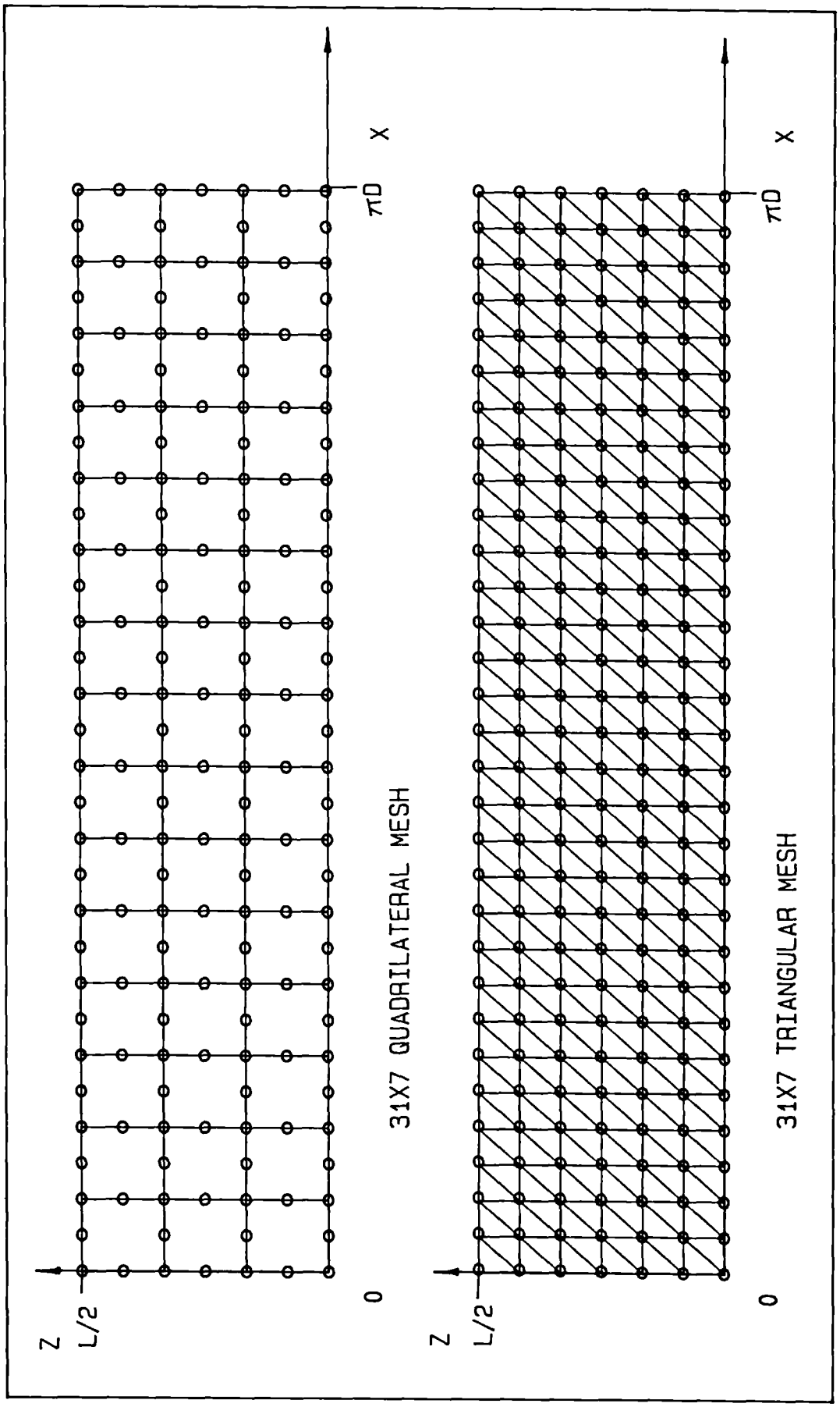

Figure 3.1 - Examples of finite element meshes used to model the lubricant film

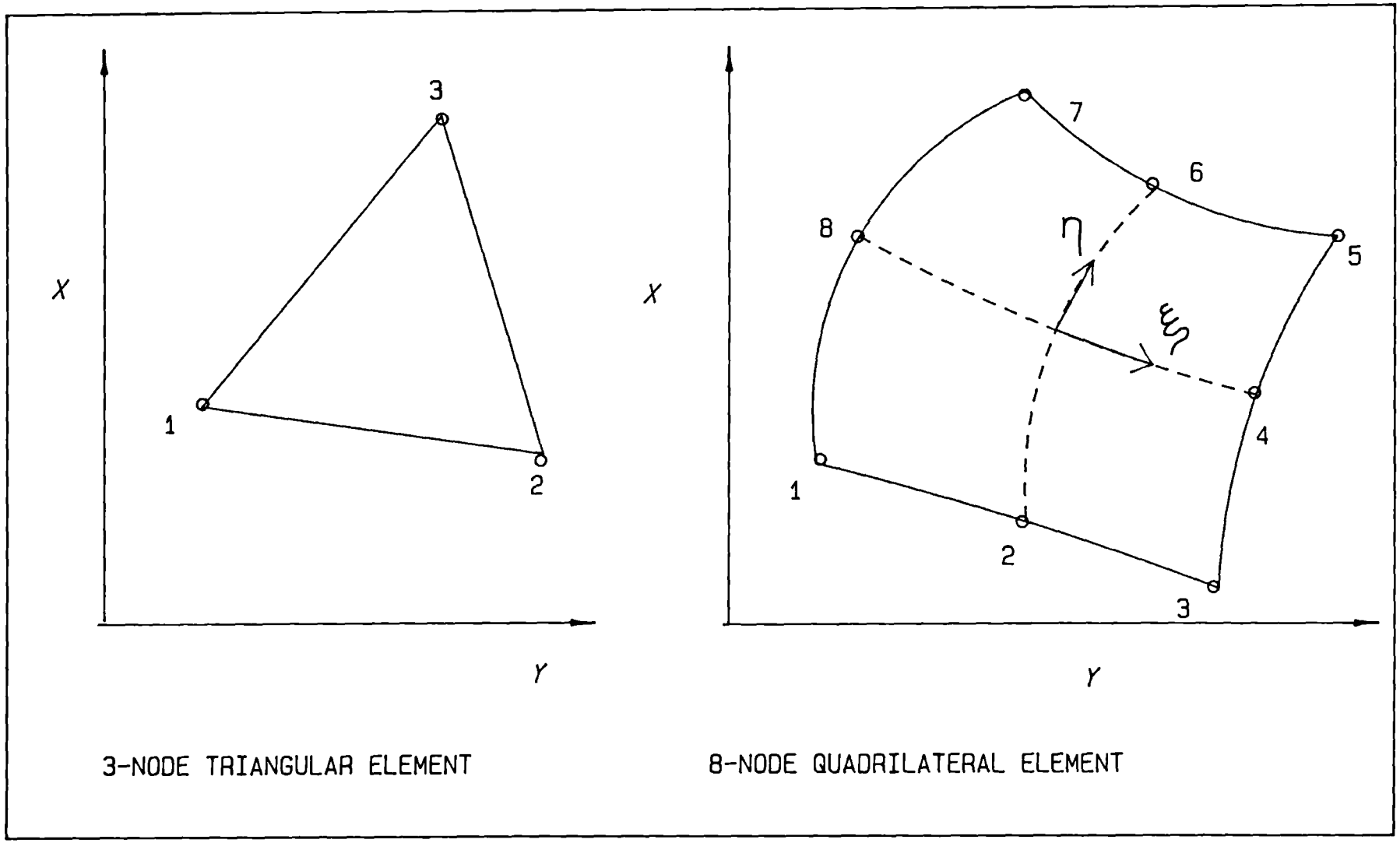

Figure 3.2 - Element types used for the lubrication analysis

Chapter 4

Rigid Bearing Analysis

4.1 Introduction

The initial work undertaken was to develop software to analyse and predict the performance of a dynamically loaded, finite rigid journal bearing. This was undertaken to gain an understanding of the problem and the factors involved, to try to develop a fast predictive technique for analysing the bearing performance, to gain an idea of the computing requirements and to develop a firm basis from which to move onto the problem of elastohydrodynamic lubrication.

One of the earliest solutions obtained for the finite rigid bearing problem was by Christopherson [8]. The finite difference method was used to model the lubricant film in the bearing. The resulting set of finite difference equations was solved using the Gauss-Seidel iterative over-relaxation technique to obtain the pressure distribution generated in the oil film. This method allowed the non-negativity pressure constraint to be applied to the pressure distribution and consequently the imposition of the Reynolds boundary condition on the solution in a simple manner. Cameron and Wood [9] also used a relaxation method, Southwells relaxation, to obtain results for a finite journal bearing. Similar methods were used by Raimondi and Boyd [11] and Pinkus [12] to produce design charts for bearing design. An improved finite difference formulation was proposed by Cameron [10], who solved for a modified pressure variable in an attempt to better resolve the steep pressure gradients occuring in the region of maximum pressure. A comprehensive review of the application of the finite difference method to the solution of Reynolds Equation is presented by Holmes and Ettles [13]. Five different equation formulations and several different iterative schemes for solving the finite difference equaitons are covered.

The finite element method, developed in the late forties for solving complex structural problems, was first applied to field problems by Zienkiewicz and Cheung [15] and Visser [16]. Field problems are generally concerned with the diffusion or flow of some quantity such as heat, or in the case of the hydrodynamic lubrication problem the flow of the lubricant. The flow can be related to gradients or potentials, in this case the pressures gradients cause the fluid flow. The development of

functionals for the lubrication problem by Hayes [17] and Tayo [18] presented the possibility of using the finite element method to solve the problem. An early solution using the finite element method was achieved by Reddi [19] for the incompressible lubrication problem and this was extended by Reddi and Chu [20] to cover the steady-state compressible problem. A comprehensive treatment of the application of the finite element method to the lubrication problem is given by Booker and Huebner [21].

This early finite element work was restricted to bearings where there was no cavitation or film rupture such as thrust or pad bearings. The problem of locating the free boundary was thus not covered. Goenka and Booker [55] incorporatd the free boundary problem into a finite element analysis of the performance of spherical bearings. A relaxation method similar to that used by Christopherson was adopted to locate the free boundary and impose the non-negativity constraint on the pressure distribution. Goenka [22], working at General Motors, used a method proposed by Chandeskharan [58] posing the problem as a complimentarity problem to locate the free boundary. It was reported that the Gauss-Seidel method previously used did not always produce a converged solution. The analysis demonstrated the full versatility of the finite element method and seventeen different bearing cases, some of them non-ideal with a variety of oil feed fea tures, were covered.

This chapter describes the development of a fast finite element method for the analysis of dynamically loaded rigid finite journal bearings. This includes a detailed discussion of the solution method and its optimisation, the method used to introduce dynamic loading, the way in which oil feed has been incorporated into the analysis and the particular choice of elements for modelling the lubricant film. Results are presented for a number of bearings, in particular the Ruston and Hornsby 6VEB Mk III marine diesel big end bearing which has been used extensively by other authors and has become a benchmark for comparing analysis techniques.

4.2 Solution method

4.2.1 Successive over-relaxaton

The first step in the analysis is to formulate the system matrices for the problem using the finite element method. Referring to equation (3.27) these matrices are given by

$$[K_p]\{p\} = \{U\}+\{\dot{H}\}$$

which may be rewritten for simplicity as

$$[K_p]\{p\} = \{Q\} \tag{4.1}$$

where $\{Q\}$ can be interpreted as the nodal flows caused by shear and squeeze effects. This formulation results in n simultaneous equations in the n unknown nodal pressures p, where n is the number of nodal points in the mesh. There are many different techniques for solving equations of this form. The Gauss-Seidel iterative solution method was chosen as it is simple to implement, can prove much more efficient than other solution methods, especially if the matrix $[K_p]$ is sparse, and, as has been shown [8], allows the non-negative pressure condition to be implemented in a routine manner.

Using Gauss-Seidel iteration the pressure p_i at node i is found from the i *th* equation of (4.1)

$$K_{p_{i,1}}p_1+....+K_{p_{i,i}}p_i+....+K_{p_{i,n}}p_n = Q_i \tag{4.2}$$

which can be rearramged to give

$$p_i = \{Q_i-K_{p_{i,1}}p_1-....-K_{p_{i,i-1}}p_{i-1}-....-K_{p_{i,i+1}}p_{i+1}-....-K_{p_{i,n}}p_n\}/K_{p_{i,i}} \tag{4.3}$$

Starting with an initial guess for the pressures a new estimate can be obtained from the equation

$$p_i^{(k+1)} = \{Q_i-K_{p_{i,1}}p_1^{(k+1)}-..-K_{p_{i,i-1}}p_{i-1}^{(k+1)}-...-K_{p_{i,i+1}}p_{i+1}^{(k)}-...-K_{p_{i,n}}p_n^{(k)}\}/K_{p_{i,i}} \tag{4.4}$$

where k is the iteration step. As soon as a new value of p_i is calculated it is used immediately for the next calculation. This process continues until the change in p_i falls below a certain amount, usually determined by

$$\frac{\sum_{i=1}^{n} |p_i^{k+1} - p_i^k|}{\sum_{i=1}^{n} |p_i^{k+1}|} < tol \qquad (4.5)$$

where *tol* is the tolerance used for the convergence, normally in the range 10^{-4} - 10^{-6}.

This process can however be slow to converge and the process can be accelerated by using successive over-relaxation (SOR). The governing equation for SOR is given by

$$p_i^{(k+1)'} = p_i^{(k)} + wf\,(\,p_i^{(k+1)} - p_i^{(k)}\,) \qquad (4.6)$$

where $p_i^{(k+1)}$ is the value of p_i calculated from the Gauss-Seidel iteration and wf is the over-relaxation factor used to modify the change in p_i between iterations to give a new value $p_i^{k+1'}$. The optimum value of the over-relaxation factor is normally in the range $1 < wf < 2$. It was reported by Goenka [22] that in some cases the Gauss-Seidel solution method did not produce a converged solution. This situation did not appear to arise using normal bearing data. It was found however when the software was being compared to the Sommerfeld solution by making the bearing very wide with an L/D ratio of about 10 that the solution became extremely slow to converge. On examining this in more detail the matrix $[K_p]$ was found to have become ill-conditioned (that is the diagonal dominance essential for the convergence of this type of solution method was lost). Since the matrices had become ill-conditioned however this meant that other solution methods would also not work so the failure to converge in this case was not due to the method that was being used to solve the equations.

4.2.2 Cavitation

Since, in practice, the lubricant can only sustain a negligible region of negative pressure due to the film tension, a large portion of the bearing will be cavitated or ruptured with the pressure equal to a constant cavitation pressure, p_c. Many analytical solutions deal only superficially with cavitation, the simplest assumption being that cavitation begins at the point of minimum film thickness and film reformation occurs at the point of maximum film thickness where the film thickness starts to

converge again. A better method for determining the cavitation region which satisfies flow continuity is Reynolds boundary condition. This states that at the point of film rupture the pressure and the pressure derivative are both equal to zero, (see section 2.5). Christopherson [8] showed that this condition could be easily implemented using SOR without having to determine the pressure gradient. To achieve this, each time a negative pressure is calculated during the relaxation process it is immediately set equal to zero. Since flow continuity is built into Reynolds equation, the resulting pressure distribution calculated using these zero pressures will automatically satisfy flow continuity at the point of film rupture.

4.2.3 Boundary conditions and oil feed

As well as the non-negative constraint imposed upon the pressure distribution there are two other boundary conditions to be incorporated into the analysis. The pressures are zero at the bearing edge and the pressure is equal to the oil supply pressure, p_s, at any oil supply holes or grooves. This was achieved in very much the same manner as the non negative pressure constraint was applied. Each time that a node was encountered during the relaxation that lay at the bearing edge or at an oil feed feature, the pressure was set to the required value and the iteration process continued. At this stage no attempt was made to accurately model the physical shape of the oil feed features. This was regarded as a refinement to the method and the work was more concerned with the development of a general predictive model. For the case of an oil feed hole the nearest node to the hole was found and the pressure was specified at that node. For the case of a partial groove the nodes nearest to the groove lying on the centre line were used. The full 360 degrees groove was modelled in one of two ways. Either the pressure at all the nodes on the centre line were set to the supply pressure, the width of the bearing being reduced by the appropriate amount to account for the width of the groove, or it was assumed that the supply pressure was negligible compared to the pressure in the rest of the bearing, each bearing land was then treated as an ideal bearing. Exploiting symmetry only one quarter of the bearing then had to be modelled. This method is similar to that used by Goenka [22].

4.2.4 Solution region and wrap around

For the present analysis the finite element mesh was fixed relative to the connecting rod axis. This was since in most of the bearings considered the oil feed features were on the surface of the connecting rod bearing. If required though it was a straightforward matter to fix the mesh relative to the crank pin. This situation would be necessary if the oil feed features were located in the crankpin. Figure 4.1 shows an example of a finite element mesh used to model the lubricant film. Since the solution region is continuous in the circumferential direction the first and last rows are coincident. This means that if there are n nodes in the mesh there are $n-mnz$ unknowns where mnz is the number of nodes in the axial direction. Therefore only $n-mnz$ equations are to be assembled so the last mnz nodes are redundant. This redundancy is eliminated during the assembly of the system matrices. For each element a steering vector is used to place the coefficients of the element matrices in the correct positions in the system matrices. This vector has the form $ksy(IN,IE)$ where IE is the element number and the entry $ksy(IN,IE)$ is the global node number corresponding to the $INth$ node in the element. By simply setting the correct global node numbers in this steering vector for the elements that lie on the last row of the mesh only $n-mnz$ equations will be asembled. For instance the element IE, which has the node $n-1$ on the last row as its second local node, the entry $ksy(2,IE)$ is set to 4 which is the corresponding node on the first row of the mesh. In this way the system matrices are assembled for a continuous film.

4.2.5 Calculation of the load vector

For a given journal position the resulting pressure distribution can be found in the way described above. From this the resultant load vector is given by

$$W_x = \int_A pR\cos\theta dA$$

$$W_y = \int_A pR\sin\theta dA$$

To find the resultant load vector from the n discrete nodal values of the pressure p, numerical integration had to be used. Two different methods were used for the two different element types. For the triangular elements, since a linear variation of the pressure was assumed over each element a linear integration method had to be

employed, in this case the trapezoidal rule. Using a higher order integration would not have been in keeping with the assumptions used to calculate the pressure distrbution and could lead to inaccurate results. For the 8-node quadrilateral elements Gauss-Legendre quadrature was used to integrate the pressure distribution over each element. Again this method was chosen on the basis of the assumptions used to calculate the pressure distribution.

4.2.6 Dynamic time stepping

The problem to be solved is to predict the journal centre orbit of the journal within the housing under the influence of an externally applied dynamic load. This is achieved by discretising time into small steps and at each step finding the journal position and velocity that will produce the required pressure distribution to balance the load applied at that time step. Finding the pressure distribution for a given eccentricity is straightforward and is simply a matter of solving the corresponding finite element equations with the appropriate boundary conditions. The main problem with both the steady state and dynamic problems is finding an efficient method for adjusting the eccentricity at each load case to produce the required pressure distribution. This is an iterative process and it is desirable that the correct journal position is found in as few steps as possible since each time a new estimate is made for the journal position the system matrices are reformulated which is very time consuming. Several different methods were developed for carrying out these iterations.

The first attempt to develop a method for finding the journal position was to use the equation for the dimensionless load generated in an infinitely wide bearing [10]

$$W = \frac{\pi\varepsilon}{(1-\varepsilon^2)^{1/2}(1+\varepsilon^{3/2})} \tag{4.7}$$

It was assumed in general that

$$W \propto \frac{\pi\varepsilon}{(1-\varepsilon^2)^{1/2}(1+\varepsilon^{3/2})}$$

therefore for two eccentricities ε_1 and ε_2 with corresponding loads W_1 and W_2

$$\frac{W_2}{W_1} = \frac{\pi\varepsilon_2}{\pi\varepsilon_1}\frac{(1-\varepsilon_1^2)^{1/2}(1+\varepsilon_1^{3/2})}{(1-\varepsilon_2^2)^{1/2}(1+\varepsilon_2^{3/2})} \tag{4.8}$$

If ε_2 is unknown, W_1 is the load generated for eccentricity ε_1 and W_2 is the required load, ε_2 can be found by rearranging (4.8) as

$$f(\varepsilon_2) = \pi\varepsilon_2 - \frac{W_2}{W_1}\frac{(1-\varepsilon_2^2)^{1/2}(1+\varepsilon_2^{3/2})}{(1-\varepsilon_1^2)^{1/2}(1+\varepsilon_1^{3/2})}\pi\varepsilon_1 = 0 \tag{4.9}$$

using Newtons method to find the required eccentricity as

$$\varepsilon_{i+1} = \varepsilon_i - \frac{f(\varepsilon_i)}{f'(\varepsilon_i)} \tag{4.10}$$

For a given load a guess was made for the eccentricity ε_1 to give a load W_1. The eccentricity, ε_2, required to balance the applied load W_2 could then be estimated. This procedure was repeated until $W_1 = W_2$. This method worked reaonably well for the steadily loaded case but gave very slow convergence if the required change in eccentricity was large particularly for the dynamically loaded case. A curve fitting program was tried with the eccentricity as a function of the load and the L/D ratio, this however was only of any use for steadily loaded ideal bearings. On examining the general relationship between the eccentricity and the log of the load W it was seen that if the required change in the eccentricity was fairly small the relationship between the eccentricity and the $\log_e$ of W would be almost linear. A new relationship was used given by

$$\varepsilon_1 \propto LnW_1 \tag{4.11}$$

for which the corresponding change in eccentricity required is

$$\Delta\varepsilon \propto LnW_1 - LnW_2$$

therefore

$$\varepsilon_1 - \varepsilon_2 = k_1(LnW_1 - LnW_2) \tag{4.12}$$

By making an initial guess for the eccentricity to get W_1 and then changing the eccentricity by a small amount $\Delta\varepsilon$ a value of ε_2 and W_2 could be found from which the value of k_1 could be determined. By substituting the applied load into (4.12) the required change in eccentricity could be obtained. This process was continued until convergence was achieved. This iteration was only for the magnitude of the eccentricity. A second iteration was performed for the angle at which the eccentricity

vector lay according to

$$k_2 = \frac{\theta_1 - \theta_2}{\psi_1 - \psi_2} \tag{4.13}$$

where θ is the angle at which the minimum film thickness occurs and ψ is the angle at which the load is acting. The iterative procedure used is shown in Figure 4.2. This method converged in about 5-6 iterations, and for the dynamic problem the values calculated for k_1 and k_2 could be carried forward to the next step since they were found to vary only by a small amount between time steps and subsequently used to provide a good initial estimate for the eccentricity at the next time step.

The final method relied upon the Newton-Raphson iterative technique in which ε_x and ε_y were solved for instead of ε and θ. Writing

$$f_1(\varepsilon_x, \varepsilon_y) = W_{ax} - W_x$$

$$f_2(\varepsilon_x, \varepsilon_y) = W_{ay} - W_y$$

the Newton-Raphson method gives

$$\begin{Bmatrix} \frac{\partial f_1}{\partial \varepsilon_x} & \frac{\partial f_1}{\partial \varepsilon_y} \\ \frac{\partial f_2}{\partial \varepsilon_x} & \frac{\partial f_2}{\partial \varepsilon_y} \end{Bmatrix} \begin{Bmatrix} \Delta\varepsilon_x \\ \Delta\varepsilon_y \end{Bmatrix} = \begin{Bmatrix} -f_1 \\ -f_2 \end{Bmatrix} \tag{4.14}$$

Initially this was evaluated by making an initial estimate for the ecccentricity, ε, and then changing ε_x by a small amount while keeping ε_y constant to numerically evaluate $\partial f_1/\partial \varepsilon_x$ and $\partial f_2/\partial \varepsilon_x$. Similarily $\partial f_1/\partial \varepsilon_y$ and $\partial f_2/\partial \varepsilon_y$ could be obtained. These values were used to calculate the required values of $\Delta\varepsilon_x$ and $\Delta\varepsilon_y$ to give a new estimte for the eccentricity. This process was highly convergent but required three iterations for each new estimate for the eccentricity. On examining the change in the values of $\partial f_1/\partial \varepsilon_x$, $\partial f_2/\partial \varepsilon_x$, $\partial f_1/\partial \varepsilon_y$ and $\partial f_2/\partial \varepsilon_y$ it was found that these varied very little during and between each time step. This method was therefore greatly improved by adopting a form of modified Newton-Raphson method [53] to

calculate the values of $\Delta\varepsilon_x$ and $\Delta\varepsilon_y$. The modified Newton-Raphson method relies on the derivatives only changing by a small amount between iterations. These values are then only calculated once at the start of the sequence of iterations and subsequently used to calculate all the new values of $\Delta\varepsilon_x$ and $\Delta\varepsilon_y$. In many cases this method is only slightly less convergent than the Newton-Raphson method and is significantly more efficient.

Starting with the values of the derivatives from the previous iteration, the corrections for ε_x and ε_y can be calculated as $\Delta\varepsilon_{x1}$ and $\Delta\varepsilon_{y1}$. Using these new values W_x and W_y can be calculated giving f_1^1 and f_2^1. This process can be repeated giving $\Delta\varepsilon_{x2}$ and $\Delta\varepsilon_{y2}$ and f_1^2 and f_2^2. From equation (4.14) this gives

$$\frac{\partial f_1}{\partial \varepsilon_x}\Delta\varepsilon_{x1}+\frac{\partial f_1}{\partial \varepsilon_y}\Delta\varepsilon_{y1} = -f_1^1$$

$$\frac{\partial f_2}{\partial \varepsilon_x}\Delta\varepsilon_{x1}+\frac{\partial f_2}{\partial \varepsilon_y}\Delta\varepsilon_{y1} = -f_2^1$$

$$\frac{\partial f_1}{\partial \varepsilon_x}\Delta\varepsilon_{x2}+\frac{\partial f_1}{\partial \varepsilon_y}\Delta\varepsilon_{y2} = -f_1^2$$

$$\frac{\partial f_2}{\partial \varepsilon_x}\Delta\varepsilon_{x2}+\frac{\partial f_2}{\partial \varepsilon_y}\Delta\varepsilon_{y2} = -f_2^2$$

which provides four equations in the four unknowns $\partial f_1/\partial\varepsilon_x$, $\partial f_2/\partial\varepsilon_x$, $\partial f_1/\partial\varepsilon_y$ and $\partial f_2/\partial\varepsilon_y$. This allows the values of the derivatives to be recalculated as the journal position iteration progresses rather than separately. This makes the iteration process considerably more efficient since it is not necessary to carry out three complete calculations to obtain one set of corrections. This method in general produced a high rate of convergence for both the steady loaded and dynamic problems, typically requiring 1-2 iterations per time step. In some cases the solution proved slow to converge or diverged. This was overcome by putting a limit on the maximum values of $\Delta\varepsilon_x$ and $\Delta\varepsilon_y$. If the process still would not converge the Newton Raphson method was used until the solution began to converge again.

4.2.6.2 Implicit and explicit time stepping

The solution for the dynamic problem is obtained by stepping through time using discrete time steps. The journal poition is known at the start of each time step and is to be found at the end of the step to balance the applied load. This value is then used for the start of the next time step. Two different methods were investigated for stepping through time which will be referred to as the implicit and explicit methods.

In the implicit method, which was the method adopted for the early part of the analysis, the film thickness, h, is a function of the eccentricity at the current time step, $h = f(\varepsilon_i)$. Therefore each time the eccentricity is altered during the time step the film thickness and the the squeeze term dh/dt are both adjusted so all the sytem matrices must be reformulated. In the explicit scheme, the film thickness is taken as a function of the eccentricity at the end of the previous time step, $h = f(\varepsilon_{i-1})$ and so is totally known at the current time step. Each time the eccentricity is adjusted the only term affected is therefore the squeeze term. The advantage with this scheme, which is similar to the time stepping scheme adopted by Goenka [22], is that since the matrix K_p given by (3.25) as

$$K_{p_{ij}}{}^{e} = -\int_{A^e} h^3 \left[\frac{\partial N_i}{\partial \theta}\frac{\partial N_j}{\partial \theta} + B^2 \frac{\partial N_i}{\partial z}\frac{\partial N_j}{\partial z} \right] dA$$

is only a function of the film thickness h it need only be evaluated once for each time step. This led to a considerable saving in computing time. Using the explicit method the problem becomes linear in the nodal pressures and the journal centre velocities, $\dot{\varepsilon}_x$ and $\dot{\varepsilon}_y$. It would therefore seem that the problem could be solved directly without having to iterate for the journal centre position. There is however still a considerable degree of non-linearity in the problem due to the film cavitation. It was also found that for large time steps (greater than 5 degrees of crank rotation) the explicit method became unstable in some cases whereas the implicit method is inherently stable.

4.2.6.3 Squeeze term verification

Verifying the results for the predicted behaviour of the bearing under steady loading was straightforward since there is already a large amount of published material giving solutions for steady loaded finite bearings [10]. Also as the width of the bearing was increased or decreased a qualitative assement could be carried out on the results which should converge towards the predicted performance given by the two analytical solutions presented in Chapter 2 for the short bearing and narrow bearing theory. However testing the software developed for predicting the dynamic behaviour of the bearing was not so straightforward. It was possible to compare the predicted journal centre orbits and peak pressures with other authors work but it was felt that a more rigorous method was required. It was important that these methods were both simple and could give a clear indication of how accurately the squeeze term was being incorporated into the analysis. Two different methods were developed to achieve this. One qualitative and the other quantitative.

The first test was to apply a steady load to the the bearing, with the journal running at a constant angular velocity at a fixed eccentricity. The bearing was then 'released', the journal centre orbit should then follow a smooth curve, ending at the steady loaded position when all the squeeze effects should have disappeared. One of these orbits is shown in Figure 4.3. The second test was on a quantitative basis and compared the performance with shear only directly to that with shear and squeeze. Consider the journal and housing rotating with angular velocities ω_j and ω_b with a constant load applied to the system rotating at an angular velocity ω_l (Figure 4.4). For the steady loaded case with the velocities measured relative to the bearing housing $\omega_j = \dot{\theta}$, $\omega_b = \omega_l = 0$. However if the reference axis is switched to the journal the velocities become $\omega_j = 0$, $\omega_b = \omega_l = -\dot{\theta}$. Since the Reynolds equation contains the term

$$\overline{U} = \frac{(U_j+U_b)}{2} = \frac{R(\omega_j+\omega_b)}{2} \tag{4.15}$$

this problem is the same as the problem where $\omega_j = \omega_l = -\dot{\theta}$, $\omega_b = 0$. Therefore if, under steady loading the bearing has a certain eccentricity ε_s, for the dynamic case with the same load applied to the system rotating at the same speed as the journal, the journal centre should settle into a circular orbit of radius ε_s (Figure 4.5). These methods proved very useful in highlighting errors in the way in which

the squeeze term had been incorporated into the analysis.

4.3 Relaxation optimisation

As previously mentioned the SOR solution method can prove very efficient for solving the type of problem encountered here. Several methods were used to optimise the relaxation process in an attempt to decrease the required solution time. One of the most significant factors influencing the rate of convergence of the sequence of iterations is the choice of over-relaxation factor, wf. Several techniques have been developed for determining the optimum over-relaxation factor, wf_{opt}, [59], but these depend very much on the nature of the problem being considered. Typically the optimum value lies in the range $1 < wf_{opt} < 2$ and in general some form of numerical experimentation is required. An investigation was carried out to determine the effect of element type, meshsize and load on the choice of wf_{opt}. Figure 4.6 shows the number of iterations required to achieve a given tolerance. The relationship between the number of iterations and the order of magnitude of the tolerance is nearly linear and therefore doubling the order of magnitude of the required tolereance would roughly double the number of iterations required. If the sequence of iterations achieves a given tolerance it does not necessarily indicate that a converged solution has been reached but that the rate of convergence has fallen below a certain value. To check the convergence of the relaxation process the results for a full Sommerfeld solution (see section 2.5) was obtained using SOR and using Gaussian elimination to solve the equations for the pressure. The Sommerfeld solution was used since there is no cavitation region to be found .The Gaussian eleimination method is non iterative, therefore if the SOR solution was well converged the two solutions should be the same. This was the case so it was reasonable to assume that the SOR solution method produced a well-converged solution for this problem. A tolerance of 10^{-4} proved adequate in all cases. This tolerance gave a maximum error in the calculated load when compared to that obtained using a tolerance of 10^{-7} of .025%. Decreasing the tolerance to less than 10^{-4} made a negligible difference to the results obtained but significantly increased the number of iterations. It was impractical to use a tolerance of less than 10^{-7} due to the rounding errors caused by the precision of the computer.

Figure 4.7 shows the effect of varying the number of circumferential nodes for the 8-node isoparametric mesh. It appears that increasing the number of circumferential nodes increased the value of wf_{opt}. The overall rate of convergence though did not seem to be very sensitive to this value, especially in the range 1.4-1.5. In general a value of 1.5 for wf proved adequate for all the meshes used. Varying the number of axial nodes however (Figure 4.8), although having little effect on the choice of wf_{opt} had a very significant affect upon the rate of convergence of the solution. Increasing the number of axial nodes greatly increaed the number of iterations and also increased the sensitivity of the solution process to the choice of wf. Figure 4.9 shows the effect of increasing the number of circumferential nodes for the 3-node triangular element mesh. In general the 3-node triangular elements behaved in very much the same way as the higher-order elements but were more sensitive to the value of wf. From this study a value of between 1.55 and 1.65 was used for the over-relaxation factor for the 3-node triangular elements, depending upon the number of circumferential nodes used. A value of 1.5 proved adequate for all cases using the 8-node isoparametric elements. It was found that varying the magnitude of the load and the introduction of dynamic loading had no effect on the choice of wf_{opt}. The affect of varying the mode of sweeping the mesh during the relaxation process was also investigated. The sweeping modes used were:

i) In the circumferential direction, 1,2,...,n

ii) In the axial direction, 1,2,....,n

iii) Sweeping alternately forwards and backwards, 1,2,....,n n,....,2,1, in the circumferential and axial directions.

iv) Sweeping alternate points, 1,3,.....n 2,4,....,n-1,in the circumferential and axial directions.

Of these the first method proved to be the most efficient, the other modes increasing the number of required iterations especially the last which increased this by almost 100%.

The second method used to optimise the SOR solution method exploited the sparsness of the matrix $[K_p]$ to reduce the amount of required computer storage and the number of calculations carried out during the solution process. In Figure 4.10 the nodes affecting each node in the two different meshes are shown. For the triangular elements each node, i, has 6 nearest neighbours and for the 8-node

isoparametric elements the number of nodes affecting a corner node, i, is 21, and a midside-node, j is 13. For a 3-node triangular element each row of the matrix $[K_p]$ has only 7 non-zero terms and therefore when the relaxation calculation, given by (4.3) as

$$p_i = \{Q_i - K_{p_{i,1}} p_1 - .... - K_{p_{i,i-1}} p_{i-1} - .... - K_{p_{i,i+1}} p_{i+1} - .... - K_{p_{i,n}} p_n \} / K_{p_{i,i}}$$

is carried out, there are a very large number of redundant calculations. Two different algorithms were developed to exploit this sparsness. The first meant that only the non zero terms in the matrix $[K_p]$ were stored. Therefore for the 3-node triangular elements this meant that the size of $[K_p]$ was reduced from n xn to nx7 and for the 8-node isoparametric elements nx22. This was achieved by using a steering vector which placed the coefficients of the matrix $[K_p]$ in the correct place during assembly. The second algorithm stored the numbers of all the nodes affecting a particular node, i, so only this number of calculations was carried out during the execution of equation (4.3). This greatly decreased the required computing time since fewer calculations were carried out and since the required computer storage was considerably reduced meaning that the computing time to access a particular coefficient of the matrix $[K_p]$ was also reduced.

The rate of convergence of the solution process was very high. Figure 4.11 shows the region of positive pressure obtained during the solution process where k is the iteration step. It was found on examining the solution convergence that when the tolerance had fallen below 10^{-1} the positive pressure region had been found. Therefore the solution procedure could be greatly improved by only carrying out the relaxation over this region once this tolerance had been reached which in some cases reduced the computing time by 50%.

4.4 Dynamically loaded engine cycle

4.4.1 Load interpolation

The external load applied to the bearing is supplied as a function of crank angle every 10 degrees of crank rotation. For the dynamically loaded engine cycle the time steps invetigated were 1, 2, 5 and 10 degrees of crank rotation. Therefore the load had to be interpolated to obtain the intermediate time steps. Initially a linear variation was assumed but this gave a very discontinuous load diagram. To improve upon this quadratic and cubic Lagragian interpolation [60] were used. Cubic interpolation gave the best approximation to a smooth curve and was adopted for the subsequent analysis. Figure 4.12 shows the polar load diagrams for two different bearings obtained using a step size of two degrees of crank rotation using linear and cubic interpolation. The improvement gained by using cubic interpolation is clear from this.

4.4.2 Startup

The problem considered is cyclic through time but must be started from a steady loaded position since there is no previous known time step from which to calculate a dynamic response. To start the solution the load was applied as a ramp input over the first 10 time steps. This gave a transient response which died away quickly and the solution was found to converge in between 1.3 and 1.5 engine cycles. This depended upon the time step size used, the example considered and to some extent the point in the engine cycle at which the solution was started from. It appeared that the best point for starting the cycle was when the load vector was moving at its slowest. Figure 4.13 shows the steady state and transient orbits. Two tests were carried out to determine if the dynamic cycle had converged. The first was to compare the journal position at each time step with that from the same step in the previous cycle, the second was to compare the magnitude and position of the maximum film pressure. If the difference in both of these had fallen below a certain amount the solution was assumed to have converged. To check that this was the converged solution the solution was run for 20 engine cycles and the results compared to those obtained after 1.5 cycles. It was found that there was no difference in

the results.

4.4.3 Solution Extrapolation

On examining the behaviour of the bearing under dynamic loading it was found that for most of the cycle the journal centre orbit was a fairly smooth curve, even when the load vector was changing rapidly. Figure 4.14 compares the position of the load vector the position of the point of minimum film thickness. It is clear that there is a lag in the response of the bearing to a change in position of the load due to the damping properties of the oil. It is therefore difficult to predict the position of the bearing at the next time step based upon the load and the load position at the next time step. It was therefore decided that since the movement of the journal generally showed no discontinuities a good estimate for the journal position could be obtained by using a second order Runge-Kutta extrapolation technique. In many cases this proved accurate enough to eliminate the need for any further iterations for the journal position at the current time step. The relaxation method was also ideally suited to the dynamic problem since the pressure distribution and the cavitation region calculated at the previous time step provided a good initial estimate for the current time step. Thereby reducing the number of iterations at the current time step.

4.5 Output parameters

The following information was required from the analysis:

i) Minimum oil film thickness

ii) Peak oil film pressure

iii) Power loss during the cycle

iv) Flow of lubricant out of the bearing

The minimum oil film thickness is obtained from equation (2.16) as

$$h_{min} = (1-\varepsilon)c$$

where ε is the bearing eccentricity ratio. Two different methods were used to obtain the peak oil film pressure, depending upon the element type used. For the 3-node triangular elements a linear variation had been assumed for the pressure distribution over each element so the peak pressure must occur at a nodal point. Fitting

a curve through the pressure distribution would not be in keeping with the assumptions used to obtain the pressure distribution. For the 8-node isoparametric elements, a quadratic variation had been assumed for the pressure and interpolation was carried out between the nodes to find the peak pressure. To achieve this the peak nodal pressure, p_1, was found (Figure 4.15). An interpolation was then carried out in the circumferential direction between nodes p_2 and p_3 using a Lagrangian interpolation formula assuming a quadratic variation of the pressure to find the maximum pressure lying on this line, p_1'. This was achieved by stepping from p_2 to p_3 in discrete steps equal to $\Delta x/100$ noting the maximum value of pressure encountered. It was assumed that the maximum overall pressure must lie somewhere on a line passing through this point. p_{max} was therefore found by first calculating the pressures p_7 and p_{11} and carrying out a similar interpolation in the axial direction.

The power loss in the bearing was obtained from equation (2.41) as

$$H = \mathbf{F}.\dot{\mathbf{e}}+R^2\Delta\omega\Delta\omega I_1+2I_2\overline{\omega}$$

This value was calculated at each time step using the two forms of numerical integration described earlier for the two different element types. Once the steady state journal centre orbit had been found the power loss was summed for each step to obtain the average power loss for the cycle.

To calculate the side flow out of the bearing use was made of the flow term $\{q\}$ in equation (3.25) which was previously ignored since it was not required to evaluate the pressure distribution. This then gives

$$[K_p]\{p\} = \{q\}+\{U\}+\{\dot{H}\}$$

and rearranging this equation results in

$$\{q\} = [K_p]\{p\}-\{U\}-\{\dot{H}\}$$

Once the required pressure distribution has been found the right-hand side of this equation is totally known. The flow out of the bearing is then found by calculating the flow terms for each node lying on the edge of the bearing in the non-cavitated region. Summing these terms gives the side flow out of the bearing. If symmetry is being exploited this value must be doubled to give the flow for the whole bearing.

4.6 Choice of element type

For the initial work undertaken 3-node traingular elements were used to model the lubricant film. This type of element has been used extensively by other authors and proves relatively easy to implement in a finite element solution. It is important that the sharp pressure peaks that occur during the most highly loaded phases of the engine cycle are accurately modelled, since these regions are the most crucial for accurate prediction of the bearing performance. Since the 3-node triangular element assume a linear variation for the pressure distribution an accurate representation can only be obtained by using a large number of elements which is computationally expensive. It is difficult to use a graded mesh with a high concentration of elements at the point of maximum loading since there may be several highly loaded phases during the engine cycle occurring at different parts of the bearing. Milne [31] used 3-, 4-, 5- and 6-node elements to examine the performance of a steady loaded plane slider bearing. He reported that the 6-node elements gave the best performance. It was therfore decided that a higher order element should give a better representation of the pressure distribution. The use of higher order elements to model the lubricant film has been looked at by very few authors as the complexities of the programming involved are significantly greater than those involved when using the 3-node triangular elements. On examining the pressure distribution in the bearing it is a fairly smooth curve with no major discontinuities except at the point of film rupture. It was therefore decided that using an element that assumed a quadratic variation in both the circumferential and axial directions should provide a better resolution of the pressure distribution. 8-node isoparametric elements were therefore chosen since these should be able to give a more accurate representation of the pressure distribution requiring fewer elements than the simpler 3-node triangular elements.

4.7 Results

4.7.1 Sample bearing example

To assess the performance of the software that was developed, and to compare the effect of the various solution parameters on the predicted bearing performance, the Ruston and Hornsby 6VEB Mk III marine diesel big end bearing was analysed. The data [5] for this particular bearing are as follows:

Crank length	$0.1840m$
Rod Length	$0.7820m$
Bearing Width	$0.1270m$
Circumferential groove width	$0.0127m$
Bearing diameter	$0.2030m$
Radial clearance	$82.55\mu m$
Engine speed	$600r/min$

This bearing was chosen as an illustrative example as it has been used by a large number of authors [5,22,61] and has become a bench mark against which to compare analysis techniques. Figure 4.16 shows the polar load diagram [5] for the bearing relative to the connecting rod axis. Results are also presented for two other bearings to show the versatility of the software [62,63]. The Ruston bearing is from a low-speed diesel engine whilst the two other bearings are the intermain bearing from a medium speed engine and the connecting rod bearing from a high speed internal combustion engine. For the predicted bearing performance the following information was obtained:

i) The journal centre orbit

ii) The minimum film thickness

iii) The peak oil film pressures

iv) The power loss

v) The side flow out of the bearing

Post processing software was developed to process all the data produced and present it in a readable form using an Apollo high resolution graphics terminal.

A comparative study is first presented showing the effects of the element type used on the predicted performance. The two different time stepping methods are then compared along with the effect of varying the time step size used for the analysis. Results are also presented to show the effect of incorporating oil feed features in the analysis.

4.7.2 Comparison of element types

In comparing the predicted performance using the two different element types results are presented for a complete dynamic analysis of the Ruston connecting rod bearing. The implicit time stepping method was used with a time step size corresponding to two degrees of crank rotation. For the example considered a centrally located 360 degree circumferential oil feed groove was incorporated and the effect of the oil supply pressure was neglected. This is the case commonly used by other authors. In this way each half of the bearing may be treated as an ideal bearing and due to symettry only one half of each bearing land need be modelled. The results are plotted against the number of circumferential nodes (M) used for each mesh. This mesh parameter was found to have a much greater effect upon the predicted bearing performance than the number of axial nodes. For the 3-node triangular element mesh 31 to 61 and 7 to 11 nodes and for the 8-node isoparametric elements 21 to 61 and 5 to 7 nodes were used in the circumferential and axial directions respectively. Using coarser meshes the solution became too inaccurate and for finer meshes it was found that there was no gain in the solution accuracy.

The variation of the predicted minimum film thickness h_{min} for the dynamic cycle is shown in Figure 4.17a. The 8-node elements show a much higher rate of convergence as the number of circumferential nodes is increased. No significant increase in accuracy is achieved by using more than 41 nodes in the circumferential direction. The triangular elements show a much slower rate of convergence, although the results appear to converge towards the solution obtained using the 8-node isoparametric elements. The results obtained by other authors are also shown and are in good agreement with the present results. Figure 4.17b shows the cyclic power loss in the bearing. Again the 8-node elements show a much higher rate of convergence although the variation here is less marked. The higher-order 8-node elements do, however, give a much better solution when using a very coarse mesh.

There is little overall difference in the journal centre orbits obtained using the two different element types (Figure 4.18) except in the region of firing. All the journal centre orbits produced were similar to those shown. As the mesh was refined the general shape of the orbit tended towards that obtained using a 61 x 5 mesh of 8-node elements. The variation in the load calculated for a medium and a high eccentricity using the two types of element is shown in Figure 4.19. The 8-node isoparametric element mesh performs very well in both cases showing a high rate of convergence as the mesh is refined. Again using the triangular elements a lower rate of convergence was obtained. Since a higher order integration method is used to obtain the calculated load when using the 8-node isoparametric elements a much better resolution is possible using fewer nodes than for the 3-node triangular elements.

The value of the calculated load that was used here, W_{av}, is the average value taken from a number of points. The reason for this is that it was found that the value of the calculated load varied slightly depending upon the position of the point of minimum film thickness relative to the mesh. This variation results from using a fixed mesh to model the pressure distribution in which the beginning and end of the positive pressure region must coincide with nodal points. This is of course an approximation as in general these boundaries will lie at some point between the nodal points. Figure 4.20 shows how two meshes in two different positions relative to the actual pressure distribution can give rise to two different nodal values for the maximum film pressure and different values for the end of the positive pressure region. The value of W_{av} was obtained by moving the point of minimum film thickness between two points on the mesh and calculating the load at discrete points. Figure 4.21 shows how this values varies as the point of minimum film thickness is moved. A cyclic variation is seen where Δx is the distance between two nodes on the mesh. As the position of the point of minimum film thickness is moved the end of the pressure region will remain fixed at one set of nodes until there is sufficient change to cause it to move to the next set of nodes. Using a coarse mesh this change in the extent of the pressure region can be quite marked and can have a significant effect upon the predicted bearing performance. For a fine mesh, however, there is little pressure generated over these regions and the effect is not significant. The variation in the calculated load is of the order of ±6 to ±1.5% and ±3 to ±1% for the 3-node triangular and 8-node isoparametric elements, respectively, depending

upon the eccentricity and mesh size used. For the dynamically loaded case where extrapolation techniques are used between time steps to predict the journal position at the next time step this variation can cause an increase in the number of iterations required at each step, especially when a coarse mesh is used. This problem could be partially remedied by using a moveable mesh to locate the actual boundary between the positive pressure region and the cavitated region. This, however, would considerably increase the complexity of the problem requiring an extra iteration loop to find the free boundary as well as requiring a considerable amount of recalculation to generate each new mesh configuration. This could also lead to problems when considering the effect of the housing elasticity since the structural and lubrication problems are normally coupled using coincident nodes on the structural and fluid finite element meshes. Again the effect of this variation due to the mesh position can be seen over the dynamic cycle in Figures 4.22 and 4.23 which show the variation of the peak film pressures during the engine cycle. The variation is seen as an oscillation in the pressure, the effect being especially marked when using a coarse mesh.

In Figure 4.24a the disadvantage of using linear elements to resolve the pressure distribution is apparent. The 8-node isoparametric elements produce a result that converges rapidly while the triangular elements do not appear to converge but appear to lie within a certain region. This is due to the linear variation assumed for the pressure distribution assumed for the triangular elements. Since the variation is linear the peak film pressure predicted using the linear triangular elements must lie at a node. The value of the maximum pressure is therefore very dependant upon the position of the pressure distribution relative to the mesh. A coarse mesh in which the actual position of the peak film pressure lies close to a node could yield a more accurate result than a fine mesh where the actual position of the maximum pressure lies well away from a nodal point.

The amount of computer time required for the analysis is shown in Figure 4.24b. This is the time required using a VAX 11/785 mainframe computer running in single precision. The software has also been run on a Cray supercomputer which is double the precision of the VAX to check for rounding errors occuring due to the highly iterative nature of the problem. There appeared to be no noticable errors. It is clear from this diagram that the 8-node isoparametric elements require a greater

amount of computing time for a given mesh size. However if two meshes with similar computing times are compared the 8-node isoparametric elements show a much higher degree of accuracy. The higher order elements are therefore a better choice for modelling the lubricant film and are better able to resolve the pressure distribution due to the quadratic variation assumed for the pressure variation over these elements.

4.7.3 Time stepping and effect of time step size

As mentioned previously two different methods were used to step the solution through time, the implicit and explicit methods. In the implicit method the film thickness, h, is a function of the eccentricity at the current time step so h and $\partial h/\partial t$ are both unknowns. Each time that the journal position is adjusted these values are recalculated. In what is known as the explicit method h is a function of the eccentricity at the previous time step so the film thickness is totally defined at the current time step. The only value that has to be recalculated during the iterative process to find the journal position is the squeeze term $\partial h/\partial t$ from which the eccentricity at the next time step may be obtained using extrapolation. Since the matrix $[K_p]$ only depends upon the film thickness it need only be calculated once at each time step. This leads to a considerable saving in computing time since the assembly of $[K_p]$ is one of the most time consuming parts of the analysis. Only the squeeze matrix $\{\dot{H}\}$ has to be recalculated during the iterative process to find the required journal position. In general the explicit method proved to be three to four times faster than the implicit method. In both cases the squeeze term $\partial h/\partial t$ was found at each node using a backward differencing formula as

$$\frac{\partial h}{\partial t} = \frac{h_i - h_{i-1}}{\Delta t} \tag{4.17}$$

where h_i is the film thickness due the eccentricity at the current time step and h_{i-1} is the film thickness at the end of the previous time step. To affect the time stepping a constant step size was used for the complete engine cycle. The step sizes used were 10,5,2 and 1 degrees of crank rotation. To assess the effect of the step size on the predictive performance the test described earlier for verifying the incorporation of the squeeze term into the analysis was used. Using this a rotating load of constant magnitude is applied to the system with the journal rotating at a

constant angular velocity. The angular velocity of the load is the same as the angular velocity of the journal. The results from this can be compared directly to the results for a steady loaded case where the step size does not effect the performance and there are no squeeze effects. Two cases were considered to obtain a quantitative assessment of the two time stepping methods and the effect of the time step size. The first was for a medium load case corresponding to an eccentricity of 0.8 and the second for an eccentricity of 0.95 which gave approximately ten times the loading in the first case.

The results of the analysis are shown in Figures 4.25-28 where the eccentricity, peak pressures, power loss and side flow are compared against the number of time steps used per engine cycle (720 degrees of crank rotation) using the two time stepping methods. The dotted line represents the value obtained for the static case. All the results converge quickly as the number of steps per engine cycle is increased. The best results being obtained when using 720 steps per cycle, this corresponds to a step size of 1 degree of crank rotation. There is, however, a difference of less than 1% in the results when a step size of 2 degrees is used. In all cases the explicit method overestimated the results and the implicit method underestimated. This would seem logical since for the explicit method the shear effects are constant at each step and the only term that changes is the squeeze term. Therefore during the iterations to find the journal position the squeeze term will be overestimated slightly due to the backward differencing. For the implicit method both the shear and squeeze terms are changed during the iterations which will lead to a slight underestimate for the squeeze term. This case is of course for a situation not arising in a normal bearing. Figures 4.29-32 compare the results predicted for the two different methods for an actual engine cycle using a step size of two degrees. Both methods compare very well, the largest differences occurring between 270 and 450 degrees of crank rotation from top dead centre as seen in Figures 4.30 and 4.31. Over this part of the engine cycle the load is moving very quickly relative to the connecting rod and therefore the squeeze effects are most predominant over this region as would be expected. From the foregoing analysis it would appear that a step size of 2 degrees is adequate for stepping through time. Using a step size of 1 degree makes little difference to the predicted performance but increases the amount of computing time required by up to 70%. Both methods for stepping through time appear to be equally accurate, the explicit method is preferable since it

requires considerably less computing time than the implicit method.

4.7.4 Effect of oil feed

The finite element method, unlike other numerical techniques, allows irregularities such as oil feed features to be easily incorporated into the analysis. For the present analysis they were incorporated by simply specifying the appropriate pressure boundary condition over the relevant part of the bearing surface. No attempt was made to accurately model the physical shape of the features.

The predicted journal centre orbits for various forms of grooving are compared in Figures 4.33-36. The orbits shown are for a full 360 degree circumferential groove, a 180 degree partial groove in the cap half of the connecting rod and in the rod half of the connecting rod and an oil hole at 0 degrees relative to the connecting rod. The full circumferential groove has the biggest effect on the predicted journal centre orbit compared to that obtained for an ideal bearing as it essentially splits the bearing in two and reduces the effective bearing width. It is interesting to note that there is no noticeable difference in the results obtained by ignoring the supply pressure and treating each bearing land as an ideal bearing so only half of one bearing land need be modelled due to symmetry, and the results obtained when the supply pressure is incorporated and all of one bearing land is modelled with the pressure specified along one side as the supply pressure. The former method is similar to that used by Goenka [22]. It was found that for all cases where the oil supply pressure was specified a greater number of axial nodes has to be used since symmetry could not be exploited to the same degree. Using 7 nodes in the axial direction proved adequate. For both cases with a partial groove the journal centre orbit is affected over the region where the groove lies, similarily for the oil hole at 0 degrees the orbit is only affect over that region of the bearing.

Table 4.1 compares the results obtained with those obtained by Goenka [22]. The results obtained for the plain bearing and the fully grooved bearing compare very well. However the results for the partially grooved bearing although showing the same general trend show quite marked differences for the minimum film thickness and the peak film pressure. This is due to the simplicity of the model used to incorporate the grooving which did not take into account the width of the partial grooves and made no attempt to physically model them as was done by General

Motors. Effectively, therefore, the bearing is assumed to be wider than it actually is in the region of the partial groove which gives a larger minimum film thickness and a lower peak pressure. The results for the bearing with a hole at 270 degrees, which is considered a 'good' location compare well, however for the bearing with a hole at 180 degrees the results do not compare so well. This case was considered a bad case by Goenka but refering to Figure4. 37, which is a plot developed to enable the most highly loaded regions of the bearing to be seen at a glance by plotting the magnitude of the load applied to the bearing at discrete time intervals. It would seem that having a hole at zero degrees, which is in the region where the bearing would be most highly loaded, would be a worse case. Indeed, these results compare well with the General Motors case with a hole a 180 degrees.

The method currently used for modelling the oil feed features appears to work well for oil holes and full circumferential grooves but for partial grooves it would seem that a more comprehensive model is required to take into account the reduction in width of the bearing over the groove region.

4.7.5 Other bearing examples

The journal centre orbits for the two other bearing examples are shown in Figures 4.38 and 4.39. The first example considered is the same as that used by Jones [33] working at the Glacier Metal Co. and compares very well with his results. Figure 4.40 shows the side flow out of this bearing which also compares very well with the results obtained by Jones using finite difference methods. This provided a useful comparison since the work by Jones is one of the few such works to present results for side flow calculations for a dynamically loaded bearing assuming the bearing to be fully flooded. The second bearing considered is from a high speed internal combustion engine. The loading on this engine is relatively high and over part of the cycle the load is moving very rapidly around the bearing. It was consequently found that the iterative process used to locate the correct journal position failed to converge if a step size of greater than two degrees was used. It was useful to use data for a number of different engines since most of the early development work was carried out using the data for the Ruston bearing which is under relatively low loading. Some of the procedures that appeared to be well behaved for this particular bearing proved not to be so when other bearings were considered having

different loadings and geometries.

4.8 Summary

This chapter has covered the development and subsequent refinement of a finite element package for the analysis of dynamically loaded rigid journal bearings. The extrapolated Gauss-Seidel solution method has been shown to be ideally suited to this problem allowing the sparseness of the matrix $[K_p]$ to be fully exploited and oil feed features to be easily incorporated using a simple oil feed model. Due to the high rate of convergence of this method a considerable time saving has been realised by exploiting the early definition of the cavitated region. Two methods have been investigated for assessing the accuracy of the the squeeze term in the analysis.

The initial work used 3-node linear triangular elements to model the lubricant film but on examining the resulting pressure distribution it was decided to use the more complex 8-node isoparametric elements. These elements have been shown to provide a much better performance despite the considerable increase in programming complexity.

An efficient technique based upon a modified form of the Newton-Raphson method was developed for locating the journal position required to balance the applied load. Two different methods of time stepping were investigated and it was found that both methods gave a similar accuracy, a considerable time saving could be achieved by using the explicit method. Computing times as low as 10 minutes for a complete analysis have been achieved. This can be compared directly to the time of 68 minutes reported by Goenka [22] by using floating point benchmarks to compare the Vax 11/785 to the IBM 370/3081 that Goenka used. These show that the IBM is approximately 8.5 times faster than the VAX which makes the current analysis method about 50 times faster. This clearly makes this method viable as a general design tool. A simple method for incorporating the effects of oil feed features has been incorporated into the analysis though it would appear that a slightly more comprehensive approach is required in some cases.

Description	$h_{min}(\mu m)$	$P_{max}(MPa)$	$PowerLoss(KW)$
No groove			
GM	8.78	21.1	1.148
KCL	8.78	20.9	1.153
360 deg groove			
GM	3.36	34.4	1.380
KCL	3.26	34.5	1.392
180 deg groove cap half			
GM	5.11	28.5	1.202
KCL	6.04	23.41	1.241
180 deg groove rod half			
GM	3.39	35.5	1.364
KCL	4.19	28.34	1.384
Hole at 270 deg			
GM	8.76	21.1	1.148
KCL	7.94	21.6	1.173
Hole at 180 deg			
GM	6.89	20.8	1.251
KCL	8.66	20.77	1.172
Hole at 0 deg			
KCL	6.70	18.36	1.225

GM General Motors
KCL Kings College

Table 4.1 Summary of results for the Ruston connecting rod bearing compared with results from the General Motors program

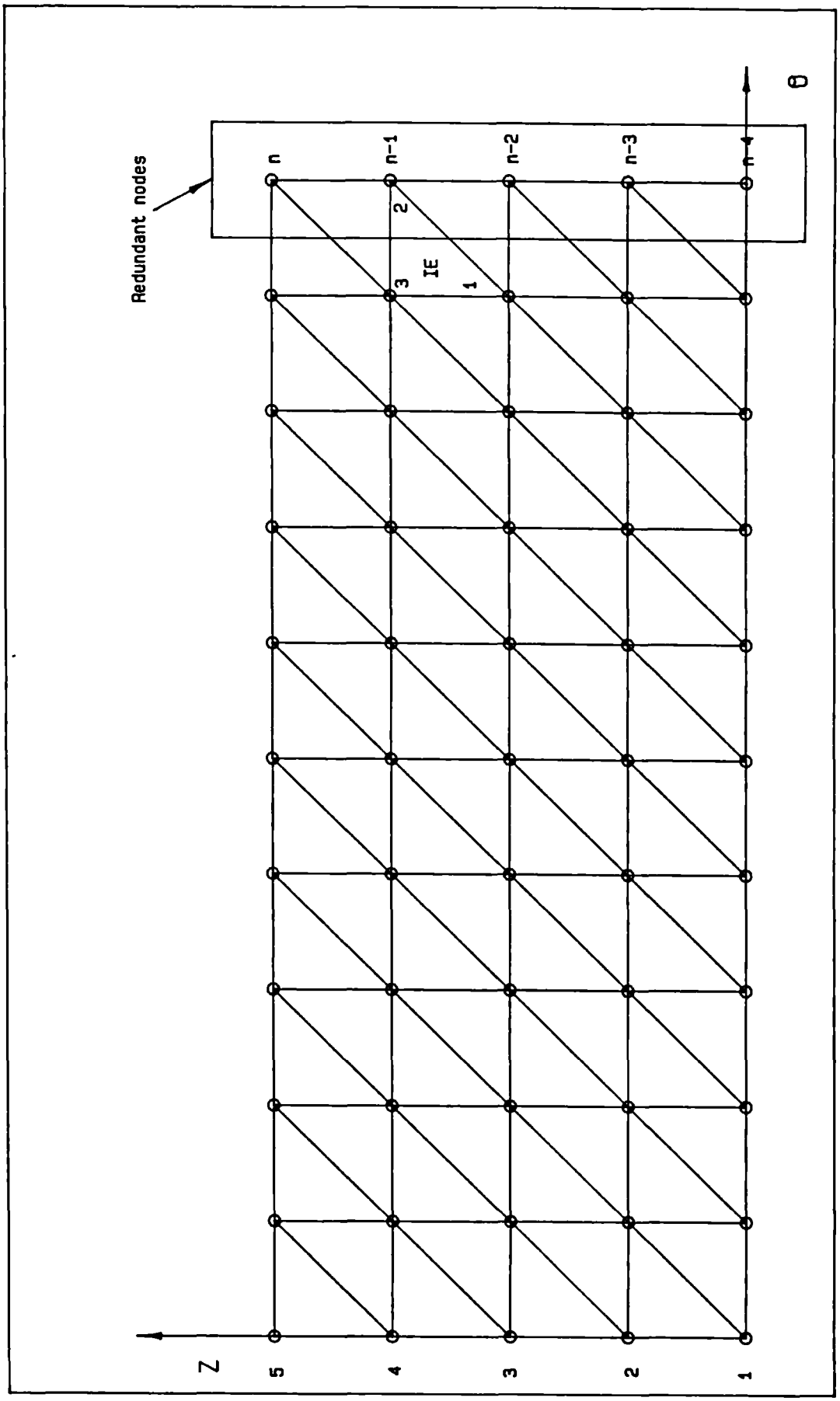

Figure 4.1 - Finite element mesh showing redundant nodes

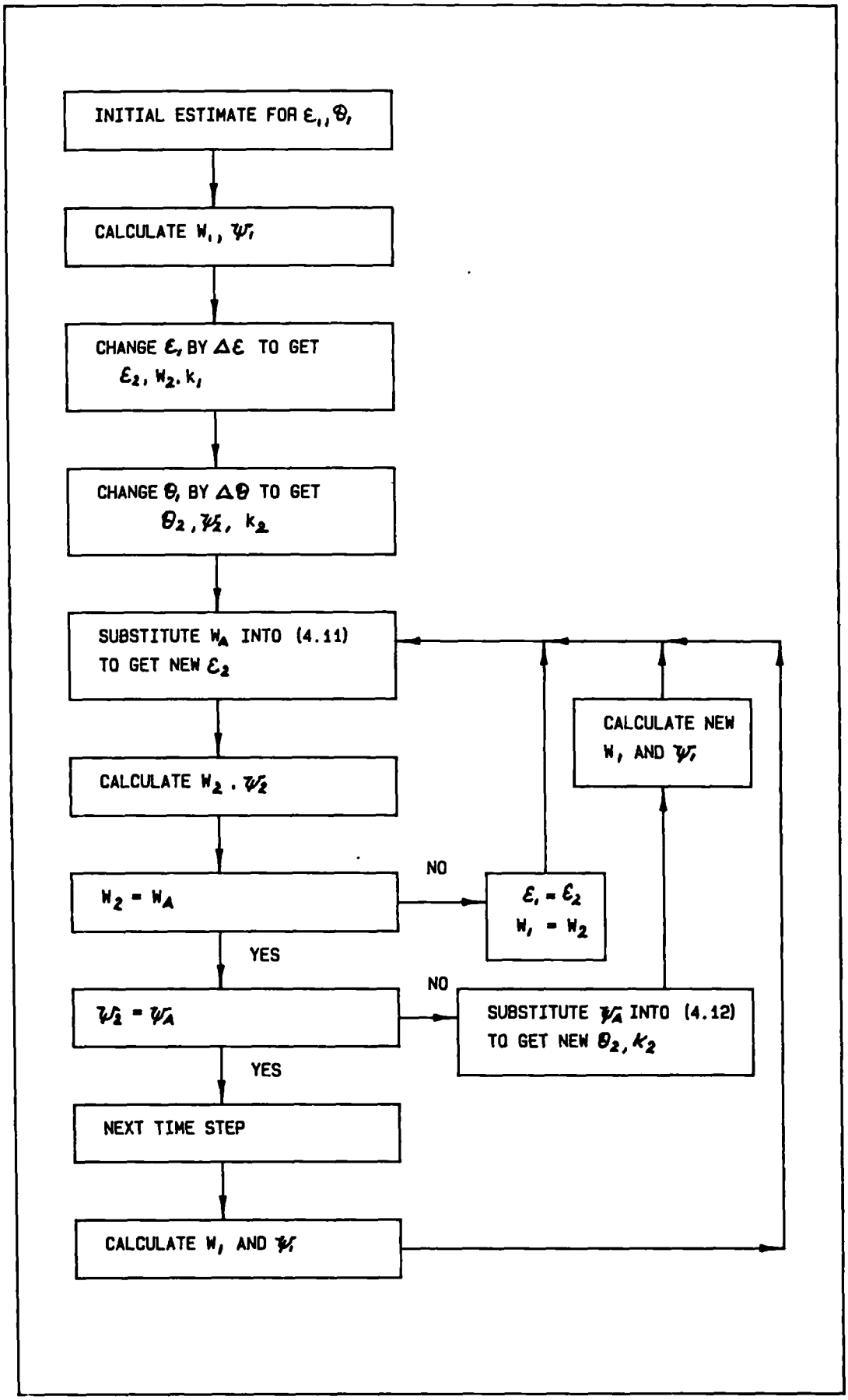

Figure 4.2 - Flow diagram for journal position iterations

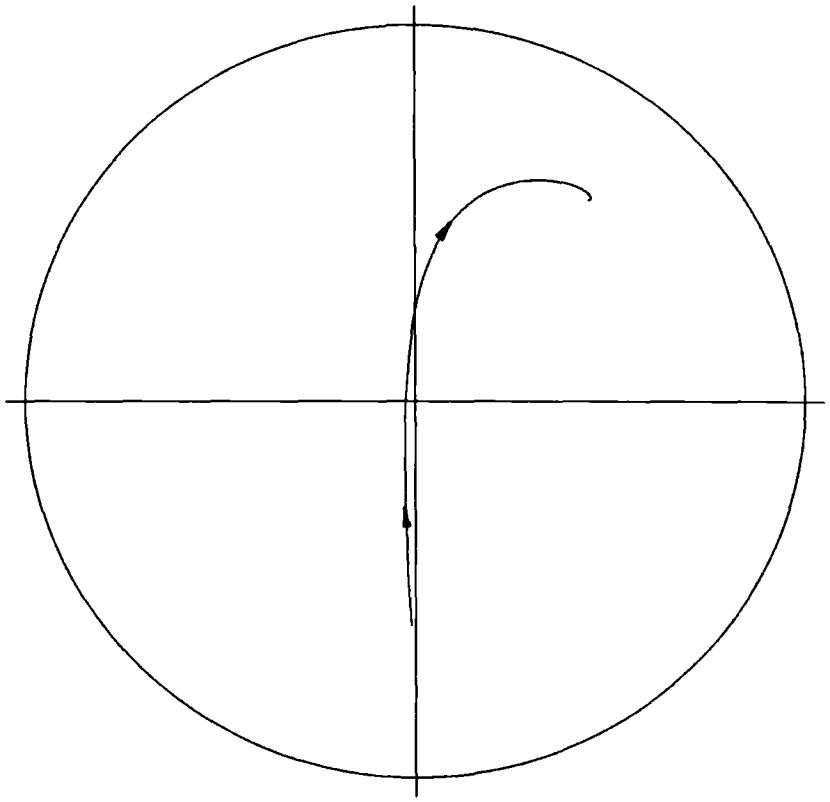

Figure 4.3 - Journal centre orbit under static load

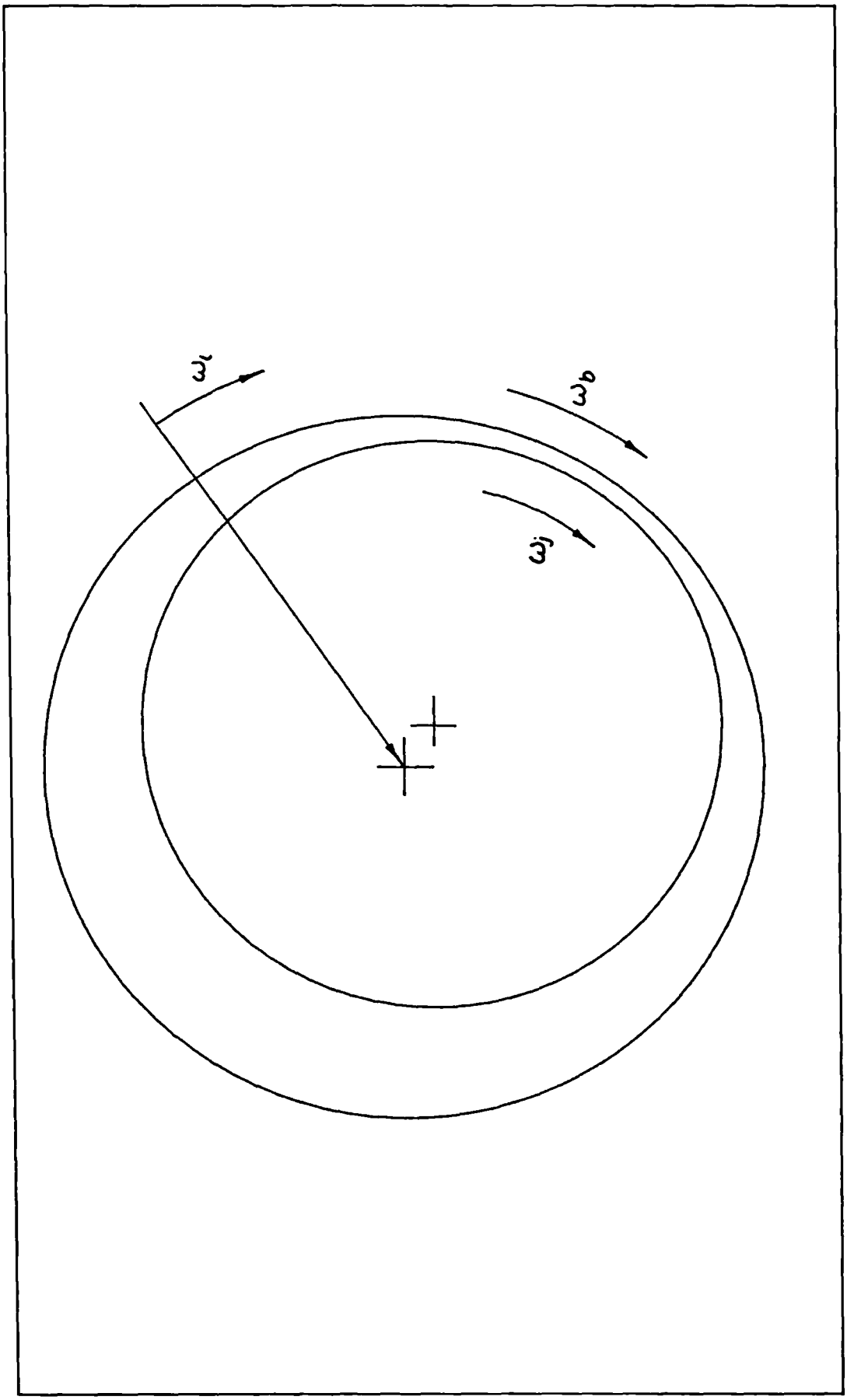

Figure 4.4 - Journal and housing with rotating load

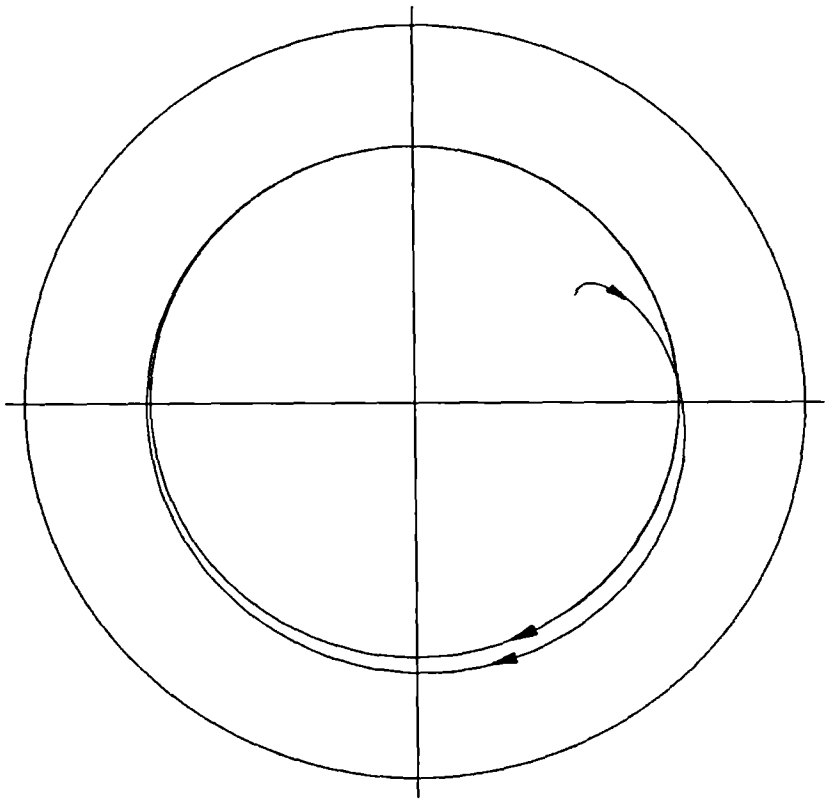

Figure 4.5 - Journal centre orbit with steady rotating load

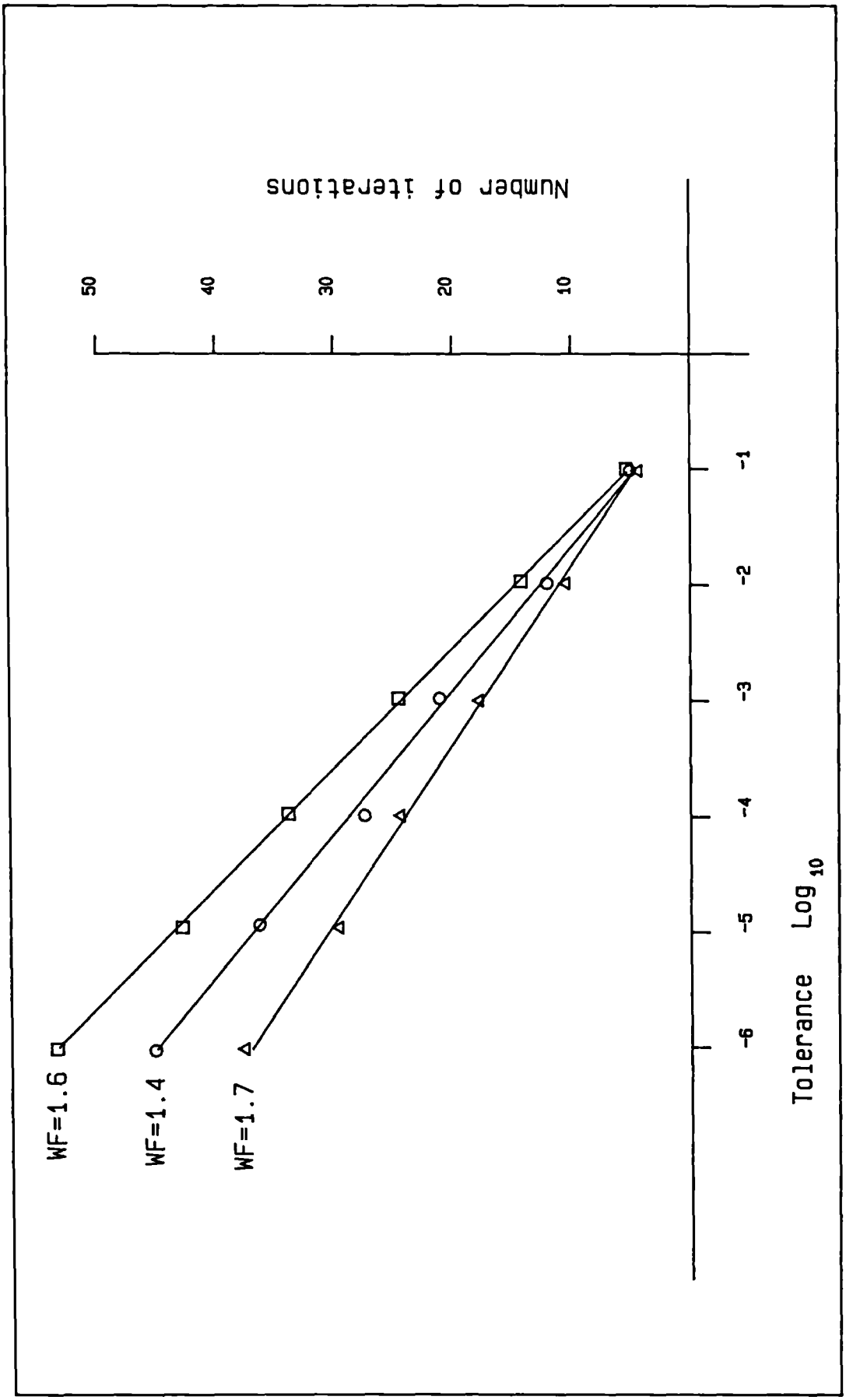

Figure 4.6 - Number of iterations against tolerance for SOR

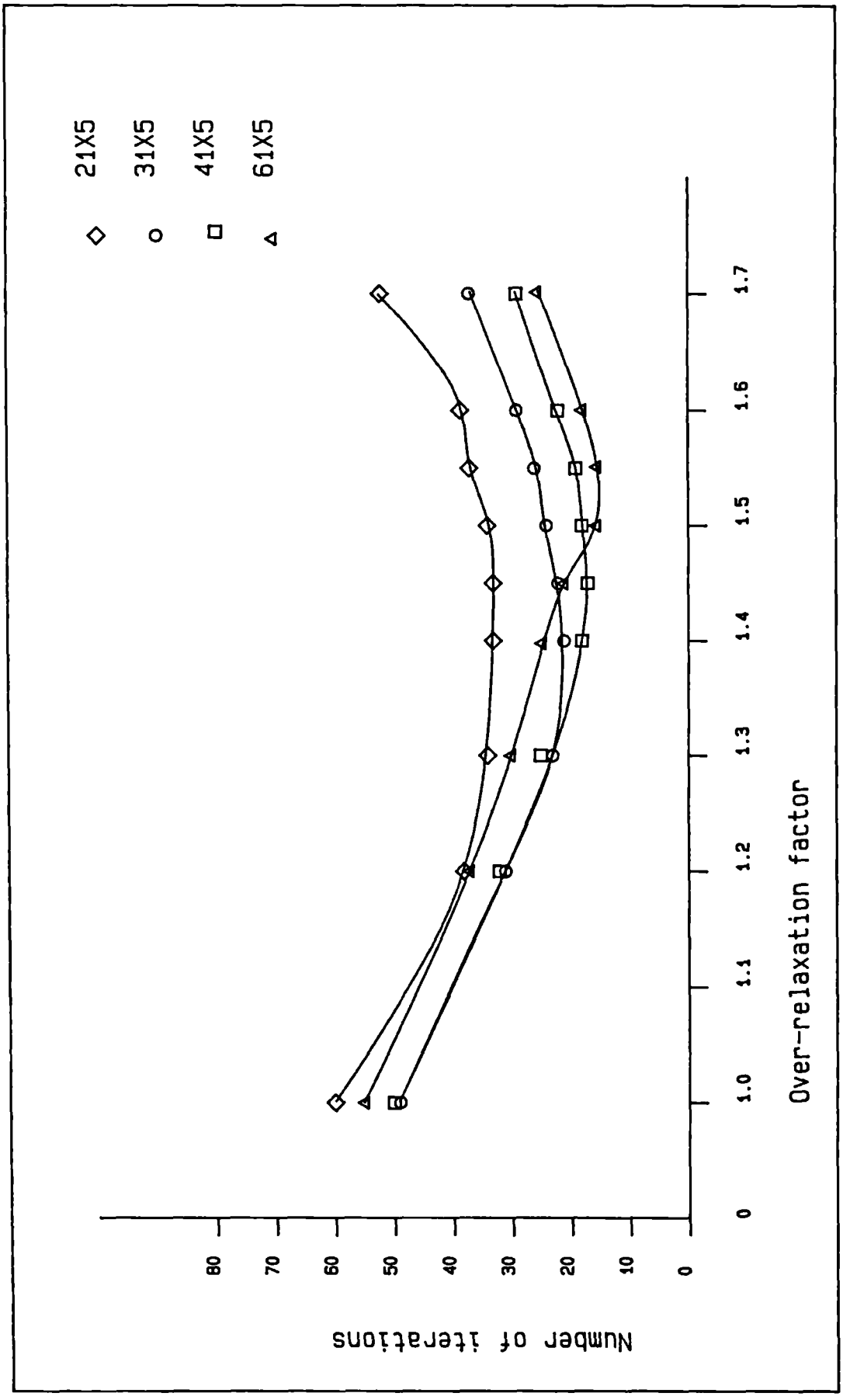

Figure 4.7 - Effect of number of circumferential nodes on wf_{opt}

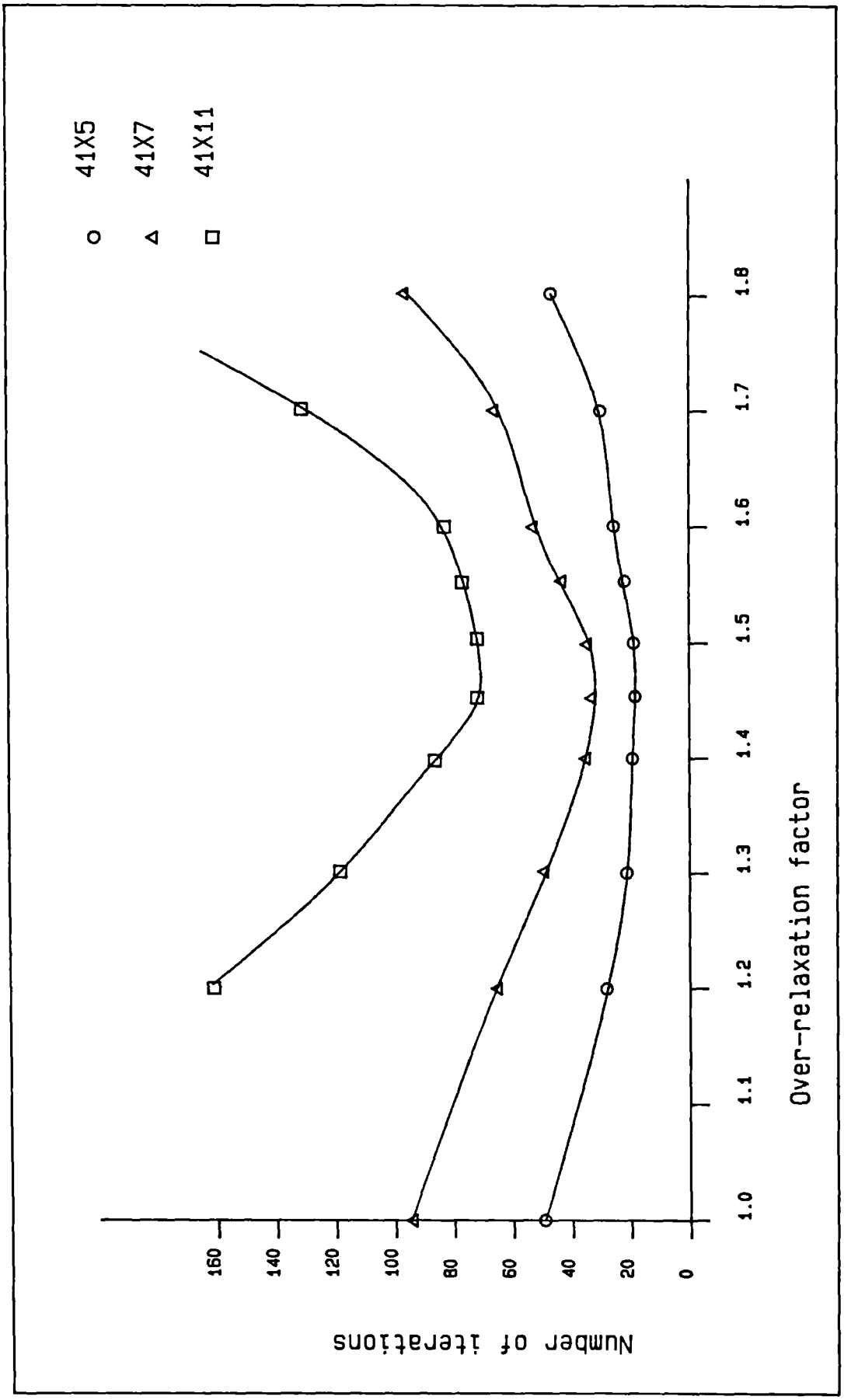

Figure 4.8 - Effect of number of axial nodes on wf_{opt}

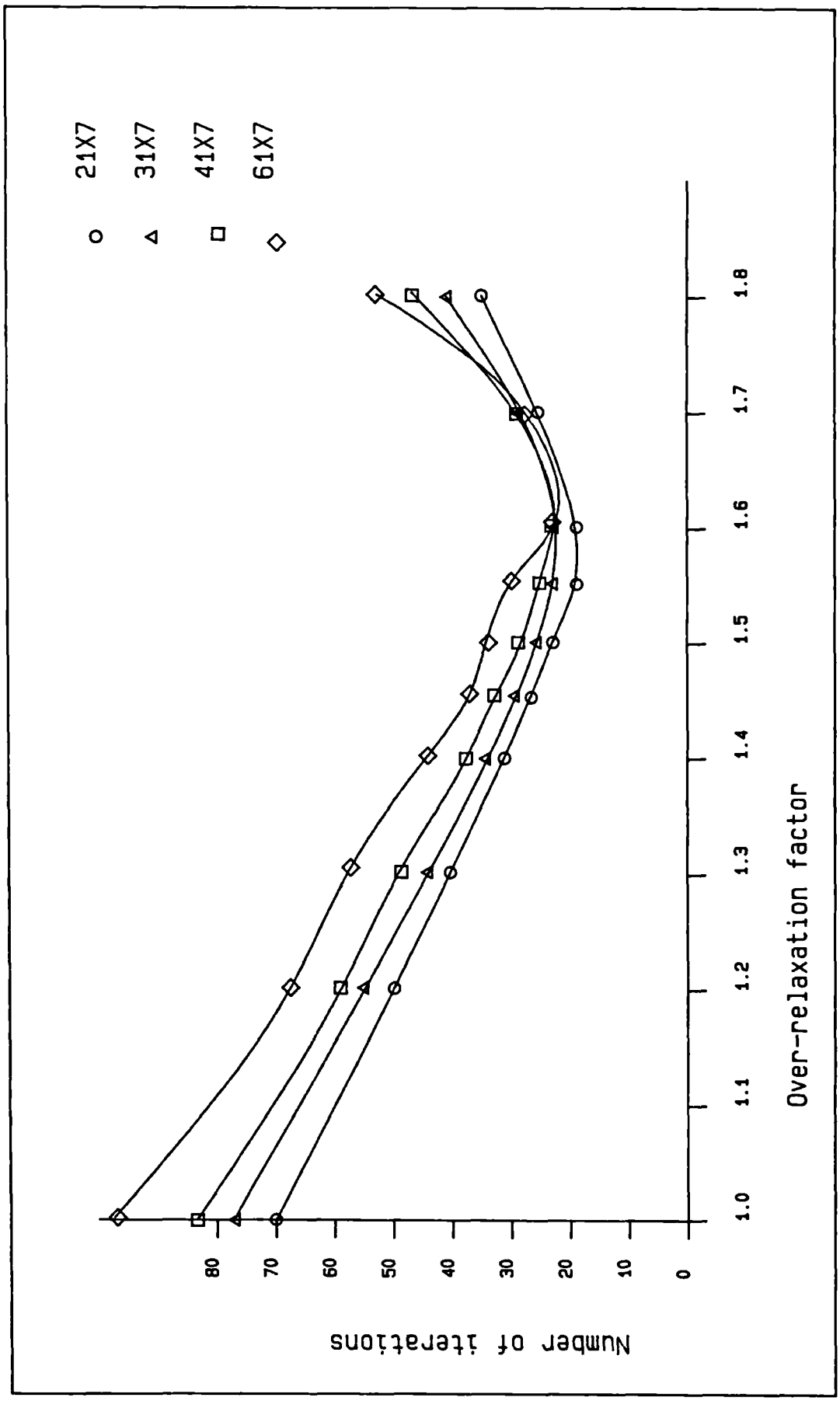

Figure 4.9 - Effect of number of circumferential nodes using 3-node triangular elements

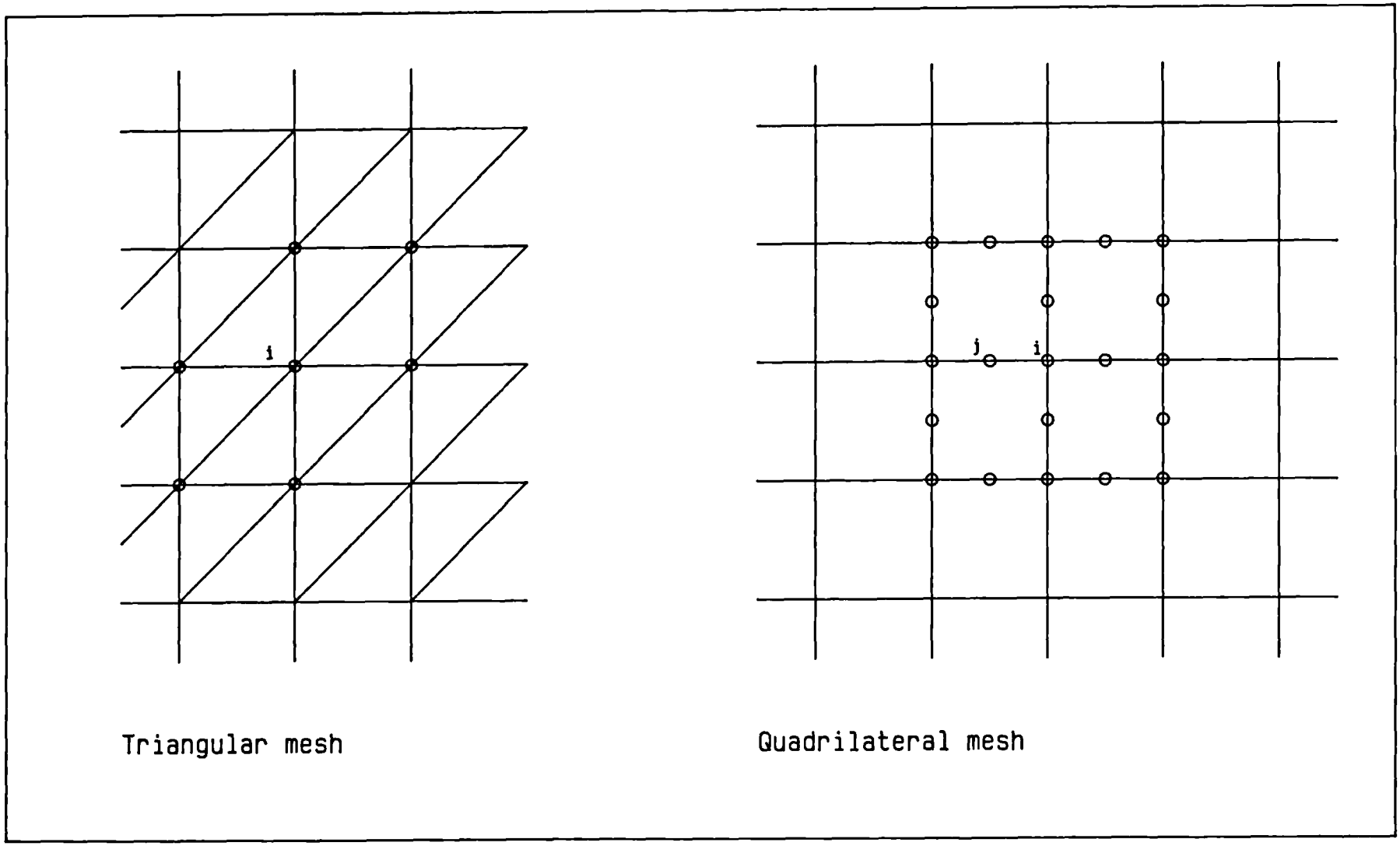

Figure 4.10 - Number of nearest nodes for two different element types

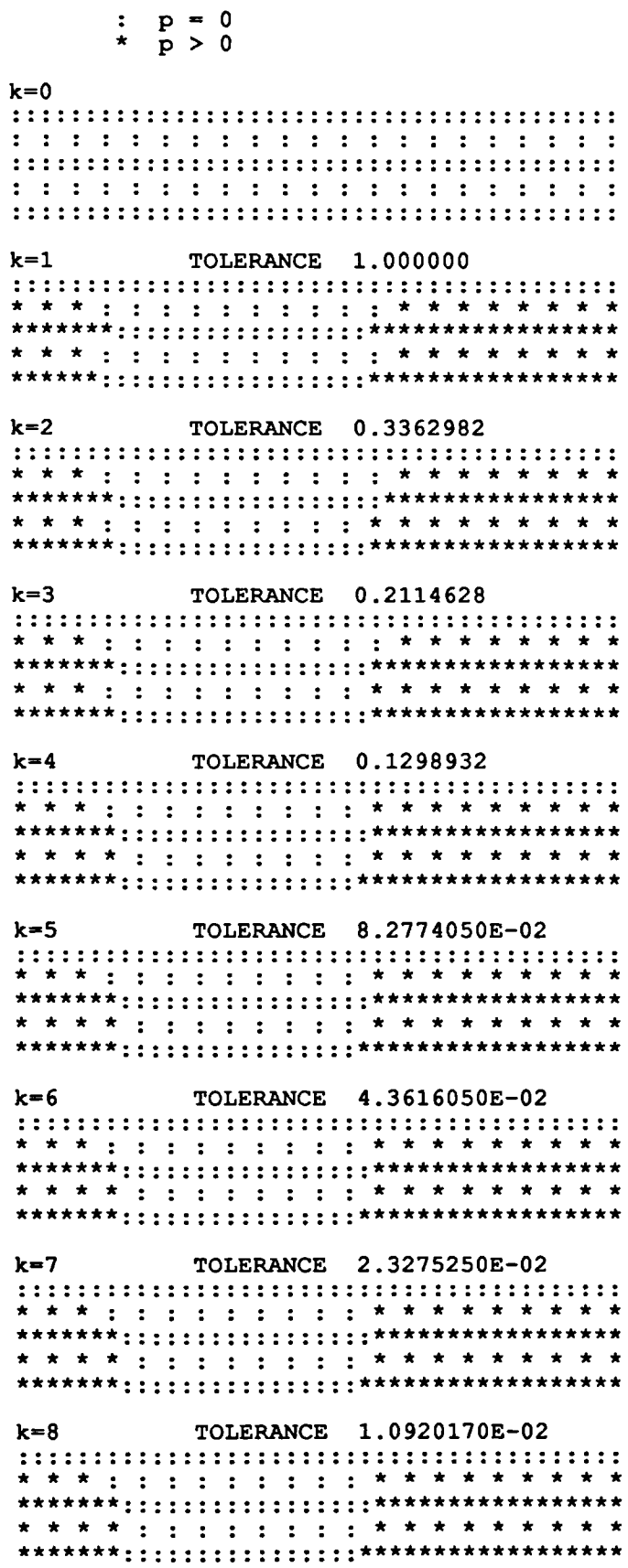

Figure 4.11 - Convergence of positive pressure region

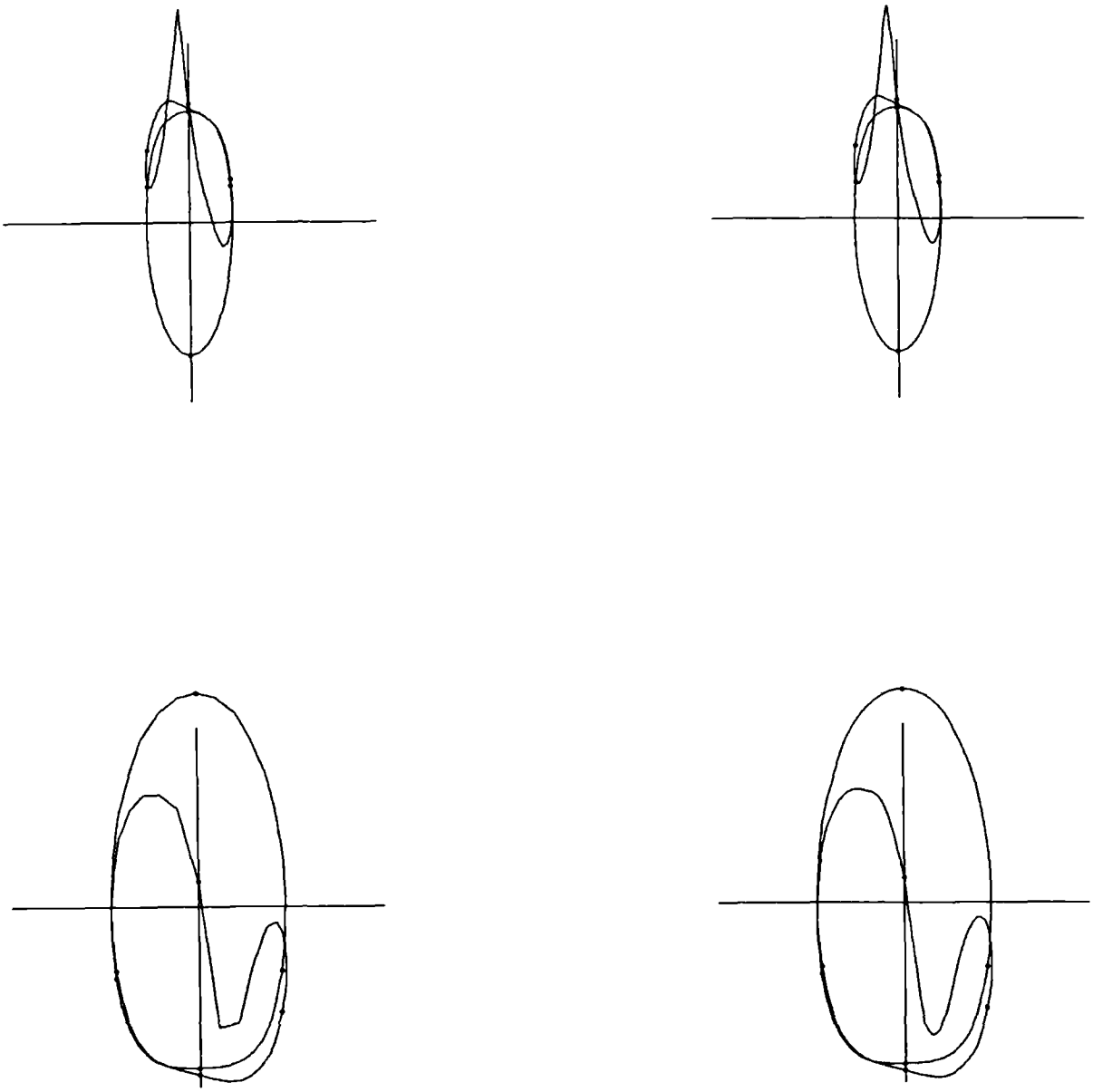

Figure 4.12 - Polar load diagrams obtained using linear and cubic interpolation.

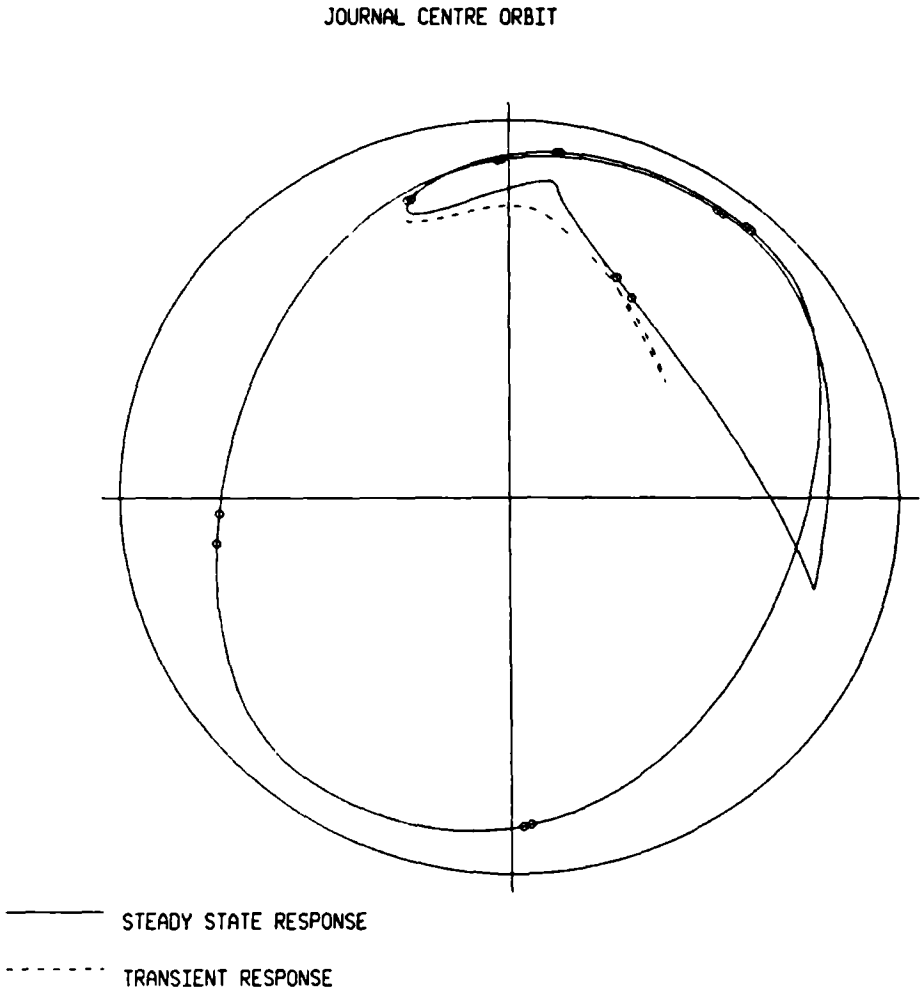

Figure 4.13 - Steady state and transient response

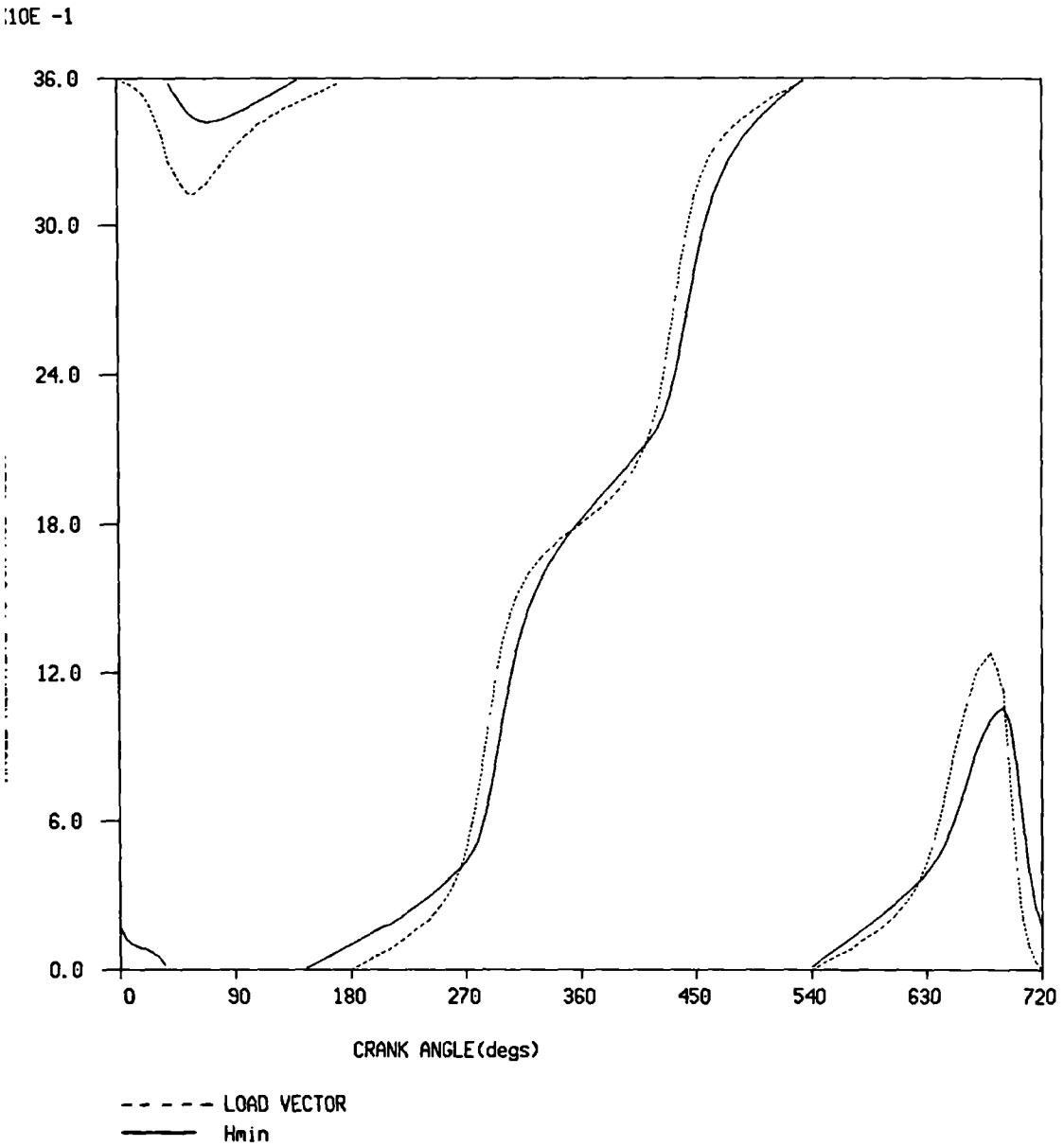

Figure 4.14 - Comparison of load and minimum film thickness position relative to connecting rod axis.

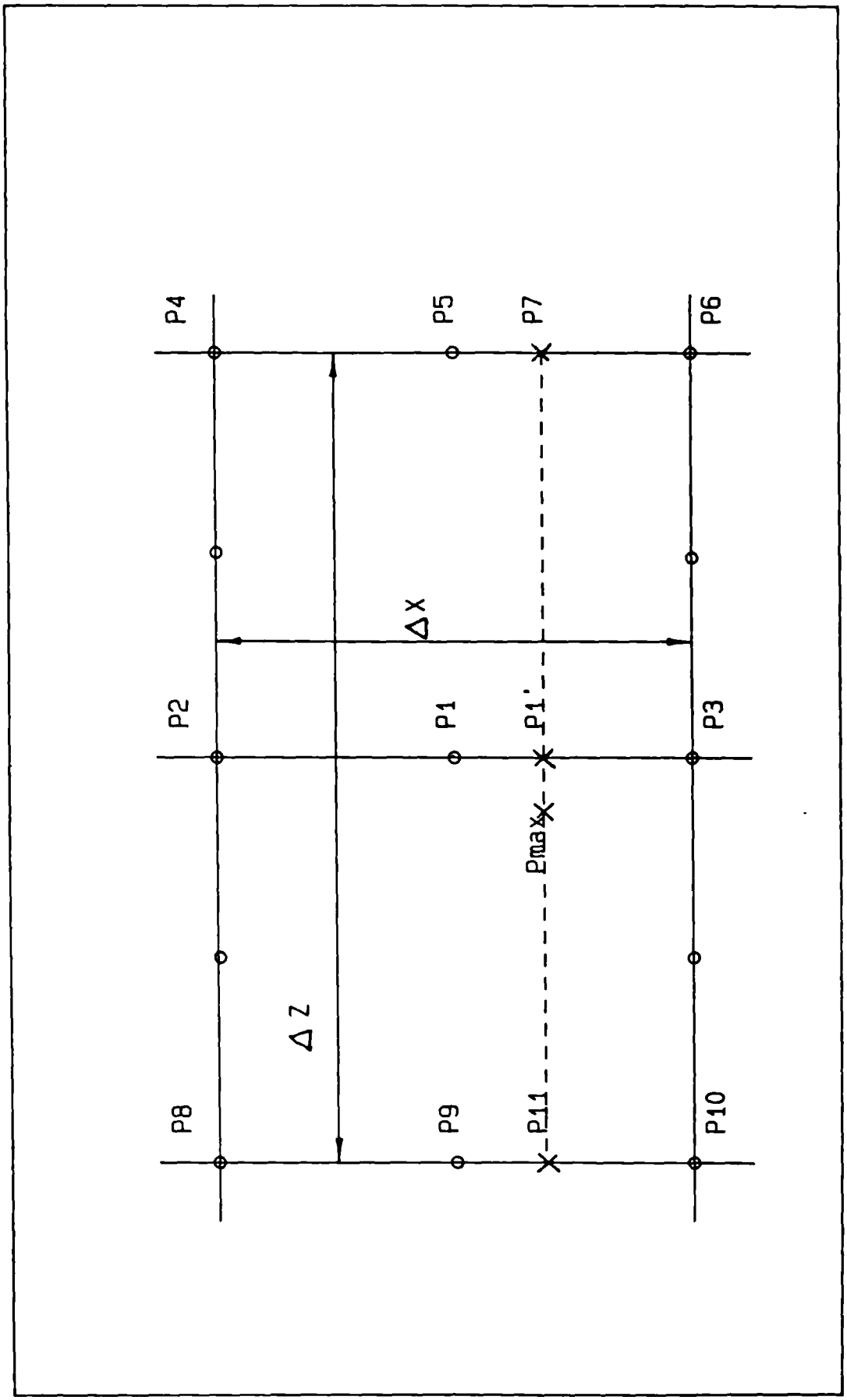

Figure 4.15 - Interpolation scheme to find Pmax for 8-node isoparametric elements

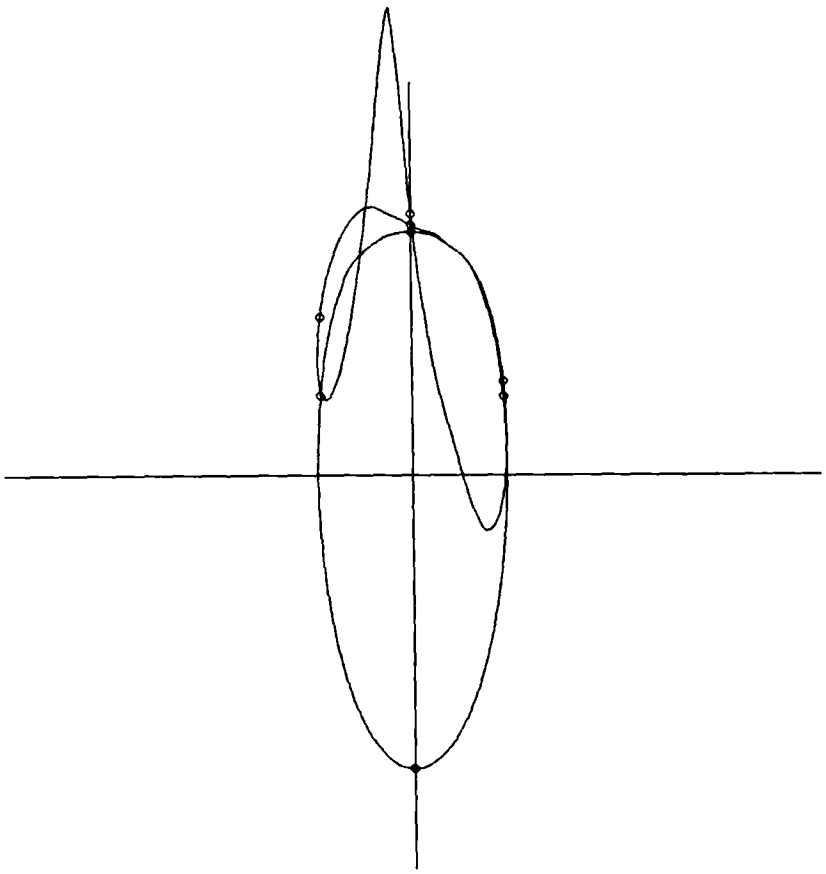

Figure 4.16 - Polar load diagram for Ruston and Hornsby 6VEB MkIII connecting rod, relative to connecting rod

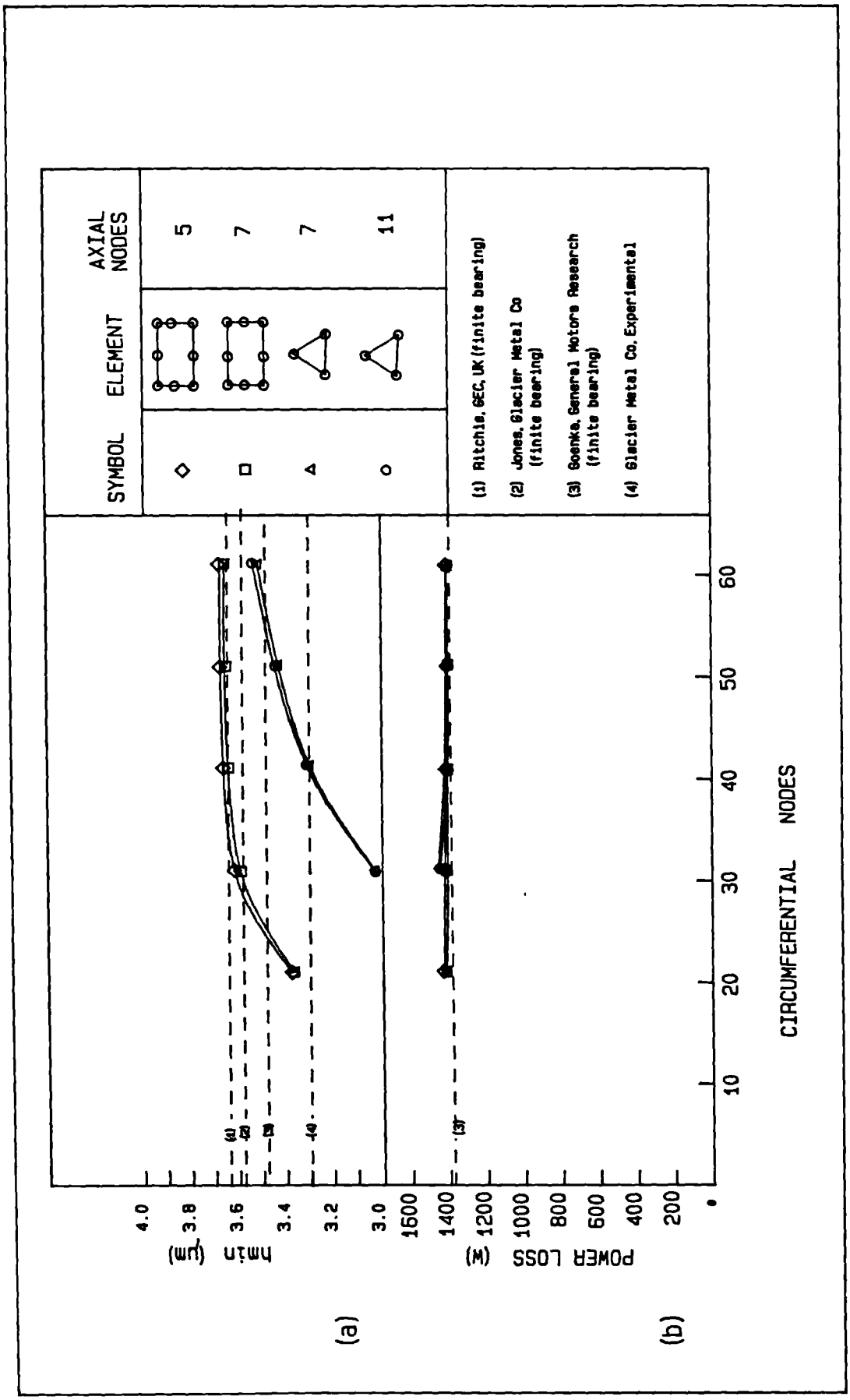

Figure 4.17 - Comparison of (a) calculated values of hmin and (b) cyclic power loss

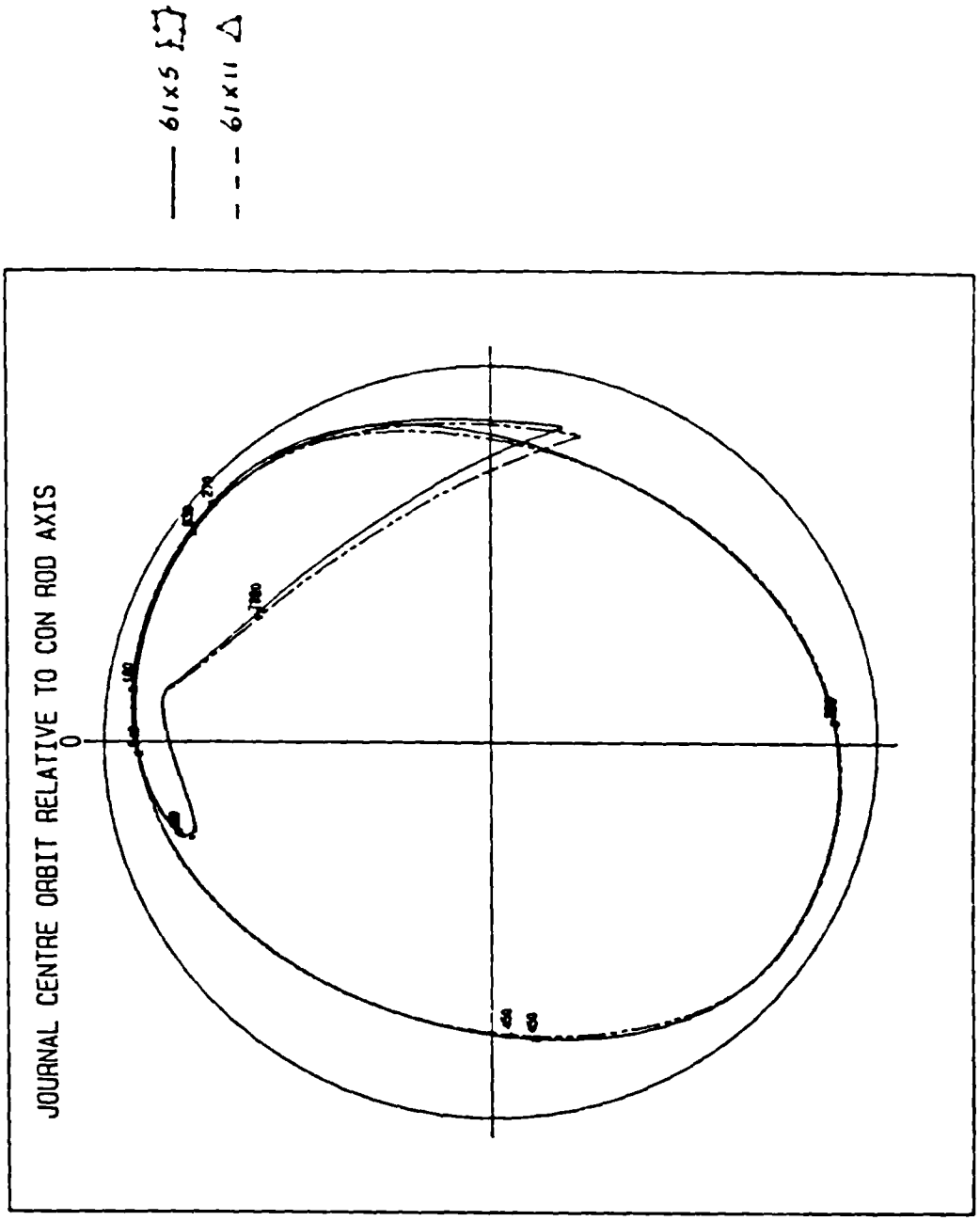

Figure 4.18 - Comparison of journal centre orbits using the two element types

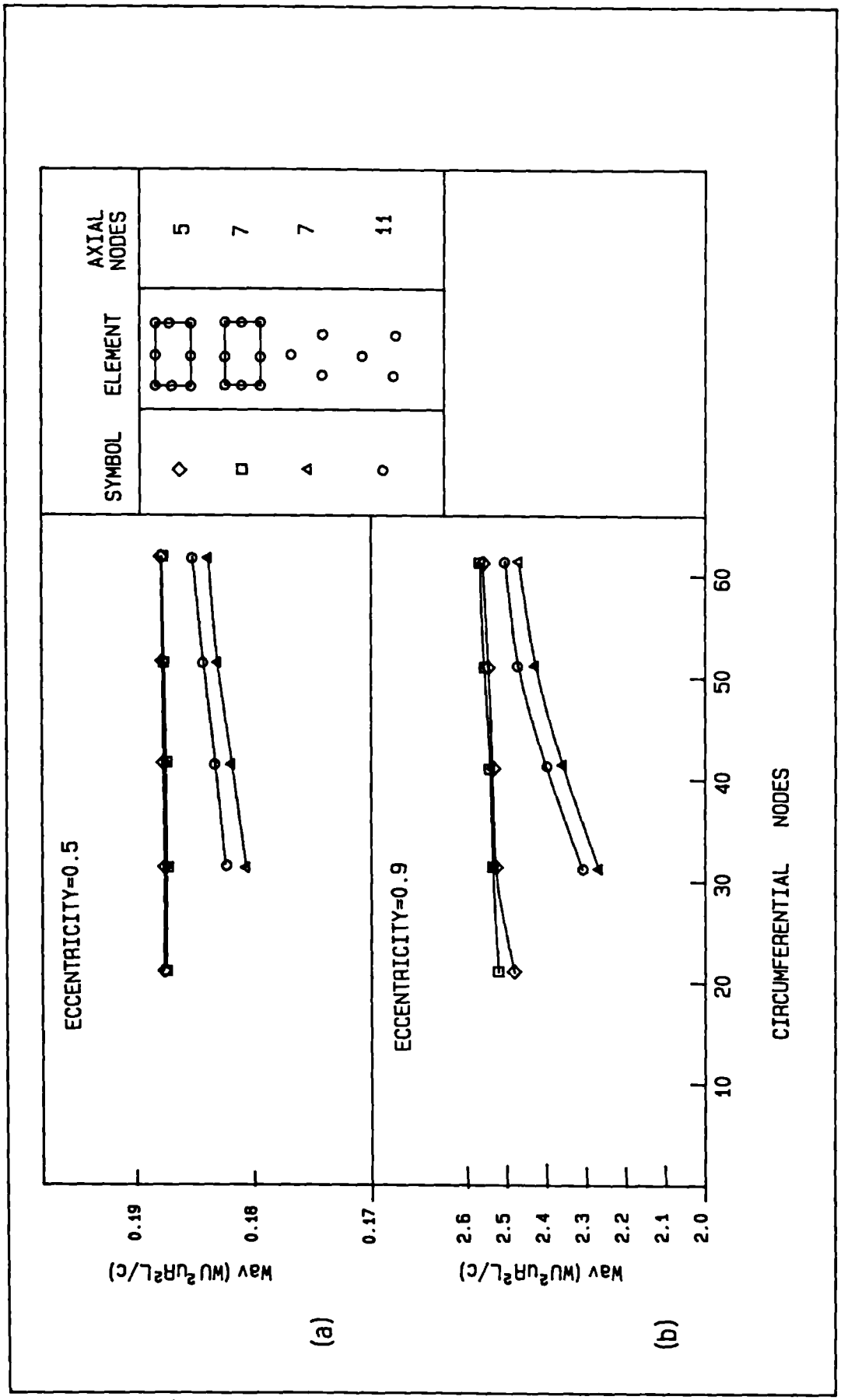

Figure 4.19 - Variation of calculated load with number of circumferential nodes for (a) eccentricity=0.5 and (b) eccentricity=0.9

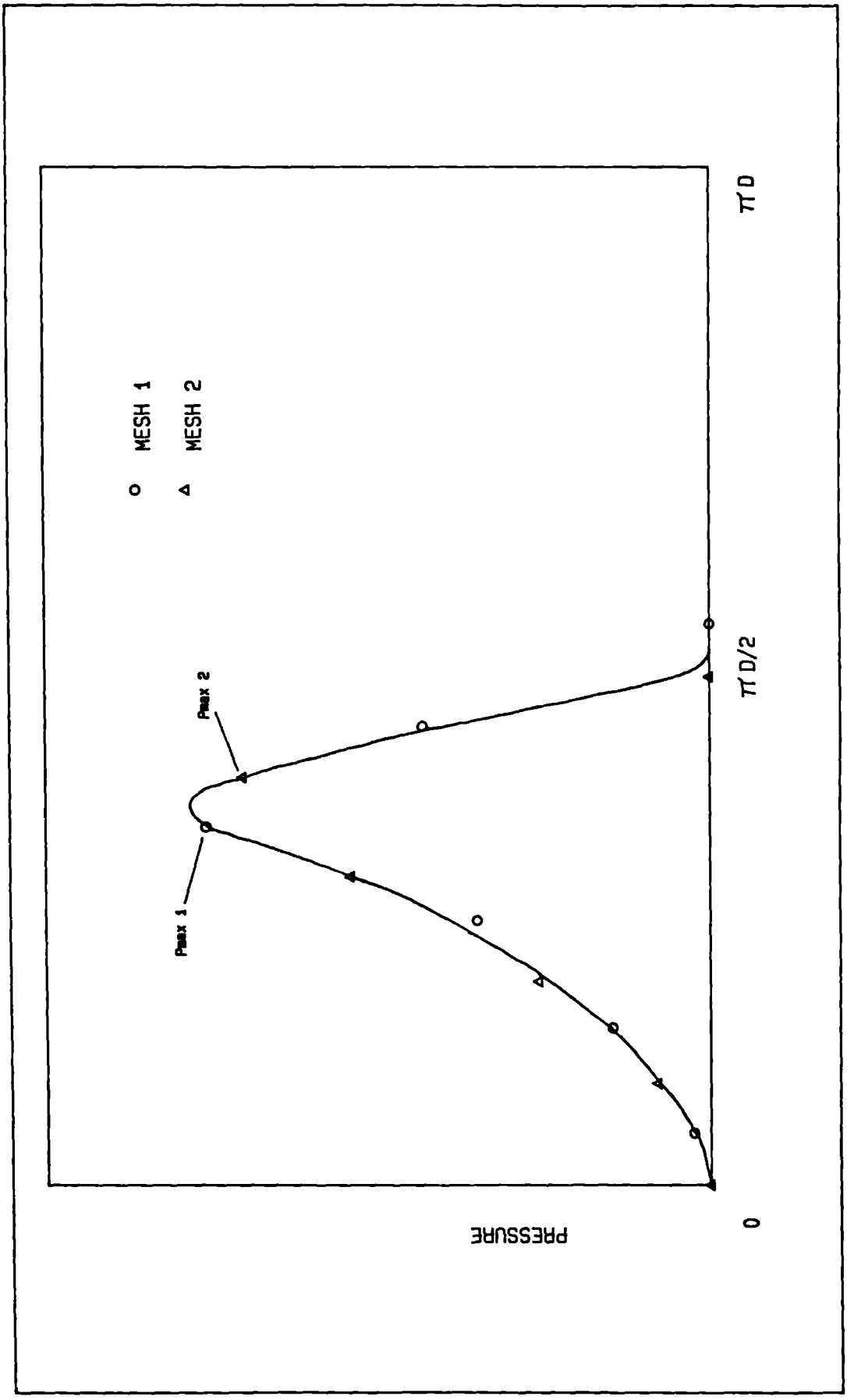

Figure 4.20 - Illustration of way in which different mesh positions can result in different values of Pmax .

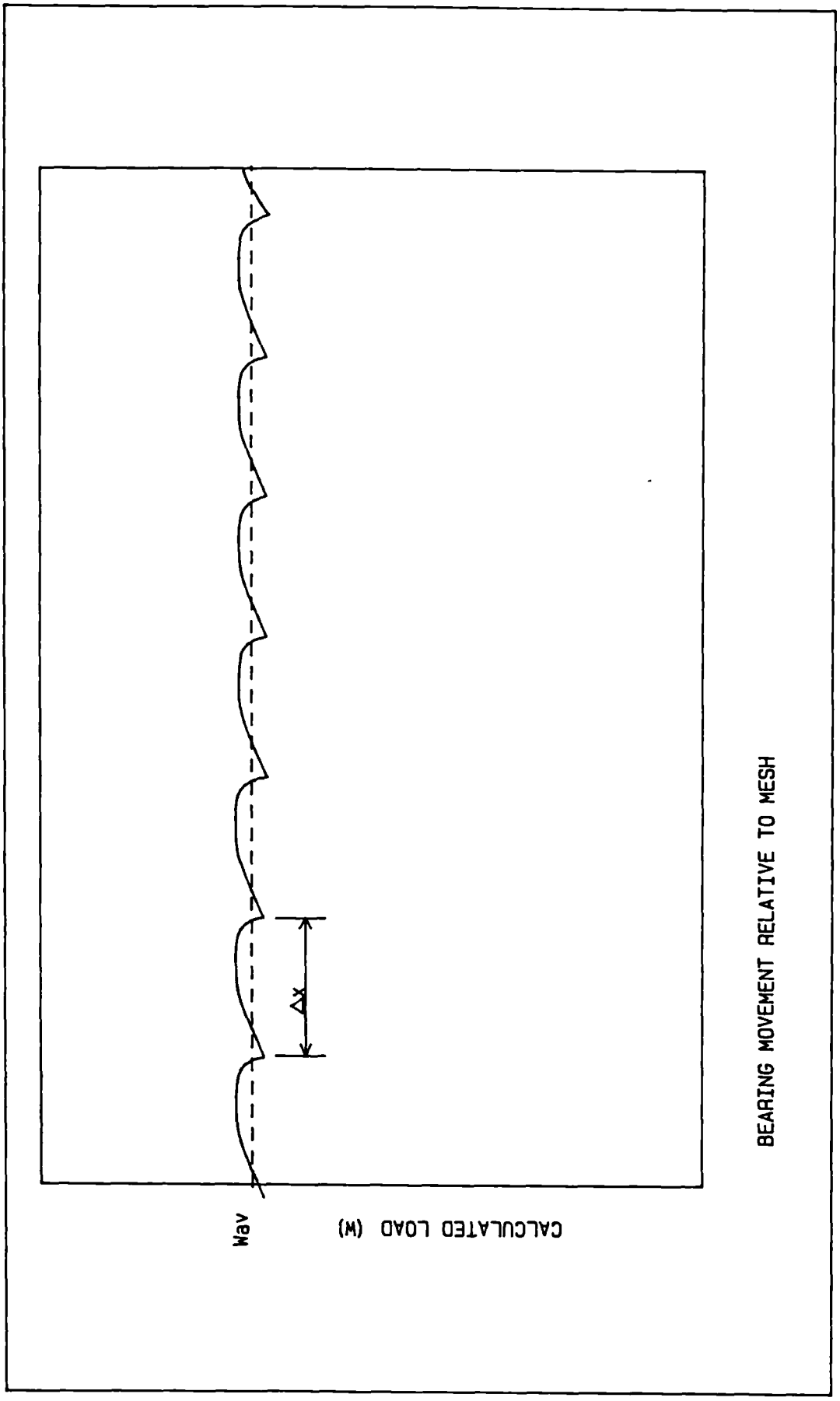

Figure 4.21 - Variation of W as position of hmin moves relative to mesh .

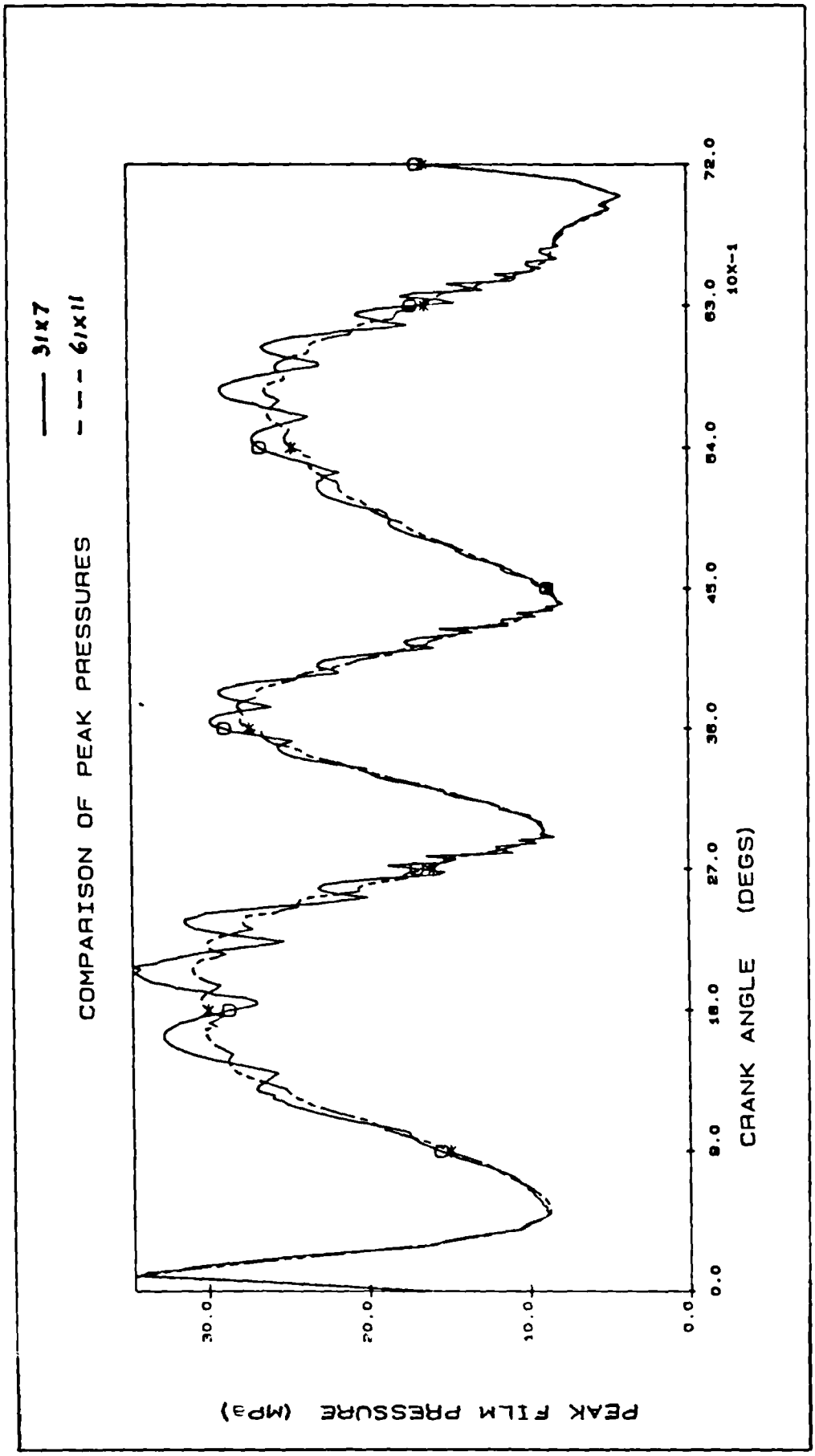

Figure 4.22 - Cyclic variation of peak film pressures using a three node triangular mesh

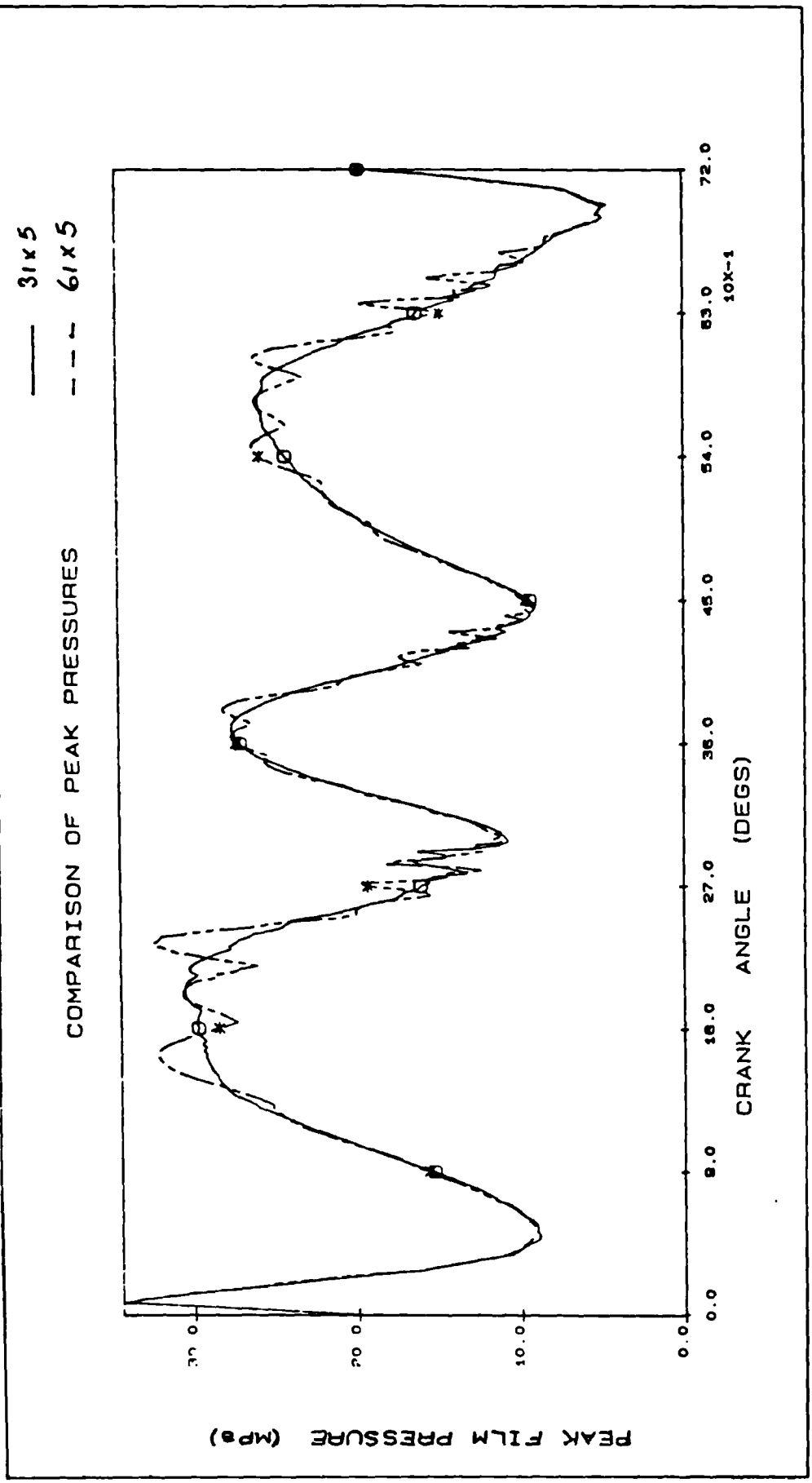

Figure 4.23 - Cyclic variation of peak film pressures calculated using an eight-node isoparametric element mesh .

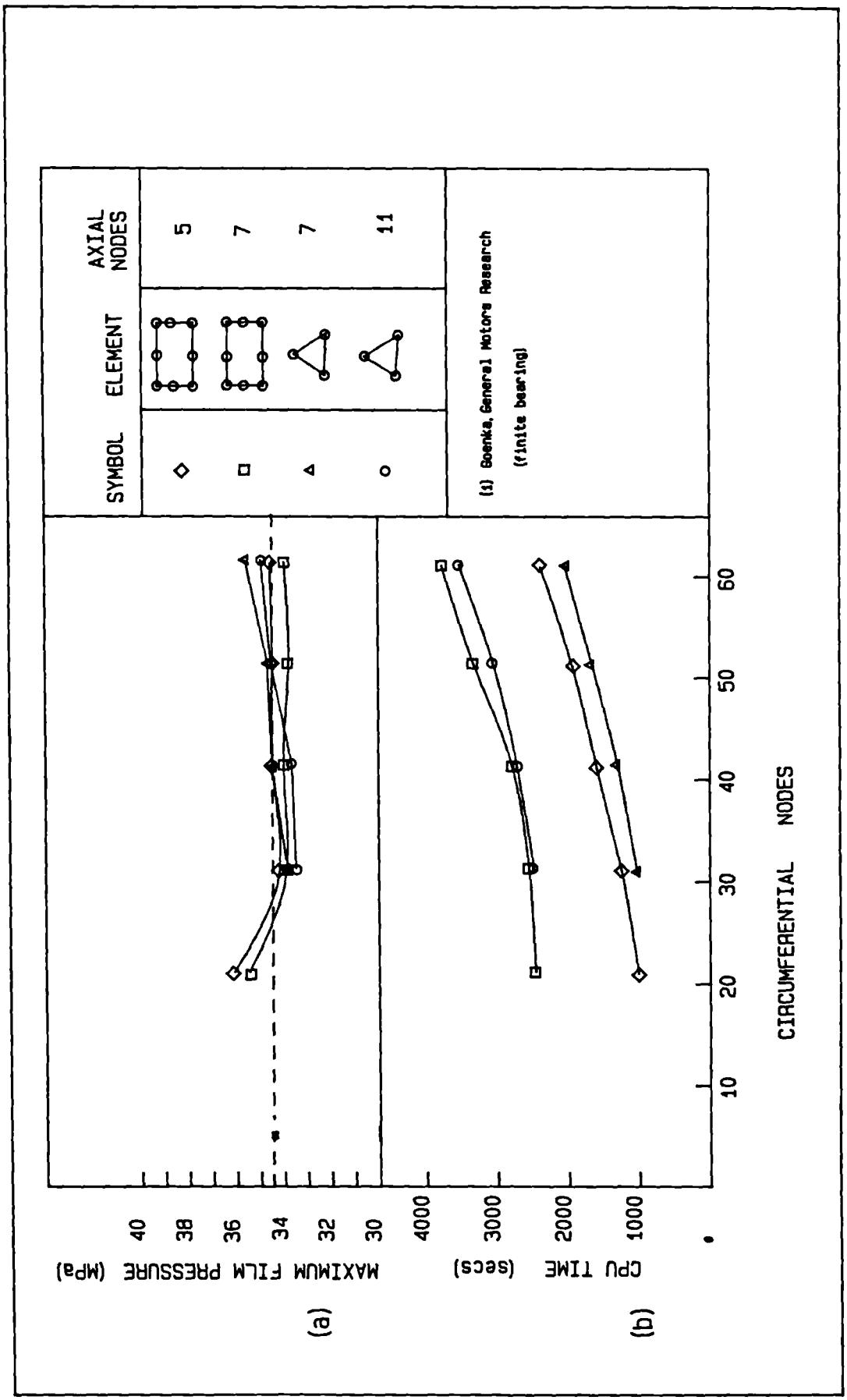

Figure 4.24 - Comparison of (a) peak film pressure and (b) computing time .

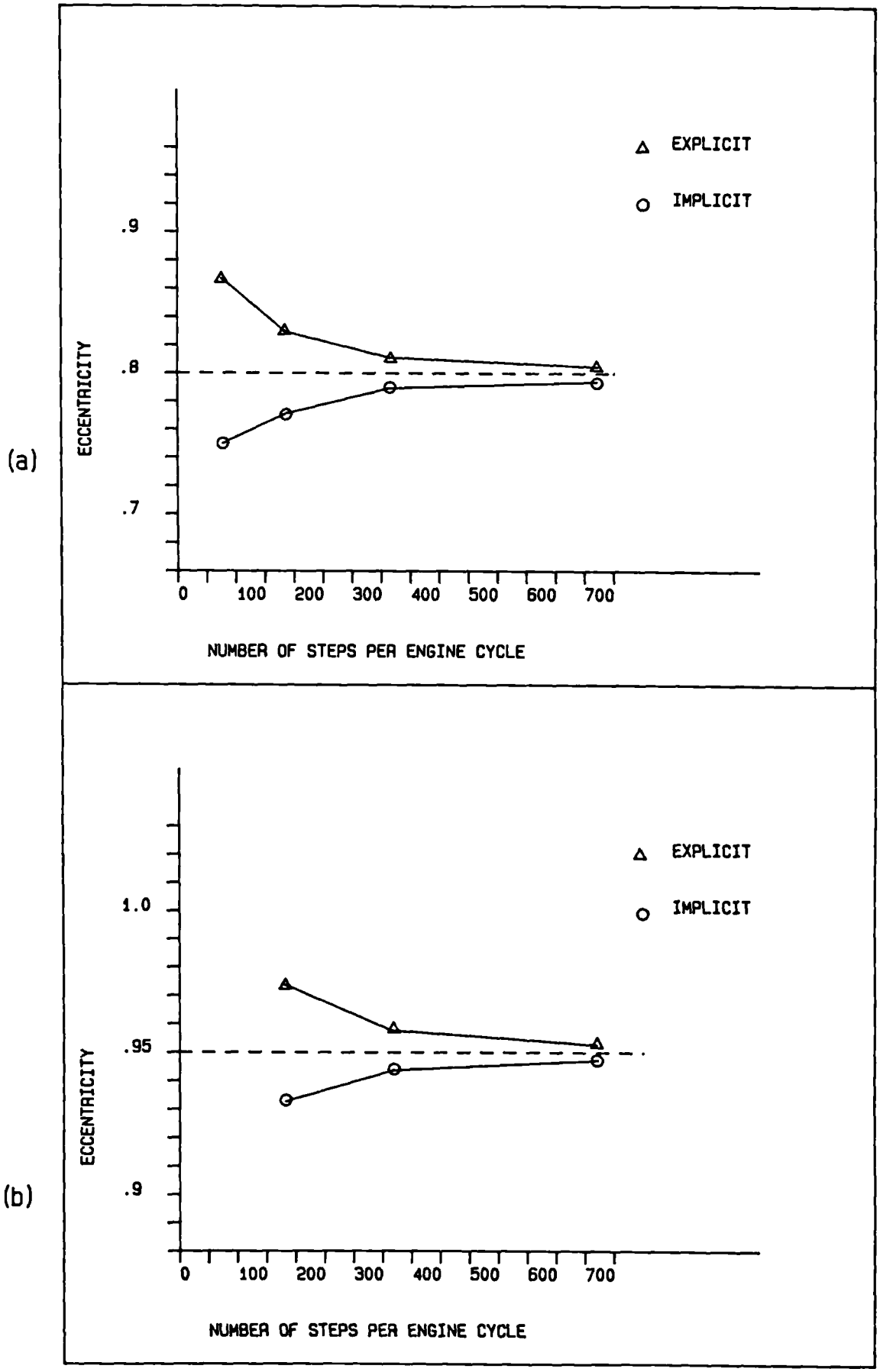

Figure 4.25 Comparison of eccentricity for (a) and (b) medium load.

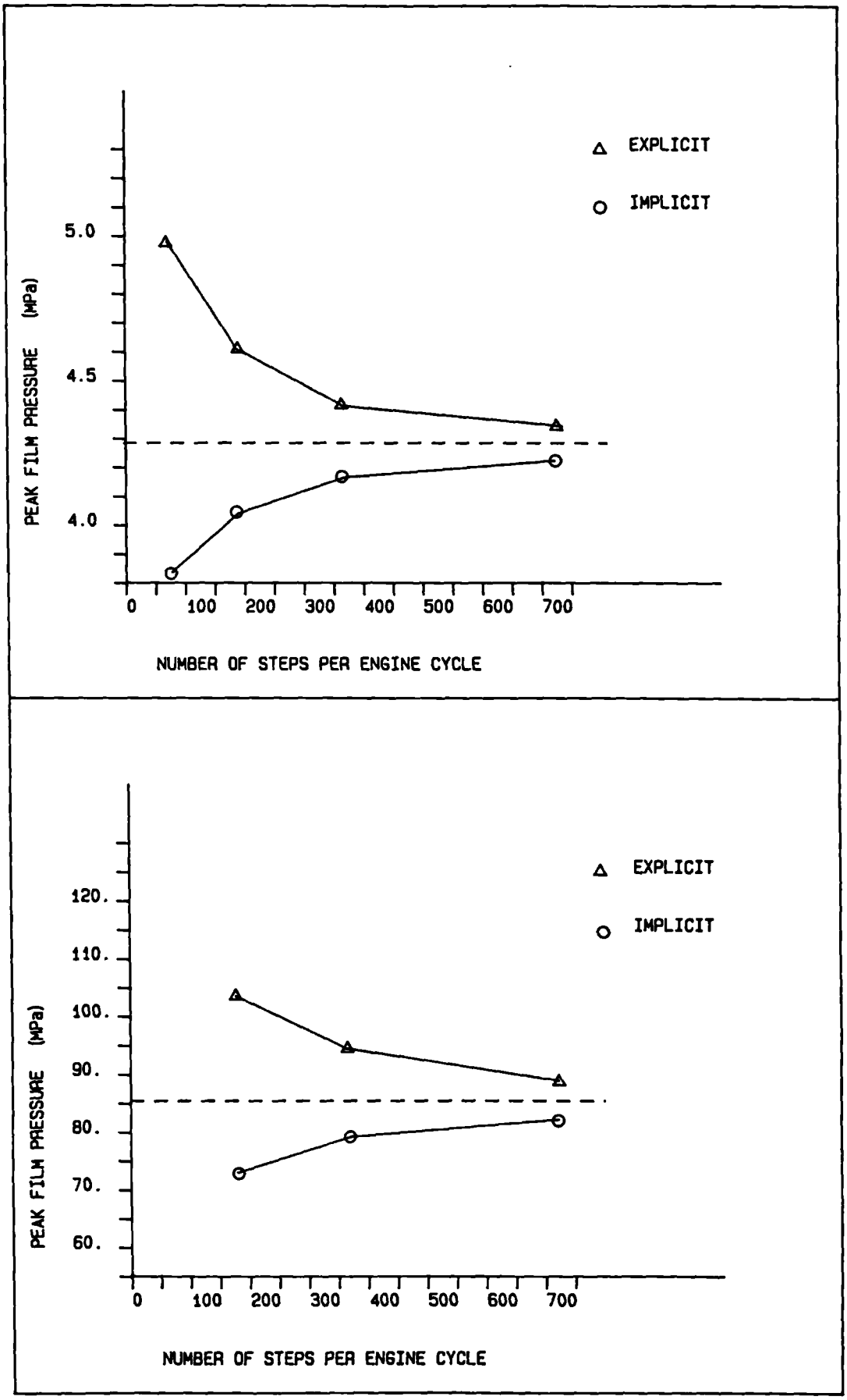

Figure 4.26 - Comparison of peak film pressure for (a) medium and (b) heavy load .

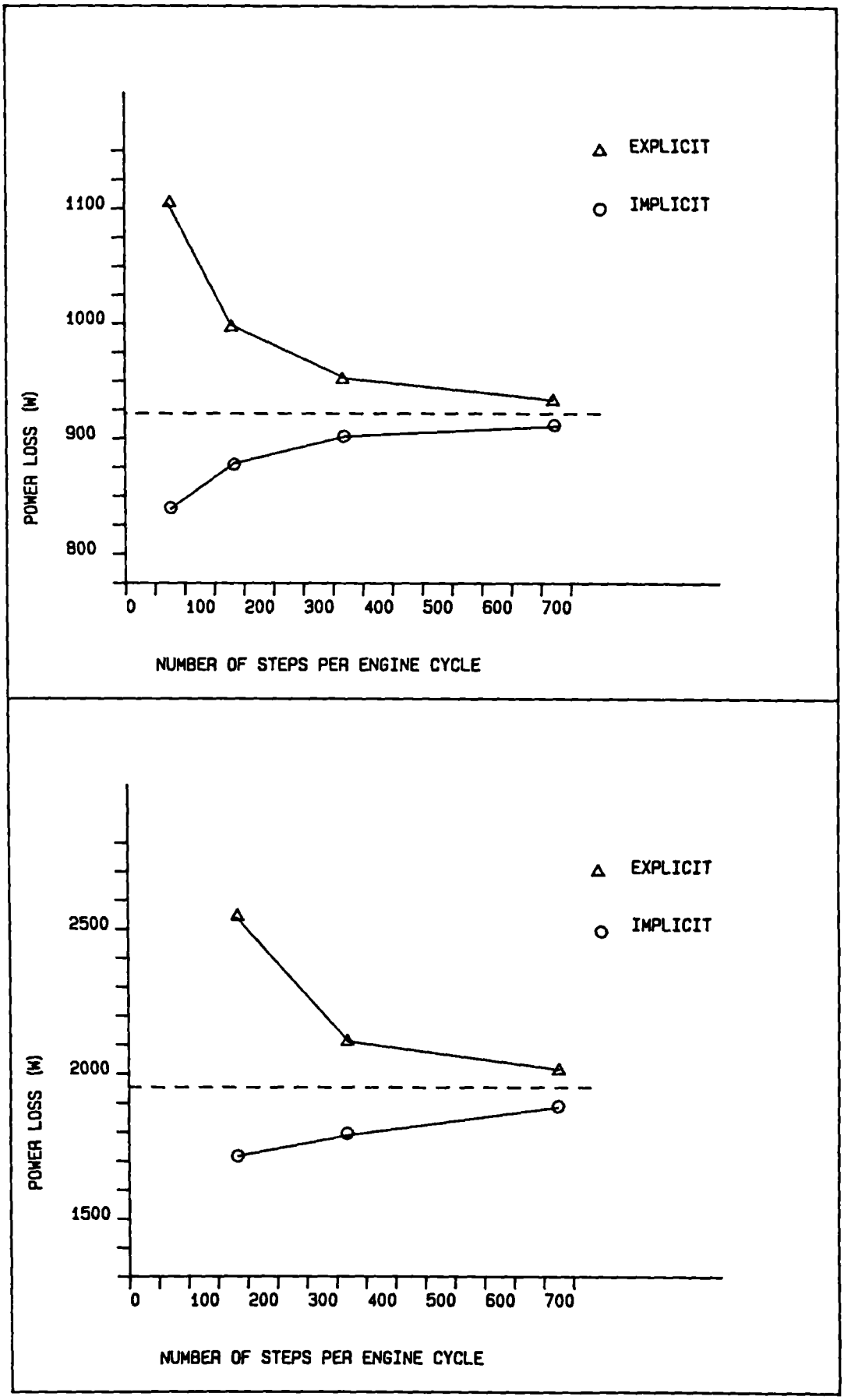

Figure 4.27 Comparison of predicted power loss for (a) medium and (b) heavy loads .

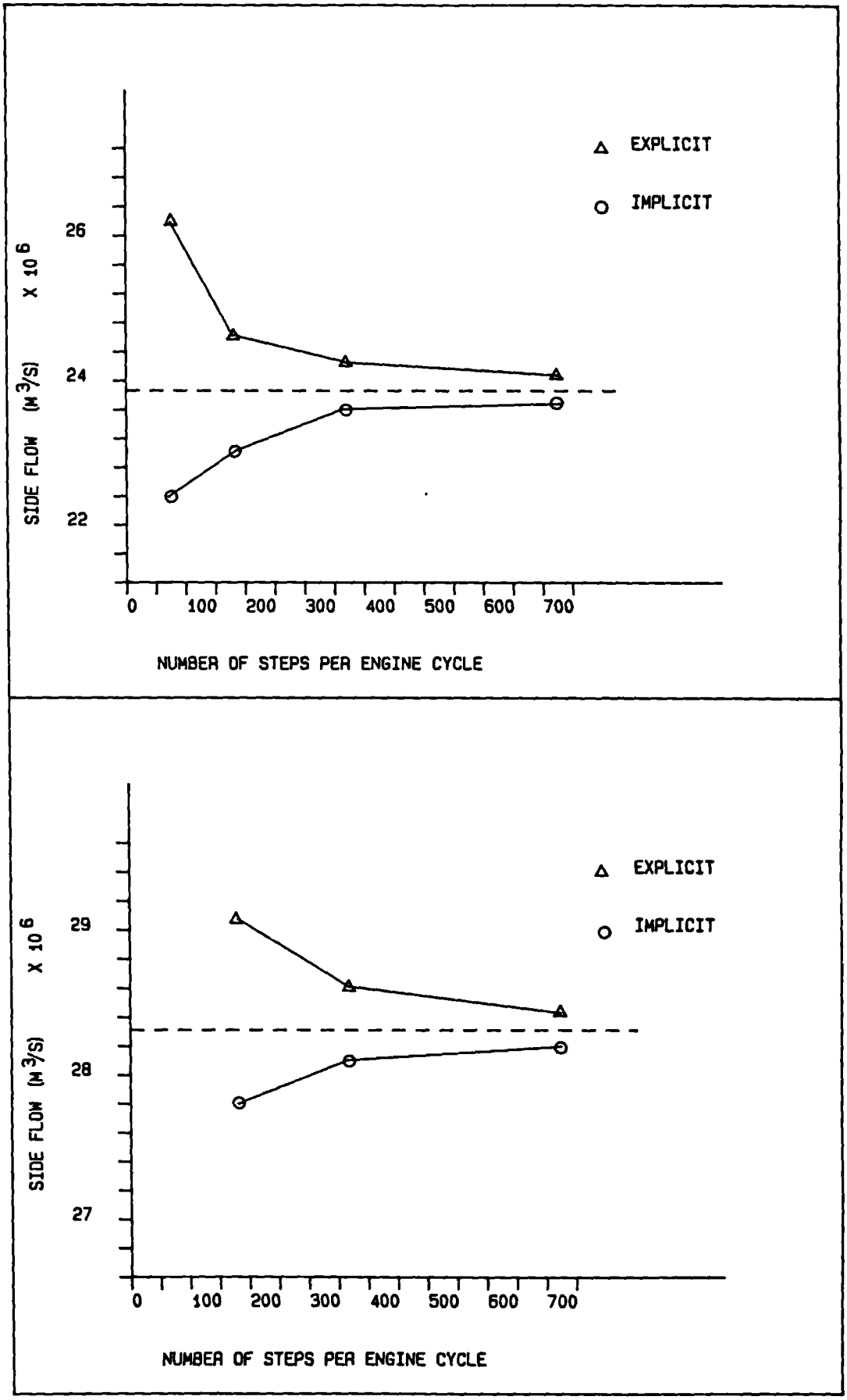

Figure 4.28 - Comparison of predicted side flow for (a) medium and (b) heavy loads .

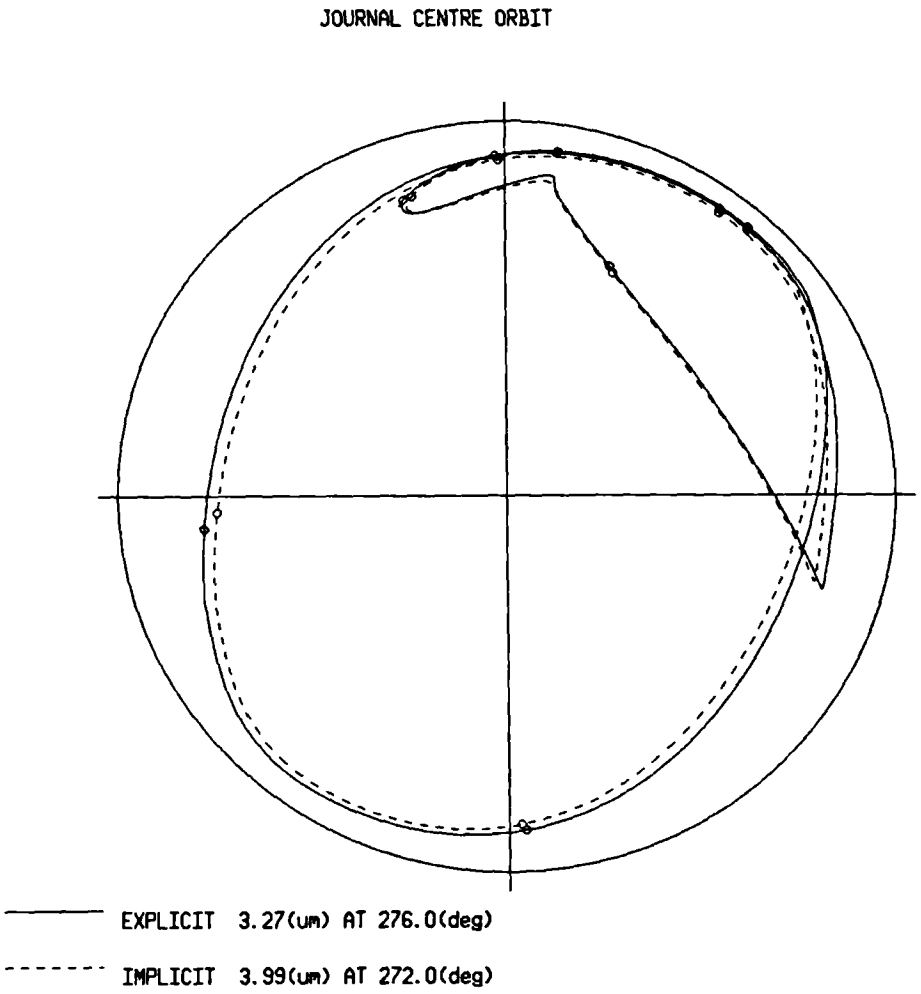

Figure 4.29 - Comparison of journal centre orbits obtained using explicit and implicit time stepping methods

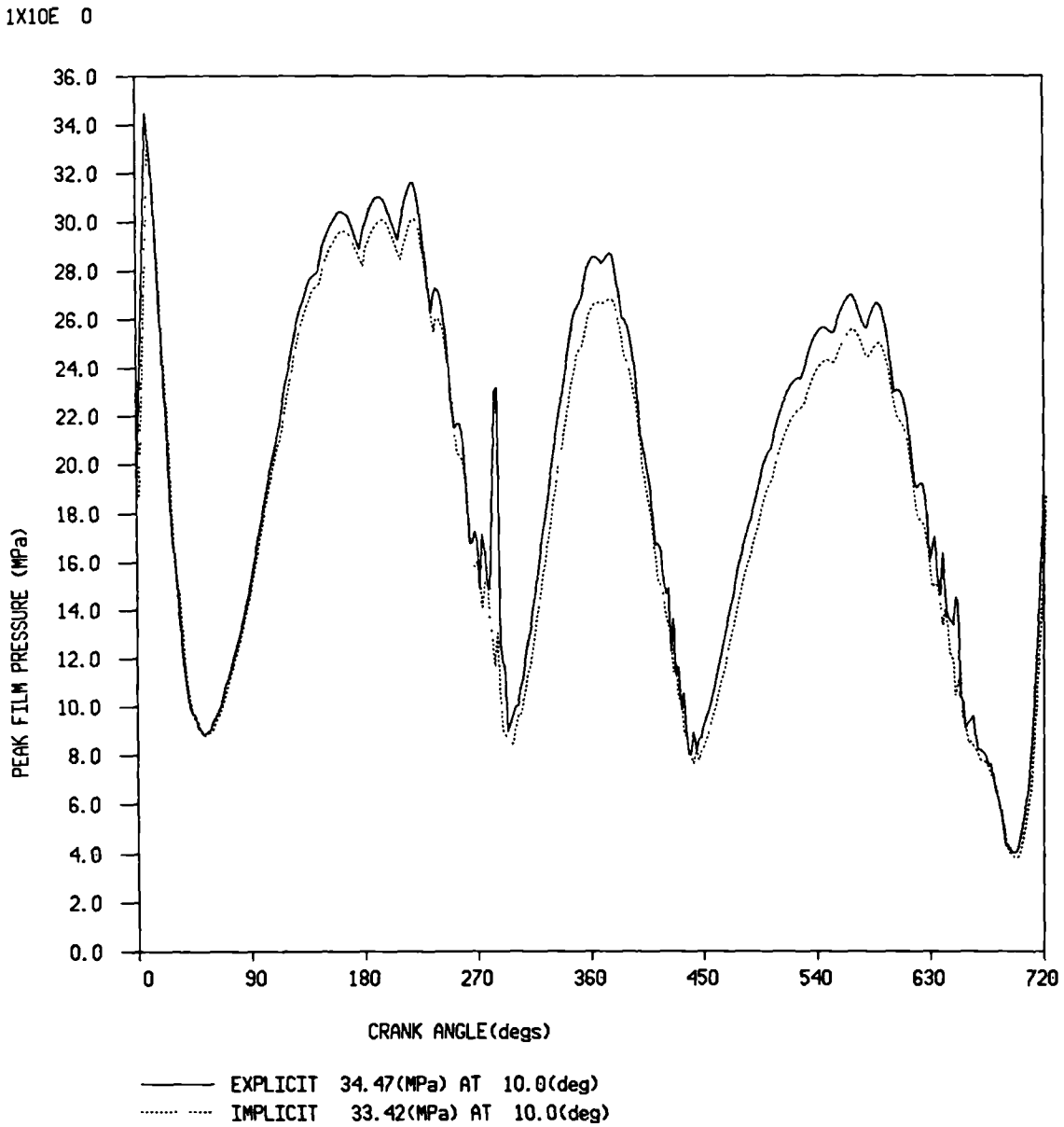

Figure 4.30 - Comparison of peak film pressure using explicit and implicit time stepping methods.

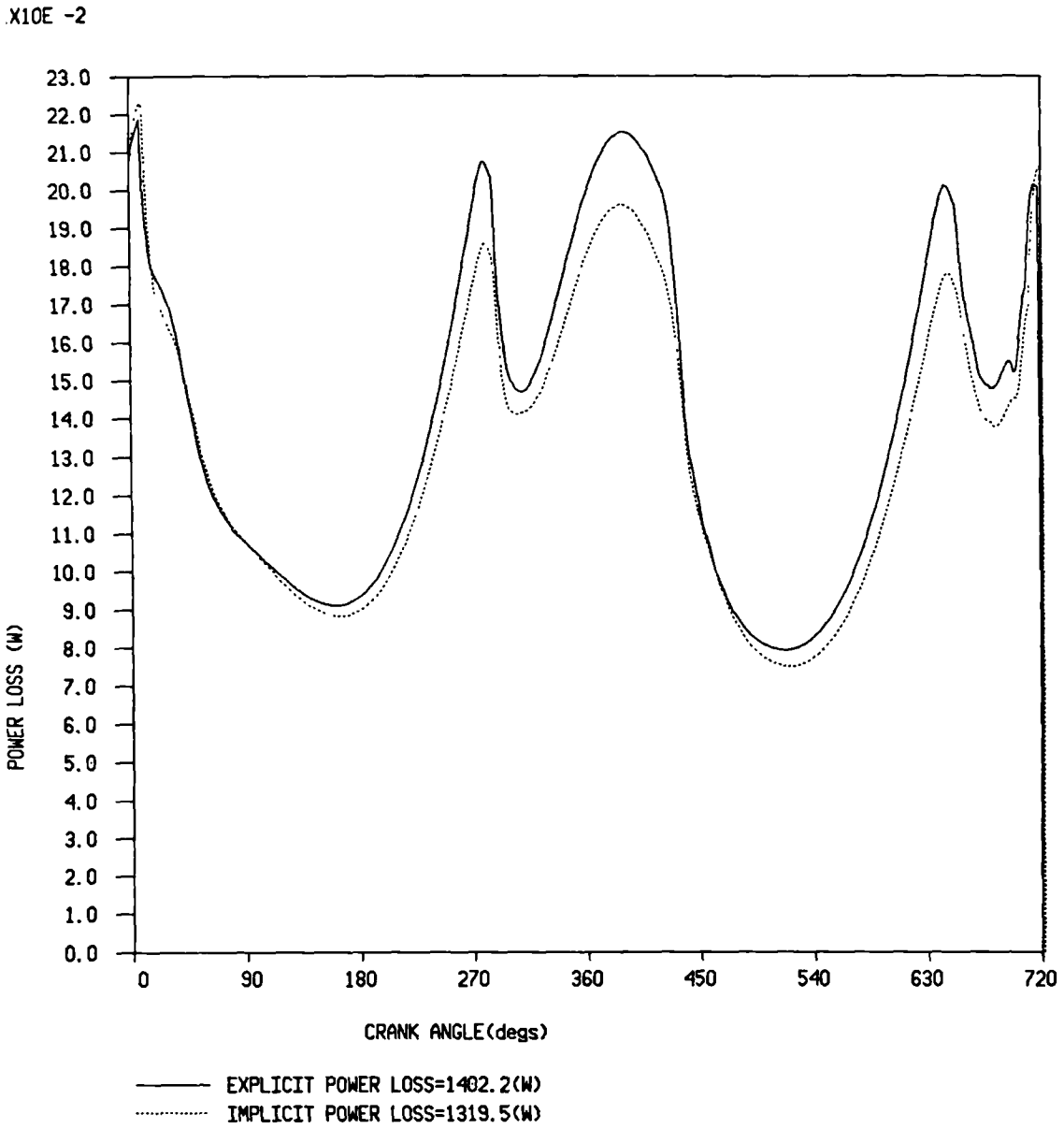

Figure 4.31 - Predicted bearing power loss using explicit and implicit time stepping .

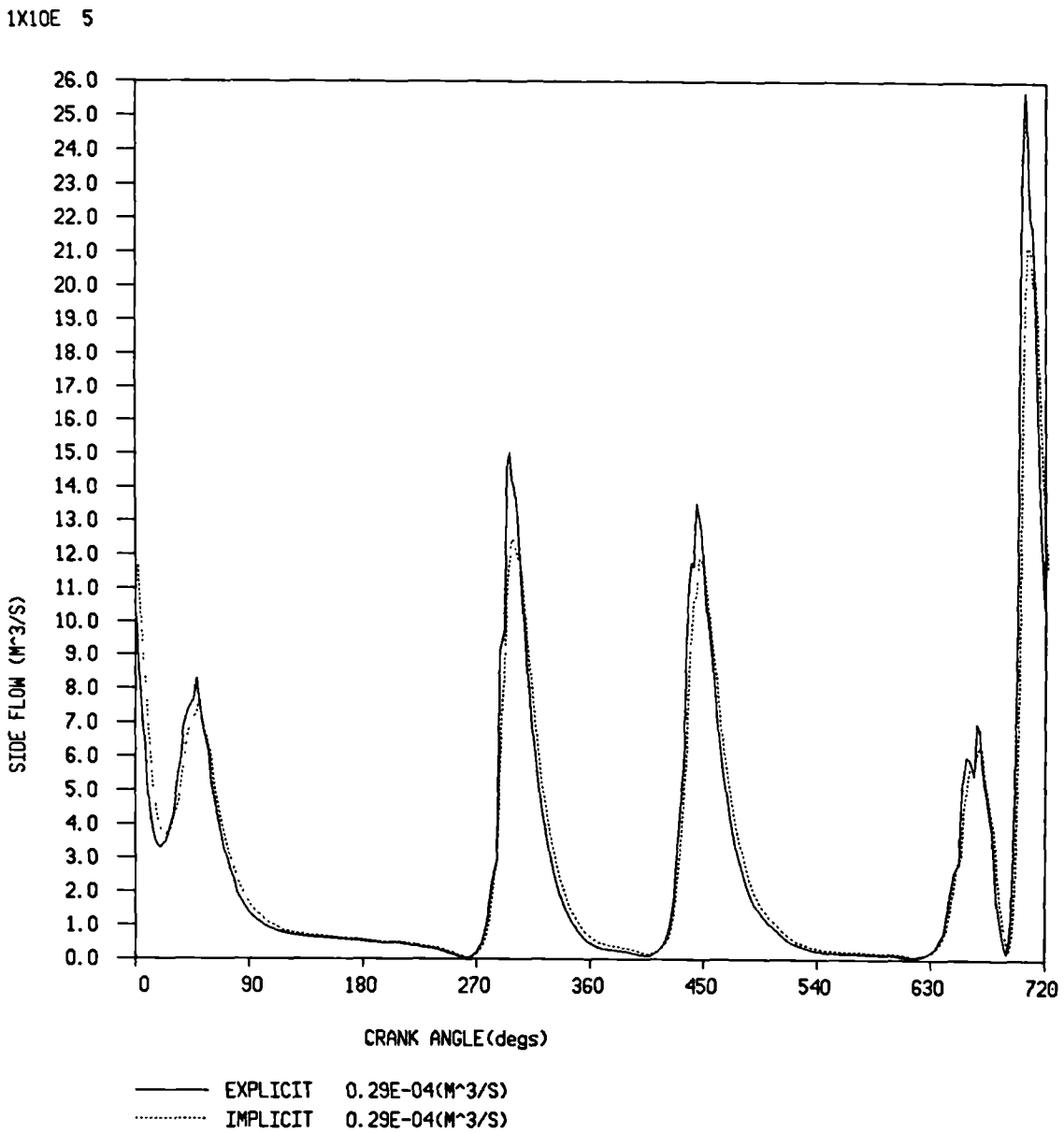

Figure 4.32 - Predicted side flow out of the bearing using explicit and implicit time stepping methods.

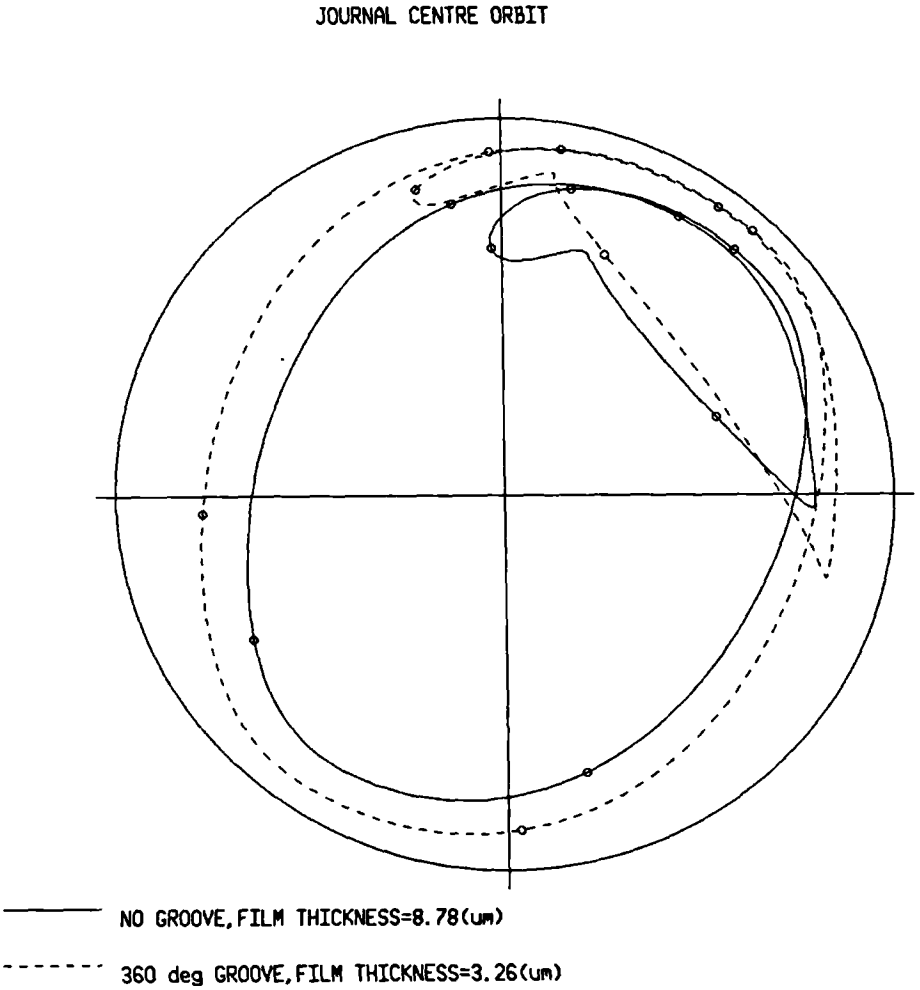

Figure 4.33 - Effect on journal centre orbit of full circumferential oil feed groove.

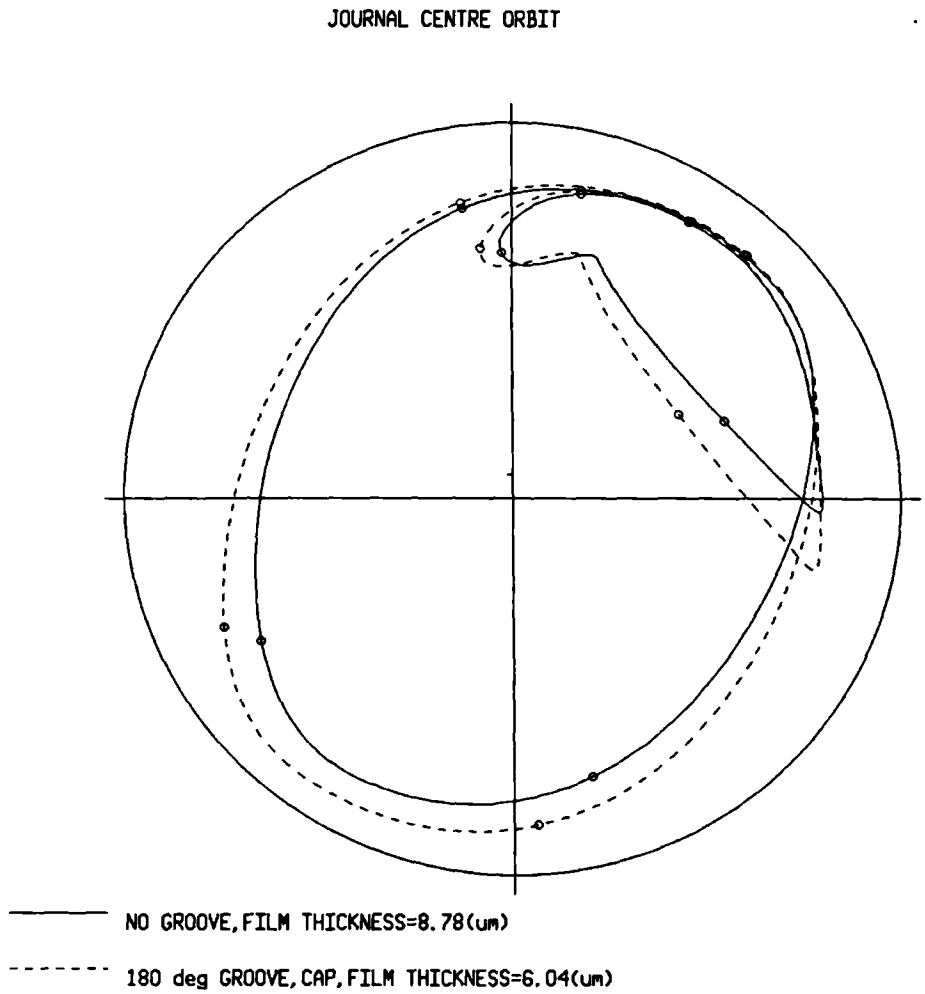

Figure 4.34 - Effect on journal centre orbit of partial groove in cap half of the bearing .

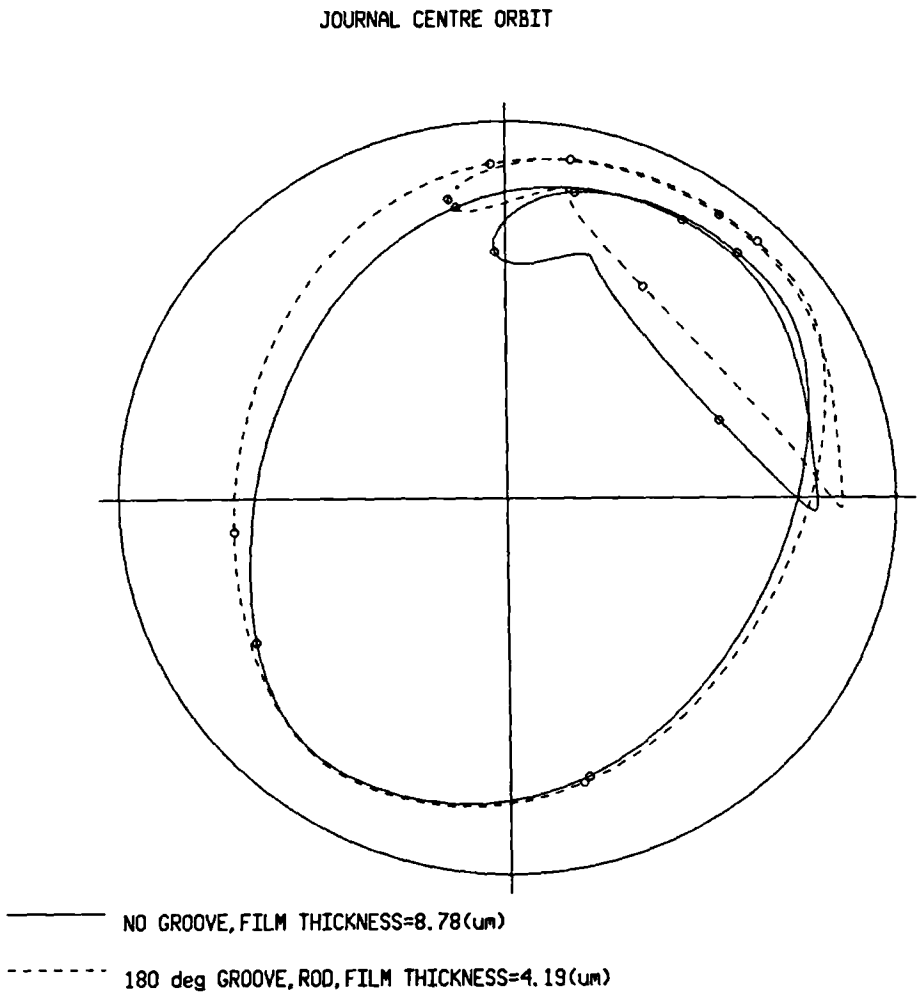

Figure 4.35 - Effect on journal centre orbit of partial groove in rod half of the bearing .

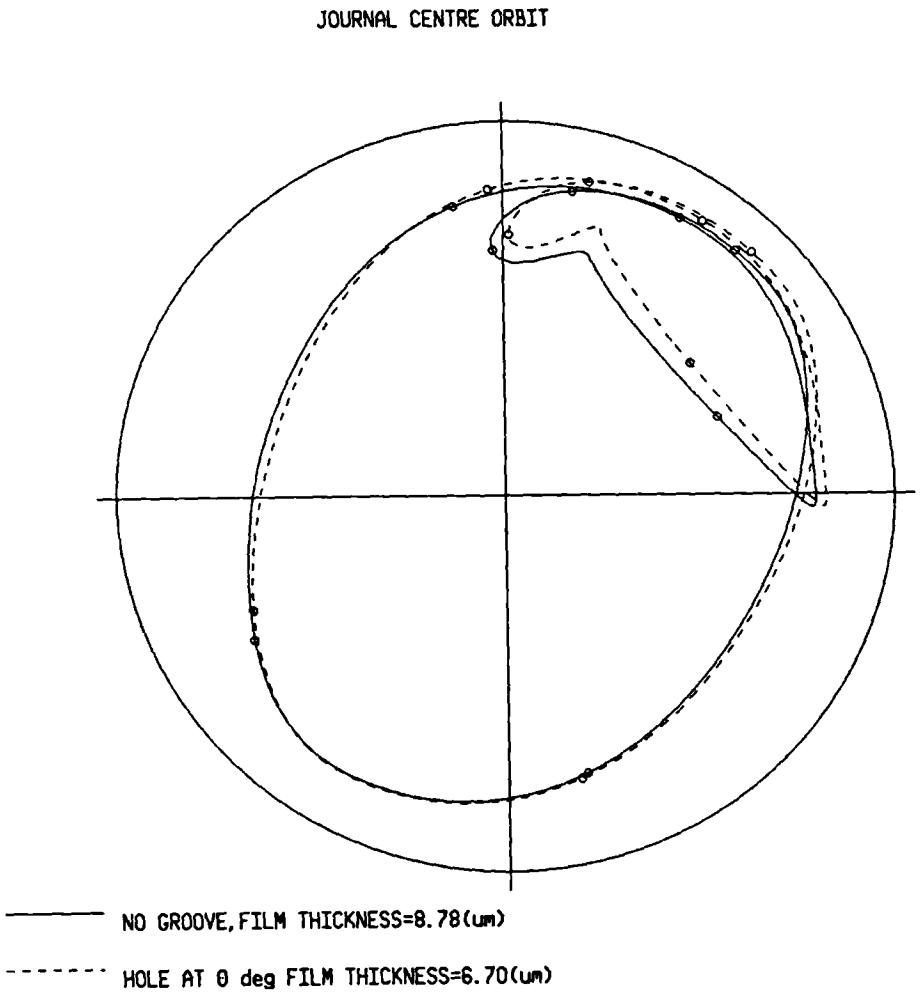

Figure 4.36 - Effect on journal centre orbit of an oil supply hole at 0 degrees

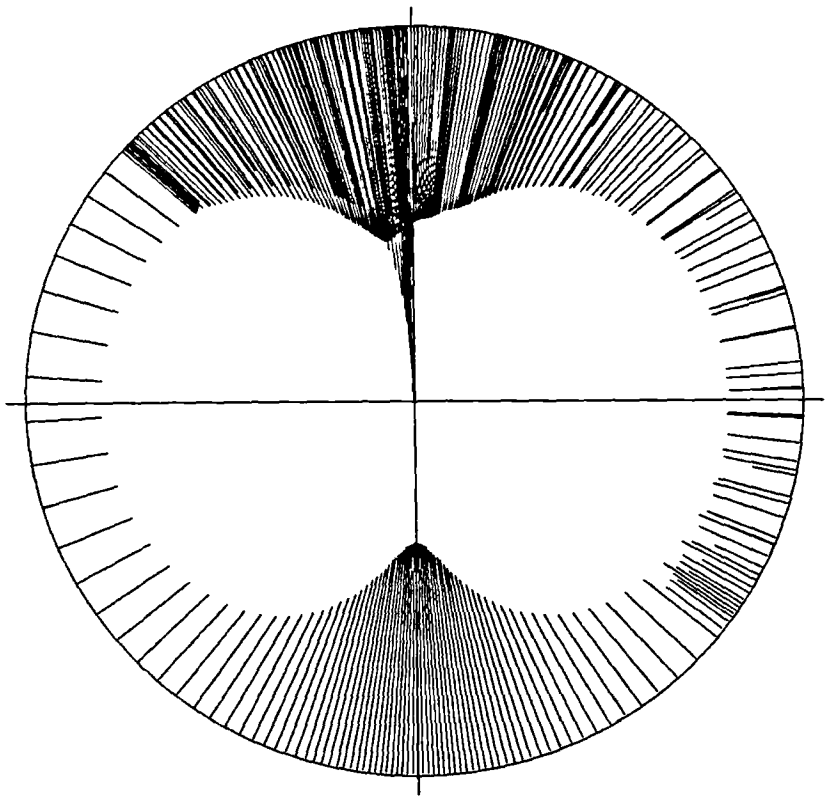

Figure 4.37 - Distribution of the load on the bearing at discrete time steps relative to the connecting rod axis .

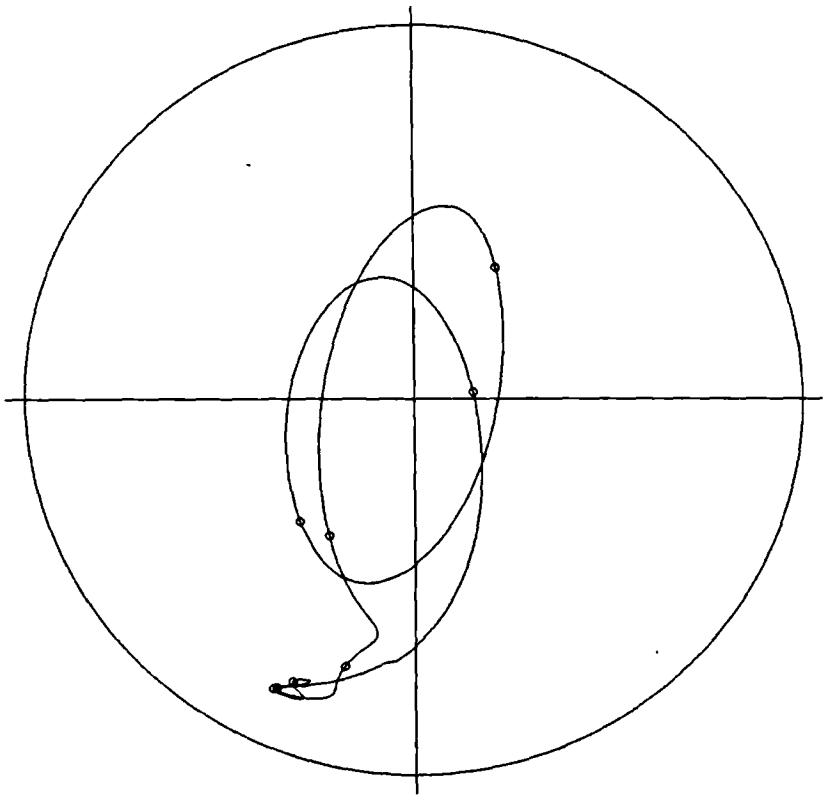

JOURNAL CENTRE ORBIT

MINIMUM FILM THICKNESS 3.69(um) AT 66.0(deg)

Figure 4.38 - Journal centre orbit for intermain bearing.

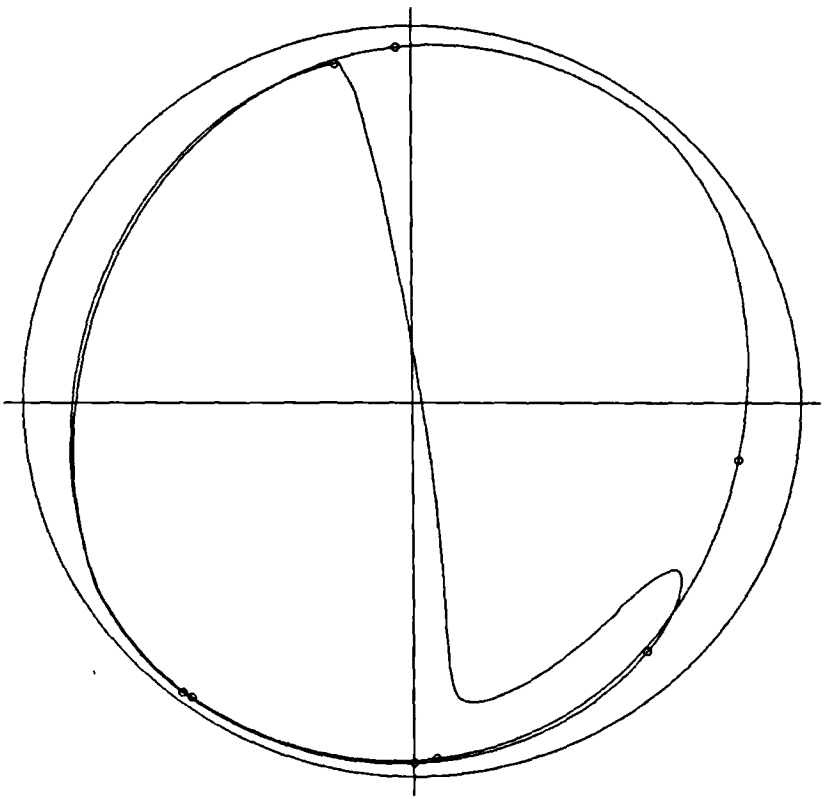

Figure 4.39 - Journal centre orbit for high speed connecting rod bearing.

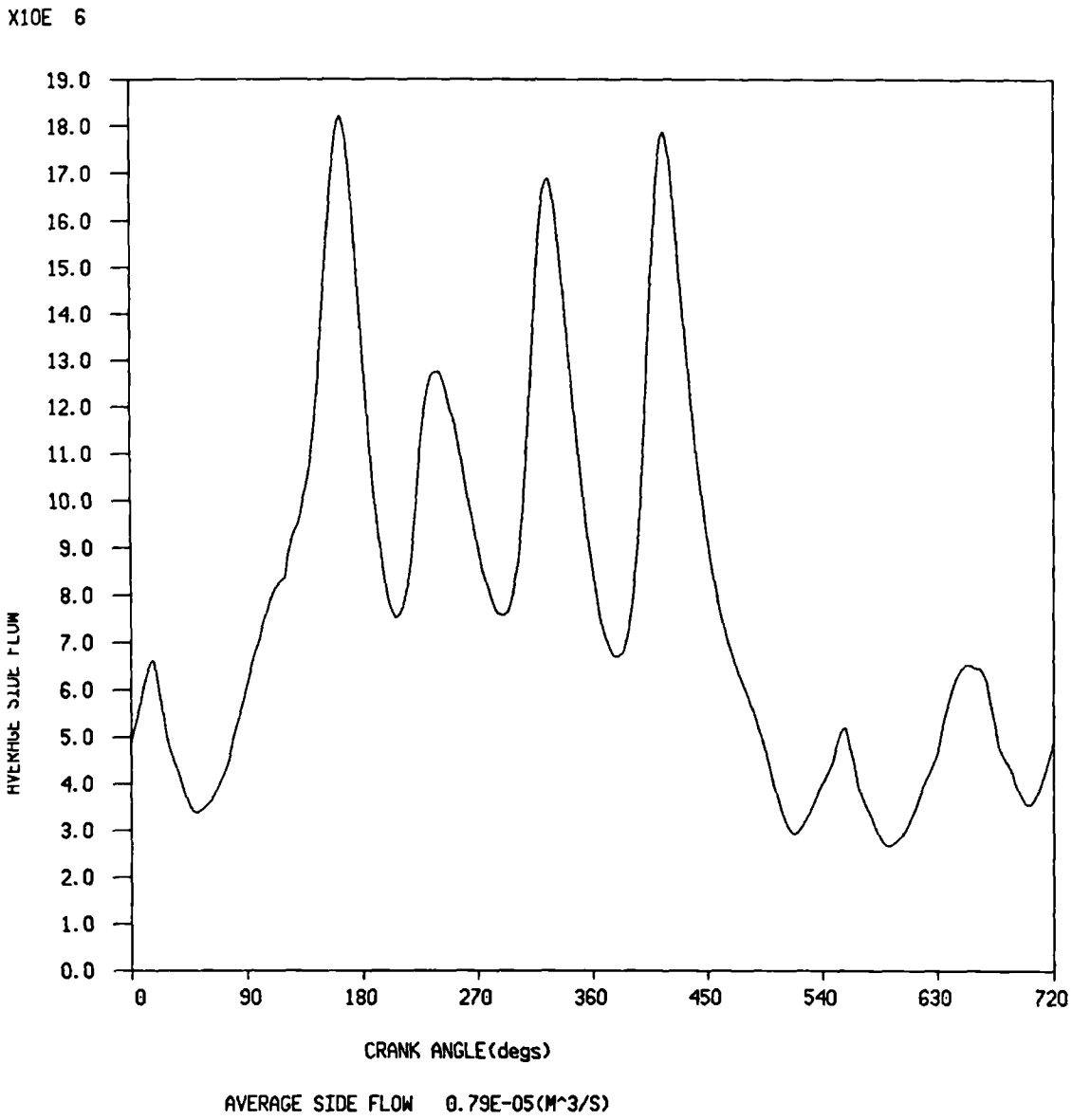

Figure 4.40 - Predicted side flow for intermain bearing.

Chapter 5

Structural Modelling and Compliance Matrix

5.1 Introduction

Once the rigid bearing model had been set up the next step in the work was to extend the analysis to consider the elastohydrodynamic (EHD) behaviour of the bearing. An EHD analysis centres around solving for the pressure distribution generated in the oil film and the corresponding housing distortions. It is possible to include a complete structural analysis in the solution procedure but this is very time consuming. Instead a relationship can be established relating the housing distortions to the pressure distribution. In finite element form this is achieved by assembling a compliance matrix that relates the nodal displacements to the nodal pressures. The advantage with this is that a structural analysis need only be carried out once for each structural model. This chapter describes the finite element structural modelling of a connecting rod and the way in which the compliance matrix is obtained from this model.

5.2 Film thickness equations

In an EHD analysis the film thickness, h, is made up of two components: one due to the motion of the journal relative to the housing, which is the film thickness for the rigid bearing problem, and one due to the housing distortion caused by the pressure distribution generated in the oil film. The expression for the film thickness is therefore given by

$$h = h_o + Lp = c - e_x\cos\theta - e_y\sin\theta + Lp \tag{5.1}$$

where h_o is the rigid bearing film thickness, e_x and e_y are the x and y components of the journal eccentricity, L is an integral operator relating the pressure distribution p to the radial displacement of the housing. Rewriting this equation in finite element form the film thickness h_i at a node i at a circumferential position θ_i may be expressed as

$$h_i = h_{oi} + [C_i]\{p\} = c - e_x\cos\theta_i - e_y\sin\theta_i + [C_i]\{p\} \tag{5.2}$$

where $[C_i]$ is the *ith* row of the structural compliance matrix $[C]$ relating the distortion at the node i to the nodal pressures, and $\{p\}$ is the column matrix of the nodal pressures. To obtain the compliance matrix $[C]$ a finite element structural model of the bearing housing was first developed. It was assumed that the journal deformations were negligible compared to the housing deformations.

5.3 Finite element structural model.

To obtain a relationship between the nodal pressures and the housing deformations a finite element structural model of the bearing housing had to be constructed. The PAFEC finite element package was used to carry out the structural modelling. Like most general purpose finite element packages the finite element mesh could be generated interactively using a graphics preprocessing package. This package was run on an Apollo Domain computer system which has extensive graphics capabilities. A three-dimensional model of the bearing housing was used. Figure 5.1 shows an idealised three-dimensional finite element model of a big-end bearing using the mesh generation preprocessor. Several other authors [38-44] have used two-dimensional models of the bearing housing to simplify the analysis, in some of these cases it was also assumed that the radial deflection was invariant in the axial direction to further simplify the model. This assumption has been shown [39] to be inadequate in some cases and in this particular case a two-dimensional model would not provide the required compliance matrix for the two-dimensional lubrication mesh.

From the previous work carried out on the rigid bearing problem it was found that the 8-node isoparametric elements gave a much better performance than the 3-node triangular elements for modelling the lubricant film. The 8-node isoparametric elements were therefore adopted for the EHD lubrication problem. When coupling the lubrication and structural analysis it is important that the two element types are compatible and, when using the 8-node isoparamteric elements, that the nodes on the inner bearing surface and the lubrication mesh coincide. The reason for this can be explained by considering the way in which the pressures are represented by equivalent nodal point forces for this type of element. Consider an element of unit area with a unit load applied to the surface of the element as a uniform pressure distribution. Integrating the pressure distribution over the surface of the element

results in a set of resultant nodal point forces as shown in Figure 5.2(a) that represent the pressure distribution for this type of element. It is important to note that these nodal point forces are not all equal and that the forces at the corner nodes act in the opposite direction to the forces at the midside nodes. This is due to the way that the shape functions are constructed and it is important that the correct form of element is used for the structural model otherwise the resulting housing deformations will be meaningless. For this reason the 20-node brick element was used for the structural modelling. This element is compatible with the 8-node isoparametric element having the required form of shape function and the nodes on this element coincide with the nodes on the lubricant mesh. This element is also very accurate for carrying out structural modelling. Figure 5.2(b) shows the 20-node brick element and the 8-node isoparametric element showing how the nodes coincide.

Initially to gain confidence in using the finite element package and to get some idea of the problems that may be involved in modelling the bearing housing a simplified housing model was constructed in two-dimensions using 8-node elements. This model consisted of a ring of elements to simply represent the big-end bearing and is shown in Figure 5.3. To check the results from the finite element model a constant pressure was applied to the inner surface of the bearing and the nodal displacements were calculated. The results for this were compared directly with the analytical solution for a thick walled cylinder under plane stress for which the radial displacement is given by

$$u_r = \frac{r}{E}\left[A(1-\nu)+\frac{B(1+\nu)}{r^2}\right] \tag{5.3}$$

with

$$A = \frac{p}{k^2-1}\ ,\ B = \frac{pb^2}{k^2-1}\ ,\ k = \frac{b}{a}$$

u_r is the radial displacement at a radius r, a is the inner radius, b is the outer radius, E is Youngs modulus, ν is Poissons ratio and p is the internal pressure.

A similar equation may also be obtained to estimate the deflection of the journal. This is achieved by assuming that the journal behaves like a cylinder under plane stress for which the radial displacement is given by

$$u_r = \frac{-r}{E}(1-\nu)p \tag{5.4}$$

For a given pressure the cylinder displacement was only about 20% of the displacement obtained for the thick walled cylinder. It therefore seems reasonable to ignore this at present.

The two sets of results compared well so the next step was to construct a three-dimensional structural model. As for the rigid bearing work the example considered was the Ruston and Hornsby 6VEB MK III marine diesel big-end bearing where the dimensions of the connecting rod were supplied by the Glacier Metal Company [64]. A simplified model of the connecting rod was constructed consisting of a ring of elements to represent the big-end bearing. This was rigidly constrained over the top 90 degrees of the bearing (Figure 5.4) as it was assumed that the distortions at the big end would be considerably greater than the distortions elsewhere in the bearing which could be ignored. The advantage of using a simplified model was that different mesh gradings could be consistently modelled without having to add extra detail to the model. The thickness of the ring was approximately equal to the average thickness of the big end bearing. This model was not an exact representation of the connecting rod but the work was more concerned with developing and quantifying a fast numerical method for solving the EHD lubrication problem rather than providing accurate results for a particular bearing. To ensure that the compliance matrix could be assembled easily it was important at this stage that the node numbering used for the nodes on the inner bearing surface coincided with that used for the lubricant mesh. To achieve this the inner nodes were constructed first with the required node numbering and the structural model was built on this nodal framework. Again to get some idea of the accuracy of the model a constant pressure was applied to the inner bearing surface and the model was constrained to act in plane stress which was simply achieved within the PAFEC software package. Again the displacements compared well with the analytical solution.

5.4 Structural compliance matrix

Two methods were investigated for obtaining the compliance matrix from the finite element structural model. The first method is one that has already been adopted by various other authors [47] and is fairly straightforward. This method

consists of applying a unit load at each nodal point in turn on the inner bearing surface and recording the resulting radial displacements at all the other nodes on the inner bearing surface. In this way a compliance matrix relating the nodal point forces to the nodal displacements could be built up a column at a time to give

$$\{u_r\} = [C_f]\{F\} \tag{5.5}$$

where $\{u_r\}$ is the column vector of the radial displacements, $[C_f]$ is the force compliance matrix and $\{F\}$ is the column vector of the nodal loads applied to the system.

It is important to note that unit loads and not pressures were applied to the system even though it is desirable to apply pressures since a pressure displacement is required. This is due to the way that the equivalent nodal point forces for a distributed pressure load were calculated within the package which did not allow single unit pressures to be applied at midside nodes. The required compliance matrix for the EHD problem is the pressure compliance matrix $[C]$ that relates the radial displacements to the nodal pressures. This may be obtained by establishing a relationship between the pressures and the equivalent nodal point forces. For a single element with a set of nodal pressures $\{p\}^e$ the equivalent set of nodal point forces, $\{F\}^e$, to represent the pressure distribution over the element may be obtained as

$$\{F\}^e = \int_{A^e} [N]^T \{p\}^e dA^e \tag{5.6}$$

where $[N]^T$ is a row matrix containing the element shape functions used to approximate the pressure distribution over the element. Using Gauss-Legendre quadrature to integrate the pressure distribution over the element an integral operator matrix $[A_I]^e$ may be assembled such that

$$\{F\}^e = [A_I]^e \{p\}^e \tag{5.7}$$

where

$$A_{ij} = \sum_{k=1}^{n} \sum_{l=1}^{n} a_k a_l N_i N_j \, |\det J| \tag{5.8}$$

where a_k and a_l are the weighting factors described in Chapter 3, N_i and N_j are the shape functions evaluated at the Gauss points, and n is the number of Gauss

points used. Both 2- and 3-point quadrature was used and since it was found that there was no significant difference in the results the 2-point method was adopted as it requires considerably fewer calculations. It is a simple operation to assemble the matrix $[A_I]$ for the complete system in the same way that the matrix $[K_p]$ was assembled in Chapter 3 by summing the individual element contributions to give

$$\{F\} = [A_I]\{p\} \tag{5.9}$$

Combining (5.5) and (5.9) gives

$$\{u_r\} = [C_f][A_I]\{p\} \tag{5.10}$$

therefore the pressure compliance matrix is $[C]$ is obtained as

$$[C] = [C_f][A_I] \tag{5.11}$$

It was, however, found that the output from the program was not in a readily useable form and required extensive editing to get it into the correct format. In addition the program only allowed 10 different load cases to be run at any one time. Thus, for example, if the compliance matrix was required for a lubrication mesh with 41 circumferential and 5 axial nodes, a total of 160 nodes, the analysis would have to be carried out 16 times which would be extremely expensive in computing time. For these reasons the method was too impractical to be generally adopted. A second method was therefore developed that proved to be several orders of magnitude faster than this method and required no editing of the output to obtain the compliance matrix.

Consider the finite element equations for the structrual problem which are

$$[K]\{u\} = \{F\} \tag{5.12}$$

where $[K]$ is the system stiffness martix for the structure, $\{u\}$ is the column vector of the nodal displacements and $\{F\}$ is the column matix of nodal point loads applied to the system. Inverting $[K]$ gives

$$\{u\} = \{F\}[K^{-1}] \tag{5.13}$$

and therefore $[C_f] = [K^{-1}]$. This gives the force compliance matrix for the entire structure, not just the inner bearing surface. It will also give the compliance matrix

for all the displacements associated with each node, that is u_r, u_θ and u_z where u_θ and u_z are the displacements in the circumferential and axial directions respectively. It is possible to construct the stiffness matrix $[K]$ for just the terms associated with the radial displacements on the inner bearing surface using condensation or sub-structuring [53]. Let the displacements be divided into two groups, $\{u_a\}$, those displacements that are required or active and $\{u_i\}$, which are the displacements that are not required or inactive. Equation (5.12) may be written as

$$[K]\{u\} = \begin{bmatrix} [K_{ii}] & [K_{ia}] \\ [K_{ai}] & [K_{aa}] \end{bmatrix} \begin{Bmatrix} \{u_i\} \\ \{u_a\} \end{Bmatrix} = \begin{Bmatrix} \{F_i\} \\ \{F_a\} \end{Bmatrix} \tag{5.14}$$

The inactive displacements or freedoms may be eliminated to give

$$([K_{aa}]-[K_{ai}][K_{ii}]^{-1}[K_{ia}])\{u_a\} = \{F_a\}-[K_{ai}][K_{ii}]^{-1}\{F_i\} \tag{5.15}$$

Since the only loading that is of concern is the radial loading applied to the nodes on the inner bearing surface $\{F_i\} = 0$, therefore

$$[K'_{aa}]\{u_a\} = \{F_a\} \tag{5.16}$$

where $[K'_{aa}]$ is the required stiffness matrix. The PAFEC software allows this matrix to be easily assembled during the analysis by simply specifying the active freedoms and this matrix can be stored in a separate output file. Since the nodes on the inner bearing surface have the same node numbering as the lubrication mesh these freedoms are the first n radial displacements, where n is the number of nodes in the lubrication mesh. The pressure compliance matrix is then given by

$$[C] = [K'_{aa}]^{-1}[A_I] \tag{5.17}$$

The matrix $[K'_{aa}]$ can be obtained from the PAFEC software requiring no further editing. The inverse was initially calculated by using the appropriate NAG library fortran subroutines. Since it would be advantageous if the EHD analysis software could be as self-contained as possible and since the inversion process could be expensive in terms of computing time a matrix inversion method was developed that was considerably faster than the NAG subroutines for this particular form of matrix and could be run on any system. This method is based very loosely upon the idea of applying point loads at each node in turn, but exploits the sparseness and symmetry of some of the matrices involved, and the fact that a lot of the

calculations are repeated for each load case. Consider first how the displacements $\{u\}$ are obtained for a given set of loads $\{F\}$.

First forward elimination is carried out on the stiffness matrix as

$$K'_{ij} = K_{ij} - K_{kj}\frac{K_{ik}}{K_{kk}} \; : k=1,2,..n-1;\; i=k+1,k+2,..n \;;j=k+1,k+2,..n \qquad (5.18)$$

During the forward elimination the right hand sides of (5.11) are modified as

$$F'_i = F_i - F_k R \qquad (5.19)$$

where R is the elimination ratio K_{ik}/K_{kk}. After the elimination process the matrix $[K]$ is in upper triangular form and $\{F\}$ has been suitably modified. To obtain the required displacements $\{u\}$ back-substitution is carried out starting with

$$u_n = \frac{F'_n}{K'_{nn}} \qquad (5.20)$$

and the subsequent displacements at the other nodal points are found as

$$u_i = \frac{(F'_i - \sum_{j=i+1}^{n} K'_{ji} u_i)}{K'_{ii}} \qquad (5.21)$$

Forward elimination need only be carried out once on the stiffness matrix regardless of the number of load cases and the elimination ratios can be stored to subsequently modify each new right-hand side $\{F\}$ for each new load case.

For the fast inversion method forward elimination is carried out as before and the elimination ratios are stored in an array $[S]$ as the elimination process is carried out. An n x n matrix is then assembled to represent all the point loads on the system. This is equivalent to grouping n column vectors for each point load together. Initially therefore

$$[B] = [I] \qquad (5.22)$$

where $[I]$ is the identity matrix. This matrix is then modified as

$$B_{ji} = B_{ji} - B_{ki} S_{kj} \; : i=1,2,..n-1;\; j=i+1,i+2,..n;\; k=j,j-1,..i-1 \qquad (5.23)$$

This is equivalent to carrying out n forward eliminations on the n column matrices

but exploits the sparseness and symmetry of $[B]$, thereby considerably reducing the required computing time. Then, rather than carrying out n backsubstitutions for the n loadcases, a matrix $[D]$ is assembled to represent all the operations carried out by $[K]$ on one right hand side during the backsubtitution process. Starting with

$$D_{ii} = \frac{1}{K_{ii}}$$

$[D]$ is assembled as

$$D_{ji} = D_{ji} - \frac{D_{ki} K_{kj}}{K_{jj}} \; : i = n, n-1, ..2; \; j = i-1, i-2, ..1; \; k = i, i-1, ..j+1 \qquad (5.24)$$

The displacements for all the loadcases are then found by multiplying $[D]$ by $[B]$ to give an $n \times n$ matrix $[\overline{u}]$ containing the required radial displacements for the n loadcases, where

$$[\overline{u}] = [D][B] = [K]^{-1} \qquad (5.25)$$

The pressure compliance matrix is then given by

$$[C] = [D][B][A_I] \qquad (5.26)$$

where $[A_I]$ is the integral operator matrix described earlier.

This method produced a time saving of more than an order of magnitude over the NAG matrix inversion routines. Table 5.1 compares the computing times required for the various methods for obtaining the compliance matrix expressing the time as a percentage of the time required to carry out the inversion for using the NAG librairies. The time given using method 1, that is applying individual point loads to the nodes on the inner bearing surface, does not include the time required to obtain the stiffness matrix $[K]$ and is estimated assuming that the software allowed all the loadcases to be calculated during one analysis rather than just allowing 10 loadcases at a time.

Method	Time
NAG	100%
Method 1	1100%
Method 2	5%

Table 5.1 : Comparison of computing times for the matrix inversion

This technique therefore allowed the compliance matrix to be easily obtained for a particular structure without extensive editing or requiring an excessively large amount of computer time. For a lubrication mesh with 160 nodes approximately 30 seconds of computing time on the VAX 11/785 system was required. In general the time was proportional to n^3. It is important to note that of the three components of the displacement at each node only the radial displacements were calculated.

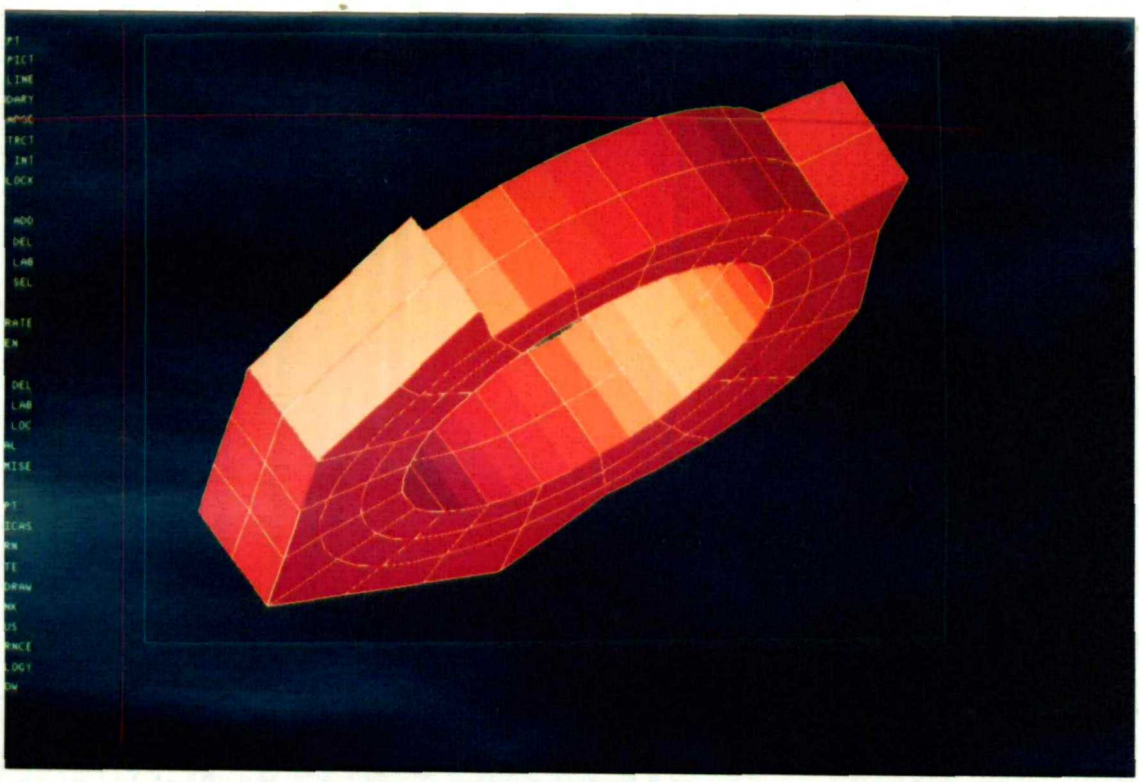

Figure 5.1 - Three-dimensional model of big-end bearing shown using the mesh generation preprocessor.

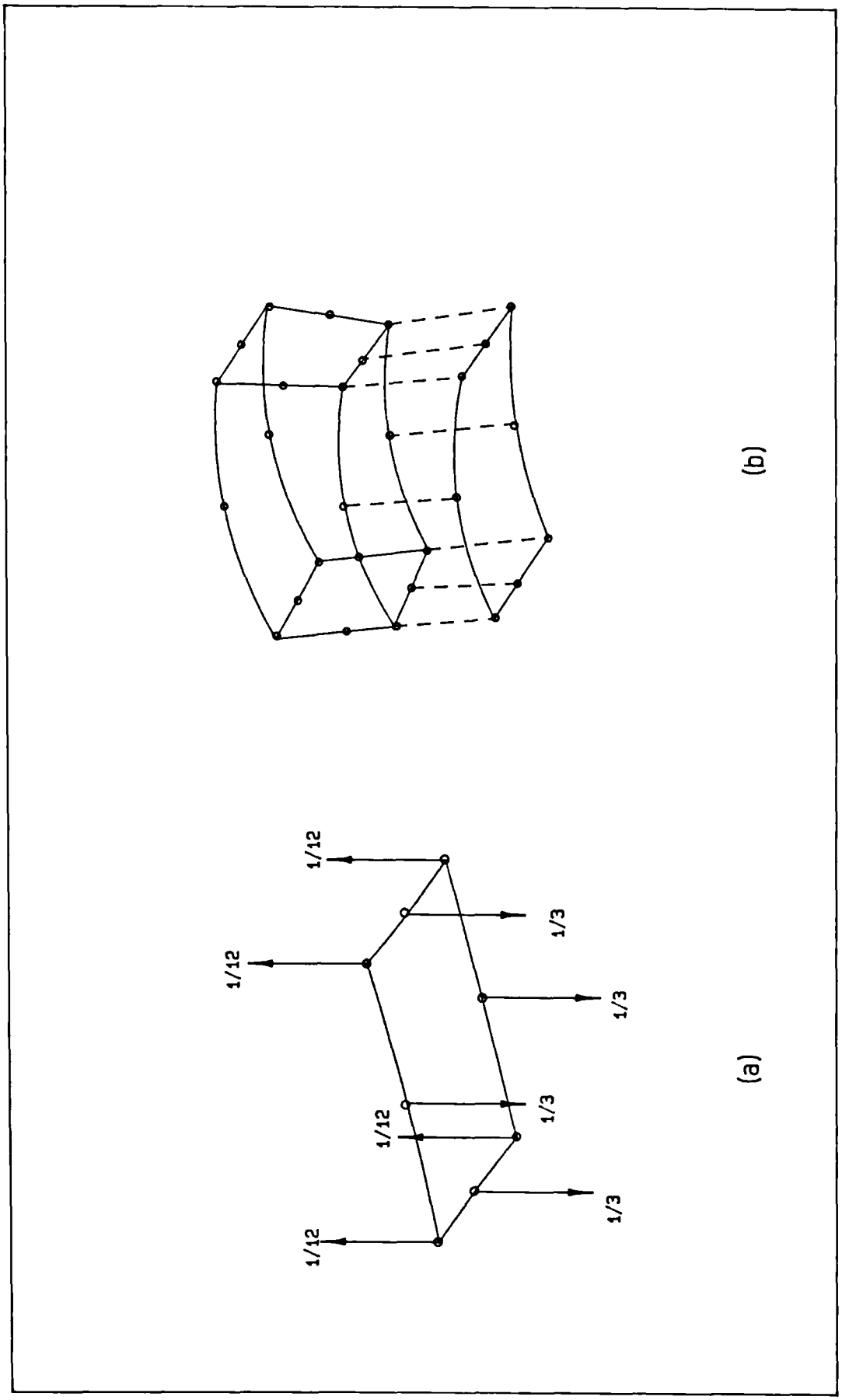

Figure 5.2 - (a) Equivalent nodal point forces for the 8-node isoparametric element
(b) 20-node brick element and 8-node isoparametric element showing coincident nodes.

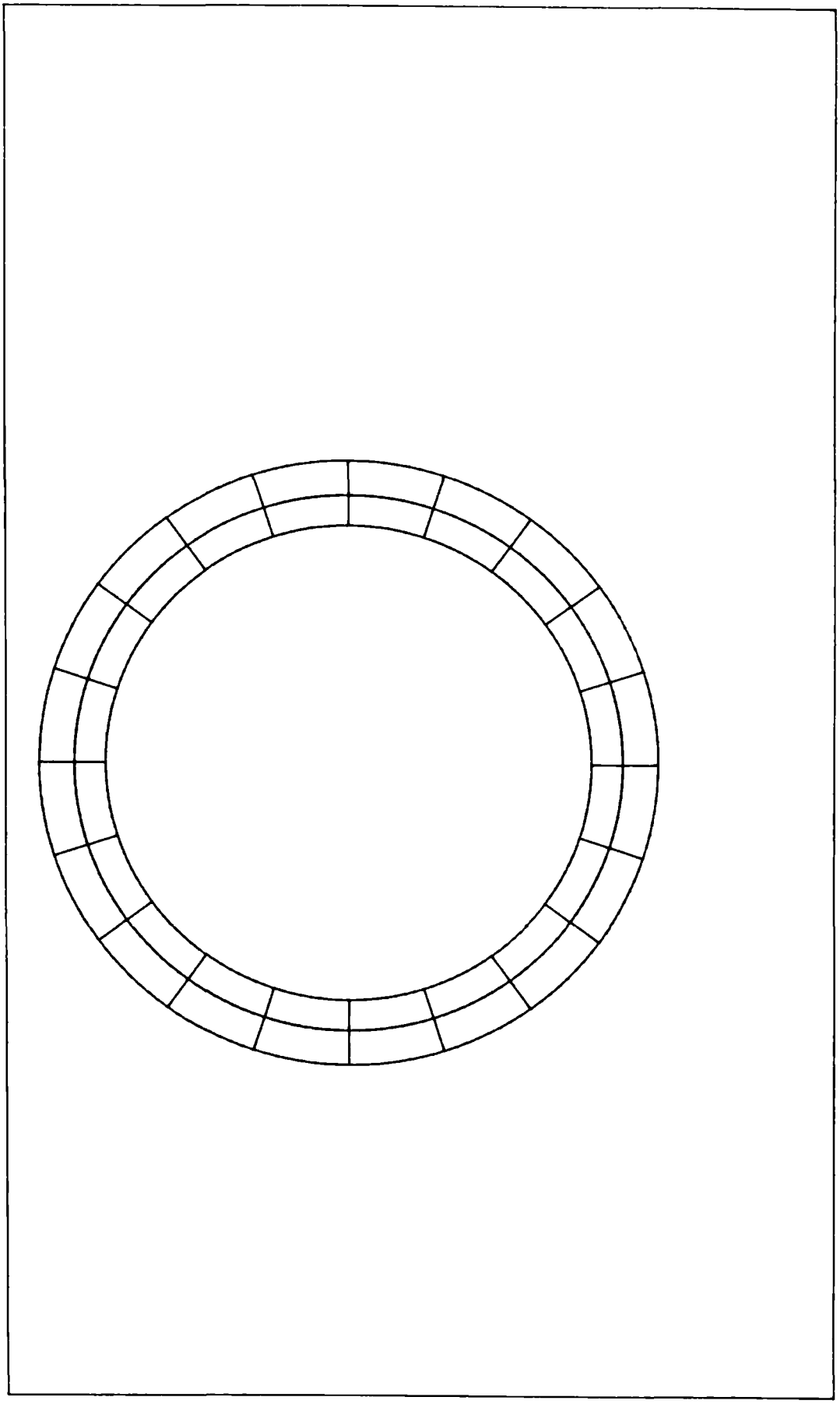

Figure 5.3 - 2D finite element ring element using 8-node elements.

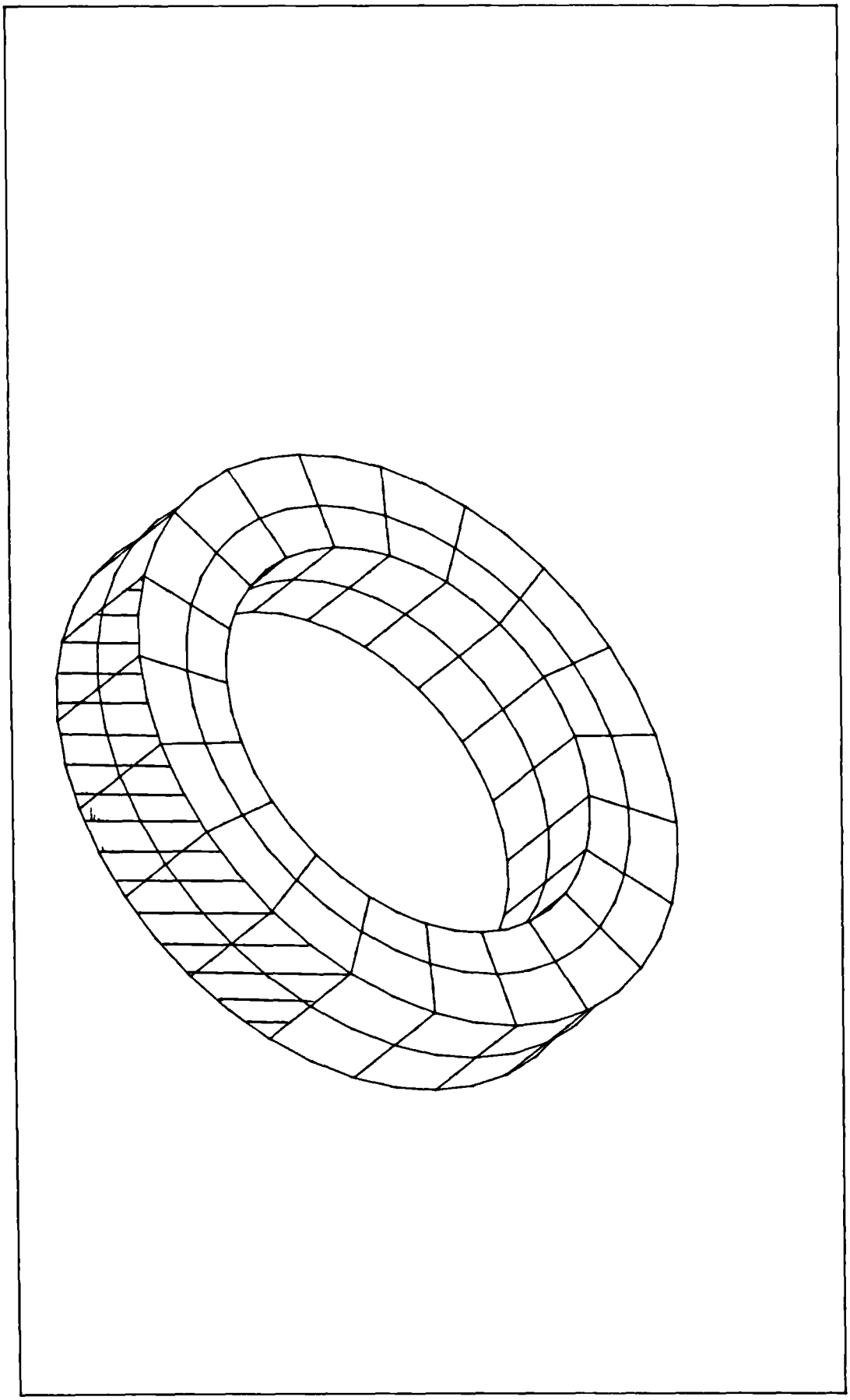

Figure 5.4 - 3D finite element model of connecting rod bearing using 20-node brick elements. Shaded portion is totally restrained.

Chapter 6

The Under-relaxation Solution Method.

6.1 Introduction

The analysis of the elastohydrodynamic (EHD) behaviour of a journal bearing centres around solving for the pressures generated in the oil film using Reynolds equation and the bearing housing deformation using solid mechanics relations. Since the pressures and deformations are directly related the resulting problem is highly non-linear and the method of solution will, therefore, require some form of iteration to couple the two problems.

Many investigations of the EHD behaviour of highly loaded contacts such as gear teeth and roller bearingshave been carried out and a comprehensive review of this work is given by Dowson and Higginson [36]. It is, however, only comparatively recently, with the increase in computing power, and the development of suitable numerical analysis techniques, that it has been possible to tackle the EHD journal bearing lubrication problem. Taylor and O'Callaghan [37] were amongst the first to apply the finite element method to the EHD lubrication problem. They analysed the behaviour of a sphere in contact with a plane and to solve the problem an initial estimate was made for the the oil film thickness, h, and the resulting pressure distribution was calculated from Reynolds equation using a finite element mesh to model the lubricant film. This presure distribution was used to calculate the surface deformation from which a new film profile was obtained. This new film profile was then used to calculate a new pressure distribution which again gave a new film profile. This iterative process was continued until the changes in the values of the nodal pressures fell below a prescribed amount defining convergence of the sequence of iterations. This method, known as the direct iteration method, converged very slowly however since a small film thickness would give rise to high pressures which in turn gave rise to large distortions which resulted in a large film thickness. The corresponding pressures would be small, which would again lead to small film thicknesses. The sequence of iterations would either be very slow to converge or would diverge. To achieve a more rapid convergence and to stop the sequence of iterations from diverging the film thickness calculated for the current

iterative step was averaged with the film thickness at the previous iteration to prevent a large change in the film profile. The new film thickness, h_{new} was therefore given by

$$h_{new} = w_f h_i + (1-w_f) h_{i-1} \tag{6.1}$$

where h_i is the film thickness for the current iteration calculated using the pressures from the previous iteration, h_{i-1} is the film thickness from the previous iteration and w_f is the under-relaxation factor. Equation (6.1) is the basic equation for under-relaxation, the value of w_f being less than 1. Taylor and O'Callaghan found that the rate of convergence of the iterations was very dependant upon the choice of w_f, a value of 0.25 produced a well converged solution for this particular example. The effect of incorporating elasticity in the analysis was to reduce the minimum film thickness and reduce the peak film pressure.

Stafford et al [38] used the under-relaxation method to couple a finite element structural and lubrication analysis for the steady state performance of a pad bearing and a journal bearing. They reported an improvement in the under-relaxation scheme by applying under-relaxation to the nodal pressures instead of the film thickness. For both the pad and journal bearings a two dimensional structural model was used. For the pad bearing they found that there was an optimum value for the weighting factor of 0.58. For the journal bearing, however, it was found that the optimum value for the weighting factor depended upon the journal eccentricity and this relationship was roughly approximated to a straight line to improve the convergence. Results were obtained for eccentricities up to a value of 0.8. Above this value it was necessary to start the iterative process from a lower eccentricity and increase the eccentricity in increments until the required value was reached to ensure convergence of the iterative process. This method was stable for eccentricites up to 1.3. It was also found that as the eccentricity was increased a distinctive bimodal pressure distribution was obtained due to the large housing deformations. In addition to decreasing the minimum film thickness and the peak pressure the region of positive pressure also increased for the journal bearing example due to the elasticity effects. Bozaci et al [39] also used a two dimensional finite element structural model to model the big-end of a connecting rod bearing and used the finite difference method for the lubrication analysis. To simplify the analysis the

assumption was made that the housing deflections were invariant in the axial direction and were calculated using the average pressure in the axial direction. Under-relaxation was applied to the values for the nodal film thickness and a method was developed to automatically adjust the under-relaxation factor to ensure convergence. Initially the weighting factor was calculated by limiting the maximum change in the film thickness to half the minimum film thickness at the first iteration. Values as low as 0.001 were obtained in some cases. This value was then used for all the subsequent iterations until the change in the pressure between iterations was less than 10%. The value of the weighting factor was then increased by a factor of 10 with a maximum value of 0.1 and the process continued until convergence was reached. Although this method did not ensure that an optimum value for the weighting factor had been obtained it did appear to ensure convergence. The results obtained were compared with experimental results and it was found that the assumption that the deflections were invariant in the axial direction was inadequate in most cases although possibly being acceptable if the L/D ratio of the bearing was less than 0.25. It was also concluded that a more realistic model of the bearing was required. Again they observed a distinct double peak in the pressure distribution under heavy loading for both the experimental and theoretical results.

A similar study was presented by Frene et al [40] again using the finite difference method to model the lubricant film, a two dimensional structural model for the big-end bearing and under-relaxation to couple the structural and lubrication analysis. The displacements were also assumed to be invariant in the axial direction. The experimental results presented showed satisfactory agreement in general trends with the theoretical model. The authors stated that the assumption that the displacements were invariant in the axial direction was justified since the variation of the housing deformations in the axial direction was only of the order of $2\mu m$ compared with the circumferential variation of $40\mu m$.

Eugene et al [41] presented further experimental results for both real and idealised connecting rod bearings and compared these to the results obtained from the previous theoretical model [40]. In this work the effect of varying the bolt tension in the connecting rod was also investigated experimentally and shown to have a negligible effect upon the bearing performance.

Fantino et al [42] presented extensive results for the steady state performance of a connecting rod bearing, including piezoviscous effects, using a two-dimensional finite difference mesh for the lubrication analysis and a two-dimensional structural finite element model. Once again the axial variation of the housing deformations was neglected. The effect of piezoviscosity was incorporated by solving for a modified pressure variable q related to the pressure p by

$$p = -\frac{1}{\alpha} Ln[1-\alpha q] \tag{6.2}$$

where α is the piezoviscous coefficient. In this analysis the under-relaxation was applied to the housing deformation h_{def} as

$$[h_{def}^{k+1}] = [h_{def}^{k}] + C_t \{[h_c^k] - [h_{def}^k]\} \tag{6.3}$$

where $[h_{def}^{k+1}]$ and $[h_{def}^{k}]$ are the column vectors of the nodal displacements used for the lubrication analysis at the iteration steps $k+1$ and k respectively and $[h_c^k]$ is the column vector of the displacements calculated from the structural part of the anlaysis using the pressures calculated at step k. The coefficient C_t was given by the empirical relationship

$$C_t = a + bk + ck^2 \tag{6.4}$$

where the value of a depends upon the loading on the bearing and the bearing dimensions, and b and c are constants. The sequence of iterations using this method converged in about 20-50 cycles, depending upon the loading and the analysis provided some interesting results. Under high loading more than two pressure peaks were observed, and if the bearing was made very flexible undesirable effects, such as large regions of film rupture, and sharp pressure peaks, resulted. It was also observed that under fairly high loading large regions of small film thickness occurred. The piezoviscous effects were only found to be significant under high loading and then proved to be secondary to the elasticity effects. It was also noted that the authors considered this method to be too time consuming for a transient analysis. In a discussion to this paper Rohde [42] noted that the large number of pressure peaks reported were a result of the numericalscheme used, and that in theory there should normally be two, or at most three, pressure peaks. In a further discussion to this paper F. Martin of the Glacier Metal Co. [42] noted that the large

regions of small film thicknesss were in agreement with experimental findings.

All of this work had been for steadily loaded bearings but, as Booker [42] pointed out, the steady state analysis of a connecting rod was a contradiction in terms. Results for the behaviour of an elastically deformed connecting rod bearing under dynamic loading were presented by Fantino et al [43] using a two dimensional finite element model for the connecting rod. In this case to reduce the amount of computing time and to simplify the analysis an analytical solution was used for the lubrication part of the analysis using the short bearing theory. The authors stated that since the L/D ratio of the bearing was 0.4 this assumption was justified. As mentioned in Chapter 2, however, it is generally believed that the short bearing theory is only applicable to bearings with an L/D ratio of less than 0.25. An under-relaxation technique was used to modify the film thickness between iterations but no details of how this was implemented were given. The authors noted that convergence of the under-relaxation process was more rapid for the dynamic problem than for the steady state problem due to the presence of the squeeze term and, since a small time step was used, the results from the previous time step provided a good initial estimate for the current time step. The general trends noted for the steady state problem also appear to apply to the dynamic problem and eccentricities of up to 3.8 were obtained. The required computing time was extremely high, however, even when using such a simplified model due to the number of iterations required for the analysis. Fantino and Frene [44] later used this method to compare the performance of a connecting rod bearing in a petrol and a diesel engine.

LaBouff and Booker [45] presented a general model for the analysis of both rigid and elastically deformed bearings under dynamic loading. A two-dimensional finite element mesh was used for the lubrication analysis and the structural information was supplied in the form of a compliance matrix, provision being made for both two- and three-dimensional structural models. Under-relaxation was applied to the nodal values for the housing deformations. The under-relaxation weighting factor was determined by limiting the maximum change in the film thickness during the under-relaxation process to a specified fraction of the of the nodal deflections at the previous time step. To further improve the initial estimate at each time step the deflections were estimated by using a linear extrapolation of the deflection changes at the previous time steps. It was, however, not possible to obtain results for a full

engine cycle for the elastically deformed bearing since the computing time would have been approximately four to five times that required for the rigid bearing analysis which was itself in the region of eleven hours.

The advantage with using the under-relaxation method to couple the structural and lubrication analysis in the EHD lubrication problem is its simplicity and the ease with which it can be incoporated into existing software for the rigid bearing problem. From the work surveyed, however, there does not seem to be a general method for ensuring that the optimum value of under-relaxation weighting factor is used, especially for the dynamic loading problem. The methods that have been employed seem somewhat arbitrary, and do not gaurantee convergence.

In this chapter an investigation is carried out into the way in which the under-relaxation method could be incorporated into the existing computer code for the rigid bearing problem. Several different methods for applying the under-relaxation to the problem are presented and several convergence improvement schemes are also presented.

6.2 Steady state analysis

The advantage with using the under-relaxation method to incorporate the bearing flexibility into the bearing problem is its simplicity, and the relative ease with which it can be incorporated into the existing software for the rigid bearing problem. The finite element formulation for the lubrication equations is identical to that used for the rigid bearing problem. The only quantity that is directly altered is the nodal film thickness. Referring to Equation (5.2) the film thickness, h_i, at a node i is given by

$$h_i = c - e_x \cos\theta_i - e_y \sin\theta_i + [C_i]\{p\} \tag{6.5}$$

As described in Chapter 5 the structural part of the analysis is supplied in the form of a structural compliance matrix $[C]$ which relates the housing deformations to the nodal pressures $\{p\}$ and need only be evaluated once for a complete analysis. The structural model used was three-dimensional since it is difficult to use a two dimensional model with the 8-node isoparametric elements that are used to model the lubricant film due to the way in which the equivalent nodal point forces are evaluated for this particular element. However, as mentioned above, previous work suggests that a three-dimensional model will give a much more realistic representation of the bearing housing. Much of the previous work in this field has been based on the simplifying assumption that the housing deflections are invariant in the axial direction. This assumption was said to be justified since, in some of the bearings considered, the displacements in the axial direction only varied by $2\mu m$ compared with a variation of $40\mu m$ in the circumferential direction. On investigating this it was indeed found that the axial variation was only about 5% of the variation in the circumferential direction. It was, however, also found that the largest variations in the film thickness occured in the region of minimum film thickness where the oil film is only a few microns thick. A small variation in the axial deflections therefore could cause the actual film thickness to vary by 100% or more in the axial direction. It follows that using a two-dimensional model for the structural analysis, although considerably simplifying the analysis, was not justified, especially under heavy loading.

To calculate the nodal deflections the column matrix of nodal pressures, $\{p\}$ was multiplied by the compliance matrix $[C]$ to obtain the column vector of the

housing deformations, $\{h_{def}\}$. That is

$$[C]\{p\} = \{h_{def}\} \tag{6.6}$$

This part of the analysis was relatively time consuming, since using standard multiplication methods each row of $[C]$ is multiplied by $\{p\}$ to obtain the corresponding term in $\{h_{def}\}$. Due to film rupture and boundary conditions as much as half of the matrix $\{p\}$ contains zero terms. This meant that a large number of redundant calculations were carried out while evaluating $\{h_{def}\}$. To eliminate these redundant calculations, and so make the process more efficient, a method called simultaneous column multiplication [65] was used. Figure 6.1 shows diagramatically the two different multiplication schemes. The standard multiplication scheme proceeds a row at a time through $[C]$ to evaluate the corresponding term in $\{h_{def}\}$ where k is the multiplication step. Using simultaneous column multiplication each element in the kth column of $[C]$ is multiplied by the kth element in $\{p\}$ to obtain all the contributions from that particular term to the right hand side. These contributions are simply summed to the previous values of $\{h_{def}\}$. The advantage with this scheme is that each time a zero term is encountered in $\{p\}$ a complete multiplication cycle may be skipped. This reduced the computing time by more than 40%.

Once the nodal displcements were calculated the nodal film thicknesses were obtained using (6.5). To couple the lubrication and structural analysis under-relaxation was carried out using

$$[h_{k+1}]' = w_f [h_{k+1}]+(1-w_f)[h_k] \tag{6.7}$$

where k denotes the iteration step, $[h_k]$ is the column matrix of the film thicknesses form the previous iteration step, $[h_{k+1}]$ is the column matrix of the nodal film thicknesses calculated from (6.5) and $[h_{k+1}]'$ are the values after under-relaxation to be used for the next iteration. For the steady state analysis the loading was applied to the cap half of the bearing at 180 degrees to the connecting rod axis which was the most flexible part of the housing. The solution procedure was identical to that used for the rigid bearing problem except there was an extra iteration loop to compute the distorted bearing shape using the under-relaxation method. The sequence of iterations was said to be converged if

$$\frac{\sum_{i=1}^{n} |p_{k+1}-p_k|}{\sum_{i=1}^{n} |p_{k+1}|} \leq z_p \tag{6.8}$$

and

$$\frac{\sum_{i=1}^{n} |h_{k+1}-h_k|}{\sum_{i=1}^{n} |h_{k+1}|} \leq z_h \tag{6.9}$$

where n is the number of nodal points in the lubricant mesh, k is the iteration step, z_p and z_h are the prescribed tolerances, in this case each equal to .001. Decreasing the tolerance beyond this point made little difference to the resulting bearing shape and greatly increased the computing time. It was however found that if too small a value of w_f was used the rate of convergence of the sequence of iterations was so slow that the given tolerances were reached before the iterative process had in fact converged. Care, therefore, had to be taken in choosing the weighting factor to ensure sufficient change in the nodal values to allow the sequence of iterations to continue. For the steady state problem under-relaxation was applied to the film thickness, pressure distribution or to both. Figures 6.2-6.4 show the number of iterations as a function of w_f for eccentricities from 0.2 (low loading) to 0.9 (high loading). It is clear that the best results are obtained when under-relaxation is applied to both the pressure distribution and the film thickness. As the eccentricity, and hence the loading, is increased the number of iterations increase, the optimum value of the weighting factor decreases and the process becomes more sensitive to the choice of weighting factor.

For eccentricities of greater than 0.9 the iterative process was started using a lower value of eccentricity and this value gradually increased until the required eccentricity was attained. For high loading it was found that due to the large bearing deformations occurring in the housing negative values of film thickness occurred during the sequence of iterations. This could have a disastrous effect on the convergence of the solution and a restriction was, therefore, placed upon the film thickness values to prevent this. It was found that it was sufficient to redefine

any negative values that occurred to one half of their pr value and using this solution scheme eccentricities of up to 1.2 were obtained took a large amount of computing time due to the large number of iterations r d at each step and it was found that to ensure convergence the eccentricity had to be increased in small increments of about 0.05, and a very small weighting factor had to be used.

For the dynamically loaded bearing problem the load is constantly changing and therefore the weighting factor must be adjusted to ensure that convergence is achieved. Too high a value and the sequence of iterations will become divergent and too low a value and the rate of convergence will be too slow. Some method therefore had to be adopted before attempting to look at dynamic loading to adjust the weighting factor to ensure convergence of the sequence of iterations. Although Fantino et al [42] had developed an empirical formula for determining the weighting factor this only applied to a particular bearing and had only been used for the steady-load case. It was, therefore, important that the method used should be as general as possible. From the previous work for the steady state performance of the bearing it appears that the best method of employing under-relaxation is to apply it to both the nodal pressures and film thicknesses. The most obvious method of adjusting the weighting factor was to allow the film thickness to vary by only a certain amount between iterations and similarily for the pressure. Initially the maximum allowable change in the film thickness was limited to a certain percentage of the radial clearance c and the pressure variation was fixed to a percentage of the peak pressure at the previous iteration. An upper limit was also set for the maximum allowable value of the weighting factor and erring on the side of caution this was set to 0.1. This method, however, proved unsatisfactory since for high ecccentricities when the film thickness was small, even a very slight change in the film thickness would greatly alter the pressure distribution so the percentage of c that was used had to be very small. This, however, meant that at medium eccentricities the rate of convergence became very low. A better method for adjusting the weighting factor was to limit the maximum change in the film thickness between iterations to a specified fractiion of the minimum film thickness at the previous iteration. This, of course, meant that under heavy loading the weighting factor was very small and for low loading with a large film thickness the weighting factor increased which ensured a good rate of convergence.

6.3 Dynamic loading

The next step in the analysis was to apply the under-relaxation method to the dynamically loaded problem. The method was identical to that used for the rigid bearing problem except that there was an extra iterative loop for the EHD part of the analysis to calculate the required bearing deformation. The analysis was started using the steady state rigid bearing shape to get the initial starting value for the film thickness. Once the correct bearing deformation was calculated the load was applied as a ramp input over the first ten steps of the cycle to 'start' the bearing, after which the correct bearing load was applied. The methods described in Chapter 4 for finding the journal position were used with the required bearing deformation calculated at each iterative step. A time step size of one degree of crank rotation was used so that the results for the oil film pressure and bearing deformation for the previous step would provide a good starting point for the iterations at the next time step.

Initial attempts were unsuccessful. For the steady loaded case a high loading corresponded to a small film thickness. For the dynamically loaded case when the load is moving rapidly over part of the cycle, causing the journal to move rapidly across the clearance space, regions of high loading can correspond to relatively large film thicknesses. Conversely, regions of low loading could correspond to regions of small film thicknesses if the previous film thickness had been small since the squeeze effect would stop the bearing from moving rapidly to adjust to the low loading. Therefore even if the change in film thickness is limited to a small percentage of the minimum film thickness at the previous step this can still allow sufficient deformations to occur for highly loaded cases to allow the solution to oscillate. Using too small a value for the weighting factor although ensuring convergence over these parts of the cycle meant that for light loading the rate of convergence was too slow. Some other method had to be found to improve the convergence. On examining the pressure variation between time steps it was found that a much better estimate for the pressure distribution at the next time step could be obtained by altering the pressure distribution as

$$p_{k+1} = p_k \frac{W_{k+1}}{W_k} \tag{6.10}$$

where W_{k+1} is the load applied at time step $k+1$ and W_k is the load applied at time

step k, $\{p_k\}$ is the pressure distribution at the end of time step k and $\{p_{k+1}\}$ is the initial estimate for the pressure distribution at time step $k+1$. It was also found that a better estimate for the film shape could be obtained by carrying out the same procedure for the nodal film deformations as

$$h_{def}^{k+1} = h_{def}^{k} \frac{W_{k+1}}{W_k} \tag{6.11}$$

This method then meant that the initial estimate for the pressures and the film shape were in general much better at each time step. Again the problem with this method was that it did not take into account the movement of the load vector applied to the system. this method did result in a better performance but it still did not gaurantee convergence of the iterations for the film shape and the computing time was extremely high due to the large number of iterations required, especially since it was impossible to gaurantee that the optimum value of the weighting factor had been found. Also a very small time step had to be used so that the change in load from step to step was not too great. It was therefore found that using this method it was not possible to produce results for a complete dynamic cycle.

6.4 Conclusions

The under-relaxation method provides a simple technique for coupling the structural and the lubrication analysis for analysing the EHD behaviour of a journal bearing. The advantage with this method is its simplicity and the ease with which it may be incorporated into an existing analysis for the rigid bearing problem. Although it is possible to obtain results for the steady loaded problem for a wide range of eccentricities it is difficult to use this method for the dynamically loaded bearing problem. The main problem lies in finding a way to automatically adjust the under-relaxation factor to ensure that a converged solution is obtained. Even if this is possible it is difficult to find the optimum value to sufficiently reduce the required number of iterations. A wide variety of schemes have been proposed by other authors for adjusting the weighting factor but they appear quite arbitrary and do not gaurantee that an optimum value has been obtained or that convergence will be obtained. Schemes, such as that proposed by Fantino et al [42], appear to work fairly well for a particular bearing, but in this work a more general approach was required. It was, therefore, concluded that the under-relaxation method was not practical for use in analysing the EHD performance of a dynamically loaded bearing.

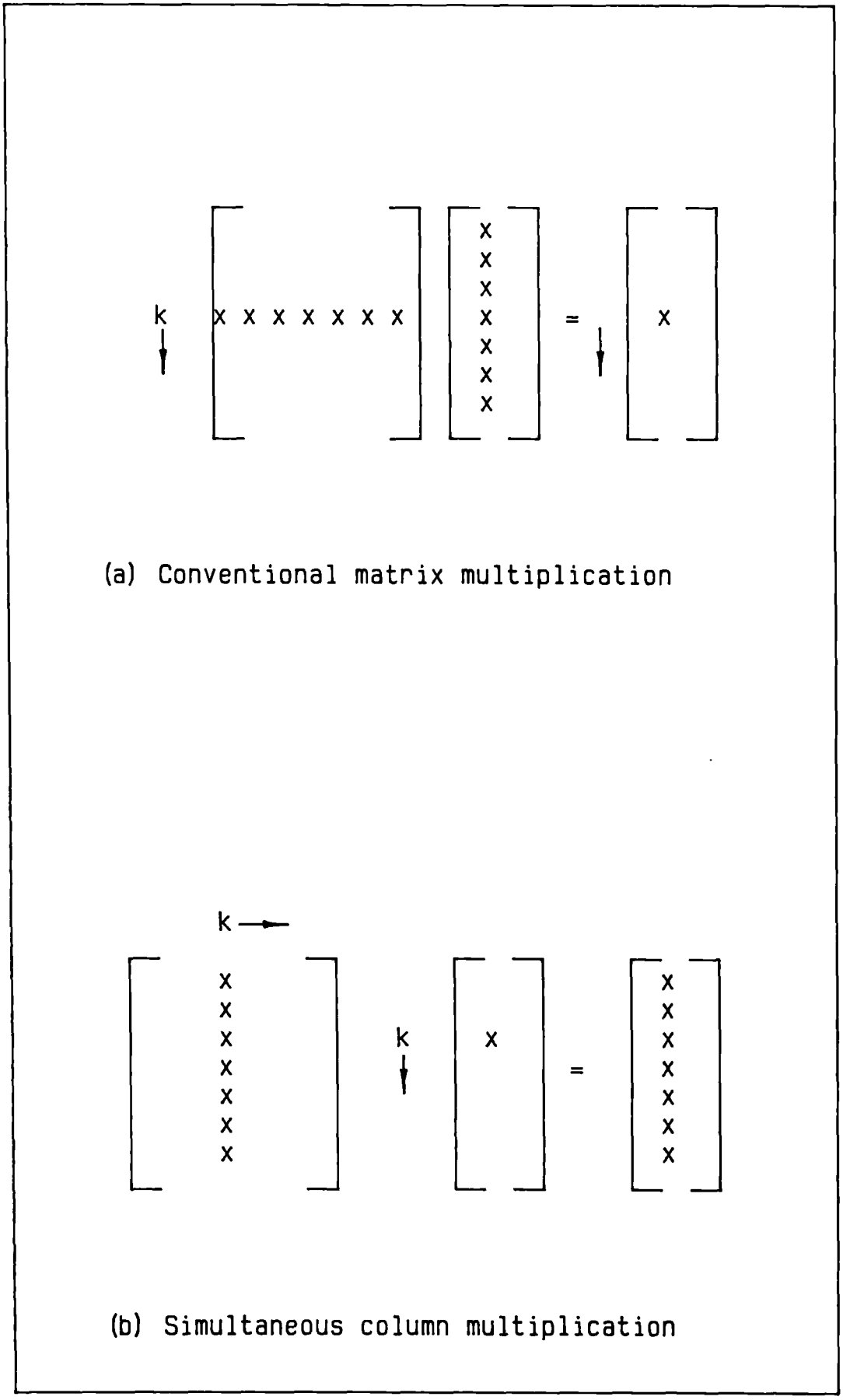

(a) Conventional matrix multiplication

(b) Simultaneous column multiplication

Figure 6.1 Schematic representation of (a) conventional and (b) simultaneous column multiplication

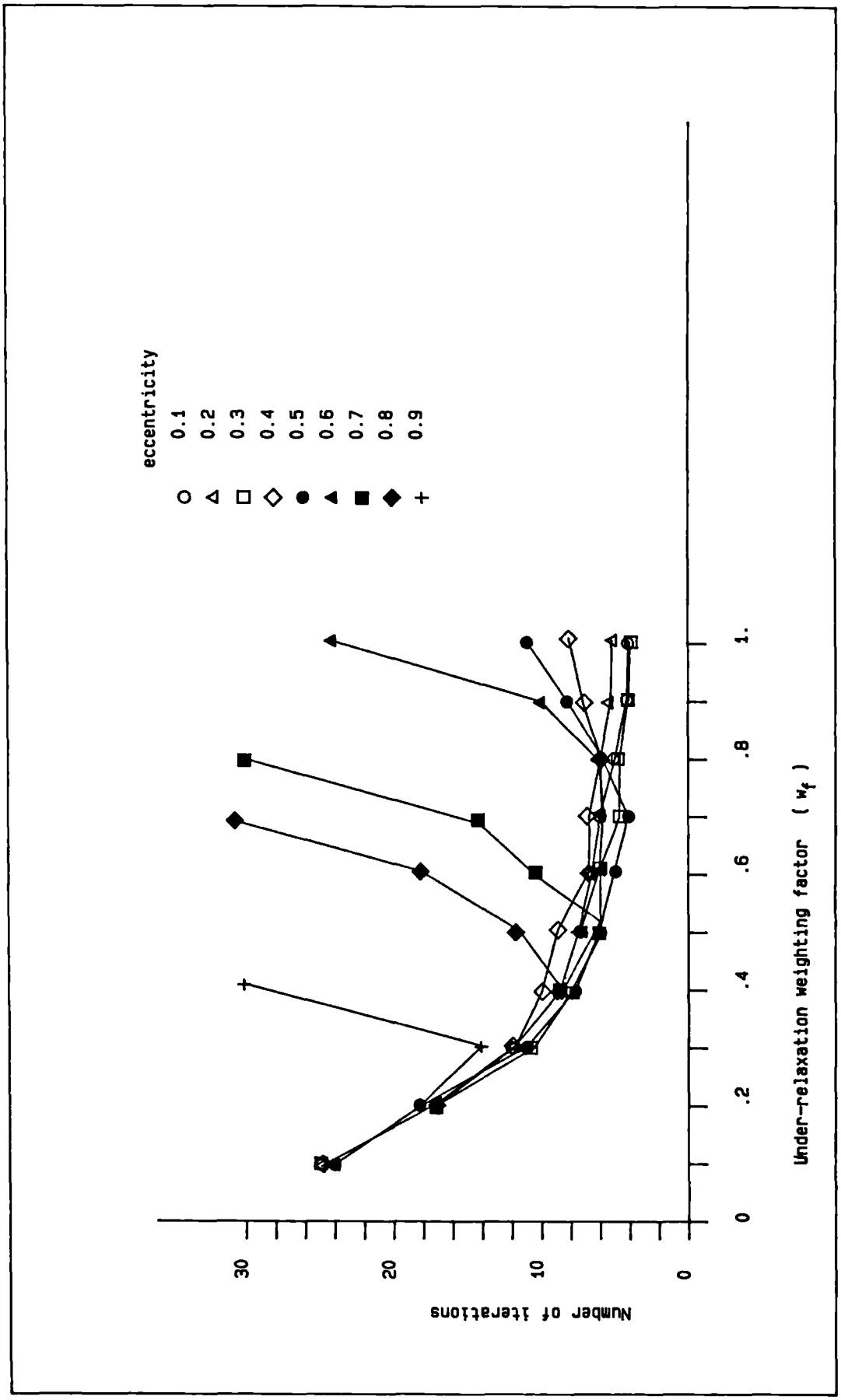

Figure 6.2 - Applying under-relaxation to the film thickness.

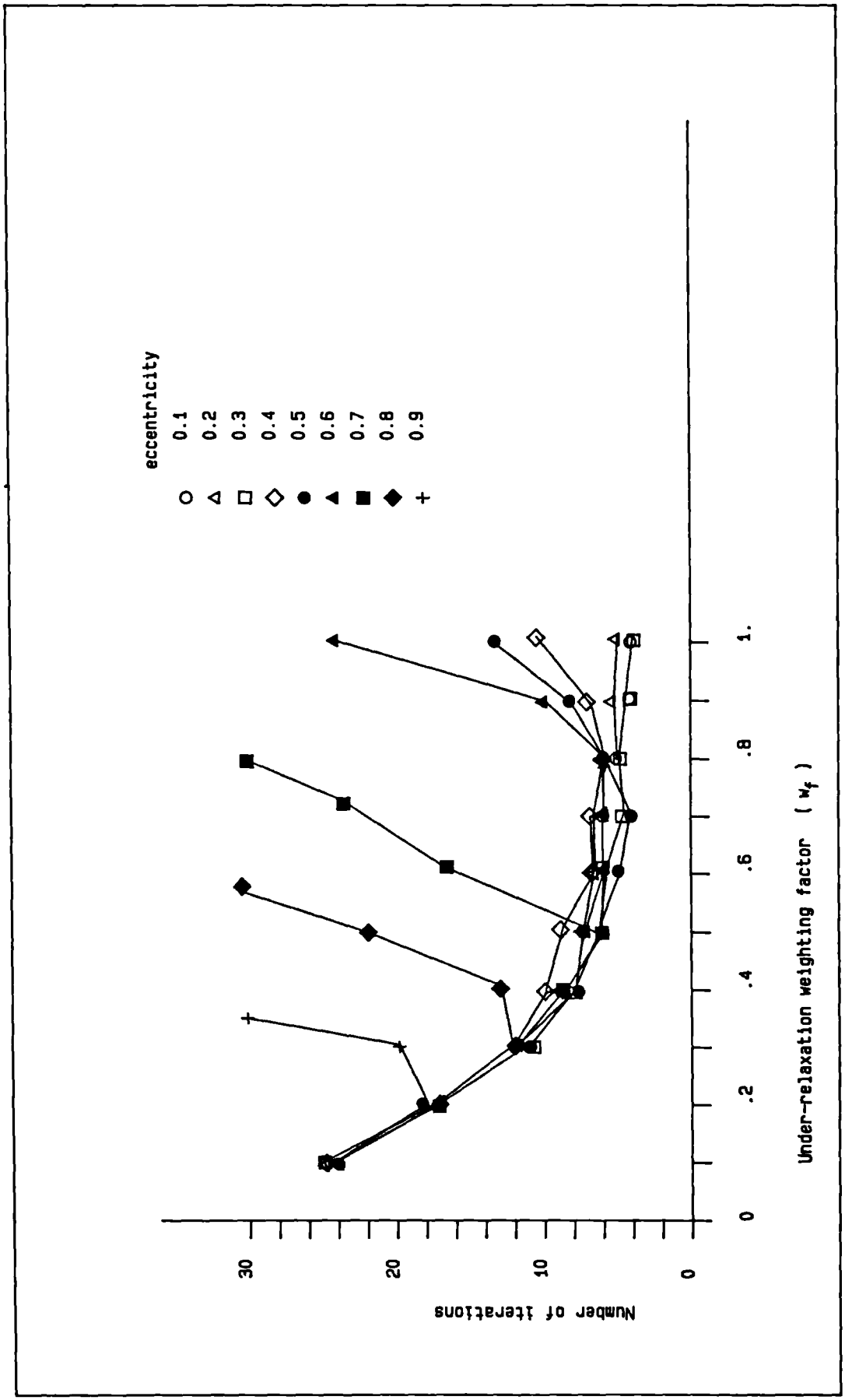

Figure 6.3 - Applying under-relaxation to the pressure.

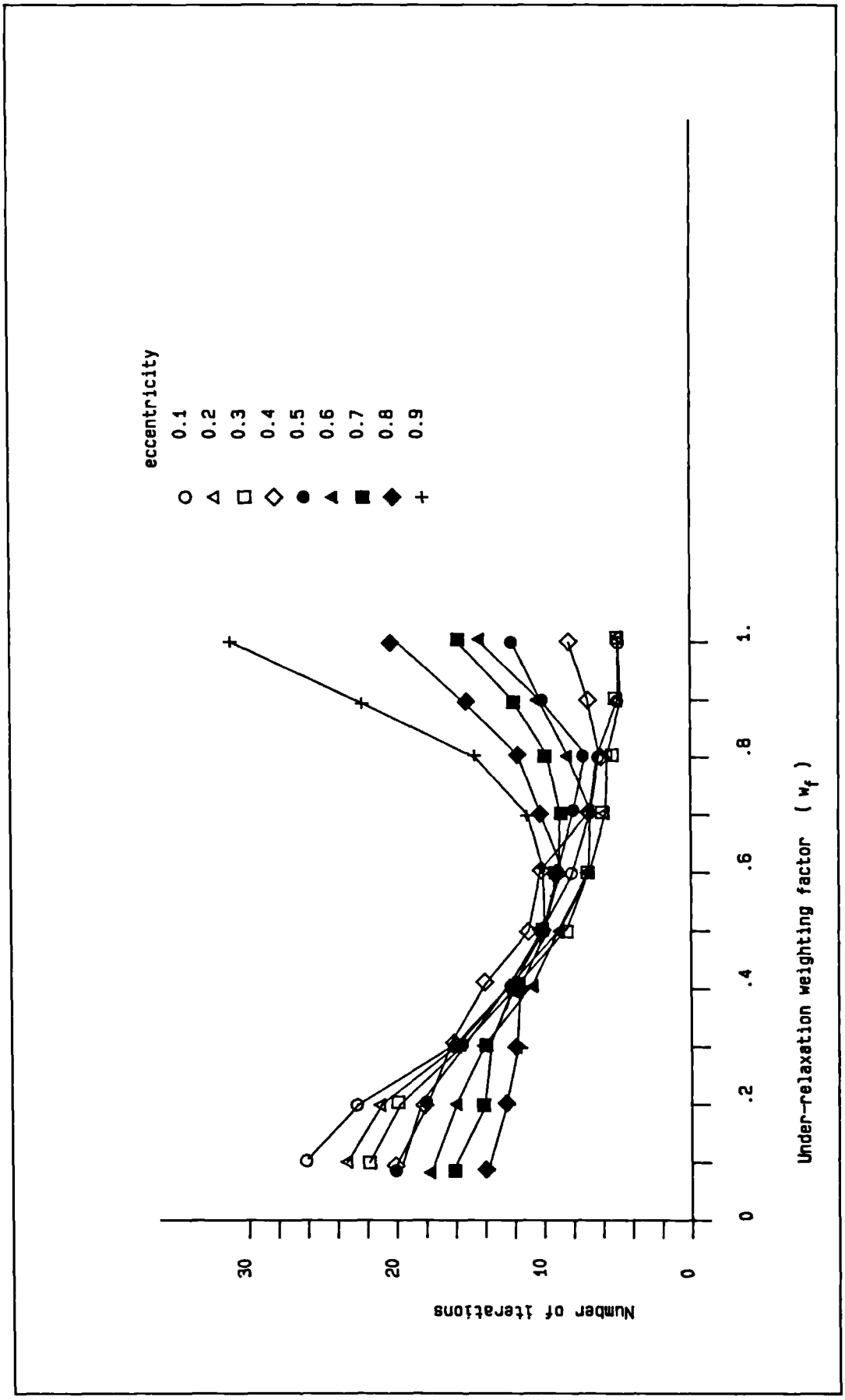

Figure 6.4 - Applying under-relaxation to the film thickness and pressure

Chapter 7

The Newton-Raphson Solution Method

7.1 Introduction

The under-relaxation solution method described in the previous chapter is one of two methods generally used for coupling the lubrication and structural analysis in the EHD lubrication problem. The second of these is the Newton-Raphson method, first used by Rohde and Oh [46] to solve the steady state EHD lubrication problem. Finite elements were used to model the oil film and results were presented for slider and roller bearings. They found that the method was highly convergent for both thick and thin film problems, an accurate solution being obtained in about 5 iterations. Higher order elements were used to model the lubricant film, Rohde and Oh suggested that linear elements might cause convergence problems for this particular problem. Using the Newton-Raphson method, however, the cavitation region, if it exists, must be defined a priori. A scheme such as that used by Christopherson [8], where the cavitation region is located during the solution process, is not possible. Rohde and Oh proposed an alternative scheme for locating the cavitation region which was expanded upon by Oh [66] who solved the EHD lubrication problem using the Newton-Raphson formulation as a nonlinear complementarity problem using an algorithm proposed by Murty [67]. This method was implemented by making an initial estimate for the cavitated region. The resulting set of Newton-Raphson equations was assembled for the complete film using the finite element method. A check was then carried out for all the nodes in the cavititated and non-cavitated regions to determine whether certain conditions had been satisfied. If so the cavititation region had been found, if not the cavitation region was adjusted and the process repeated.Oh and Goenka [47] further extended this analysis to predict the performance of a dynamically loaded journal bearing. This method proved highly convergent and robust but, due to the large number of calculations involved, the required computing time was approximately 35 hours. This clearly means that the method is impractical as a general design tool and in an effort to reduce this time Goenka and Oh [48] proposed a solution for the problem based upon the short bearing theory assuming a parabolic pressure distribution in the axial direction. This

method was approximately an order of magnitude faster than the previous method although there were discrepancies in the results obtained using the two methods, especially for the value of the minimum film thickness. The assumption that the pressure distribution is parabolic in the axial direction, although being fairly accurate for the rigid bearing case, does not hold for the elastic case, especially under heavy loading when the housing deformations are quite significant. Goenka and Oh [49] did, however, show that this simplified method was useful for optimising the design of a connecting rod at the early design stages using the more rigorous method for the final stages.

In this chapter the formulation of the Newton-Raphson solution method is presented for predicting the performance of a dynamically loaded journal bearing. This solution method is then highly modified to produce a solution method that is more than two orders of magnitude faster than the method developed at General Motors. Once again higher-order finite elements are used for the structural and lubrication analysis. Results are presented for the Ruston and Hornsby 6VEB Mk III marine diesel big end bearing.

7.2 Equation derivation

7.2.1 The Newton-Raphson method

Consider the Taylors series expansion of a function $f(x)$

$$f(x+\delta) = f(x)+\delta f'(x)+\frac{\delta^2}{2!}f''(x)+\frac{\delta^3}{3!}f'''(x)+\cdots \tag{7.1}$$

where $f(x+\delta)$ is the value of the function if x is changed by a small amount δ. Assume a solution is required for $f(x) = 0$. If an initial estimate is made for x as x_i then the Taylor series expansioin of f may be written as

$$f(x) = f(x_i)+\delta f'(x_i)+\frac{\delta^2}{2!}f''(x_i)+\frac{\delta^3}{3!}f'''(x_i)+\cdots \tag{7.2}$$

Ignoring terms in δ^2 and higher and setting $f(x) = 0$ (7.2) becomes

$$0 = f(x_i)+\delta f'(x_i) \tag{7.3}$$

Therefore the required correction, δ, to the initial estimate, x_i, is given by

$$\delta = -f(x_i)/f'(x_i) \tag{7.4}$$

This process is then repeated until $f(x_i) = f(x) = 0$.

Suppose that instead there are n functions in n unknowns, $f_i(x_1, x_2, \ldots, x_n) = 0$, $i = 1,2,..n$ The Newton-Raphson method can be used to solve these by writing the n functions in matrix form [68] as

$$\begin{bmatrix} \frac{\partial f_1}{\partial x_1} & \frac{\partial f_1}{\partial x_2} & \cdots & \cdots & \cdots \\ \vdots & \vdots & & & \\ \vdots & \vdots & & & \\ \vdots & & & & \vdots \\ \cdots & & \cdots & \frac{\partial f_n}{\partial x_{n-1}} & \frac{\partial f_n}{\partial x_n} \end{bmatrix} \begin{Bmatrix} \delta_1 \\ \vdots \\ \vdots \\ \vdots \\ \delta_n \end{Bmatrix} = \begin{Bmatrix} f_1 \\ \vdots \\ \vdots \\ \vdots \\ f_n \end{Bmatrix} \tag{7.5}$$

and solving them as a set of simultaneous equations to obtain the required corrections $\{\delta\}$.

7.2.2 Application to the lubrication problem

For the lubrication problem the governing equation is the two-dimensional Reynolds equation which may be written in polar coordinates as

$$f_1 = \nabla(h^3\nabla p) - 6\mu\left(u\frac{\partial h}{r\partial\theta} + 2\frac{\partial h}{\partial t}\right) = 0 \tag{7.6}$$

In the EHD lubrication problem the film thickness, h, is made up of two components: one due to the journal position relative to the housing, the second due to the housing distortion caused by the pressure distribution generated in the lubricant film. Thus

$$h = h_o + Lp = c - e_x\cos\theta - e_y\sin\theta + Lp \tag{7.7}$$

where h_o is the component due to the journal position, e_x and e_y are the x and y components of the journal eccentricity, L is an integral operator relating the pressure distribution p to the housing distortion. The journal eccentricity components e_x and e_y are also unknowns in the problem so the equations

$$f_2 = \int_A p\cos\theta R dA - w_x = 0 \tag{7.8}$$

$$f_3 = \int_A p\sin\theta R dA - w_y = 0 \tag{7.9}$$

which ensure the equilibrium of the calculated pressures and the applied load, must be included in the analysis. These equations give rise to a set of highly non-linear equations in p, e_x and e_y .

Let $p^{(r)}$, $e_x^{(r)}$, $e_y^{(r)}$ denote the rth trial solution for the problem, and $f_i^{(r)}$ denote the corresponding values of the function f_i. In the Newton-Raphson method the $(r+1)th$ trial solution is written as

$$\begin{aligned} p^{(r+1)} &= p^{(r)} + \delta p^{(r)} \\ e_x^{(r+1)} &= e_x^{(r)} + \delta e_x^{(r)} \\ e_y^{(r+1)} &= e_y^{(r)} + \delta e_y^{(r)} \end{aligned} \tag{7.10}$$

and the corrections $\delta p^{(r)}$, $\delta e_x^{(r)}$, $\delta e_y^{(r)}$ are found by using the first order Taylor series expansions of the functions $f_i^{(r+1)}$ given by

$$f_i^{(r+1)} = f_i^{(r)} + \left[\frac{\partial f_i}{\partial p}\right]^{(r)} \delta p^{(r)} + \left[\frac{\partial f_i}{\partial e_x}\right]^{(r)} \delta e_x^{(r)} + \left[\frac{\partial f_i}{\partial e_y}\right]^{(r)} \delta e_y^{(r)} \qquad (7.11)$$

where the partial derivatives are evaluated for the *rth* trial solution. The solution requires that $f_i = 0$ and by setting the left-hand sides equal to zero equation (7.11) may be written in matrix form as

$$\begin{Bmatrix} f_1^{(r)} \\ f_2^{(r)} \\ f_3^{(r)} \end{Bmatrix} + \begin{bmatrix} \left[\frac{\partial f_1}{\partial p}\right]^{(r)} & \left[\frac{\partial f_1}{\partial e_x}\right]^{(r)} & \left[\frac{\partial f_1}{\partial e_y}\right]^{(r)} \\ \left[\frac{\partial f_2}{\partial p}\right]^{(r)} & \left[\frac{\partial f_2}{\partial e_x}\right]^{(r)} & \left[\frac{\partial f_2}{\partial e_y}\right]^{(r)} \\ \left[\frac{\partial f_3}{\partial p}\right]^{(r)} & \left[\frac{\partial f_3}{\partial e_x}\right]^{(r)} & \left[\frac{\partial f_3}{\partial e_y}\right]^{(r)} \end{bmatrix} \begin{Bmatrix} \delta p^{(r)} \\ \delta e_x^{(r)} \\ \delta e_y^{(r)} \end{Bmatrix} = 0 \qquad (7.12)$$

to obtain the corrections to the *rth* trial solution. To evaluate this the derivatives of f_1, f_2, and f_3 with respect to p, e_x, e_y must be found. These may be approximated by using the appropriate Taylor series expansion of each function about a point. The Taylor series expansion of f_1 about a point p, e_x, e_y, to obtain the derivative $\partial f_1/\partial p$, is given as

$$f_1(p+\delta p, e_x, e_y) = f_1(p, e_x, e_y) + \delta p \frac{\partial f_1}{\partial p}(p, e_x, e_y) \qquad (7.13)$$

$$f_1(p+\delta p, e_x, e_y) = \nabla(h^3 \nabla(p+\delta p)) - 6\mu\left(u\frac{\partial h}{r\partial\theta} + 2\frac{\partial h}{\partial t}\right) = 0$$

Substituting (7.7) into this gives

$$f_1(p+\delta p, e_x, e_y) = \nabla((h_o+C(p+\delta p))^3\nabla(p+\delta p))$$

$$-6\mu(u\frac{\delta(h_o+C(p+\delta p))}{r\partial\theta}+2\frac{\partial(h_o+C(p+\delta p))}{\partial t})$$

$$= \nabla((h_o^3+3h_o^2C(p+\delta p)+3h_oC^2(p^2+2p\,\delta p+\delta p^2)+C^3(p^3+3p^2\delta p+3p\,\delta p^2+\delta p^3))\nabla(p+\delta p))$$

$$-6\mu(u\frac{\partial(h_o+C(p+\delta p))}{r\partial\theta}+2\frac{\partial(h_o+C(p+\delta p))}{\partial t})$$

Ignoring terms in δp^2 and higher this becomes

$$= \nabla((h_o^3+3h_o^2C(p+\delta p)+3h_oC^2(p^2+2p\,\delta p)+C^3(p^3+3p^2\delta p))\nabla(p+\delta p))$$

$$-6\mu(u\frac{\partial(h_o+C(p+\delta p))}{r\partial\theta}+2\frac{\partial(h_o+C(p+\delta p))}{\partial t})$$

$$= f_1(p, e_x, e_y)+\nabla(3h^2C\,\delta p\,\nabla p)+\nabla(h^3\nabla\delta p)-6\mu(\frac{u}{r}\frac{\partial(C\,\delta p)}{\partial\theta}+2\frac{\partial(C\,\delta p)}{\partial t})$$

therfore

$$\delta p\frac{\partial f_1}{\partial p} = \nabla(3h^2C\,\delta p\,\nabla p)+\nabla(h^3\nabla\delta p)-6\mu(\frac{u}{r}\frac{\partial(C\,\delta p)}{\partial\theta}+2\frac{\partial(C\,\delta p)}{\partial t}) \qquad (7.14)$$

Similarily to obtain $\partial f_1/\partial e_x$

$$f_1(p, e_x+\delta e_x, e_y) = f_1(p, e_x, e_y)+\delta e_x\frac{\partial f_1}{\partial e_x}(p, e_x, e_y) \qquad (7.15)$$

$$= \nabla(h-\delta e_x\cos\theta)^3\nabla p-6\mu(\frac{u}{r}\frac{\partial(h-\delta e_x\cos\theta)}{\partial\theta}+2\frac{\partial(h-\delta e_x\cos\theta)}{\partial t})$$

$$= \nabla(h^3-3h^2\delta e_x\cos\theta)^3\nabla p-6\mu(\frac{u}{r}\frac{\partial(h-\delta e_x\cos\theta)}{\partial\theta}+2\frac{\partial(h-\delta e_x\cos\theta)}{\partial t})$$

$$= f_1(p, e_x, e_y)-\nabla(3h^2\delta e_x\cos\theta\nabla p)-6\mu(\frac{u}{r}\delta e_x\sin\theta-2\frac{\partial(\delta e_x\cos\theta)}{\partial t})$$

therefore

$$\delta e_x\frac{\partial f_1}{\partial e_x} = -\nabla(3h^2\delta e_x\cos\theta\nabla p)-6\mu(\frac{u}{r}\delta e_x\sin\theta-2\frac{\partial(\delta e_x\cos\theta)}{\partial t}) \qquad (7.16)$$

Similarily

$$\delta e_y \frac{\partial f_1}{\partial e_y} = -\nabla(3h^2 \delta e_y \sin\theta \nabla p) + 6\mu\left(\frac{u}{r}\delta e_y \cos\theta + 2\frac{\partial(\delta e_y \sin\theta)}{\partial t}\right) \qquad (7.17)$$

This method may also be used to obtain the derivatives of f_2 and f_3 with respect to p.

$$f_2(p+\delta p, e_x, e_y) = \int_A (p+\delta p)\cos\theta R dA - wx = f_2(p, e_x, e_y) + \int_A \delta p \cos\theta R dA$$

therefore

$$\delta p \frac{\partial f_2}{\partial p} = \int_A \delta p \cos\theta dA \qquad (7.18)$$

and

$$\delta p \frac{\partial f_3}{\partial p} = \int_A \delta p \sin\theta dA \qquad (7.19)$$

The remaining derivitives are given by

$$\frac{\partial f_2}{\partial e_x} = \frac{\partial f_2}{\partial e_y} = \frac{\partial f_3}{\partial e_x} = \frac{\partial f_3}{\partial e_y} = 0 \qquad (7.20)$$

Equation (7.12) may be written in matrix form as

$$[A]\{X\} = \{R\} : \{X\} = \left\{\delta p \;\; \delta e_x \;\; \delta e_y\right\}^T \qquad (7.21)$$

To assemble these equations the finite element method is used to construct $n+2$ functions, f_i, where n is the number of nodal points in the lubrication mesh. Starting with the Newton-Raphson expression for f_1

$$\delta p \frac{\partial f_1}{\partial p} + \delta e_x \frac{\partial f_1}{\partial e_x} + \delta e_y \frac{\partial f_1}{\partial e_y} = -f_1 \qquad (7.22)$$

In dimensionless form (7.22) may be written as

$$\frac{\partial}{\partial\theta}\left[h^3\frac{\partial}{\partial\theta}\delta p\right]+B^2\frac{\partial}{\partial y}\left[h^3\frac{\partial}{\partial y}\delta p\right]+3\frac{\partial}{\partial\theta}\left[h^2L\,\delta p\frac{\partial p}{\partial\theta}\right]+3B^2\frac{\partial}{\partial y}\left[h^2L\,\delta p\frac{\partial p}{\partial y}\right]$$

$$-\frac{\partial\theta_r}{\partial\alpha}\frac{\partial(L\,\delta p)}{\partial\theta}-2\frac{\partial(L\,\delta p)}{\partial\alpha}-3\frac{\partial}{\partial\theta}\left[h^2\delta e_x\cos\theta\frac{\partial p}{\partial\theta}\right]-3B^2\frac{\partial}{\partial y}\left[h^2\delta e_x\cos\theta\frac{\partial p}{\partial y}\right]$$

$$-\frac{\partial\theta_r}{\partial\alpha}\delta e_x\sin\theta+2\frac{\partial(\delta e_x\cos\theta)}{\partial\alpha}-3\frac{\partial}{\partial\theta}\left[h^2\delta e_y\sin\theta\frac{\partial p}{\partial\theta}\right]-3B^2\frac{\partial}{\partial y}\left[h^2\delta e_y\cos\theta\frac{\partial p}{\partial y}\right]$$

$$+\frac{\partial\theta_r}{\partial\alpha}\delta e_y\cos\theta+2\frac{\partial(\delta e_y\sin\theta)}{\partial\alpha}=-\frac{\partial}{\partial\theta}\left[h^3\frac{\partial p}{\partial\theta}\right]-B^2\frac{\partial}{\partial y}\left[h^3\frac{\partial p}{\partial y}\right]$$

$$+\frac{\partial\theta_r}{\partial\alpha}\frac{\partial h}{\partial\theta}+2\frac{\partial h}{\partial\alpha} \tag{7.23}$$

using the same dimensionless quantities as used in Chapter 2. Applying Galerkins principle as before and using the Green-Gauss theorem (7.23) becomes

$$\int_{A^e}\left\{-\frac{\partial N^T}{\partial\theta}h^3\frac{\partial}{\partial\theta}(\delta p)-B^2\frac{\partial N^T}{\partial y}h^3\frac{\partial}{\partial y}(\delta p)-3\frac{\partial N^t}{\partial\theta}h^2L\,\delta p\frac{\partial p}{\partial\theta}-3B^2\frac{\partial N^T}{\partial y}h^2L\,\delta p\frac{\partial p}{\partial y}\right.$$

$$+\frac{\partial\theta_r}{\partial\alpha}\frac{\partial N^T}{\partial\theta}L\,\delta p-2N^T\frac{\partial(L\,\delta p)}{\partial\alpha}+3\frac{\partial N^T}{\partial\theta}h^2\delta e_x\cos\theta\frac{\partial p}{\partial\theta}+3B^2\frac{\partial N^T}{\partial y}h^2\delta e_x\cos\theta\frac{\partial p}{\partial y}$$

$$-N^T\frac{\partial\theta_r}{\partial\alpha}\delta e_x\sin\theta+2N^T\frac{\partial(\delta e_x\cos\theta)}{\partial\alpha}+3\frac{\partial N^T}{\partial\theta}h^2\delta e_y\sin\theta\frac{\partial p}{\partial\theta}+3B^2\frac{\partial N^T}{\partial y}h^2\delta e_y\sin\theta\frac{\partial p}{\partial y}$$

$$\left.+N^T\frac{\partial\theta_r}{\partial\alpha}\delta e_y\cos\theta+2N^T\frac{\partial(\delta e_y\sin\theta)}{\partial\alpha}\right\}dA=\int_{A^e}\left\{-\frac{\partial N^T}{\partial\theta}h^3\frac{\partial p}{\partial\theta}-B^2\frac{\partial N^T}{\partial y}h^3\frac{\partial p}{\partial y}+h\frac{\partial N^T}{\partial\theta}\frac{\partial\theta_r}{\partial\alpha}\right.$$

$$\left.-2N^T\frac{\partial h}{\partial\alpha}\right\}dA \tag{7.24}$$

Similarily for f_2

$$\delta p\frac{\partial f_2}{\partial p}+\delta e_x\frac{\partial f_2}{\partial e_x}+\delta e_y\frac{\partial f_2}{\partial e_y}=-f_2 \tag{7.25}$$

which may be written in dimensionless form as

$$\int_{A^e}\delta p\sin\theta dA+0+0=w_x-\int_{A^e}p\cos\theta dA \tag{7.26}$$

and

$$\delta p\frac{\partial f_3}{\partial p}+\delta e_x\frac{\partial f_3}{\partial e_x}+\delta e_y\frac{\partial f_3}{\partial e_y}=-f_3 \tag{7.27}$$

becomes

$$\int_{A^e}\delta p\sin\theta dA+0+0=w_x-\int_{A^e}p\cos\theta dA \tag{7.28}$$

Using these equations the elements in the matrices $[A]$ and $\{R\}$ may be assembled as

$$A_{ij}=\int_A\left\{-h^3\frac{\partial N_i}{\partial\theta}\frac{\partial N_j}{\partial\theta}-B^2h^3\frac{\partial N_i}{\partial y}\frac{\partial N_j}{\partial y}-3\frac{\partial N_j}{\partial\theta}h^2L\frac{\partial p}{\partial\theta}N_i\right.$$

$$\left.-3B^2\frac{\partial N_j}{\partial y}h^2L\frac{\partial p}{\partial y}N_i+\frac{d\theta_r}{d\alpha}\frac{\partial N_j}{\partial\theta}LN_i-2L\frac{N_iN_j}{d\alpha}\right\}dA\ ;\ i,j=1,2,..n \tag{7.29}$$

$$A_{i\ n+1}=\int_A\left\{3h^2\frac{\partial N_i}{\partial\theta}\cos\theta\frac{\partial p}{\partial\theta}+3B^2h^2\frac{\partial N_i}{\partial y}\cos\theta\frac{\partial p}{\partial y}-N_i\frac{d\theta_r}{d\alpha}\sin\theta+2\frac{\cos\theta N_i}{d\alpha}\right\}dA$$

$$i=1,2,..n \tag{7.30}$$

$$A_{i\ n+1}=\int_A\left\{3h^2\frac{\partial N_i}{\partial\theta}\sin\theta\frac{\partial p}{\partial\theta}+3B^2h^2\frac{\partial N_i}{\partial y}\sin\theta\frac{\partial p}{\partial y}+N_i\frac{d\theta_r}{d\alpha}\cos\theta+2\frac{\sin\theta N_i}{d\alpha}\right\}dA$$

$$i=1,2,..n \tag{7.31}$$

$$A_{n+1\ i}=\int_A N_i\cos\theta dA\ ;\ i=1,2,..n \tag{7.32}$$

$$A_{n+2\ i}=\int_A N_i\sin\theta dA\ ;\ i=1,2,..n \tag{7.33}$$

$$R_i = \int_A \left\{ -\frac{\partial N_i}{\partial \theta} h^3 \frac{\partial p}{\partial \theta} - B^2 \frac{\partial N_i}{\partial y} h^3 \frac{\partial p}{\partial y} + h \frac{\partial N_i}{\partial \theta} \frac{d\theta_r}{d\alpha} - 2N_i \frac{\partial h}{\partial \alpha} \right\} dA \quad ; \; i = 1,2,..n \tag{7.34}$$

$$R_{n+1} = w_x - \int_A p \cos\theta dA \tag{7.35}$$

$$R_{n+2} = w_y - \int_A p \sin\theta dA \tag{7.36}$$

7.2.3 Element matrix assembly

As for the under-relaxation method 8-node isoparametric elements were used to model the lubricant film and Gauss-Legendre quadrature was used to numerically evaluate the terms in $[A]$ and $\{R\}$. This was carried out in the same way as the element matrix formulation described in Chapter 3, evaluating each nodal variable at the relevant Gauss point. However, in the finite element method the operator L is replaced the matrix operator $[C]$ which is the pressure compliance matrix, the formulation of which is described in Chapter 5. This meant that at each Gauss point a row matrix was also evaluated for the contribution of the compliance matrix to the element formulation. Therefore, rather than assembling an 8x8 element matrix for $[A]^e$ an $8xn$ element matrix had to be assembled. Consequently the system matrix $[A]$ was fully populated. Using the Newton-Raphson formulation either the implicit or explicit time stepping method may be used. This is achieved by using the relevant expression for the film thickness h. Unlike the rigid bearing analysis method the computing time is not effected by the time-stepping method used since the same amount of matrix assembly is required in both cases.

7.3 Film Cavitation

An important source of non-linearity in the problem is the inadmissibility of negative pressures in the fluid film. (In practice the oil film can only support a very slight negative pressure before film rupture occurs). As previously mentioned it is not possible to use an algorithm such as that adopted by Christopherson [8] since the cavitated and non-cavitated regions must be specified a priori. It is, however, possible to locate the two regions by combining the complementarity problem with the Murty algorithm [66,67] This is an iterative process and requires that an initial estimate be made for the extent of the cavitated region. For the nodes that lie in the

cavitated region it is assumed that $p = 0$, whilst in the non-cavitated region p is found by solving Reynolds equation using the finite element formulation described. Once the pressures are calculated the designation of the cavitated region is checked. The complementarity formulation assumes that over the solution domain the pressure is either found from Reynolds equation, providing the pressure is positive, or that $p = 0$ if the cavitation condition holds. That is, when the film thickness is diverging at such a rate that

$$\nabla(h^3\nabla p)-6\mu\,(u\frac{\partial h}{r\partial\theta}+2\frac{\partial h}{\partial t}) \le 0 \qquad (7.37)$$

Therefore any nodes in the non-cavitated region where $p \le 0$ are placed in the cavitated region and any nodes in the cavitated region where the cavitation condition given by the inequality (7.37) is not satisfied are placed in the non-cavitated region. This process continues until the conditions are satisfied by all the nodes in the mesh. The process was found to converge very rapidly, typically in two to three iterations. Goenka [22] stated that to ensure convergence of this method only one node should be altered at each iteration. It was however found that there were no convergence problems when all the violating nodes at each step were altered. In practice it was also found that in certain cases a single node would remain oscillating between the two regions due to the assumption that the boundary between the cavitated and non cavitated regions had to lie at a series of fixed nodes. In this case no further iterations were performed and the solution was assumed to have converged.

7.4 Solution procedure

7.4.1 The full Newton-Raphson method

The iterative steps involved in the Newton-Raphson method are shown in Figure 7.1. The solution was started by making an initial estimate for the eccentricity components and carrying out a rigid bearing analysis using the Gauss-Seidel method. This gave the first set of pressures and an initial estimate for the cavitated region. Using these pressures the Newton-Raphson equations were assembled. These equations were then solved using Gaussian elimination and back substitution, a method already described in Chapter 5. In this case, though, the boundary

conditions also had to be applied for the nodes at the bearing edge, in the cavitated region and at the oil supply features where $\delta p = 0$. A convenient way of applying these boundary conditions is to multiply the diagonal coefficient A_{ii} by a very large number, in this case 10^{20} and to set the corresponding term R_i to 0. The *ith* equation therefore becomes

$$A_{i1}\delta p_1 + \ldots + A_{ii}\,10^{20}\delta p_i + \ldots + A_{in+2}\delta e_y = 0 \tag{7.38}$$

The term $A_{ii}\,10^{20}\delta p_i$ dominates the left hand side therefore $\delta p_i \approx 0$.

Once the equations have been solved the nodal pressures and the eccentricity components are modified using the values obtained for δp, δe_x, δe_y and the process is repeated until a converged solution is obtained. The process was said to have converged if

$$\frac{\sum_{i=1}^{n} |\delta p_i|}{\sum_{i=1}^{n} |p_i|} \leq 10^{-5} \tag{7.39}$$

To check this method the results obtained for the elastic case were compared to those obtained using the under-relaxation method. By setting the compliance matrix equal to zero a solution could also be obtained using this method for the rigid bearing problem and compared to the solution using the rigid bearing method developed earlier. All results showed good agreement.

7.4.2 Modified Newton-Raphson method

The Newton-Raphson method, although proving robust and highly convergent, required a prohibitively large amount of computing time, in some cases up to 16 hours, to complete a full dynamic analysis. Some means therefore had to be found to reduce the amount of computing time by at least an order of magnitude but still retain the high rate of convergence. The most time consuming parts of the analysis are the assembly of the matrix $[A]$, since for the flexible case this is fully populated, and the forward elimination process. It was, therefore, decided to try to apply the modified Newton-Raphson method to the problem. Using the Newton-Raphson

(NR) method the matrix $[A]$ is evaluated at each step in the N-R loop (Figure 7.1). Using the modified Newton-Raphson (MNR) method $[A]$ is only evaluated once for each cavitation loop. Subsequently only the right-hand side $\{R\}$ has to be formulated. The equation for the iterative process then becomes

$$[A]_1\{X\} = \{R\}_i \tag{7.40}$$

where i is the iteration step. Forward elimination is carried out on $[A]$ at the start of the cavitation loop and the elimination ratios are stored and used to subsequently modify the new right hand sides assembled at each iterative step. In general this method proved only slightly less convergent than the NR method but significantly faster. A limit was placed upon the number of iterations in case this method proved to be too slow to converge. If this limit was exceeded the solution process was restarted using the NR method to ensure convergence and the MNR method was then started again at the start of the next cavitation step. This happened at most 2 or three times during a complete engine cycle analysis, usually at a point where the load was changing rapidly in size or direction.

Since the MNR method produced such a high rate of convergence it was reasoned that rather than assembling $[A]$ once at the start of each cavitation step it should just be assembled once for several cavitation steps. The obvious problem with this method is that for each cavitation step different boundary conditions are applied. $[A]$ is altered according to these during the forward elimination process and so cannot be used in its modified form at subsequent cavitation steps. To avoid having to reformulate $[A]$ a temporary store was used so that when $[A]$ was formulated for the first time it was copied into a temporary file store. When the boundary conditions changed (that is when the cavitation conditions altered), the values of the temporary store were copied back into $[A]$ and forward elimination was again carried out, essentially using the old values but new boundary conditions. Clearly one formulation for $[A]$ would not be sufficient for carrying out a complete engine analysis. The matrix $[A]$ was therefore reformulated when either the rate of convergence fell below a certain value, or when the solution began to oscillate. It was found that there was an optimum range for the limit on the number of iterations in the N-R loop to produce an optimum computing time of between 7 and 11 steps. It was found that when the solution began to diverge the values of δe_x and δe_y began to increase. It was, therefore, easy to check for divergence simply by monitoring

these values and if they increased above a certain amount the solution was stopped and $[A]$ reformulated. This method, called the fast modified Newton-Raphson method (FNR), proved highly effective.

7.5 Results

7.5.1 Example considered

Results are presented for the Ruston and Hornsby 6VEB Mk III marine diesel big end bearing, data for which is given in Chapter 4. As previoiusly mentioned this has become a benchmark for comparing different forms of analysis. It was possible to compare the results for the elastically deformed bearing with the previous results for the rigid bearing. A simplified model of the connecting rod was used to obtain the compliance matrix as described in Chapter 5. Although this model was not an exact representation of the actual connecting rod it allowed the effect of varying the mesh density to be simply carried out and allowed the general effects of incorporating elasticity into the analysis to be assessed. For the dynamic analysis the implicit time stepping method was used since this is a more stable method than the explicit method as mentioned in Chapter 4. For the analysis it was assumed that the connecting rod was made from mild steel with Youngs modulus E of $209x10^9\ Nm^{-2}$ Poisson's ratio of 0.3.

7.5.2 Graphics software

The analysis of a dynamically loaded journal bearing generates a very large amount of data which is difficult to interpret when in numerical form. Graphics software was therefore developed for postprocessing the data. Initially this simply plotted the journal centre orbit and the variation of the peak film pressure, minimum film thickness, power loss and side flow against crank angle, and allowed comparative plots for different sets of data to be presented. It was however felt that some other means of presenting the data had to be developed. This was especially important for the dynamically loaded flexible journal bearing problem where the bearing deformation greatly alters the bearing performance. It was, therefore, decided to develop software to produce an animated display through time to show how the bearing was performing, and how the various bearing parameters were influencing each other. Figure 7.2 shows a 'frame' produced by this software. It shows the crank angle, the journal position on the journal centre orbit, the applied load, the deformed bearing shape (exaggerated), the pressure distribution around the bearing and the varation of the film thickness around the bearing. Presenting the

data in this way gave a much better feel for the manner in which the bearing was behaving and some idea of the rates of change of the various parameters with time. Since such a large amount of data was presented in an easily readable format this form of data presentation also proved useful for detecting any errors arising in the analysis. The software allowed the animation to be frozen at any time-step and, if required, a hard copy could be produced of that particular frame.

7.5.3 Comparison of Newton-Raphson Methods

The time required for the three different solution methods used are compared in Table 7.1 below with the required computer time being expressed as a percentage of the computer time required for a full analysis of the Ruston bearing using the NR method.

Method	Time
NR	100%
MNR	29%
FNR	11%

Table 7.1 : Comparison of computing times for various N-R methods

Using the FNR method the fully-populated matrix $[A]$ only had to be reformulated 60-80 times during the analysis of a complete engine cycle compared to 6000 or more times for the NR method and about 1000 times for the MNR method. All three sets of results were identical. As the solution converges the right hand sides $\{R\}$ tend to zero and so to do the corrections $\{X\}$. Since $\{R\}$ is re-evaluated at each iterative step it follows that all three sets of results must be nearly identical since the only difference between the three methods is the rate of convergence of the solution which is governed by $[A]$ which may be regarded as a set of forcing coefficients. Using a mesh size of $41x5$ a solution was obtained in 17 minutes using a VAX 80800 mainframe computer. Oh and Goenka [45] report a solution time of 35 hours using an IBM 360/8081 mainframe computer. Floating point benchmark tests show that this computer is 1.7 times faster than the VAX. The current method of analysis is, therefore, approximately 200 times faster than the

previous method. The main reason for this is the new fast Newton-Raphson method and the use of higher-order elements to model the lubricant film. Use of the latter requires considerably fewer nodal points for a given solution accuracy than the linear 3-node tringular elements used in the analysis presented by Oh and Goenka [47].

7.5.4 Steadily loaded case

To assess the effect of varying the mesh density used for the analysis and the general effects of incorporating elasticity into the anlysis the steady loaded bearing was first looked at. The load was applied in the cap half of the bearing at 180 degrees to the connecting rod axis. This meant that the pressure generated in the oil film was acting over the most flexible part of the bearing where the elasticity effects would be most pronounced.

The solution procedure was started by using the rigid bearing analysis method to give an initial set of pressures and an initial estimate for the cavitated region. The Newton-Raphson method was then applied to find the correct journal position, housing deformation and pressure distribution for the particular load case. The load on the bearing was then increased incrementally and the housing deformations and journal position were found for each load case. This was continued until the minimum film thickness became negative. It was possible to restrain the nodal film thickness values to prevent a negative film thickness occuring at a node but since a quadratic variation was assumed for the nodal variables when using the higher order elements it was not possible to ensure that the internodal values for the film thickness would remain positive. Unlike the under-relaxation method it was possible to use comparatively large increments to increase the load due to the highly convergent nature of the Newton-Raphson method. For all but the most heavily loaded cases a solution could be obtained without having to start the solution procedure at a lower load and increase it gradually. Eccentricities of up to 3.5 were obtained.

The meshes compared had 41x5, 61x5 and 41x7 nodes in the circumferential and axial directions respectively. The maximum loading applied to the bearing was in the region of 500KN. The maximum loading for this bearing in practice is 200KN which occurs in the more rigid rod half of the bearing. This load was therefore considerably higher than that normally applied to the bearing. Figures 7.3 and

7.4 compare the minimum film thickness, peak film pressure, power loss and side flow for the different meshes. The minimum film thickness, power loss and side flow all show very good agreement. As the loading becomes very high discontinuities appear in the predicted values for the peak film pressure. These occur when the node at which the peak pressure occurs changes. Even though a quadratic Lagrangian interpolation was used to locate the peak film pressure this method becomes less accurate as the pressure profile develops sharper peaks. These discontinuities, however, occur when the applied load is much greater than that actually applied to the bearing.

Figures 7.5 and 7.6 compare the minimum film thickness, peak film pressure, power loss and side leakage for the rigid and elastic bearing. As expected, the elastic bearing shows a lower peak pressure and film thickness than for the rigid bearing. The values for the power loss and side flow show a marked increase for the elastic bearing especially for high loading, the power loss increases as the contact arc is greater for the elastic bearing therefore the shear losses are greater. Figures 7.7 and 7.8 compare the oil film and pressure profiles for the rigid and elastic bearings under a medium load. The film profile for the elastic bearing shows a considerable region of small film thickness. This is consistent with the observations of Fantino et al [42]. The pressure profile shows a distinct double peak and the value of the peak pressure is considerably lower for the elastically deformed bearing. The extent of the positive pressure region is also increased due to the relatively large region of small film thickness.

7.5.5 Dynamic loading

Again for the dynamically loaded bearing the meshes considered had 41 x 5, 61 x 5 and 41 x 7 nodes in the circumferential and axial directions, respectively. A time step corresponding to two degrees of crank rotation was used to compare the meshes. Oh [66] noted that convergence problems were encountered on the first step of the dynamic problem when iterating for the journal position for the steady loaded case. This problem was avoided by keeping the journal position fixed for the first step and then using this as a starting point for the next step. Consequently, when iterating for the journal position squeeze effects are present which have a damping effect on the iterations and reduce any convergence problems. It was also

found that it was not necessary to interpolate between time steps for the journal position due to the high rate of convergence of the Newton-Raphson method, in fact, using interpolation tended to result in an increase in the number of iterations.

Figures 7.9-7.12 show the predicted journal centre orbits and film pressures for the three meshes, the datum point for these orbits was taken as the totally restrained part of the connecting rod. There is little difference between the results yet the coarsest mesh, 41 x 5, required approximately a quarter of the computing time that was required for the two finer meshes for a complete analysis. It would seem therefore that this mesh size is adequate for modelling the oil film, a conclusion which is consistent with earlier work carried out on the rigid bearing.

Decreasing the step size to one degree of crank rotation made a negligible difference to the predicted performance (Figures 7.13 and 7.14). It is interesting to note that although twice as many time steps were required for the second analysis only twenty percent more computing time was required. Even though the time step was doubled the number of complete reformulations of $[A]$ only increased slightly, this is since each formulation should not be regarded as causing convergence for a certain number of time steps but for a given amount of crank rotation.

The predicted bearing performance for the rigid and elastic bearings showed quite significant differences. The predicted journal centre orbits are shown in Figure 7.15 where it is seen that for the elastic bearing an eccentricity greater than one occurs over much of the cycle, especially when the loading is in the cap half of the connecting rod, eccentricities of up to 1.3 being predicted. Figure 7.16 shows the peak film pressures to be considerably lower for the elastic bearing. The elastic bearing also gave a much larger region of positive pressure and in some parts of the cycle showed a bimodal pressure distribution. Figure 7.17 shows the minimum film thickness variation. There is only a small difference between the predicted minimum film thickness for the complete cycle because in each case this occurs at a part of the bearing that is comparatively rigid. The power loss and side flow (Figures 7.18 and 7.19) show little difference over the cycle. As expected, though, for the elastic bearing both these values are slightly greater. The differences here are not as marked as for the steady loaded bearing since for a relatively large part of the engine cycle the load is relatively low so the elasticity effects will not be so pronounced. The midplane pressure profiles for the engine cycle are compared in

Figure 7.20 where it is clear that for the flexible bearing the pressure distribution does not show such sharp pressure peaks. This is again seen in Figures 7.21 and 7.22. In these diagrams the peak film pressure at each time step is plotted out as a vector relative to the connecting rod axis. The difference is especially marked when the peak pressure is in the cap half of the bearing when the pressure variation is much less pronounced for the elastic case. This type of plot proved to be very useful for locating the most highly loaded regions of the bearing. It also served as a useful check on the results since the shape produced should in general have a similar form to the same plot used to display the load on the bearing (see Figure 7.23). The extent of the pressure region for the two cases is shown in Figures 7.24 and 7.25. For the rigid bearing there are two distinct continuous regions for the cavitated and non-cavitated film. For the elastic case however especially between 360 and 390 degrees crank angle there are regions where the cavitated region splits in two due to the housing deformations. Figure 7.26 shows the variation of the mid plane film profile through the cycle. Both plots are inverted, that is the vertical axis have been reversed so that the regions of minimum film thickness are most prominent. Both appear similar except in the region around 360 degrees crank angle where there is a large amount of deformation since the loading is in the cap half of the bearing and a region of flattening is obvious for the flexible bearing. This is again seen in Figure 7.27 which shows the post processed output for 360 degrees crankangle. Considerable deformation and a large region of small film thickness are evident. This compares well with results presented by Martin in a discussion of the under-relaxation work carried out by Fantino et al [42]. It is interesting to note the extent to which the bearing sides are pulled inwards due to the stretching of the housing. The same output is shown in Figure 7.28 for 10 degrees of crank angle which corresponds to the point of maximum loading. In this case there is relatively little deformation even though the load is considerably greater than the previous case since the bearing is relatively stiff over this region.

7.6 Summary

This chapter has covered the Newton-Raphson formulation of the dynamically loaded EHD journal bearing problem. As for the rigid bearing analysis 8-node isoparametric elements were used to model the lubricant film and a mesh size of 41 circumferential and 5 axial nodes gives a very good resolution of the pressure

distribution. Although the formulation for this problem is considerably more complex than for the under-relaxation method it has proved to be highly convergent and there appear to be none of the convergence problems that were encountered when using the under-relaxation method. A cavitation algorithm has been introduced that locates the free boundary in a straightforward manner. The Newton-Raphson formulation has subsequently been heavily modified to produce a solution method that is 200 times faster than that developed by Goenka and Oh working at General Motors. This means that this new method is viable as a general design tool. Results have been presented for the Ruston bearing for both the steady and dynamically loaded cases. Both sets of results showed the same general trends, the peak film pressure and the values of the minimum film thickness decreased and the power loss and side flow increased when elasticity was incorporated in the analysis. Graphical software has also been described which allows the behaviour of the bearing to be presented in an easily readable form.

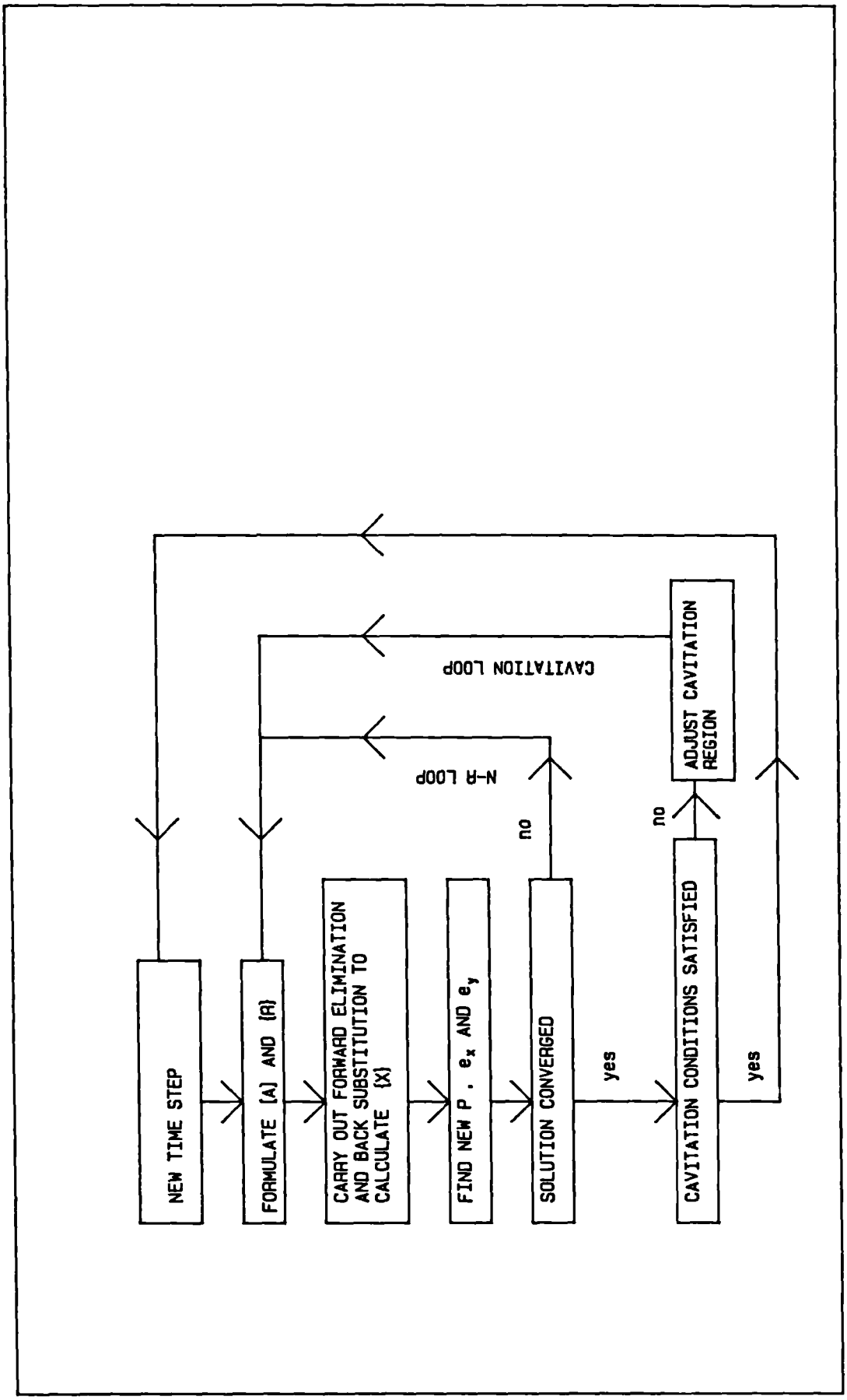

Figure 7.1 - The Newton-Raphson solution method applied to the EHD journal bearing problem.

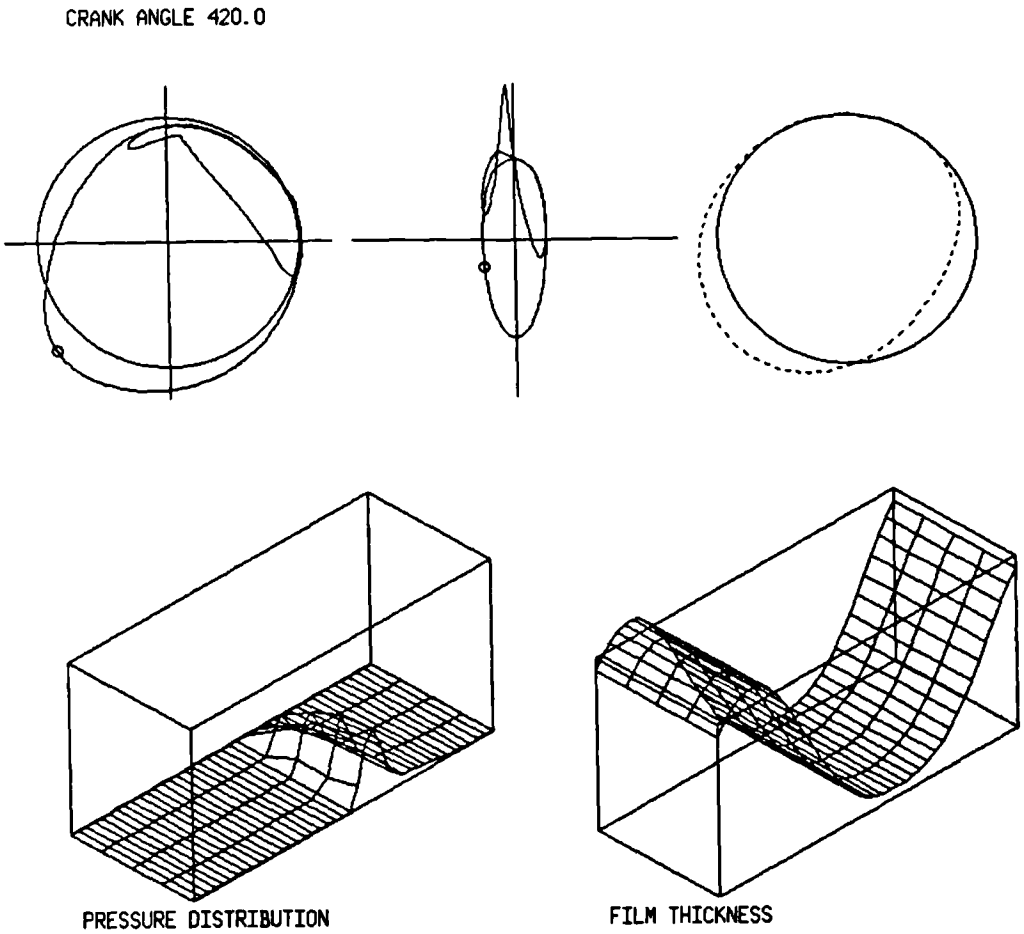

Figure 7.2 - Typical frame produced by animated post processing software

(a)

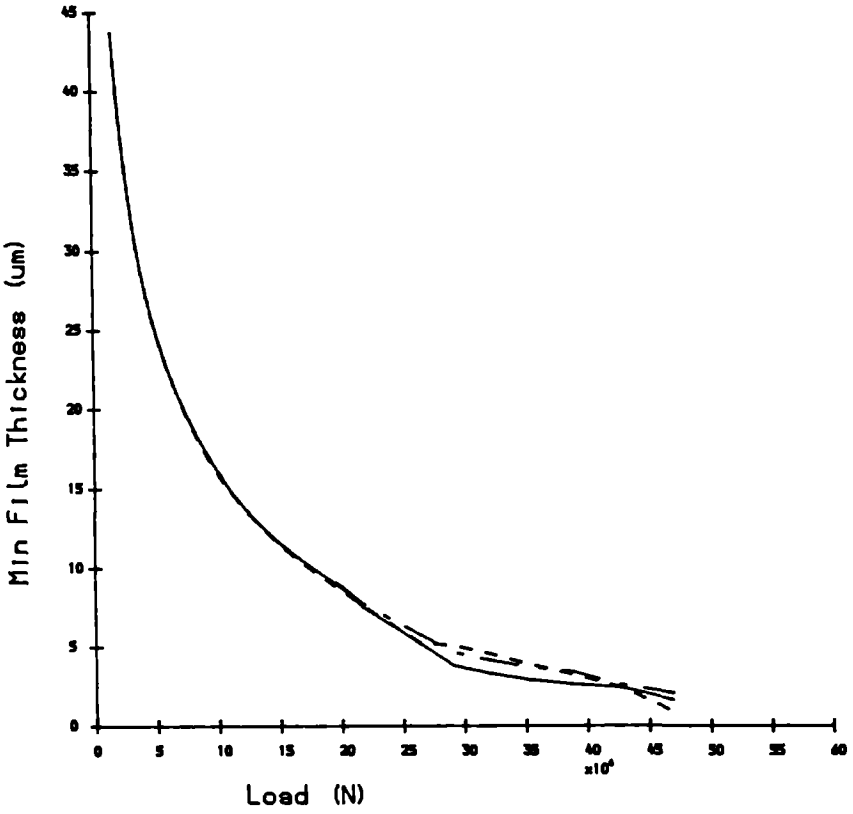

(b)

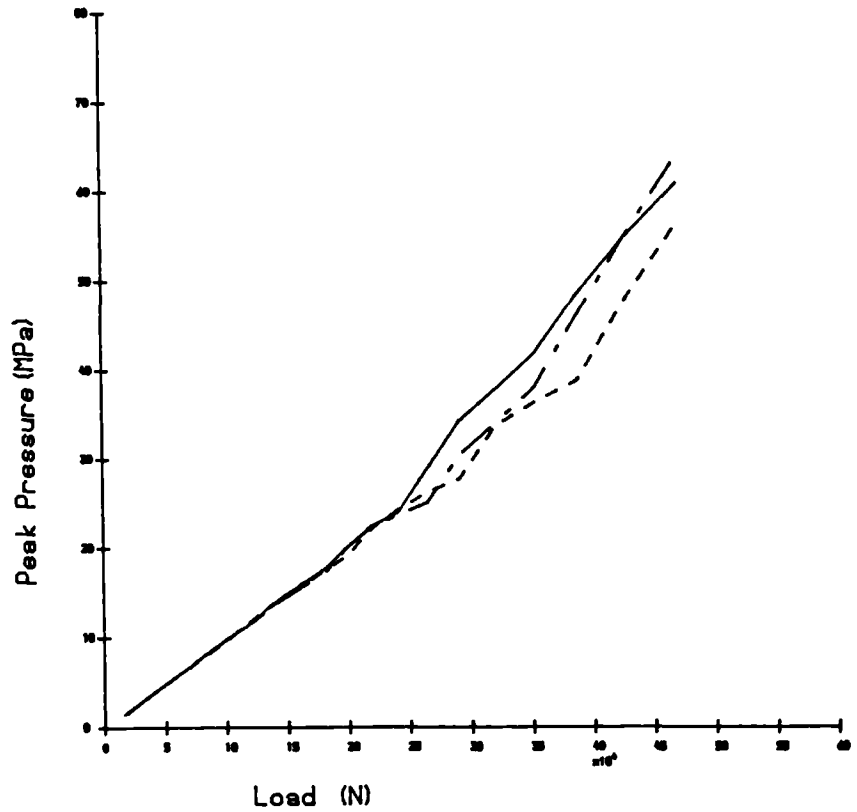

Figure 7.3 - Steady loaded flexible bearing
(a) Min film thickness (b) Peak film pressure.
——— 41x5 —— - - 61x5 — - - - 41x7

(a)

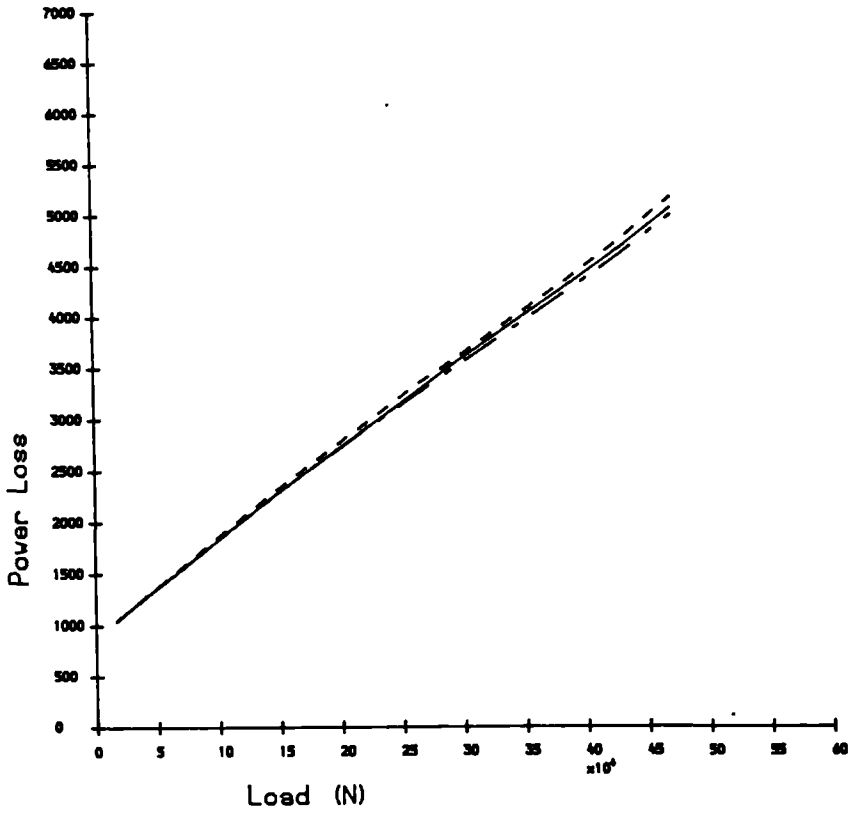

(b)

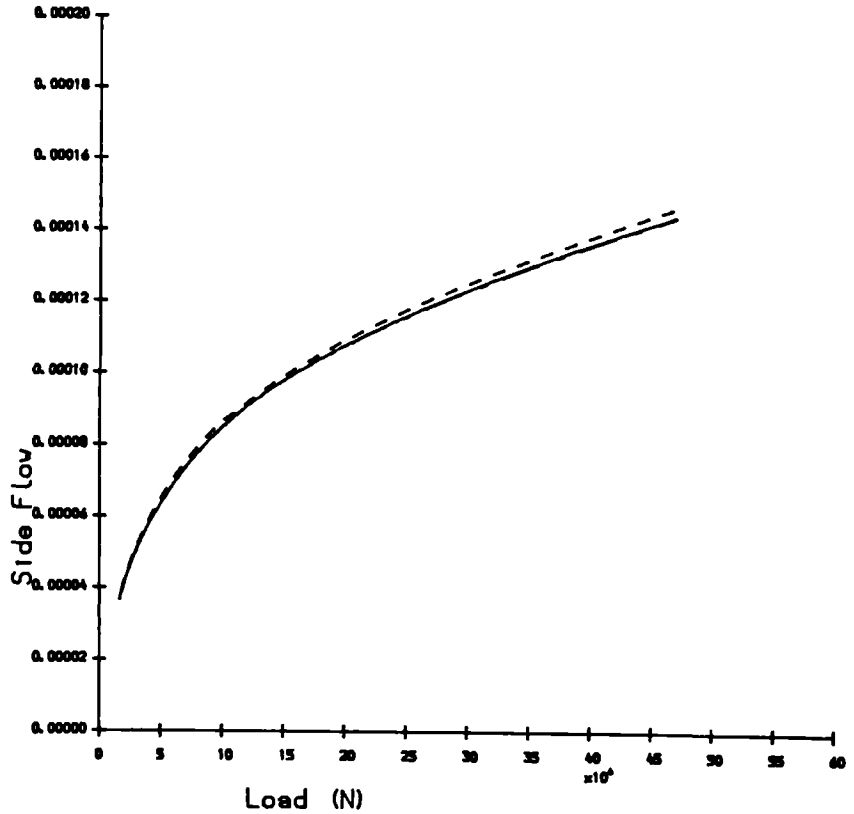

Figure 7.4 - Steady loaded flexible bearing
(a) Power loss and (b) Side flow
——— 41x5 —— – – 61x5 – – – – 41x7

(a)

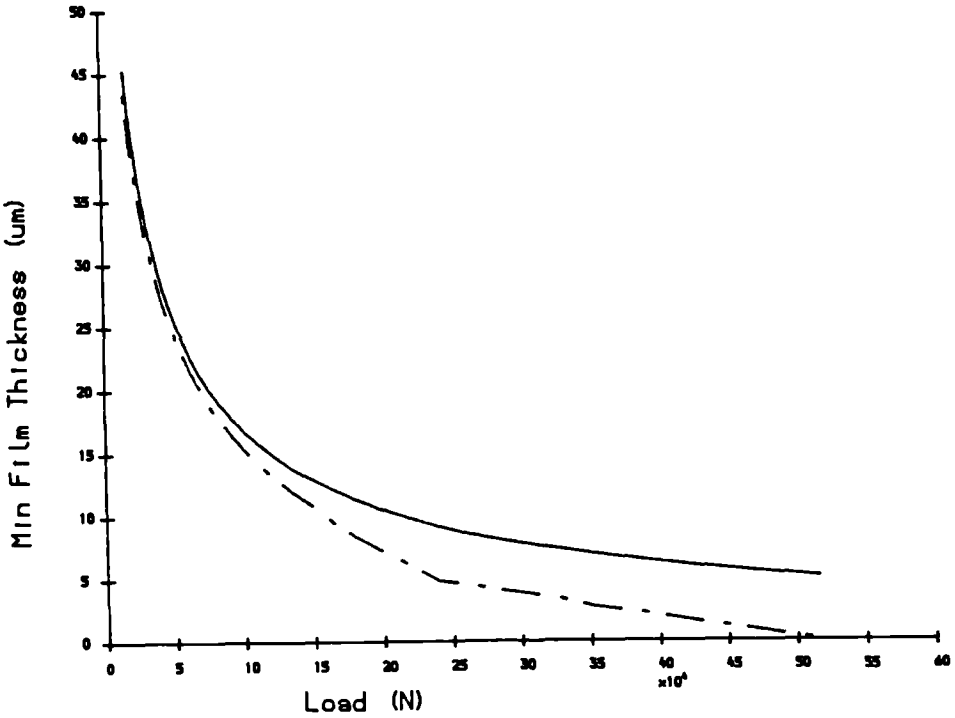

(b)

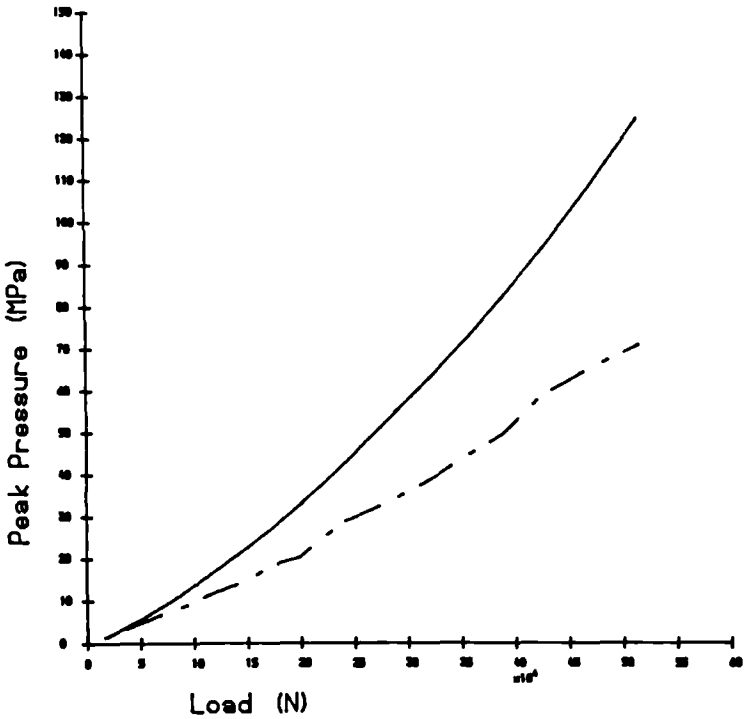

Figure 7.5 - Steady loaded bearing performance
(a) Min film thickness (b) Peak film pressure.
——— Rigid —·—·— Elastic

(a)

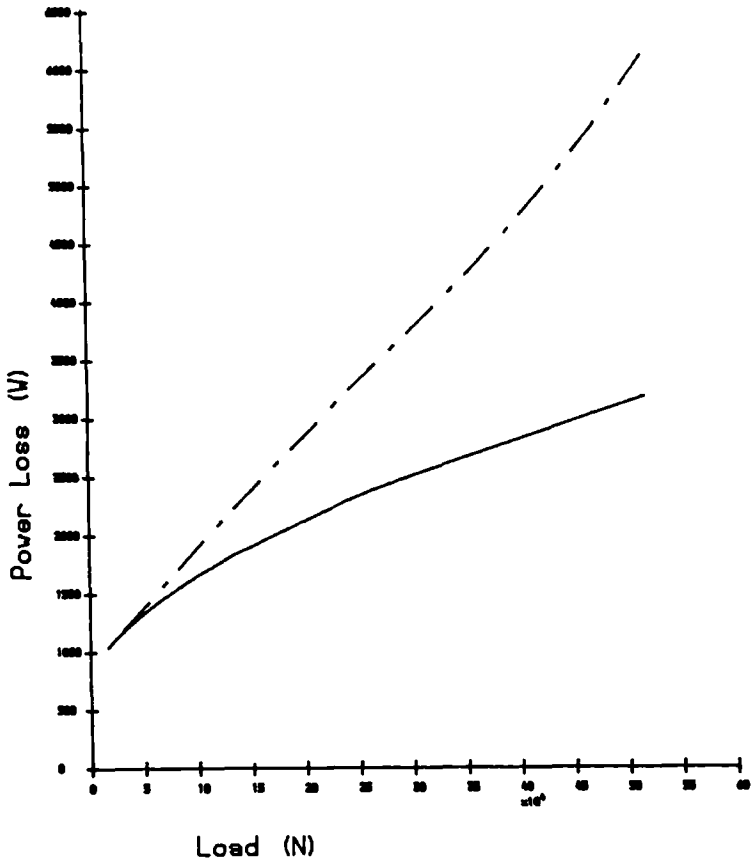

(b)

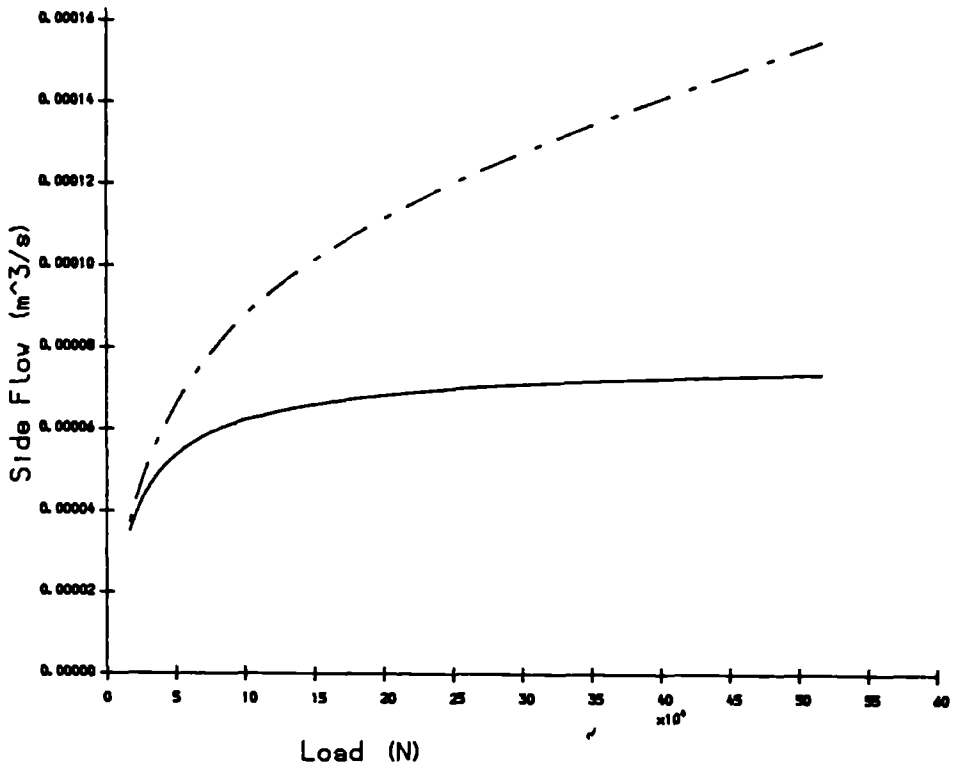

Figure 7.6 - Steady loaded bearing performance
(a) Power loss (b) Side flow.
——— Rigid ----- Elastic

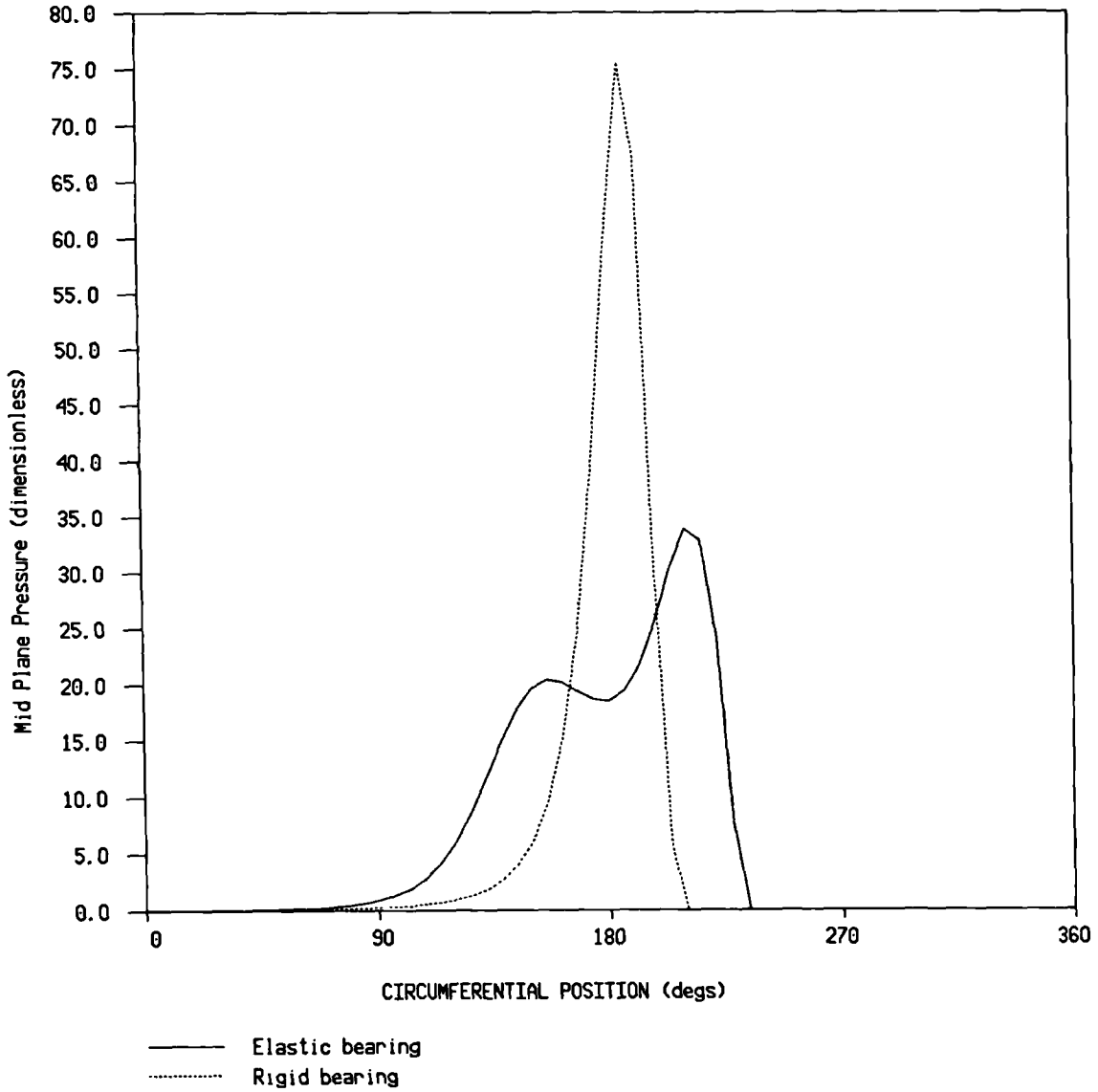

Figure 7.7 - Midplane pressure profile for a rigid and elastic bearing under a steady load.

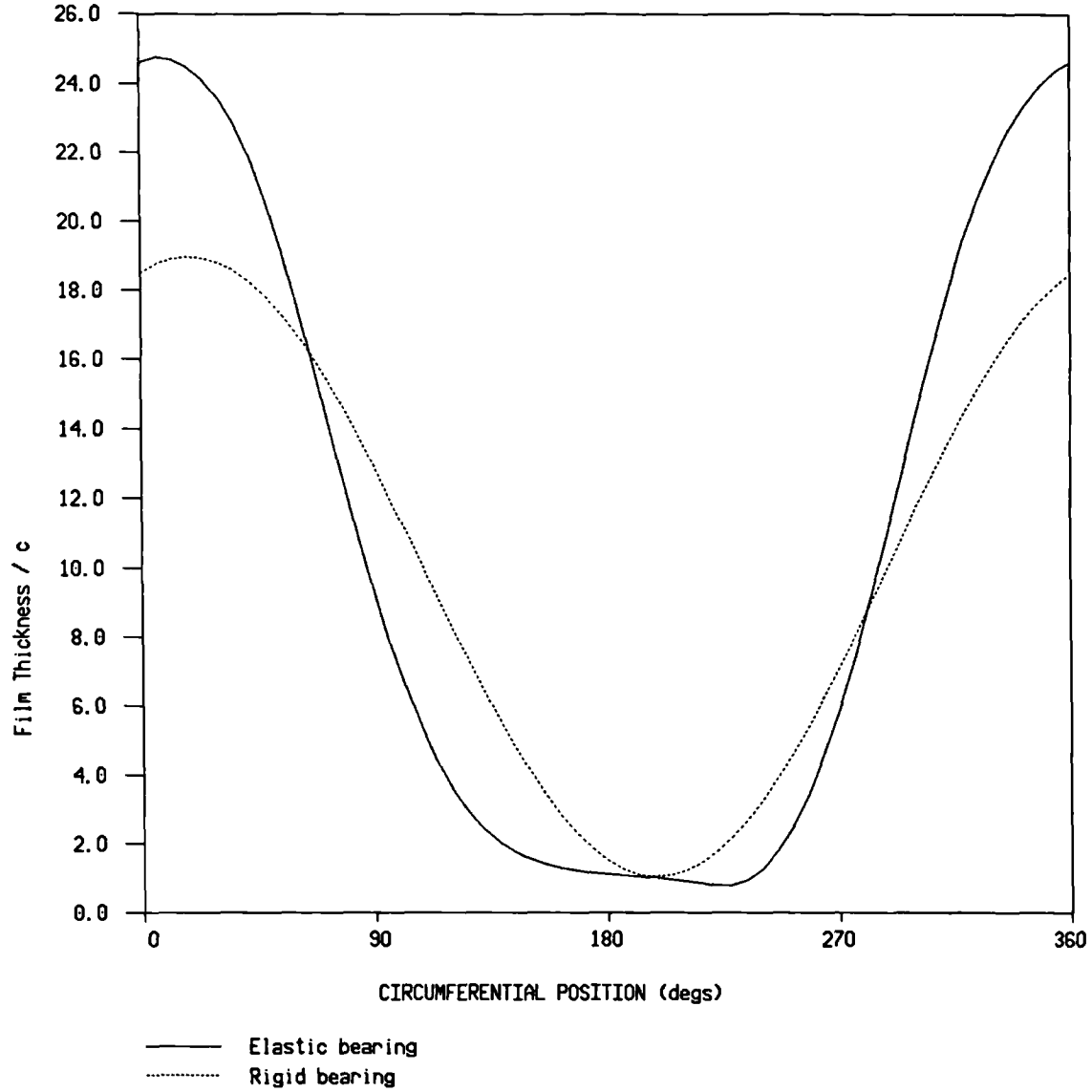

Figure 7.8 - Midplane film profile for a rigid and elastic bearing under a steady load.

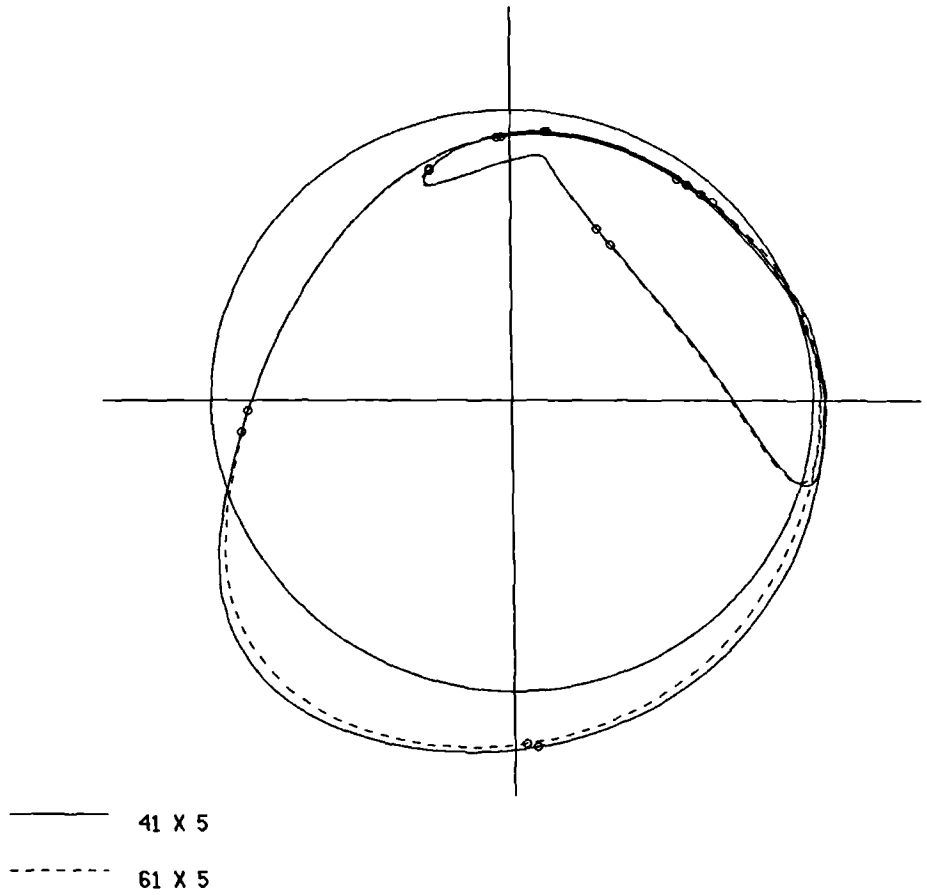

Figure 7.9 - Comparison of journal centre orbits using 41x5 and 61x5 meshes.

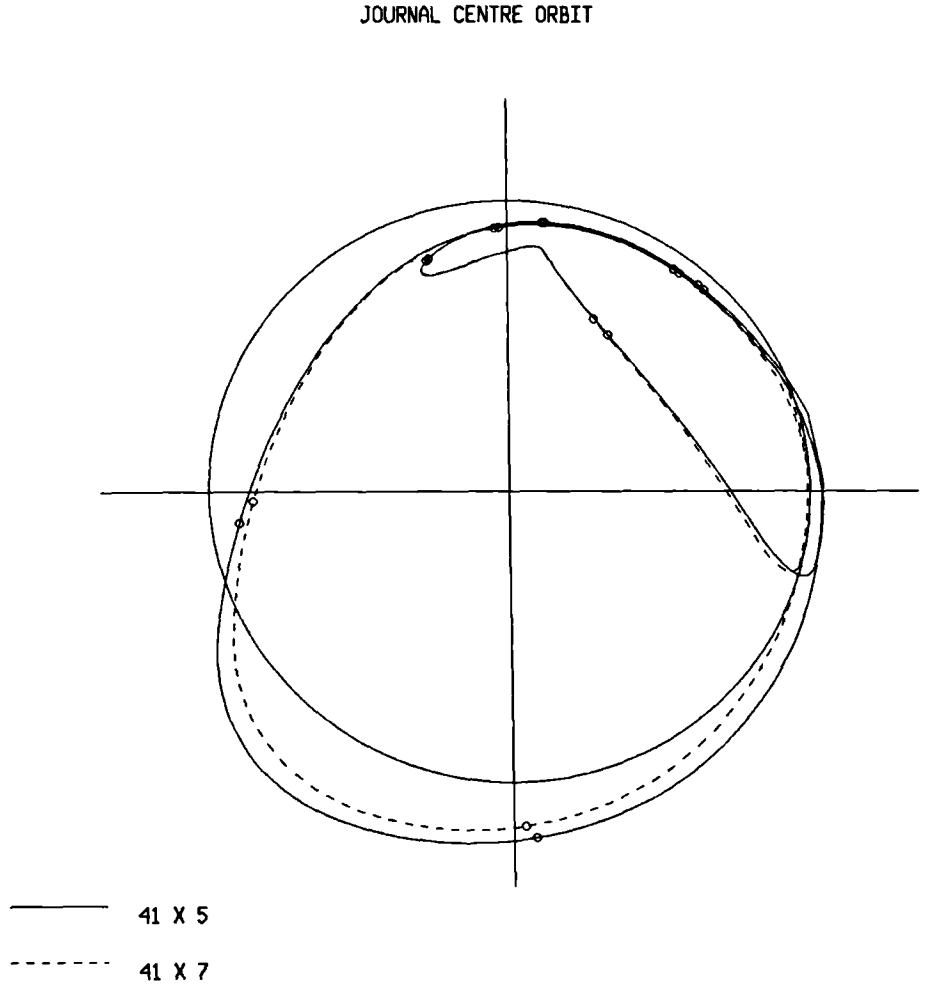

Figure 7.10 - Comparison of journal centre orbits using 41x5 and 41x7 meshes.

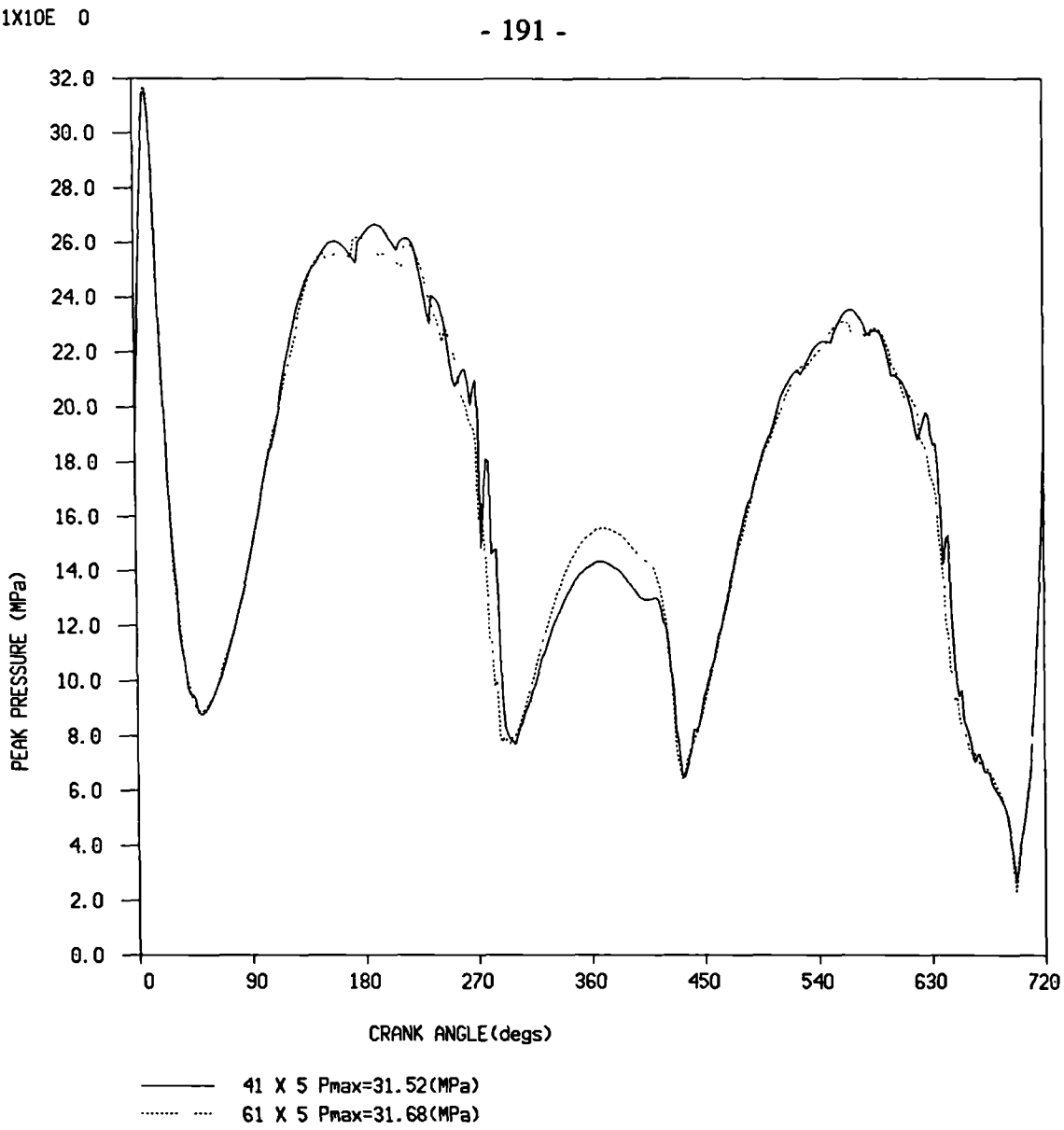

Figure 7.11 - Peak film pressures obtained using 41x5 and 61x5 meshes.

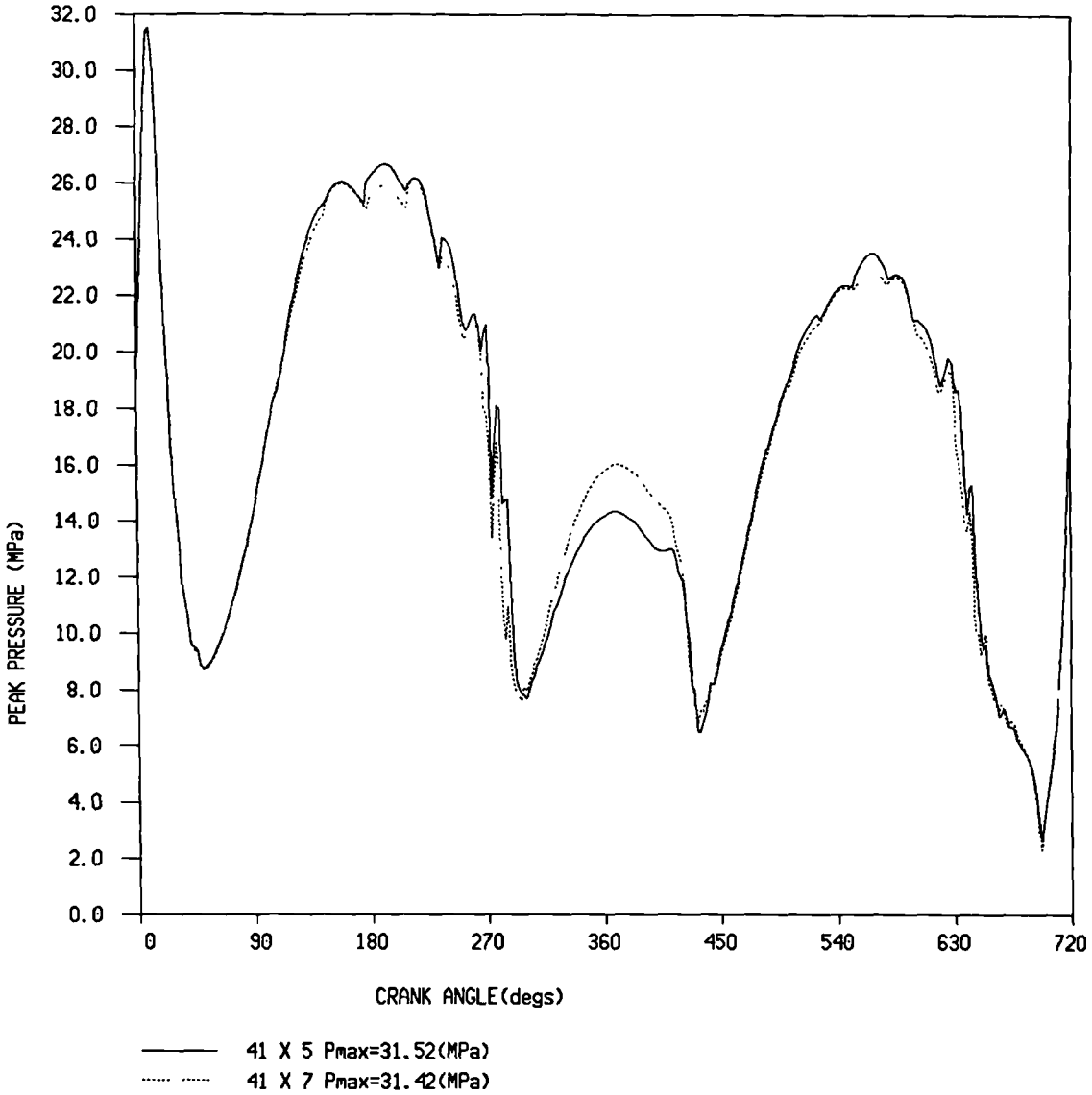

Figure 7.12 - Peak film pressures obtained using 41x5 and 41x7 meshes.

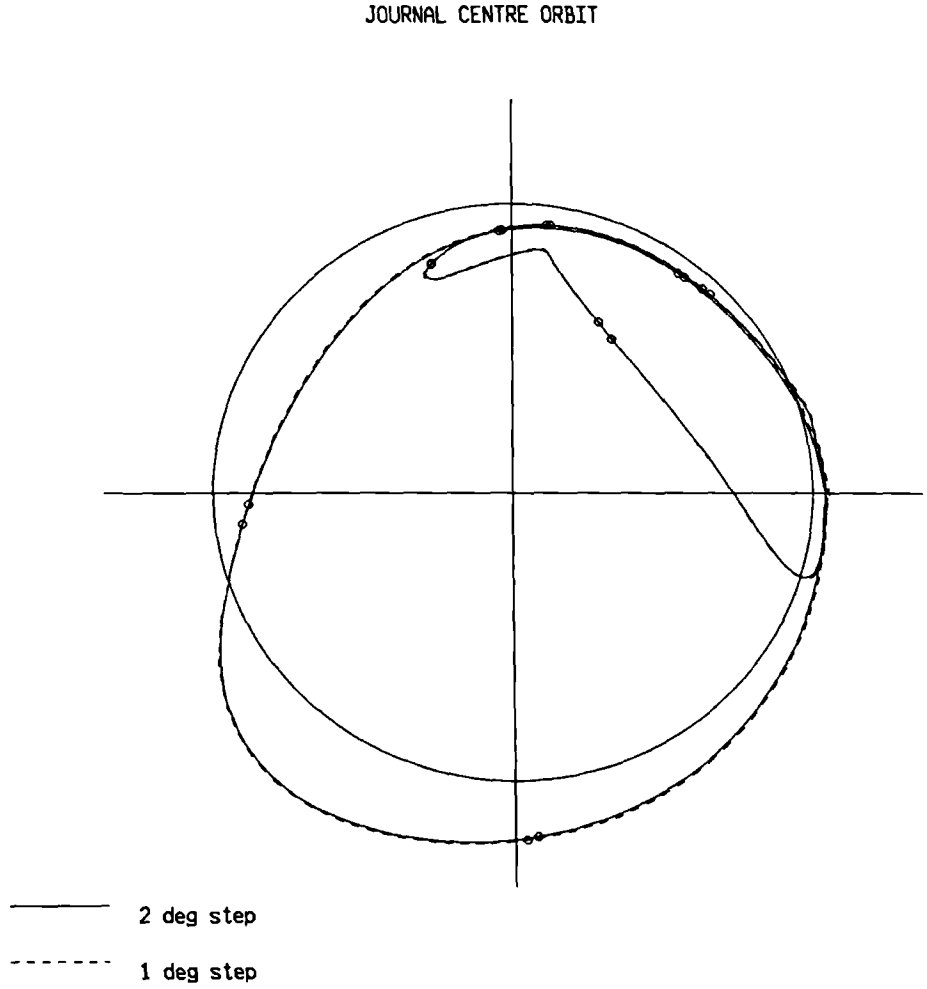

Figure 7.13 - Effect of varying time step on predicted journal centre orbit.

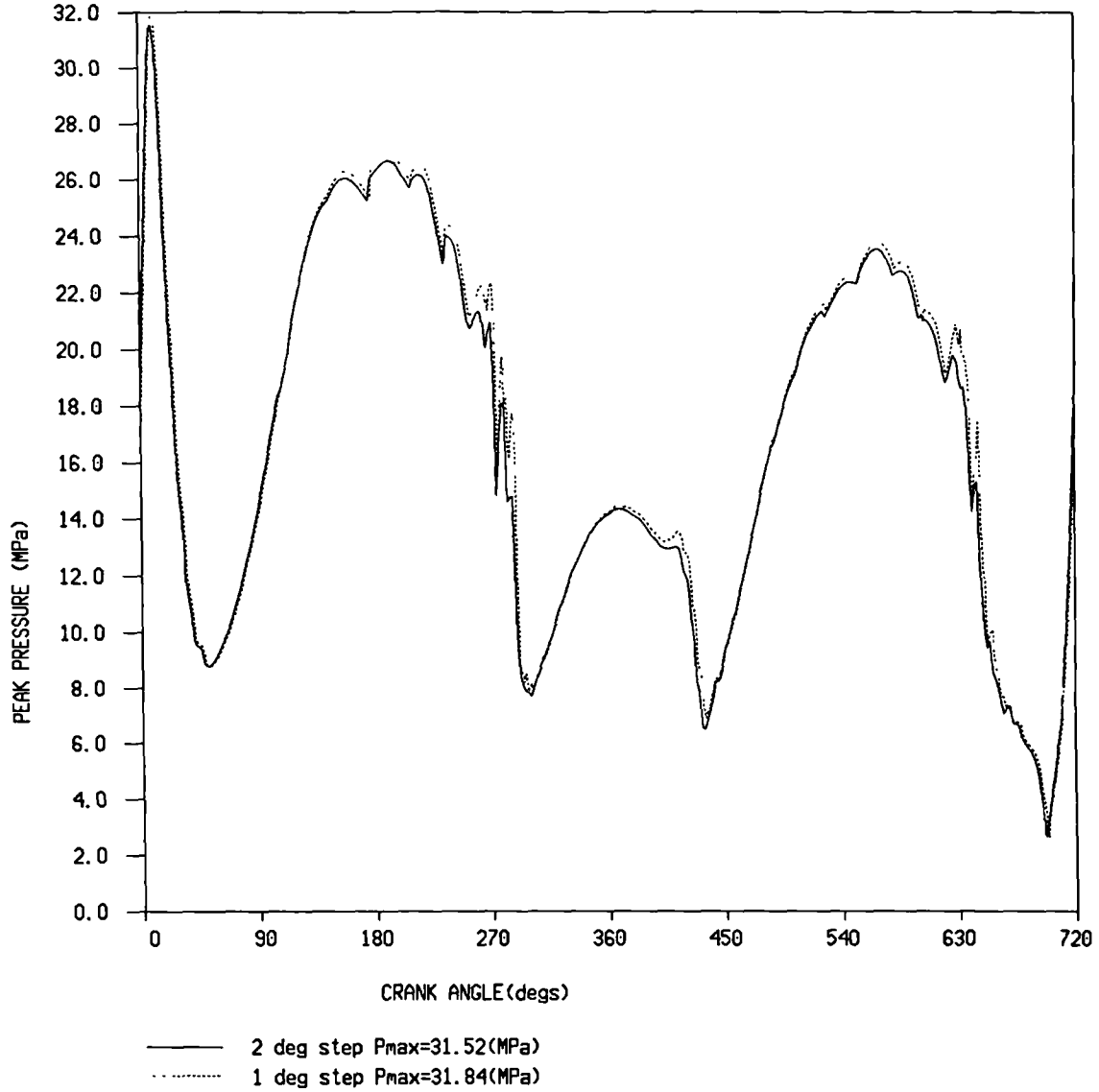

Figure 7.14 - Peak film pressures obtained using 2 degrees and 1 degree time steps.

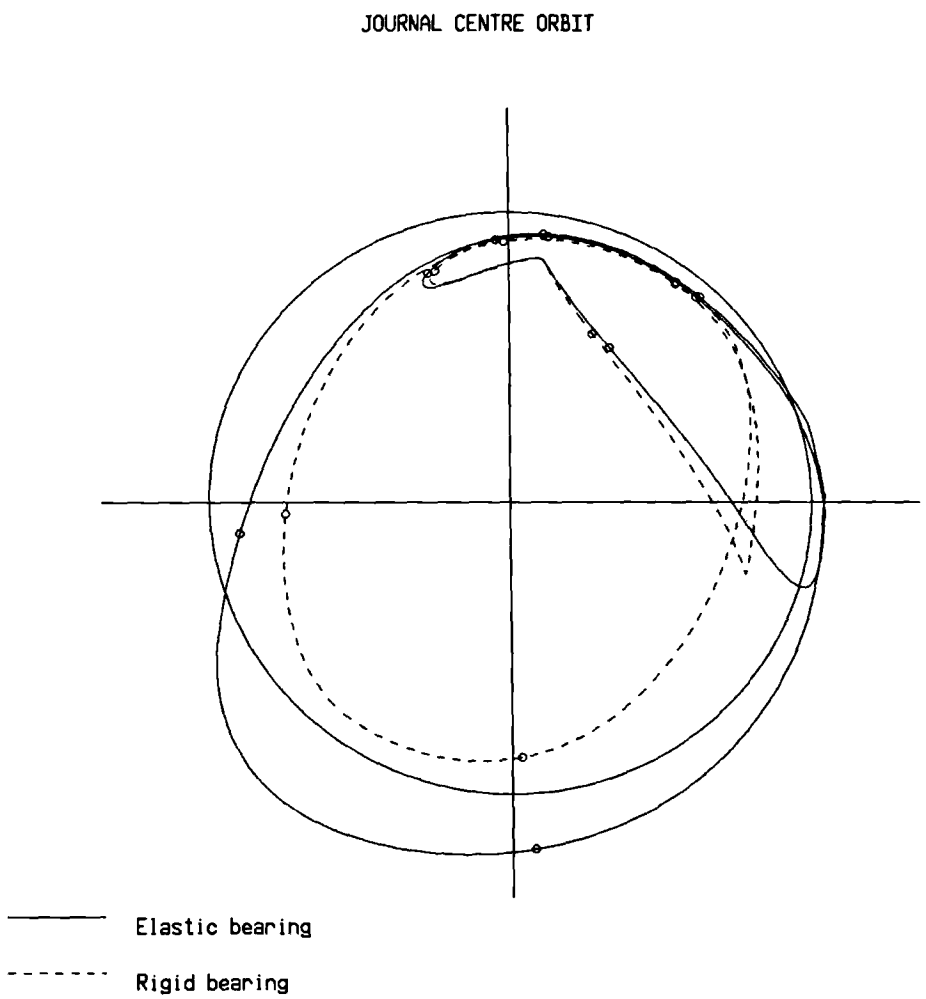

Figure 7.15 - Comparison of predicted journal centre orbits for the rigid and elastic bearing examples.

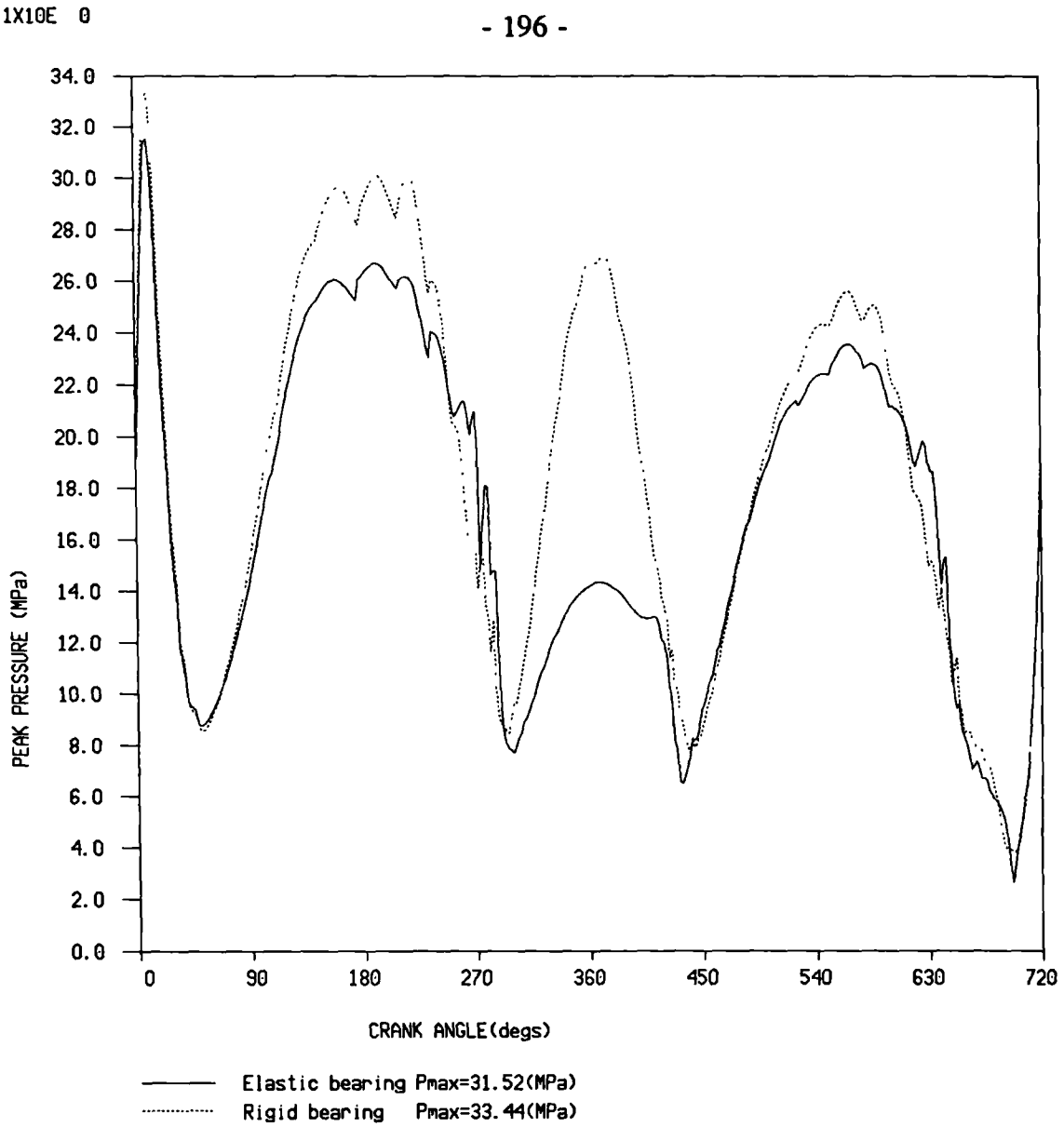

Figure 7.16 - Comparison of the predicted peak film pressures for the rigid and elastic bearing examples.

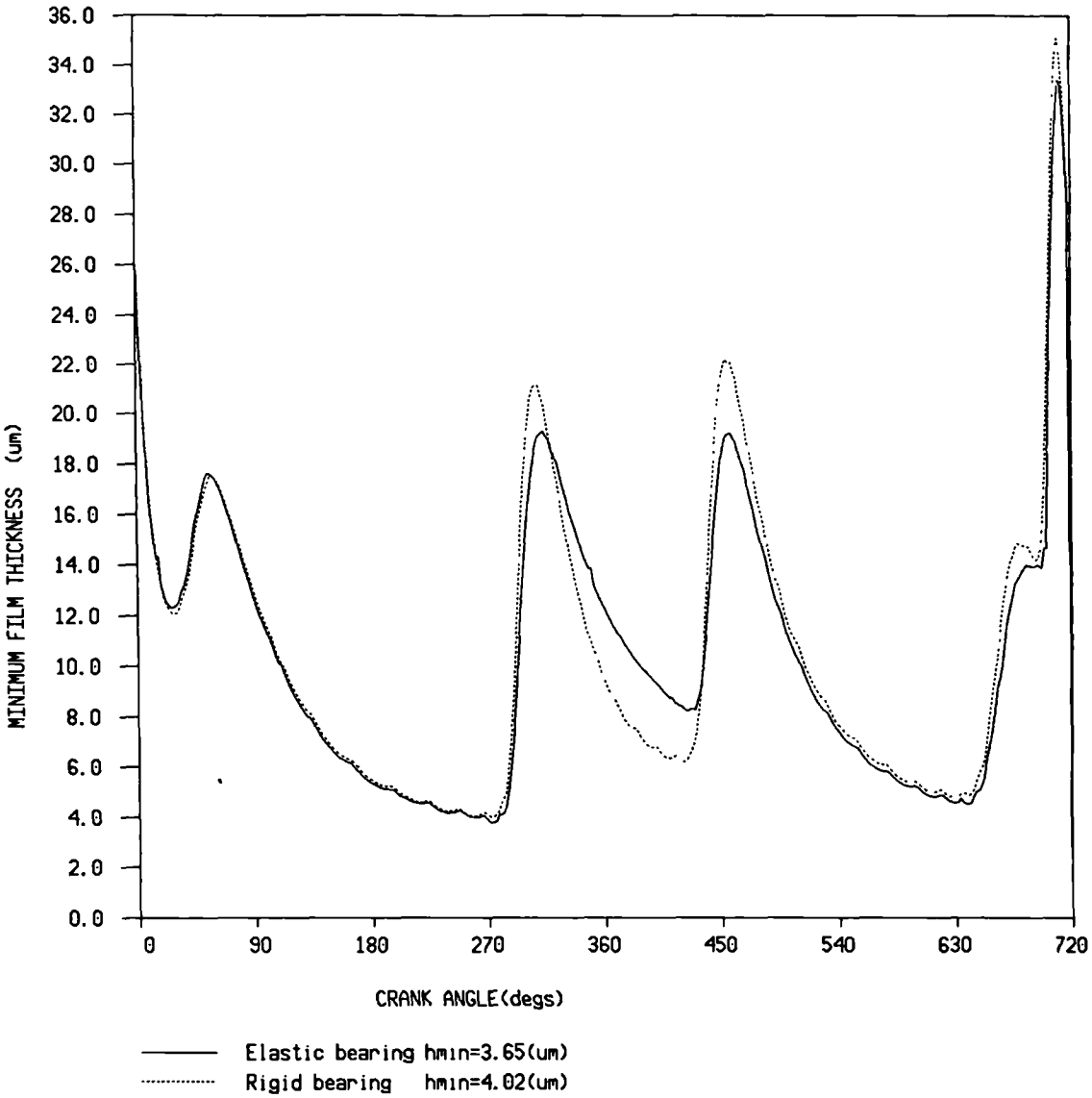

Figure 7.17 - Cyclic variation of the minimum film thickness for the rigid and elastic bearing examples.

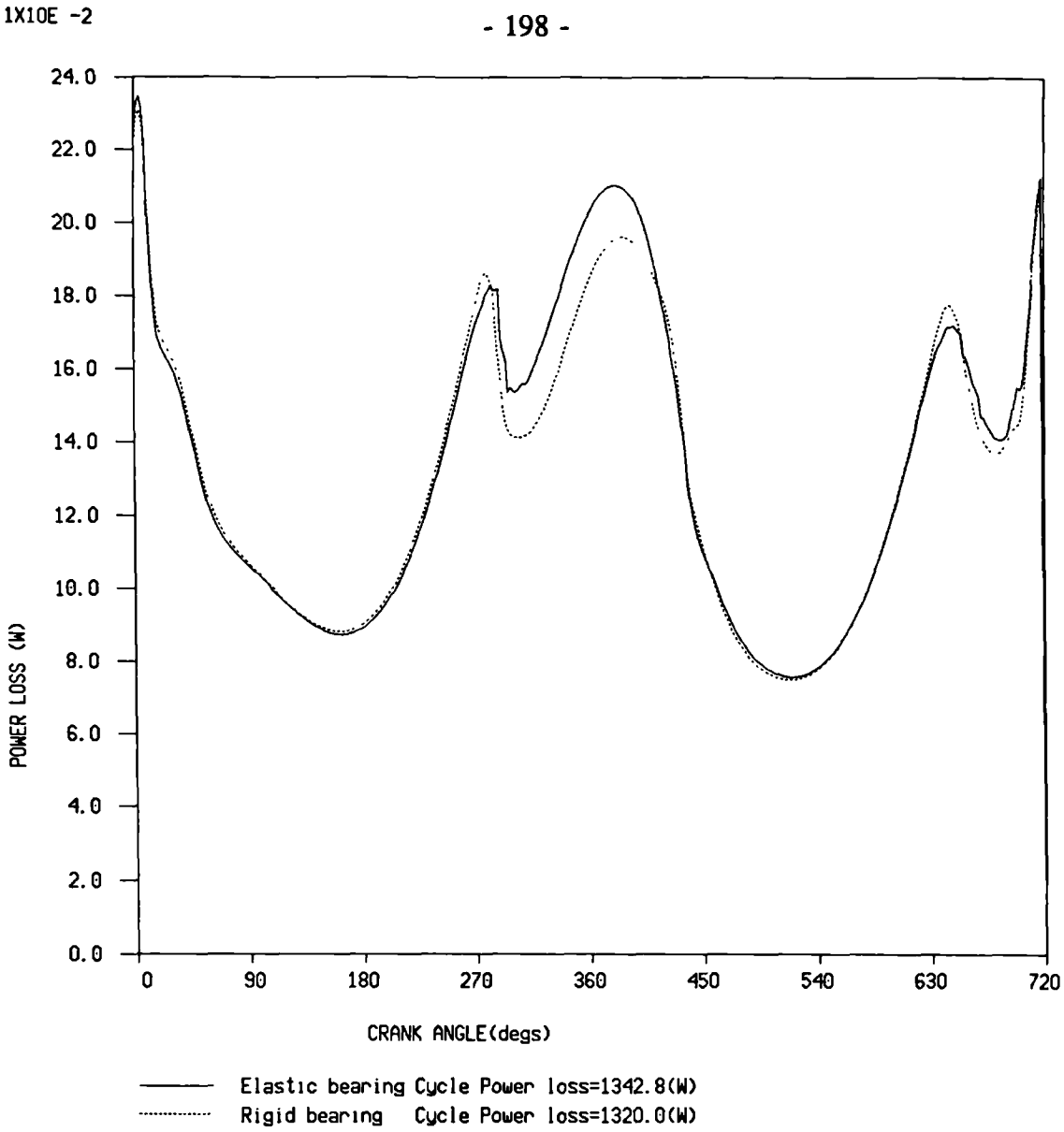

Figure 7.18 - Cyclic power loss for the rigid and elastic bearing examples.

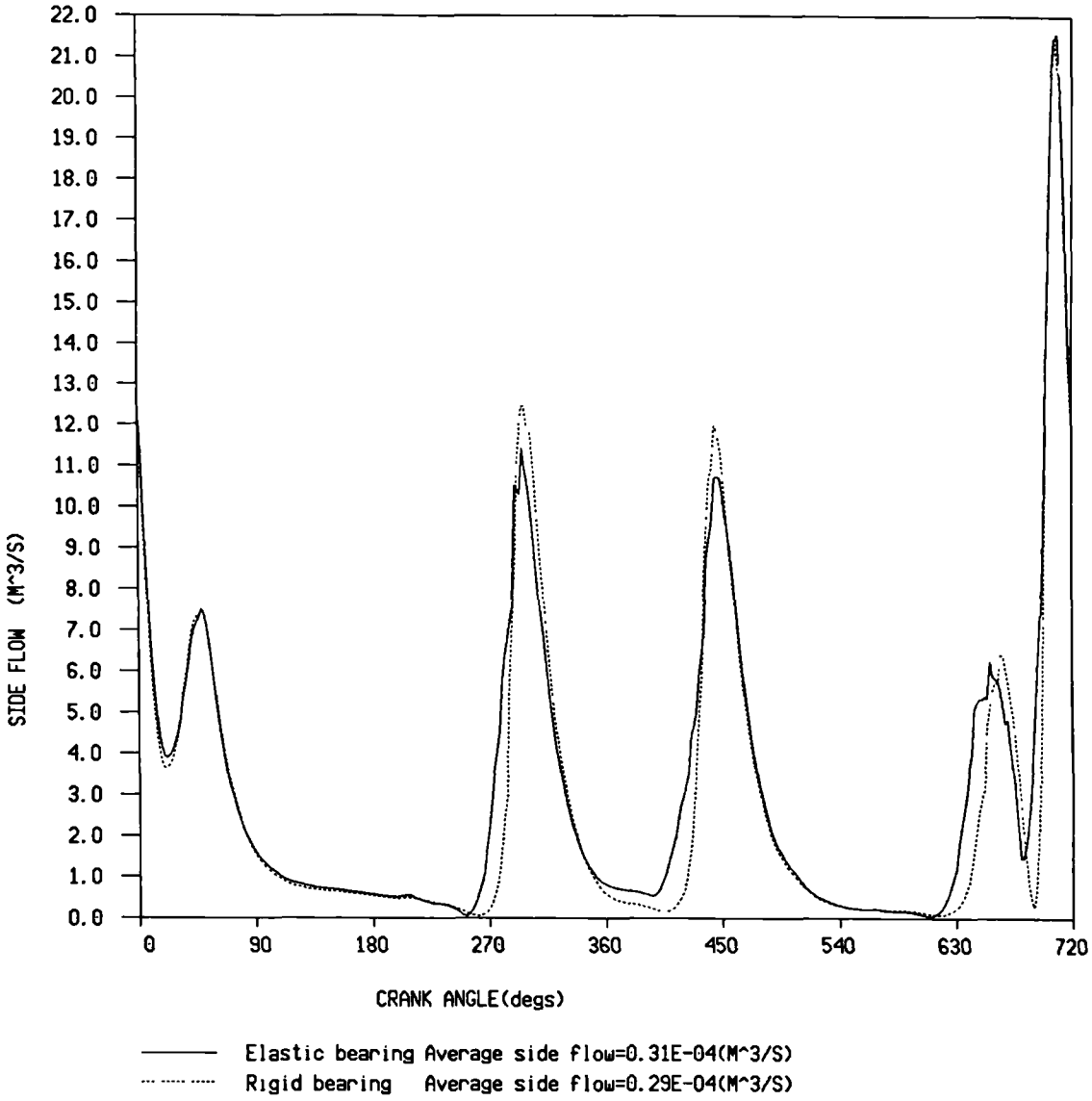

Figure 7.19 - Predicted side flow for the rigid and elastic bearing examples.

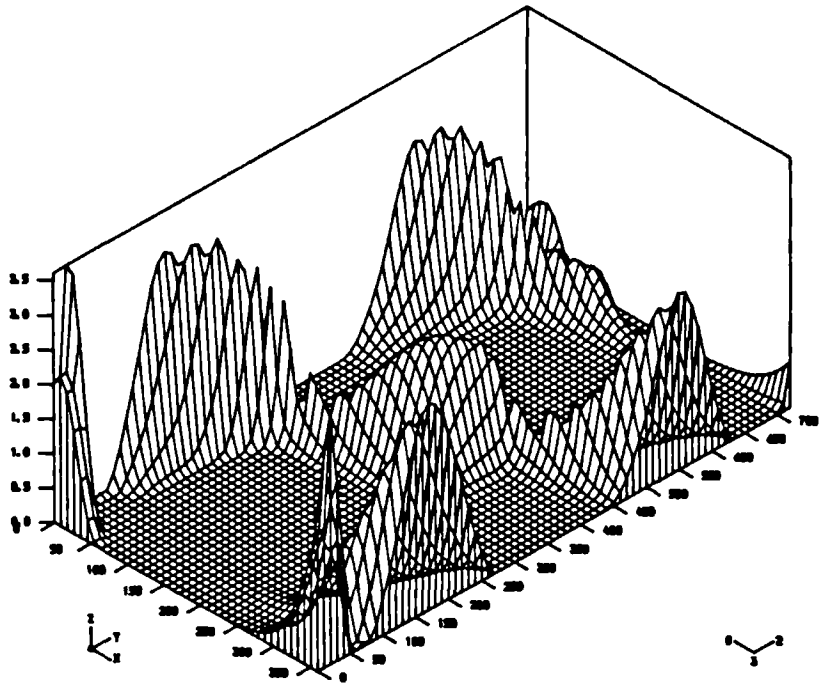

Flexible bearing

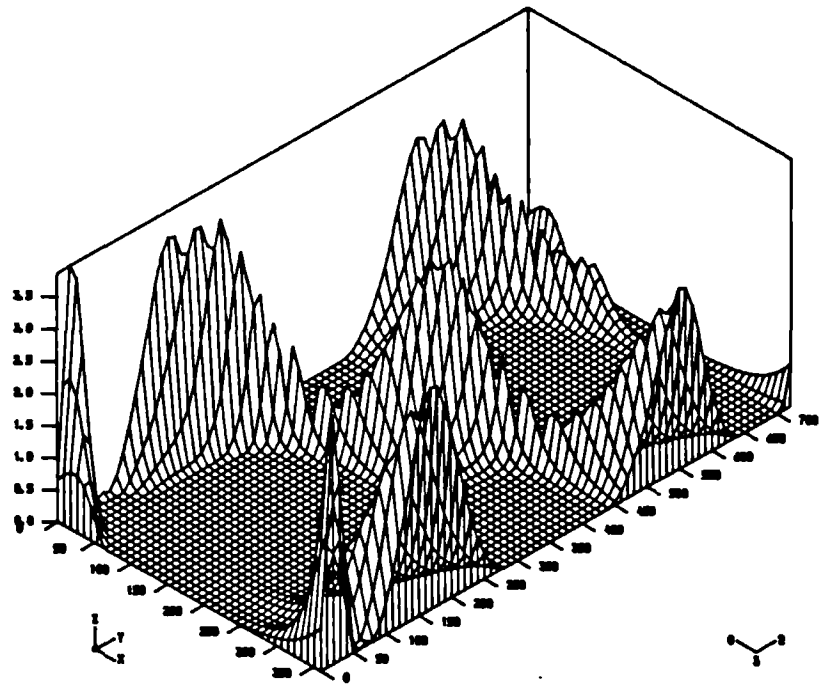

Rigid bearing

Figure 7.20 - Midplane pressure variation during an engine cycle for the rigid and elastic bearing.

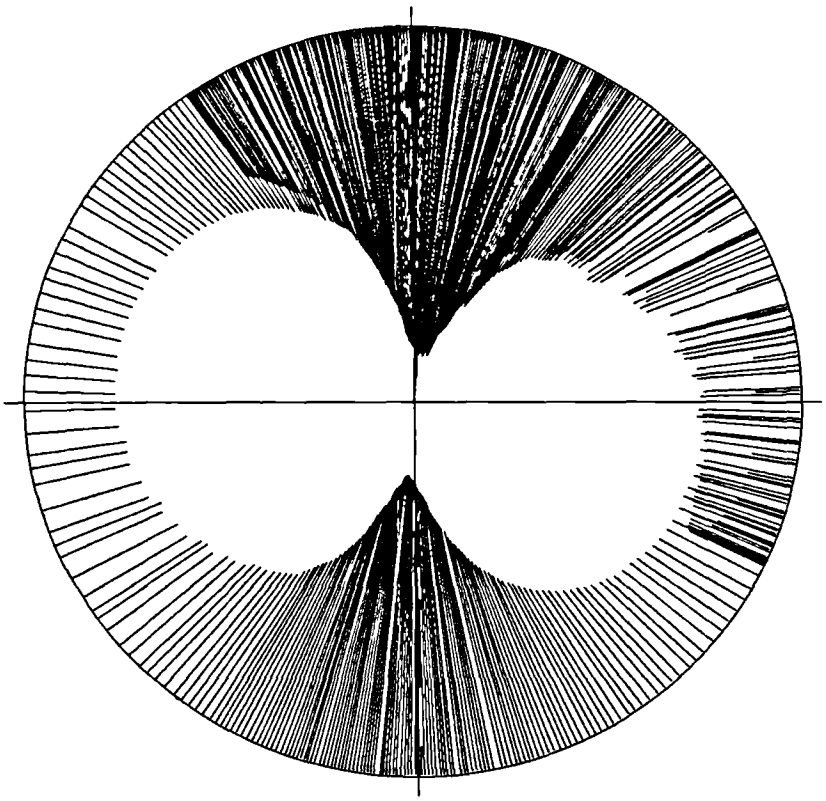

MAXIMUM FILM PRESSURE 33.44(MPa) AT 10.0(deg)

Figure 7.21 - Vector plot of peak film pressures for the rigid bearing.

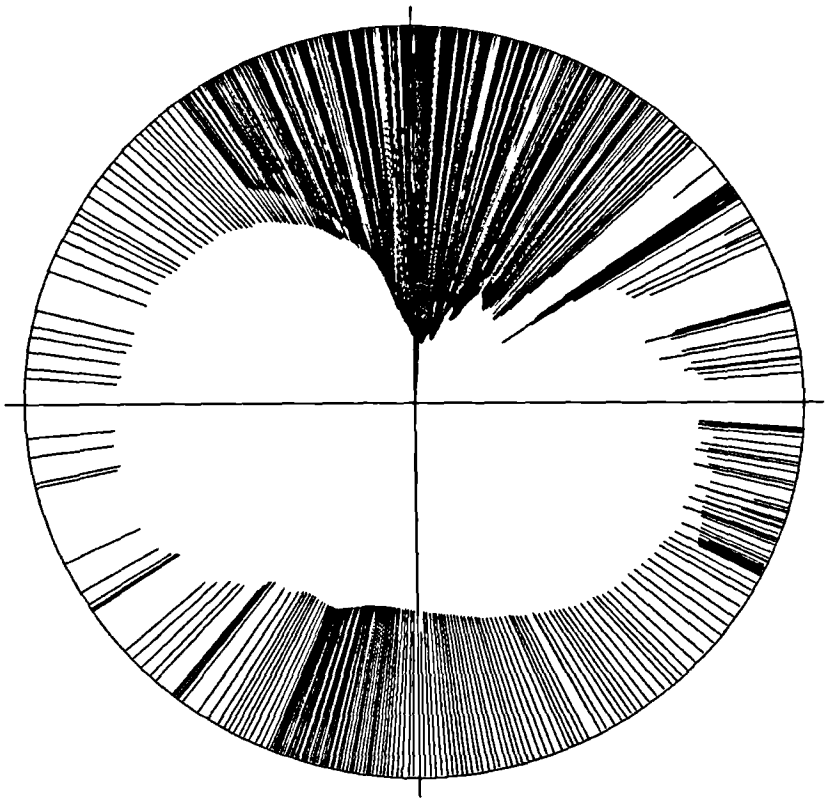

MAXIMUM FILM PRESSURE 31.52(MPa) AT 10.0(deg)

Figure 7.22 - Vector plot of peak film pressures for the elastic bearing.

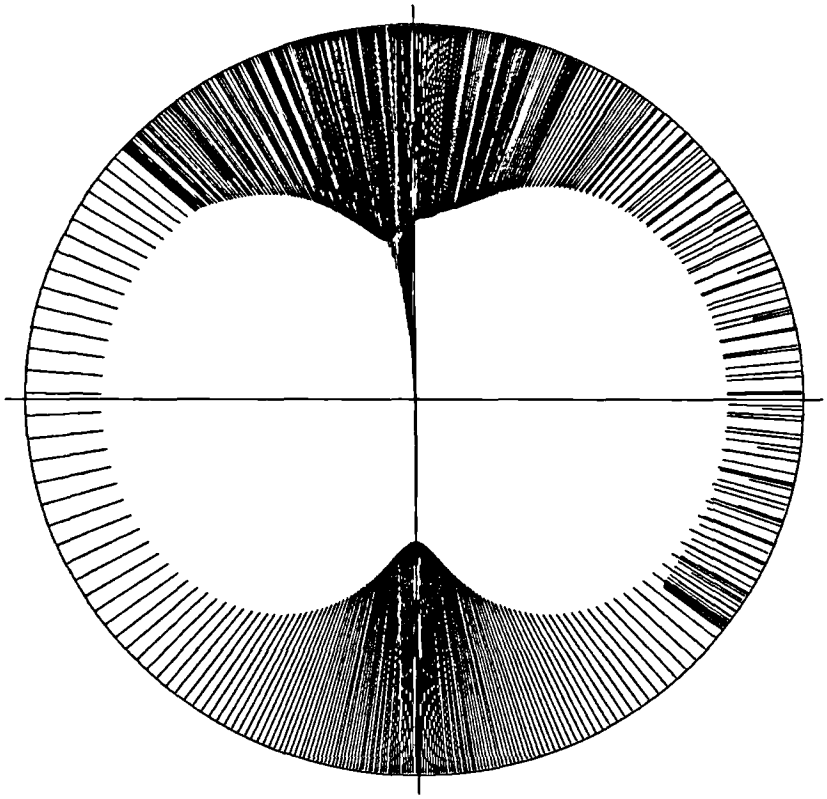

Figure 7.23 - Vector plot of bearing loads.

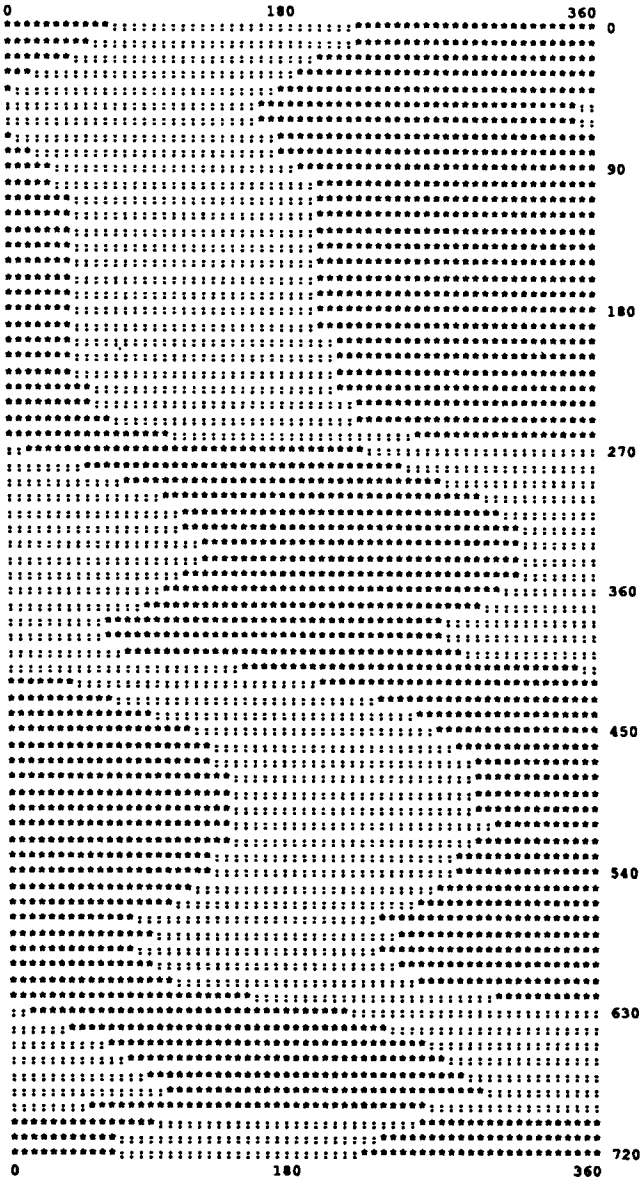

Figure 7.24 - Pressure map for the rigid bearing example.

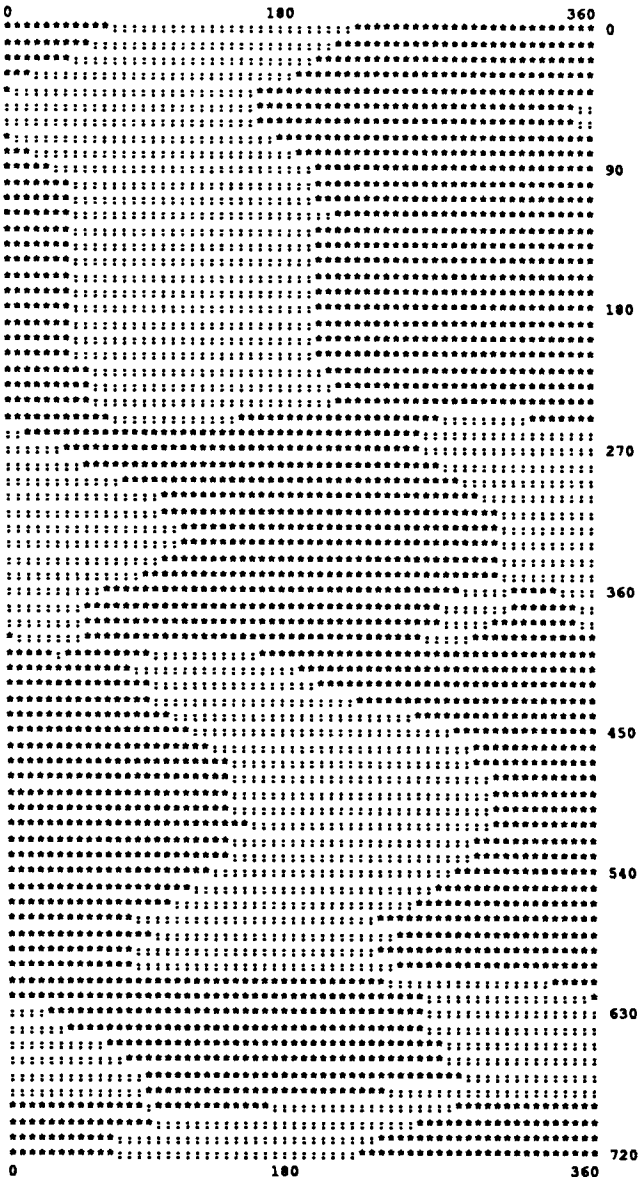

Figure 7.25 - Pressure map for the elastic bearing example.

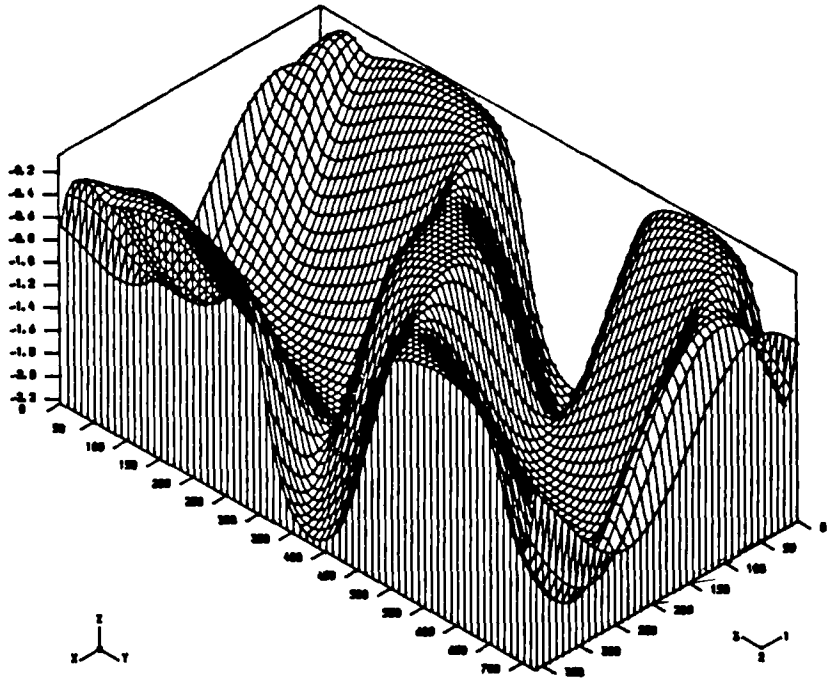

Flexible bearing

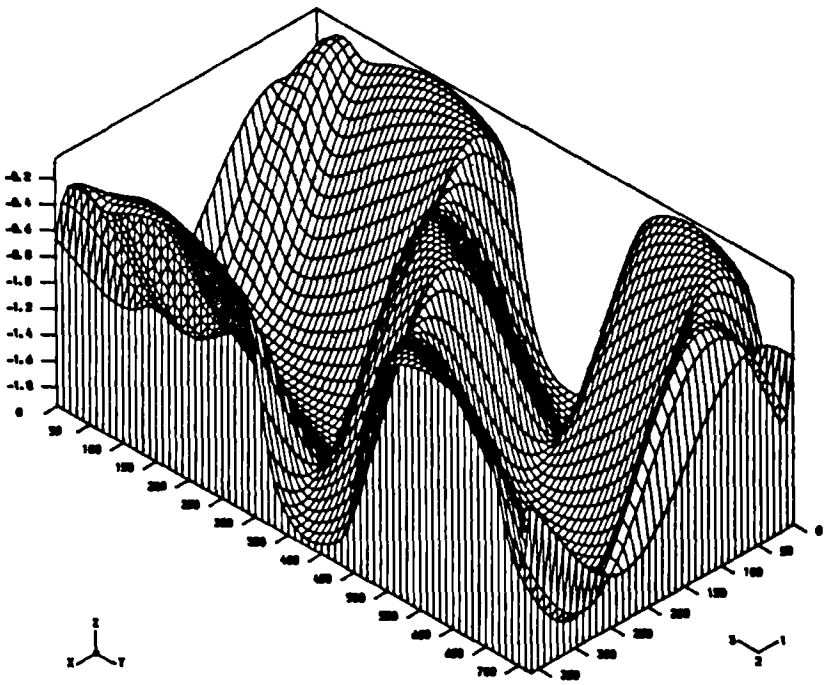

Rigid bearing

Figure 7.26 - Variation of midplane film profile during engine cycle .

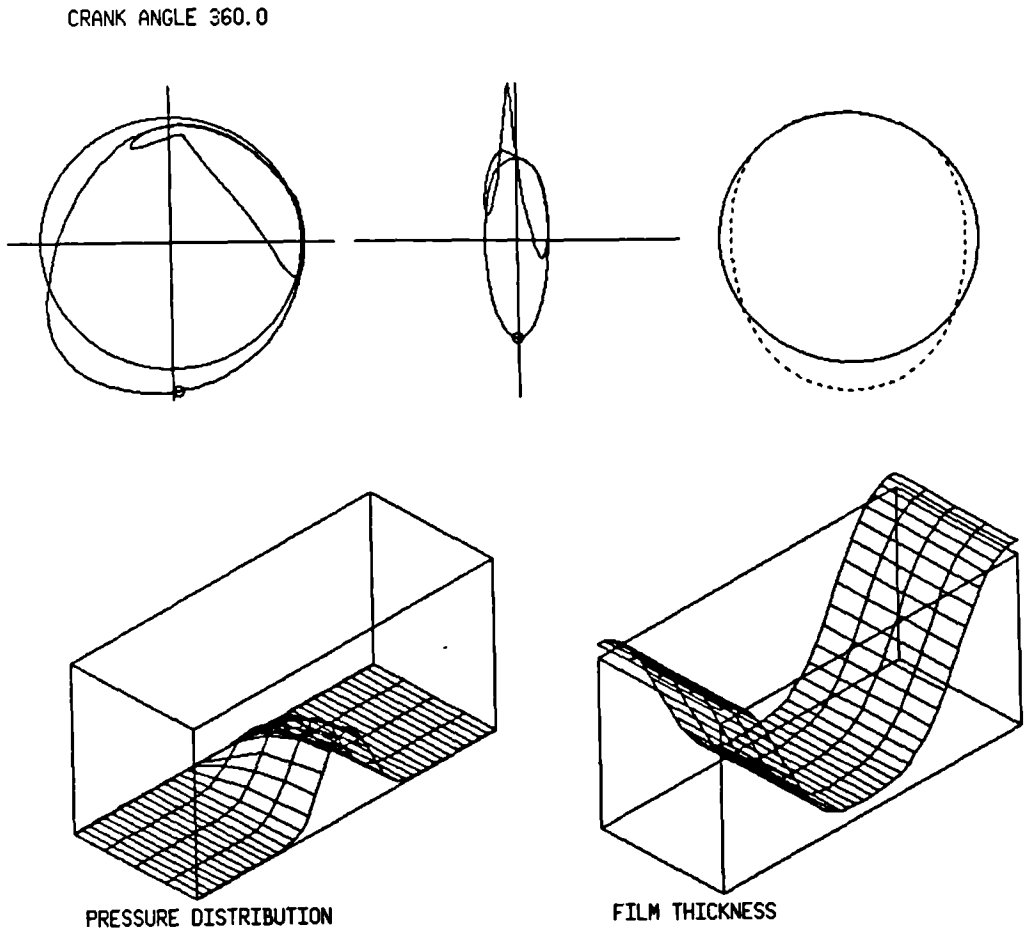

Figure 7.27 - Data plot at 360 degrees crank angle.

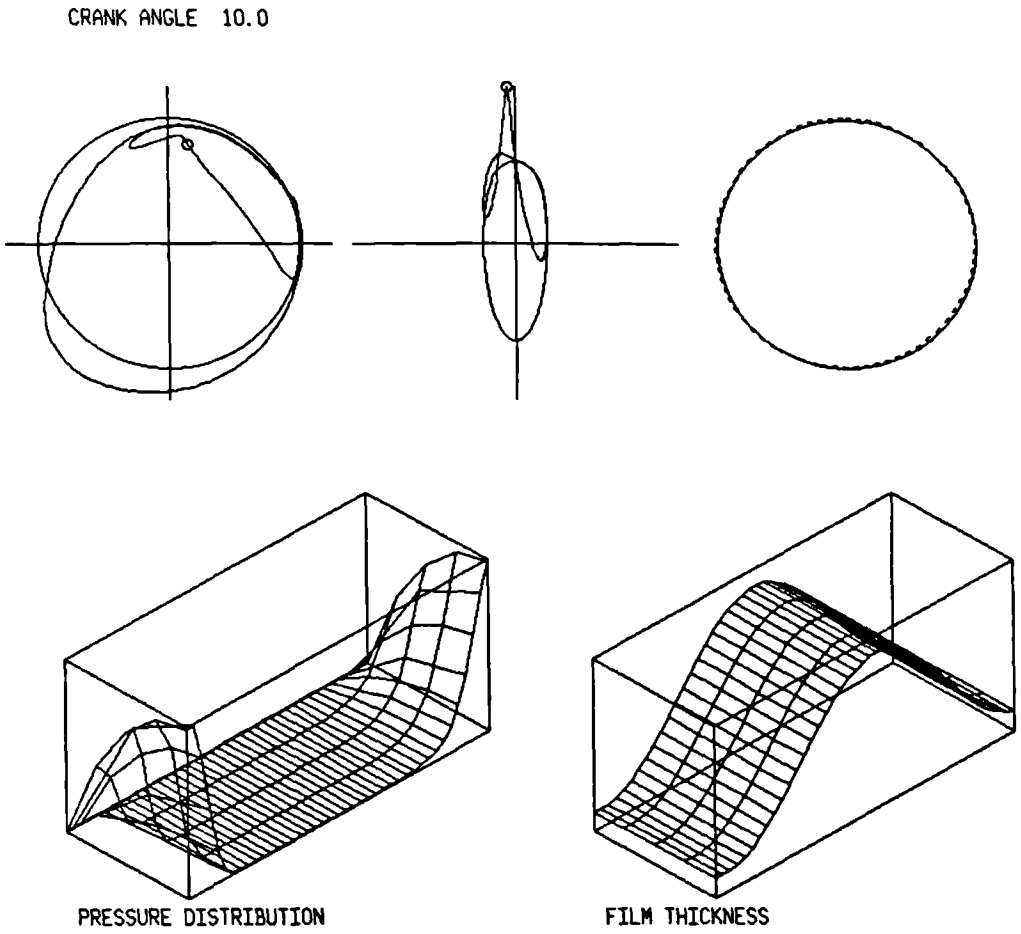

Figure 7.28 - Data plot at 0 degrees crank angle.

Chapter 8

Conclusions

8.1 Rigid bearing work

The object of the work was to develop a fast and efficient method for the predictive analysis of dynamically loaded, flexible journal bearings. The initial part of the work that was carried out was to first develop a method for analysing the rigid bearing problem. The finite element method was used to model the problem, two different element types being investigated. Initially 3-node triangular elements, which have been widely used by other authors, were used. Subsequent work [50], however, showed that 8-node isoparametric elements, although being considerably more complex to implement, were better able to resolve the pressure distribution requiring considerably fewer nodes for a given degree of accuracy.

The Gauss-Seidel over-relaxation technique was used to solve the finite element equations and using this method the Reynolds boundary condition and the non-negative pressure constraint could easily be incorporated during the solution process. Due to the high convergence rate of this method it was possible to reduce the number of calculations required by exploiting the early definition of the cavitated region. It was also possible to exploit the sparseness of the system matrices by the appropriate use of steering vectors during the matrix assembly and the subsequent over-relaxation process. An optimum value of over-relaxation factor was found to be between 1.55 and 1.65 for the 3-node triangular elements, depending upon the mesh size, and 1.5 for the 8-node isoparametric elements. The latter elements proved to be less sensitive to the choice of over-relaxation factor.

Two different time stepping methods were investigated, the implicit and explicit methods, both of which showed a comparable degree of accuracy. The explicit method, although being unstable if a large time step was used, considerably reduced the number of complete matrix assemblies required during the soution process, thereby considerably reducing the required computing time. Two different methods were also developed for assessing the accuracy of the squeeze term in the finite element formulation, one quantitative, the other qualitative.

An efficient and highly convergent method based upon the modified Newton-Raphson method was developed for finding the required journal position to balance the applied bearing load. It was also found that the number of iterations at a given time step to obtian the required journal position could be reduced by extrapolating from previous time steps. A relatively simple method was developed for incorporating oil feed features into the analysis which appeared to work well for full circumferential grooves and oil holes but for partial grooves it was found that a more rigorous approach would be required.

The analysis method developed for the rigid bearing problem proved to be extremely fast, being more than an order of magnitude faster than previous methods. It was concluded that for an accurate analysis, using 8-node isoparametric elements to model the lubricant film, a mesh size of 41 circumferential and 5 axial nodes, (7 axial nodes if oil feed features were to be included), and a time step size of two degrees of crank rotation were required.

8.2 Flexible bearing work

The first part of the flexible bearing analysis was to construct a model of the bearing housing to obtain a relationship between the nodal pressures and the housing distortions. Finite elements were used to construct a three-dimensional model of the bearing housing. Since 8-node isoparametric elements were to be used for the lubricant film 20-node brick elements were used for the structural modelling since, due to the way in which the equivalent nodal point forces are obtianed for the 8-node elements, it was important that the two elements types were compatible. The relationship between the nodal pressures and the housing deformations was obtained in the form of a structural compliance matrix. This was achieved by using condensation to obtain a reduced finite element stiffness matrix for the nodes on the inner surface of the housing relating the nodal forces to the radial displacements at these nodes. This was then inverted to obtain the required compliance matrix. A fast matrix inversion method was developed to achieve this which proved to be more than an order of magnitude faster than the corresponding NAG matrix inversion subroutines.

The under-relaxation method was intially used to couple the structural and lubrication problems. This method proved simple to implement in the existing rigid

bearing program and showed satisfactory results for the steady loaded bearing problem, an improvement on existing under-relaxation methods being proposed by applying under-relaxation to both the nodal film thickness and the nodal pressures. It was, however, found that this method proved unsatisfactory for the dynamically loaded bearing problem. This was due to the difficulty in finding a general method for ensuring that an optimum value was being used for the under relaxation factor.

The Newton-Raphson method that was subsequently used to couple the two problems proved highly convergent for all cases but required a prohibitively large amount of computing time to achieve a solution. In an attempt to reduce the computing time this method was highly modified to produce a fast Newton-Raphson method [51]. This method was generally based upon the modified Newton-Raphson method and relied upon assembling the fully populated matrix $[A]$ as few times as possible during the analysis.

It was found that the general effect of incorporating elasticity into the bearing analysis is that the peak pressure and the value of the minimum film thickness both decrease and the power loss and side flow increase for both the steady loaded and dynamically loaded problems. The extent of the pressure region also increases, and over some parts of the engine cycle large regions of small film thickness are observed. Under heavy loading, especially where the peak in the corresponding pressure distribution occurs over a region of high flexibility when a distinctive bimodal pressure distribution is observed.

Several graphics packages have also been developed that simplify the interpretation of the results obtained from the analysis. The animation is particularly useful for determining the behaviour and can convey considerably more information and give a much better understanding for the way in which the bearing is behaving than a static plot.

The method developed for the EHD analysis of dynamically loaded journal bearings proved to be more than two orders of magnitude greater than previous methods making this method viable as a general design tool, previously an EHD analysis of this form had merely served as a one off bench mark to compare the accuracy of more simplified analysis methods.

8.3 Future work

In the work presented in this thesis two methods have been developed for the analysis of dynamically loaded rigid and flexible journal bearings. Both methods, particularly the EHD analysis method, have proved more than an order of magnitude faster than any previous methods for finite bearings. Now that the major hurdle encountered in this form of analysis has been crossed, namely the prohibitively large amount of computing time required, the ground has been opened for a variety of further work.

Clearly there are a large number of refinements that can be made to the existing programs. A more realistic model could be developed for incorporating oil feed features into the analysis. The effects of the housing distortion due to bolt tension, stepped bearings and the effects of barrelling and hour glassing can also be incorporated. These effects can easily be included since the finite element method used for the analysis allows irregularities such as these to be easily incorporated in a routine fashion. Due to the way in which the Newton-Raphson equations are formulated piezoviscous effects can be included in the analysis requiring only a few minor adjustments to the existing code without requiring any further iteration loops to be added.

It would also be useful to use a more realistic structural model of the housing. Since the work presented was more concerned with developing and quantifying a general method for predicting the bearing performance than presenting accurate results for a specific bearing the structural model used was very simplified. It would, therefore, be advantageous to investigate how much of the connecting-rod needs to be modelled to give an accurate prediction of the bearing performance.

Since the two methods that have been developed are significantly faster than any previous methods (the rigid bearing analysis method only takes a few minutes to run) it is now viable to begin to examine the bearing behaviour under transient engine conditions such as throttling which requires the bearing performance to be predicted over a large number of engine cycles rather than just a single cycle with the engine running at a constant speed. It should also be possible to begin work on developing a model to analyse all the engine bearings at once. This will allow more realistic load sharing calculations to be performed and effects such as the crankshaft flexibility and the heat flow within the engine to be included in the analysis.

References

[1] Reynolds, O., On the theory of lubrication and its application to Mr Beauchamp's tower experiments including the experimental determination of the viscosity of olive oil, Philosophical Transactions of the Royal Society of London, England, Vol 177, 1887, 157-234.

[2] Sommerfeld, A., Fur hydrodynamischen Theorie der Schmiermittelreibung, Zeit angew. Math. u. Physik., 1904, 50, 97-155

[3] Mitchell, A. G. M., Progress in fluid film lubrication, Trans ASME, 1929, 51, M.S.P.51.21.,153-163.

[4] Ocvirk, F. W. and DuBois, G. B., Analytical derivation and experimental evaluatioin of short bearing approximations of full journal bearings, N.A.C.A. Tech. Rep., 1953, 1157.

[5] Campbell, J., Love, P. P., Martin, F. A. and Rafique, S. O., Bearings for reciprocating machinery : a review of the present state of theoretical, experimental and service knowledge, Proc. I. Mech. Eng., 1967, 182 Part(3A), 51-74.

[6] Booker, J. F., Dynamically loaded journal bearings, mobility method of solution, Trans ASME, Jnl. Basic. Engg., 1965, 187, 537-546.

[7] Jones, G. J., Lee, C. S. and Martin, F. A., Crankshaft bearings : Advances in predictive techniques incorporating the effects of oil holes and grooving, AE Symposium, April 1982

[8] Christopherson, D. G., A new mathematical method for the solution of film lubrication problems, Proc. I. Mech. Eng., 1942, 146, 126-135.

[9] Cameron, A. and Wood, Mrs W. L., The full journal bearing, Proc. I. Mech. Eng., 1949, 161, 59-69.

[10] Cameron, A., *The principles of lubrication,* Longmans, Green and Co Ltd, 1966.

[11] Raimondi, A. and Boyd, J., A solution for finite journal bearings and its application to analysis and design, pts I,II and III, Trans ASLE, 1958, Vol 1, No1, 159-209.

[12] Pinkus, O., Solution of Reynolds equation for finite journal bearings, Trans ASME, 1958, Vol1, No1, 858-864.

[13] Holmes, A. G. and Ettles, C. M. Mc C., A study of iterative solution techniques for elliptical partial differential equations with particular reference to the Reynolds equation, Comp. Meth. Appl. Mech. Eng., 1975, 5, 3, 309-328.

[14] Gero, L. R. and Ettles, C. M. Mc C., An evaluation of finite difference and finite element methods for the solution of Reynolds equation, Trans ASLE, 1986, 29, 2, 166-172.

[15] Zienciewicz, O. C. and Cheung, Y. K., Finite elements in the solution of field problems, The Engineer, 1965, 220, 507.

[16] Visser, W., A finite element method for the determinaation of non stationary temperature distribution and thermal deformations, Proc. Conf. Matrix Meth. Struct. Mech., 1965, (Wright-Patterson Air Force base Ohio)

[17] Hayes, D. F., A variational approach to lubrication problems and the solution of the finite journal bearing, Trans ASME, J. Basic Engg., 1959, 13-23.

[18] Tao, L. N., On the variational principle and the Lagrange equations in the studies of gas dynamics, Trans ASME, J. Appl. Mech., 1964, 86, 43-46

[19] Reddi, M. M., The finite element solution of the incompressible lubrication problem, Trans ASME, J. Lub Tech., 1969, 191, 524-533.

[20] Reddi, M. M. and Chu, T. Y., Finite element solution of the steady state compressible lubrication problem, Trans ASME, J. Lub. Tech., 1970, 92, 495-503.

[21] Booker, J. F. and Huebner, K. H., Application of finite element methods to lubrication; An engineering approach, Trans ASME, J. Lub. Tech., 1972, 94, No4, 313-323.

[22] Goenka, P. K., Dynamically loaded journal bearings : finite element method analysis, Trans ASME, J. Trib., 1984, 106, 429-439.

[23] Goenka, P. K., Analytical curve fits for solution parameters of dynamically loaded journal bearings, Trans. ASME, J. Trib., 1984, 106, 421-428

[24] Rohde, S. M. and Mc Allister, G. T., A variational formulation for a class of free boundary problems arising in hydrodynamic lubrication, Int. J. Engg. Sci., 1975, 13, 841-850.

[25] Jakobsson, B. and Floberg, L., The finite journal bearing considering vaporisation, Trans Chalmers Univ. Tech., Goteburg, Sweden, No216, 1957.

[26] Olsson, K., Cavitation in dynamically loaded bearings, Trans Chalmers Univ. Tech., Goteburg, Sweden, No308,1965.

[27] Elrod, H. G. and Adams, M. L., A computer program for cavitation and starvation problems. Leeds-lyon conference on cavitation, Leeds Univ., 1974, 37-41.

[28] Elrod, H. G., A cavitation algorithm, Trans ASME, J. Lub. Tech., 103, No3, 1981, 350-354.

[29] Brewe, D. E., Theoretical modelling of the vapour cavitation in dynamically loaded journal bearings, Trans ASME, J. Trib., 1986, 108, 628-638.

[30] Milne, A. A., Variations of film extent in dynamically loaded bearings, 1st Leeds-Lyon Symposium, 1974, Paper iv(i), 79-90.

[31] Milne, A. A., A finite element method of calculating oil flow in bearings, NEL Report No 569, 1974.

[32] Milne, A. A. Transient variation of film extent, NEL Report 565, 1974.

[33] Jones, G. J., Crankshaft bearings: oil film history, Proc 9th Leeds-Lyon Symposium on Tribology, Sept 1982, 82-88.

[34] Jakeman, R. W., A numerical analysis method based on flow continuity for hydrodynamic journal bearings, Trib. Int., 17, No6, 1984, 325-333.

[35] Jakeman, R. W., Journal orbit analysis taking account of oil film history and journal mass, 4th International Conference on Numerical Methods in Laminar and Turbulent FLow, Swansea, July, 1985, 199-210.

[36] Dowson, D. and Higginson, G. R., *Elastohydrodynamic lubrication,* Pregamon Press, Oxford, 1966

[37] Taylor, C. and O'Callaghan, J. F., A numerical solution of the elastohydrodynamic lubrication problem using finite elements, J. Mech. Eng. Sci., 1972, 14, No4, 229-237.

[38] Stafford, A. C., Henshell, R. D. and Dudley, B. R., Finite element analysis of problems in elastohydrodynamic lubrication, 5th Leeds- Lyon Symposium on Tribology, Leeds, England, 1978, 35-41.

[39] Bozaci, A., Dudley, B. R., Middleton, V. and Allen., D. G., Steady load performance of a journal bearing with an elastic housing, 5th Leeds-Lyon Symposium on Tribology, Leeds, England, 1978, 320-328.

[40] Frene, J., Desailly, R. and Fantino, B., Hydrodynamics of an elastic connecting rod bearing; comparison of theoretical and experimental results, 5th Leeds-Lyon Symposium on Tribology, Leeds, England, 1978, 329-338.

[41] Eugene, P., Frene, J., Fantino, B., Roussel, G. and Du Parquet, J., Theory and experiments on elastic connecting rod bearings under steady state conditions,9th Leeds-Lyon Symposium on Tribology, Leeds, England, 1982, 49-54.

[42] Fantino, B., Frene, J. and Du Parquet, J., Elastic connecting rod bearing with a piezo-viscous lubricant : analysis of the steady state characteristics, Trans ASME, J. Lub. Tech., 1979, 101(2), 200-211.

[43] Fantino, B., Godet, M. and Frene,J., Dynamic behaviour of an elastic connecting rod bearing : theoretical study, SAE/SP-539, Studies of engine bearings and lubrication, Paper No 83037, 1983, 23-32.

[44] Fantino, B. and Frene, J., Comparison of the dynamic behaviour of elastic connecting rod bearings in both petrol and diesel engines. Trans. ASME, J. Trib., 1985, 107, 87-91.

[45] La Bouff, G. A. and Booker, J. F., Dynamically loaded journal bearings : a finite element treatment for rigid and elastic surfaces, Trans. ASME, J. Trib., 1985, 107, 505-515.

[46] Rohde, S. M. and Oh, K. P., A unified treatment of the elastohydrodynamic lubrication problem using higher order finite element methods, Proc. Roy. Soc. (London), 1975, Series A, 343, 315-331.

[47] Oh, K. P. and Goenka, P. K., The elastohydrodynamic solution of a journal bearing under dynamic loading, Trans. ASME, J. Trib., 1985, 107, 3, 389-395.

[48] Goenka, P. K. and Oh, K. P., An optimum short bearing theory for the elastohydrodynamic solutioin of journal bearings, Trans. ASME, J. Trib., 1986, 108, 294-299.

[49] Goenka, P. K. and Oh, K. P., An optimum connecting rod design study, a lubrication viewpoint, Trans. ASME, J. Trib., 1986, 108, 487-496.

[50] Mc Ivor, J. D. C. and Fenner, D. N., An evaluation of eight-node quadrilateral finite elements for the analysis of a dynamically loaded journal bearing, Proc. I. Mech. Eng., 1988, Vol 202, No C2, 95-101.

[51] Mc Ivor, J. D. C. and Fenner, D. N., Finite element analysis of dynamically loaded flexible journal bearings : a fast Newton-Raphson method, submitted to Trans. ASME, J. Trib., August 1988.

[52] Booker, J. F., Goenka, P. K. and Van Leeuwen, H. J., Dynamic analysis of rocking bearings with multiple offset segments, Trans ASME, J. Lub.Tech., 1982, 104, 4, 478-490.

[53] Zienkiewicz, O. C., *The finite element method,* McGraw-Hill Book Co (UK) Ltd, 1977.

[54] Hinton, E. and Owen, D. R. J., *Finite element programming,* Academic Press, 1977.

[55] Goenka, P. K. and Booker, J. F., Spherical bearings; Static and dynamic analysis vis the finite element method, Trans. ASME, J. Lub. Tech., 102, 3, 1980, 308-319.

[56] Stasa, F. L., *Applied finite element analysis for engineers,* CBS Publishing, Holt Reinhardt and Winston, Dryden press, Saunders College Publishing, 1985.

[57] Huebner, K. H., *The finite element method for engineers,* John Wiley and sons, 1975.

[58] Chandrasakeran, R., A special case of the the complementarity problem, Opsearch, 1970, 7, 263-268.

[59] Anderson, D. A., Tannehill, J. C., Pletcher, R. H., *Computational fluid mechanics and heat transfer,* Hemisphere publishing Co., Mc Graw-Hill Book Co, 1984.

[60] Chapra, S. C., Canale, R. P., *Numerical methods for engineers with personal computer applications,* Mc Graw-Hill Book Co., 1985.

[61] Martin, F. A., Developments in engine bearing design, Trib. Int., 1983, 106(3), 147-164.

[62] Martin, F. A., Private communication.

[63] Ricardos Consulting Engineers, Private communication.

[64] Martin, F. A., Private communication.

[65] Jennings, A., *Matrix computation for engineers and scientists,* Wiley-Interscience Publications, John Wiley and Sons, 1977.

[66] Oh, K. P., The numerical solution of dynamically loaded elastohydrodynamic contact as a nonlinear complimentarity problem, Trans ASME, J. Trib., 1984, 106, 88-95.

[67] Murty K. G., Note on a bard type scheme for solving the complementarity problem, Opsearch, 1974, 11 123-130.

[68] Ortega, J. M. and Rheinboldt, N. C., *Iterative solution techniques of non-linear equations in several variables,* Academic Press, 1970.